7-2018

Wireless Sensors for Health Monitoring of Marine Structures and Machinery

Francisco David Rojas Calvente
Cork Institute of Technology

Wireless Sensors for Health Monitoring of Marine Structures and Machinery

Francisco David Rojas Calvente

Nimbus Centre for Embedded Systems Research

Department of Electronic Engineering
Cork Institute of Technology

Supervised by Prof. John Barrett

A thesis submitted for the Degree of

Doctor of Philosophy

to Cork Institute of Technology, July 2018

Declaration

This thesis is entirely the candidate's own work except where otherwise accredited and has not been submitted for an award at any other institution.

The research presented in this thesis was carried out in compliance with the CIT Code of Good Practice in Research.

Candidate: _____ **Date:** _____

Supervisor: _____ **Date:** _____

Acknowledgements

I would firstly like to thank my supervisor John Barrett for his help and advice during the course of this PhD, and also internship students Simon Vanson, Raphael Bresson, Valentin Lacquemant, and Pierre-Louis Bergues for their support in hardware and software testing. I would also like to thank the people of my office: Ramona, Victor, Sameera, Roland, Dylan and the lost ones Pablo and Alejandro, for their help with Contiki and Trident, as well as their insights into software development, networking, and signal processing; to Juanfran for being always so helpful with providing and setting up all sorts of equipment, tools, and material in Nimbus.

This project would not have been possible without the help and support of Conor Mowlds, Vivian Gough, Paul Nash and Tim P. Forde from the National Maritime College of Ireland (NMCI), as well as Commodore Hugh Tully, Lieutenant Commander David Memery, and Lieutenant (NS) Padraig Reaney from the Irish Naval Service (INS). A thank you also to Tony Compagno of Tyndall for the use of the salt mist chamber.

On a personal note, I would like to thank my parents, sister, and Pilar for supporting me during this long journey. Finally, to the rest of the fine people in Nimbus for their nice and interesting discussions over coffee: Bill, Manuel, Juanma, Kritchai, Javier, and the rest.

This work was supported by Science Foundation Ireland through The SFI Centre for Marine and Renewable Energy Research (MaREI) under Grant 12/RC/2302.

List of Publications

1. **David Rojas** and John Barrett. Link Quality Evaluation of a Wireless Sensor Network in Metal Marine Environments, *Wireless Networks, Springer.* April 2018.
2. **David Rojas** and John Barrett. A Novel 3D Embedded Module for Displacement Measurement in Metal Structures, *IEEE Transactions on Components, Packaging and Manufacturing Technology.* Volume: 7, Issue: 11, pp. 1765-1773, Nov. 2017.
3. Ramona Marfievici, Pablo Corbalan, **David Rojas**, Alan McGibney, Susan Rea, and Dirk Pesch. Tales from the C130 Horror Room: A Wireless Sensor Network Story in a Data Center, *FAILSAFE'17, the* 1^{st} *ACM International Workshop on the Engineering of Reliable, Robust, and Secure Embedded Wireless Sensing Systems.* Delft, The Netherlands, pp. 24-31, November 2017.
4. **David Rojas** and John Barrett. A Hardware-Software WSN Platform for Machine and Structural Monitoring, *28th Irish Signals and Systems Conference.* Killarney, Ireland, pp. 1-6, June 2017.
5. **David Rojas** and John Barrett. Experimental Analysis of a Wireless Sensor Network in a Multi-Chamber Metal Environment, *Proceedings of the 22nd European Wireless Conference (European Wireless 2016).* Oulu, Finland, pp. 1-6, May 2016.

List of Other Publications

1. Sameera Palipana, **David Rojas**, Piyush Agrawal, and Dirk Pesch. FallDeFi: Ubiquitous Fall Detection using Commodity WiFi Devices, *Proceedings of the ACM on Interactive, Mobile, Wearable and Ubiquitous Technologies (IMWUT).*, Volume: 1, Number: 4, pp. 155-175 , January 2018.

Abstract

Remote structural and machinery health monitoring (SMHM) of marine structures such as ships, oil and gas rigs, freight container terminals, and marine energy platforms can ensure their reliability. However, the wired sensors currently used in these applications are difficult and expensive to install and maintain. Wireless Sensor Networks (WSN) can potentially replace them but there are significant capability gaps that currently prevent their long-term deployment in the harsh marine environment and the structurally-complex, compartmentalised, all-metal scenarios with high volume occupancy of piping, ducting and operational machinery represented by marine structures. These gaps are in sensing, processing and communication hardware and firmware capabilities, reduction of power consumption, hardware assembly and packaging for reliability in the marine environment, reliability of wireless connectivity in the complex metal structures, and software for WSN deployment planning in the marine environment. Taken together, these gaps highlight the need for a systems integration methodology for marine SMHM and this is the focus of the research presented in this thesis. The research takes an applied approach by first designing the hardware and firmware for two wireless sensing modules specifically for marine SMHM, one a novel eddy-current-based 3D module for measuring multi-axis metal structural displacement, the second a fully-integrated module for monitoring of structure and machinery reliability. The research then addresses module assembly and packaging methods to ensure reliability in the marine environment, the development of an efficient methodology for characterising the reliability of wireless connectivity in complex metal structures, and development of user interface software for planning WSN deployment and for managing the collection of WSN data. These are then individually and collectively characterised and tested for performance and reliability in laboratory, land-based and marine deployments. In addition to the research outcomes in each of these individual aspects, the overall research outcome represents a systems integration methodology that now allows deployment, with a high expectation of reliability, of marine SMHM WSNs.

Abbreviations & Acronyms

WSN	Wireless Sensor Network
MAC	Medium Access Channel
FBG	Fiber Bragg Grating
CCA	Clear Channel Assessment
GUI	Graphic User Interface
IP	Internet Protocol
PCB	Printed Circuit Board
COTS	Commercial Off-the-shelf
CAD	Computer-aided Design
SHM	Structural Health Monitoring
SHMS	Structural Health Monitoring System
SMHM	Structural and machine health monitoring
IC	Integrated Circuit
AC	Alternating Current
CRAC	Computer Room Air Conditioning
PDR	Packet Delivery Ratio
RSSI	Received Signal Strength Indicator
LVDT	Linear Variable Differential Transformer
LQI	Link Quality Indicator

Contents

List of Figures

Chapter 1

Introduction

1.1 Objectives of the work

The objective of the research presented in this thesis was the development and validation of a "whole-system" methodology for the design and deployment of wireless sensor networks (WSN) for structural and machinery health monitoring (SMHM) in offshore marine applications in large, metal structures such as ships, oil/gas and marine renewable energy platforms. In particular, it addressed the following key components in the whole-system approach:

- Miniaturisation, hardware systems integration, and reliability of networked multi-sensor wireless sensing nodes for SMHM in harsh marine environments.
- A systematic and time-efficient methodology for characterising WSN wireless link performance and reliability in complex, multi-chamber all-metal environments with a high concentration of operating machinery.
- Hardware/firmware/software co-design for SMHM wireless sensing networks. Hardware refers to the integration of microcontroller, memory, and sensors in a packaged module, while firmware is the code that is programmed in the microcontroller. Software refers to the program that runs in the PC connected to the gateway node.

In the broad context of addressing the gaps that currently restrict the deployment of marine SMHM WSNs, the specific research objectives are:

- A miniaturised, low power method to measure relative metal displacement between adjacent components in a structure.
- A fully integrated WSN module with vibration and acoustic sensors for SMHM.
- A firmware architecture for the WSN modules focused on sensing experiments, compatible with current embedded networked OS, with a user interface for remote experiment control and data collection.

The research therefore addresses 'systems integration', developing and integrating these key components to put in place the whole-system solution. Each component was individually validated through both laboratory and field testing and the overall methodology was validated through WSN deployment and testing in an on-board ship application.

1.2 Context of the work

Marine offshore structures have been deployed at sea for decades, whether for extraction of fossil fuels or the more recent wind and wave renewable platforms. Due to their difficult access and maintenance, the reliable monitoring of these structures and associated machinery becomes a key issue to ensure their own safety and that of their surrounding elements. This issue also affects naval and cargo vessels, as they are immersed in the same marine environment and contain structures and machinery of similar characteristics. To ensure a reliable collection of data, the monitoring and sensing system has to be made itself reliable. Traditional wired systems used for structural and machine monitoring of these platforms are of high cost and complexity. A Wireless Sensor Network (WSN) can reduce this complexity and cost, simplifying the deployment and maintenance of the system.

However, in the literature review in Chapter 2 it is shown that:

- Current WSN modules are not suitable for marine applications due to having one or more of the following limitations:
  - Not being able to process high-data rate sensors necessary for this application such as vibration and acoustic sensors.
  - Not integrating the aforementioned necessary sensors.
  - Lack of compatibility with current networked embedded OSs, to allow to fully take advantage of the networking capabilities of a WSN.
  - Not being properly packaged, encapsulated, and tested to survive and collect data reliably in these harsh environment scenarios.
- Current WSN characterisation techniques suffer from either of these issues:
  - They do not provide a full all-to-all physical link characterisation, with no upper-layer protocols in a synchronised manner.
  - They have not been properly evaluated and analysed in real-world metal marine environments.

These limitations and gaps are addressed in the work presented in this thesis by:

- Designing and developing autonomous wireless sensing modules that are suited for the marine environment, as well as characterising and testing them.
- Developing and testing a methodology for WSN characterisation that can be used in metal marine environments.

1.3 Thesis preview

- Chapter 2 starts with an overview of the marine offshore application environment that sets up the work in this thesis, followed by the current state of the art for the sensors used to monitor these structures and related machinery. Eddy-current sensing is identified as a potentially suitable method for monitoring structural stresses in these structures that are mainly composed

of metal. Vibration and acoustic sensing is shown to be the most common method for fault detection in machinery, which can also be used for structural monitoring; however, marine-graded modules have not been found that integrate these type of sensors. The chapter also examines the application of wireless sensor modules and WSN in these environments, finishing with a review of methods and systems to characterise wireless performance in WSN in general and its application in particular to the complex metal environments.

- Chapter 3 presents the design and development of a novel multi-axial sensor based on eddy-current inductive sensing, for measuring relative displacement between adjacent components in a steel framework. This sensor is further integrated into a fully encapsulated wireless module, with a cuboid shape made out of PCBs, 3D-printed plastic components and integrated battery. The sensor and module are characterised in one and two axes for different conditions such as metal thickness, type, and angle of inclination, as well as testing the effects of water, battery integration, and encapsulant. The characterisation was done by developing two different custom test setups, one for general one/two axis testing and another one for plate inclination testing. The characterisation of the sensor demonstrated a sensing range of 0-20 mm and a resolution of 0.5 mm.

- Chapter 4 describes a new hardware/software WSN architecture for monitoring machinery in marine and harsh environments using COTS vibration, acoustic, and temperature/humidity sensors, which overcomes the limitations of current WSN platforms. The electronics design, module integration and encapsulation are described, as well as the firmware running in the microcontroller. This module improves on the main CPU, radio, and power of the hardware platform described in Chapter 3, adapting it to the necessary sensors. It addresses the issues of current WSN modules in terms of power, marine reliability, and OS compatibility, which allows research and industry to deploy WSN for machine and structural monitoring in marine scenarios. The sensor module is able to sample and save accelerometer data at 476 Hz

and audio data at 7.5 KHz at the same time. A full-featured UI is also presented, which allows data collection and visualisation, experiment control, and 3D-view support of the environment. The platform was validated in laboratory conditions by testing it on different electro-mechanical setups.

- Chapter 5 presents a methodology to fully characterise wireless link communications in 802.15.4 networks, extending the state of the art methodologies and tools described in Chapter 2, to be applied to complex, 3D, metal marine environments. This methodology and experimental setup focus on the physical layer instead of application-level or networking-level layers typically found in the literature. The methodology was validated in three different metal scenarios with increasing complexity: an indoor-outdoor multi-chamber metal environment composed of three freight containers; a large engine room emulator containing a ship's engine, several generators and large amounts of metal piping, ducting, and gantries; a real naval vessel's engine room and its adjacent compartment. Different variables were studied such as door openings, node location and orientation, and effect of heavy machinery. Moreover, the methodology was also applied to a non-marine scenario in a real application deployed in a data centre, in which unknown issues were causing several node failures. With the applied methodology, the root causes of the failures were found and subsequently corrected.

- Chapter 6 presents the validation of the modules for the marine environment by accelerated reliability stress testing to marine and military standards. The modules were subjected to vibration, humidity/temperature, and salt mist stress tests. A network of SMHM sensor modules is also deployed in different real-world marine environments, to prove the reliability of the data collection, such as a river bridge during a storm, the motor of a RIB, and a naval vessel's engine room and adjacent compartments.

- Chapter 7 presents the overall conclusions and discusses the impact in the research and application fields of WSN, miniaturisation, packaging, systems integration, reliability, and the deployment of offshore marine WSN. Future

work is discussed, including further validation of the inductive sensor module in real structural applications as well as long-term deployment of a large WSN in an exposed marine environment.

Chapter 2

Literature Review

2.1 Application environment: marine structures and machinery

2.1.1 Introduction

Structural and machine health monitoring (SMHM), using wireless sensor networks, is being widely used for a wide range of land-based structures and machinery, such as bridges, buildings, and industrial scenarios. Marine structures such as oil and gas drilling platforms, ships, and renewable energy devices can benefit from SMHM, as they are deployed at sea for long periods and therefore exposed to exceptionally harsh environmental and mechanical stresses, but the nature of the structures and the stresses make SMHM design and deployment much more difficult. These mechanical stresses correspond to the bending and flexing of the different parts and components of the structure, produced by storms, wind gusts, and wave impact, which can slowly deteriorate the structure leading to cracking and eventually failure.

This section describes the stresses affecting marine deployments that can impact their reliability, setting up the context environment for the sensing needs to monitor and improve the reliability of these platforms.

2.1.2 The offshore environment

Offshore structures have been deployed around the world for decades, with great concern about their structural reliability due to the harsh environment conditions. The continuous high humidity and wetting produced by the salt water they are immersed in as well as rain can cause corrosion in the long term [12–14]. In addition, the salt in the sea water can accelerate this corrosion, which can affect not only the structure and machinery of these deployments but also the electronics that compose their sensing systems [15]. Another important issue in floating platforms is the continuous motion induced by wave and wind, which causes cyclic mechanical stresses, as well as random high mechanical strains and shocks produced by wind gusts and wave impact [16–18]; these can be specially severe during specific climatic episodes such as storms or hurricanes [19]. All of these stresses cause fatigue and cracking in the structure, which can ultimately lead to deterioration or even catastrophic failure of the platform [20, 21]. The severity of these environmental and mechanical stresses also makes offshore structures an exceptionally harsh environment for deployment of electronics. Moreover, the large amount of metal in the structure and high levels of electrical noise from heavy machinery also makes it a difficult environment for wireless propagation, as described in more detail in Section 2.5.

2.1.3 Applications: ships, platforms, and their associated machinery

Drilling platforms consist of large pumping systems that extract gas and oil from the bottom of the ocean, built on a metallic structure generally made out of steel. To ensure their survivability, the first approaches have tried to address it by developing a strong and durable structure with a predictable lifetime. The literature describes many probability-based models and studies focused on predicting the effects of fatigue and cracking in the structure by the effects of wave loading and other stresses [22–24]. However, this failure prediction does not replace the need for continuous monitoring and a SHM system is still necessary.

Naval and cargo vessels, although serving a different purpose than offshore platforms and not permanently anchored, still share many of the characteristics of these platforms: they are deployed at sea, run similar high-power industrial machinery, and are large metal structures. As a consequence, they also suffer from similar reliability problems, specially related to bad weather episodes [25] when mechanical strains and wave impact shocks are worsened by the motion of the vessel.

Although drilling platforms and ships are the best-known marine offshore metal structures, in recent years, as the demand for renewable energy has expanded, there have been large-scale deployments of offshore wind-energy platforms [26] and numerous deployments of individual test platforms for the less-mature technology of wave and tidal energy harvesting [27]. Being exposed to the same harsh environmental and mechanical stresses but being unmanned, they have an even greater need for remote SMHM. In the particular case of wave energy platforms, they have the added need for collection of detailed structural and machinery performance and reliability data for proof-of-concept and as input to redesigns, as there are many different mechanisms that have been proposed for wave energy extraction and the most efficient and reliable are yet to be found [28].

The machines used in all types of offshore deployments, despite their differences, also have several common characteristics: for energy generation, large turbine-generators are mostly used [29], while conversion and storage requires power converters and, typically, battery banks [30, 31]. Although ships are not used to generate energy, the engines and pumps that are necessary to run them are also composed of similar rotating parts, piping, wiring, and electrical converters [32], and are also subject to the same stresses. Therefore, all of these structures and devices could benefit from a SMHM system that targets metal structures and high power machinery in the specific context of the marine environment.

2.1.4 Conclusions

Although a great deal of work has been done over the years to ensure robust structural design in offshore platforms, a SMHM system can help to further improve

the reliability of drilling platforms and ships, as well as push forward renewable energies such us wave, tidal, and wind by driving down costs while also improving the reliability of supply.

Given this broad context and the objectives of the research, this literature review is therefore structured as follows:

- Sensors for health monitoring of structures and machinery.
- Sensors and WSN for marine environments.
- Wireless sensor modules.
- WSN wireless performance characterisation.

2.2 Sensors for health monitoring of metal structures and machinery

2.2.1 Introduction

As shown in the previous Section 2.1, continuous monitoring of offshore structures is important to prevent failures, as they are subject to harsh environmental stresses. Visual inspection is expensive, time consuming, and specially hard for unmanned and offshore structures with difficult access. Sensing systems can provide this continuous monitoring and act as a prognostics tool to avoid these failures.

In this section, the most common techniques for structural health monitoring are introduced, with a specific focus on metal structures, as well as the monitoring of machinery found in these types of scenarios.

2.2.2 Sensors for health monitoring of metal structures

Structural Health Monitoring Systems [33] (SHMS) are composed of an array of sensors deployed in a structure with the objective of detecting atypical loading or structural deterioration or damage. Sensors include foil [34] or fiber-optic strain [35], accelerometer-based inclinometer [36] and vibration [37], laser [38],

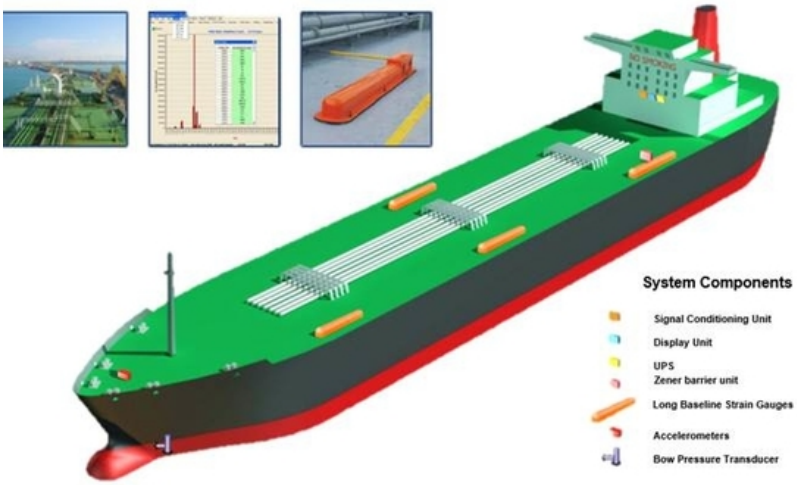

Figure 2.1: Commercial ship hull monitoring system using long strain gauges [1].

radar [39], guided wave [40], impedance [41], imaging [42], and Linear Variable Differential Transformer (LVDT) [43]. Foil strain sensors have a high dependency with temperature and are difficult to calibrate and install. Also, they can be bulky, specially the long guages used for hull monitoring (Fig. 2.1), and the transducer needs to be attached separately from the conditioning electronics. Guided waves methods also need several transducers attached to the structure, with complex electronics and signal processing to produce and read the necessary signals that travel through the structure. Inclinometers offer limited information as they only provide absolute inclination of individual members. Radars are used in SHM also for measuring inclination, but they need a stationary large screen at the opposite side of the structure to reflect the signal and measure the displacement. MEMS accelerometers however are a low-cost solution that can provide not only inclination but vibration data, although these data can be difficult to interpret and process, as evidenced by the active research field of SHM vibration analysis [44]. Impedance-based sensors have also recently benefited from MEMS miniaturisation, but they require to be embedded in the structure during construction and the data analysis is not straightforward either. Light-based sensors such as laser and fibre-optics need complex conditioning electronics and high power to drive the laser/LED light sensors, which also makes them

considerable large and expensive. Imaging as a sensing tool can be even more complex and demanding systems, as they need cameras and image-processing algorithms, which make them difficult to embed in battery-powered modules. LVDT is used to measure the relative distance between components in a structure, however the mechanical working principle of the sensor makes it large, difficult to install, and requires either direct contact between both components of the structure or a large adapting structure (Fig. 2.2). Table 2.1 shows the sensing ranges and resolution for the described sensing technologies that use displacement as a measurement.

Figure 2.2: LVDT sensor for measuring displacement in a concrete bridge [2].

SHMS may also look for material deterioration, e.g. cracking or corrosion, using surface or bulk material sensors including strain, guided wave, impedance, acoustic [45], optical, imaging and eddy-current sensors [46]. Except for eddy-current sensors, all of these are again large (strain gauges), expensive (all) or involve complex, in-contact measurement set-ups (all). Eddy-current sensors, on the other hand, involve only a relatively straightforward, non-contact measurement of inductive coupling to metal on the principle that metal deterioration

Table 2.1: Characteristics of different displacement sensing technologies

Sensing technology	Sensing range	Resolution
Laser	0-25 mm	1 *um*
Radar	not specified	1 mm
Imaging	not specified	1 mm
LVDT	0.6-12 mm	0.06 mm
Kypris and Markham magnetic fields	0-50 mm	0.5 mm
Commercial eddy-current	0-10 mm	2 *um*
This work	0-20 mm	0.5 mm

will change the coupling between the sensing inductor and the metal. These sensors are also widely used for position sensing and gap measurement in rotating machinery [47, 48]. The basic principle of eddy-current sensing is based on the circulating currents induced in the metal target, which are produced by a sensing coil fed with an AC current. These induced currents produce a variation in the inductance of the sensing coil, which is proportional to the properties of the target material such as size, material, and distance to the coil (Fig. 2.3).

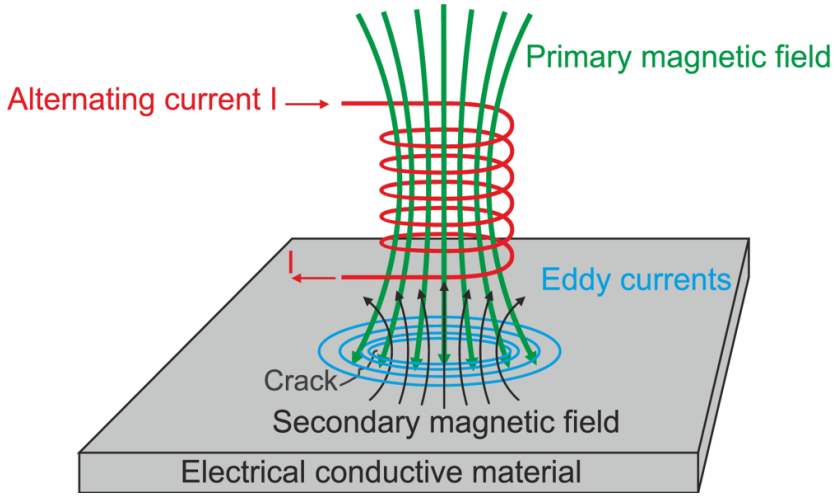

Figure 2.3: Eddy-current sensing principle of operation [3].

Interestingly, however, despite many apparent advantages for measurement of structural movement in SHMS, eddy-current sensors have been little used for

this. For SHMS, they have the advantage of low sensitivity to dust and humidity in the measurement gap [49]. They have the disadvantage of sensitivity to temperature [50] but this is less of a concern in SHMS where temperature is typically at atmospheric ambient, temperature gradients are small and temperature variations are slow. Where temperature is a concern, a temperature sensor can anyway be used for compensation. Kypris and Markham [4] describe an eddy-current sensor for SHM, focused specifically on monitoring of expansion gaps and cracks in concrete structures. It employs triaxial rectangular coils, offering 3-D positioning with sub-0.5 mm accuracy, which can be used in different configurations. However, it has two important drawbacks: the sensor conditioning is still based in large bench-sized commercial instrumentation, and it needs a separate transmitter and receiver that need both to be either embedded or attached to the structure as it can be seen in Fig. 2.4.

Traditionally, eddy-current sensors needed custom electronics [50, 51] and sometimes solenoid-type large sensing coils (Fig. 2.5). However, new state-of-the-art sensor ICs, such as the LDC1000 [52] and LDC1614 [53] from TI, allow for integration in autonomous sensor modules, due to the reduced size and power consumption. These sensor ICs are optimised for use with PCB coils, which allow further miniaturisation and packaging alternatives.

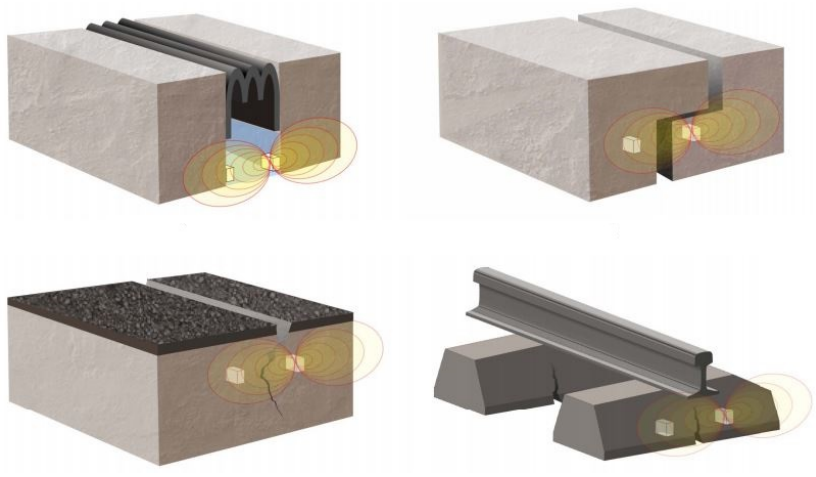

Figure 2.4: Different use cases for the eddy-current sensor node developed by Kypris and Markham [4].

Figure 2.5: Commercial eddy-current displacement sensor by Keyence [5].

As large structures such as bridges and offshore platforms bend and flex due to environmental forces, the relative displacement between each of their different beams and parts can change even in normal conditions. A sensor that can measure this relative displacement could detect damage or impending failure if this distance is above certain threshold or if it deviates from the expected patterns of natural movement. Although the distance and resolution needed for detecting early failure in such structures depends on the size, components, and material of the structure, the experimental data shown in [42], where loading is performed in a large-scale arch-truss bridge testbed, suggests that a 20 mm measuring range and 0.5 mm resolution could be a starting point for a relative displacement sensor in this type of structures. In [54], a composite bridge was statically loaded until intensive cracks appeared on the concrete slab. The cracks started to appear when the vertical displacement was between 10-20 mm, and the relative displacement in the same axis, measured with strain gauges, was around 1 mm. This confirms that a sensor with this range that can measure displacement between two components orthogonal or in the same axis could detect these failures. Developing and characterising such a displacement sensor with a sensing range of 0-20 mm and a resolution of 0.5 mm, and its associated electronics would be novel and is an objective of the research in this thesis.

2.2.3 Sensors for health monitoring of machinery

The machinery found in offshore deployments and ships is generally composed of large engines, motors, turbines, pumps, and generators, which in many cases produce strong vibrations, electrical noise, and overheating that can lead to failure. These devices and their parts such as gearboxes, bearings, rotors, and power supplies need to be constantly monitored in a similar way as the structures where this machinery is placed.

Lu *et. al* [55] provides a summary of typical gearbox component monitoring techniques, which includes vibration, torque measurement, oil/debris analysis, temperature, acoustic emission, and stator current/power. Vibration and acoustic sensors are specially interesting due to their reliability and ability to detect early-stage faults in a wide range of components. They have been widely used for prognostics and fault diagnosis of bearings [56], motors [57], and different types of machinery [58,59]. Vibration sensors can also be used for monitoring the structure of the platform or facility where the machinery is deployed [60]. However, traditional vibration and acoustic sensors are regarded as expensive, intrusive, and requiring a high sampling rate [55, 59, 61]. To reduce cost and ease installation, high-end wired vibration-based sensor systems are being replaced with low-cost wireless sensor modules using MEMS and other COTS sensors [62, 63], although it is a challenge to achieve the required sampling rate of 100-200 Hz for vibration [56,57] with low-power wireless systems. These WSN modules not only reduce cost in terms of the hardware modules themselves but also in the associated overhead of installing and repairing the wiring, which is especially costly in these complex structures located in environments with difficult access. The low cost of the hardware also means that redundancy can be built into the system by deploying a larger number of sensor, therefore if a sensor fails it does not need immediate replacement as the rest of the network would keep working.

In [6], a WSN is used to monitor the condition of a marine gearbox, with nodes based on the assembly of several off-the-shelf boards: a Zigbee module, an accelerometer, and an energy harvester. Severino et al. [7] showed a similar platform but focused on structural health monitoring using a TelosB [64] mote connected to an acquisition board and accelerometer. While these experiments

demonstrate the feasibility of using wireless sensors and MEMS to monitor devices in these environments, most of the platforms used present a series of drawbacks: they are either based on old platforms developed for networking research with limited processing capabilities and memory (e.g. TelosB and MicaZ), which limits also the sampling rate of the sensors, or on more powerful platforms with higher power consumption and that do not support current standard WSN operating systems such as Contiki-OS [65]. As shown in [7], the popular TelosB can only reach 100 Hz when using an external ADC aquisition board, which would make it even less viable if an acoustic sensor in the KHz range is also used simultaneously. Moreover, accelerometer and acoustic sensors are never used together in these studies that use low-power WSN platforms, even though the literature shows methods that can combine both sources of data to improve fault detection [58, 66, 67]. In addition, the use of different modules for communications, acquisition, and sensors attached with cables or connectors instead of a single integrated board complicates the packaging and encapsulation, as well as increasing the cost and power consumption. This can be seen in Fig. 2.6, which shows the vibration-based WSN nodes discussed previously for marine gearbox and structural monitoring. This highlights the need for a more advanced integrated wireless sensing platform based on vibration and acoustic sensors that is low-cost and low-power, but at the same time delivering performance necessary to sample and store the data from those high data rate sensors as well as reliable in the marine environment. This is an objective of the research presented in this thesis.

2.2.4 Conclusions

Although many different sensing technologies have been used for structural health and machine monitoring, most of them have several disadvantages including cost, power consumption, and size. Vibration and acoustic sensors have been shown to provide reliable data for monitoring and prognostics of machinery as well as structures, and with the advances of MEMs they can be integrated into low-cost modules. However, none of the wireless modules found in the literature are designed specifically to withstand harsh environments. In addition, for monitoring large metal structures eddy-current sensing potentially provides a low-cost

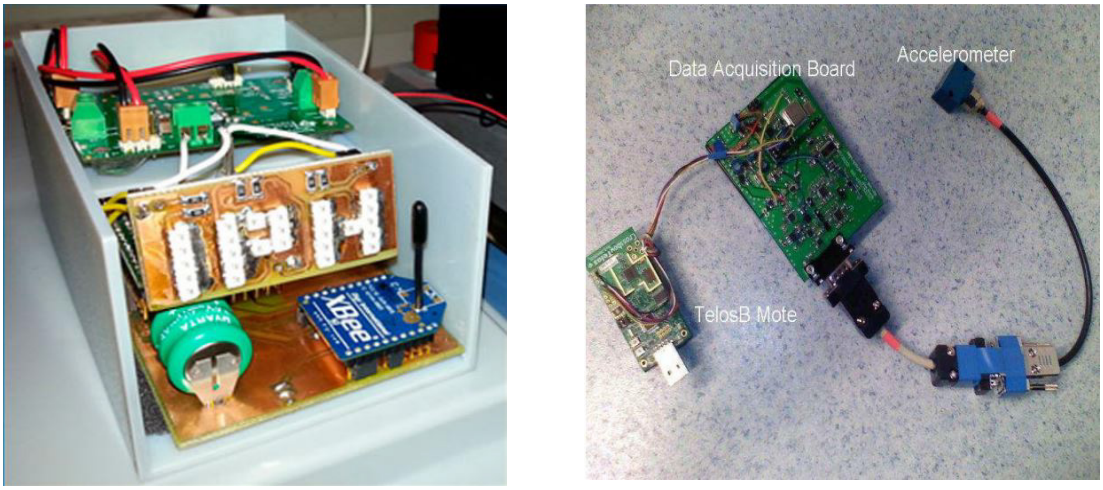

(a) (b)

Figure 2.6: Vibration-based WSN platforms for machine and structural monitoring by Schirrmacher [6] (a) and Severino [7] (b).

contactless method that can be used to detect relative displacement between components, but it has yet to be proven if it can meet the required range and resolution as well as be integrated in an autonomous reliable module.

2.3 Sensors and WSN for marine environments

2.3.1 Introduction

Deploying sensors in marine environments is very challenging due to the environmental stresses that are subject to, such as fouling, corrosion from water and salt, wildlife interference, and vibration/shock produced by the waves and storms. For this reason, marine sensors need extra protection to be able to survive these extreme conditions.

This section describes the typical uses of the sensors for marine environments and shows different types of WSN deployments done in these scenarios.

2.3.2 Sensors for marine environments

Many of the sensors for structural and machine monitoring described in the previous Section 2.2 are being deployed in marine offshore environments, but they are general structural or industrial sensors and not designed particularly for the marine environment [6,68,69]. When dealing with marine environments specifically, most of the work found in the literature is focused on environmental sensing such as water quality [70], ocean [71] and wildlife monitoring [72], instead of structural/machine health monitoring.

Smart buoys are the most common example of integrating and deploying marine environmental sensors, and have been extensively covered in the literature [73–75]. The common components in the electronics contained in these smarts buoys are similar to any autonomous sensing module: processing unit (CPU), power system, sensors, and communication system. For the CPU, a variety of different microprocessors have been used, although the trend lately is shifting toward newer low-power microcontrollers [76]. Different sensors and signal conditioning are employed depending on the application, with motion sensors such as accelerometers being common to most of them. Although they are battery-powered, photovoltaic cells can be added to extended their battery life [73]. The communication system is usually wireless by GPRS, 3G, or other long-range technologies when they are in isolation. However, many buoys can be networked with low-power radios into a WSN, as described in the next Section 2.3.3. Some of these buoys can have part of their components submerged [77], although the communication system is usually on the surface, as normal wireless transmission through water is difficult to achieve. Energy harvesting can be used to extend the life of these autonomous systems, depending on the deployment scenario. For sensors deployed outside or in closed chambers with artificial light, solar panels can be installed. Vibration energy harvesting is also an alternative for buoys, wave energy platforms, and sensors placed on top of heavy vibrating machinery. Moreover, although these sensors are battery-powered, they could also be connected to a close power source if available.

These custom buoy systems are geared towards miniaturisation and integration, to save cost and power but commercial sensors used in marine deployments

are still bulky and expensive and do not offer the necessary range of wireless networking options. Moreover, even though they are designed to be reliable in this type of environments, the literature shows failures when deploying monitoring systems with commercial sensors. The deployment described in [78] of a scaled-down oscillating water column (OWC) device encountered a number of issues in the reliability of the power and sensing systems, resulting in costly failures and loss of data. A failure in the the water cooling system, caused by design problems in the hydraulic, power system, and diesel generator, resulted in seawater pumped into the control room, and also overheating of the generator, ultimately causing its shutdown. This, coupled with the short life of the battery bank and the high power consumption of the information and control system, led to the complete drain of the batteries in less than 24 hours. A better planning of the power system and the use of a low power monitoring system could have avoided this issue. Regarding the sensors, a few shortcomings were highlighted in the hydraulic and mechanical brake sensors. Some extra temperature and air flow sensors would have helped in the early detection of the problems experienced in those systems. Moreover, the improper sizing of the mooring strain gauges resulted in poor resolution in the measurements. Finally, the complex tubing of the turbine pressure transducers caused it to become clogged with water after a strong storm. This showed the importance that the monitoring system has on the reliability of the platform in off-shore deployments. Lowering the cost of manufacturing and deployment of these systems would permit the deployment of a larger number of sensors, which would increase the redundancy of the monitoring system. However, the systems integration, miniaturisation and wireless autonomy that have been achieved for many land-based SMHM deployments have not yet been applied to SMHM in the marine domain and this is one of the objectives of the research in this thesis.

2.3.3 Wireless Sensor Networks in marine environments

As the coverage area in marine environments is large, many sensors usually need to be deployed. Due to the difficulty of running cables in this scenario, WSN are optimal for aquaculture and ocean ecosystem monitoring [79–81]. These systems

are composed of wireless sensing buoys randomly deployed at sea, where the radio propagation and drifting of the nodes needs to be studied to guarantee a reliable data collection [82, 83].

The sensors and techniques described in Section 2.2 to monitor marine structures and machinery can also be integrated and deployed in a WSN of sensing nodes. Although they are not subject to the same stresses and radio propagation characteristics of the water as with the floating buoys, they may still suffer from splash and will be certainly exposed to high humidity, salt atmosphere, and other harsh marine environmental conditions. Moreover, the large amount of metal in these structures affects the communications due to multi-path fading, as discussed in Section 2.5. The literature shows many application-oriented WSN deployments in different marine and similar environments, such us oil and gas [84, 85], bridges [9, 86, 87], wind turbines [88], and ships [10, 11, 89, 90]. Xiong *et al.* [89] presented a vibration monitoring system for ships composed of IEEE 802.15.4 WSN nodes in a star topology, but it was built with separate modules with no packaging and was only tested in a vibration plate. Another WSN network using 802.15.4 technology was deployed in a real naval ship to monitor the hull [90], where some of the nodes used accelerometers only while others interfaced with strain gauges already present on the ship. These same nodes were also deployed in a different ship in [11]. In [10], a different node made of stacked modules is developed to replace the wired pressure tank gauge system on a ship.

All of these deployments present the following drawbacks, some of them already described in Section 2.2:

- The hardware modules used are:
  - Based on multiple modules and evaluation modules wired together, some of them in separate enclosures, which affects the reliability of the system as well as power consumption [9–11, 86–90].
  - Not designed and packaged specifically to resist the hostile marine conditions and not tested following marine reliability standards [84–89].

  - Either not supporting current networked embedded OS [10, 11, 84–86, 88–90], or based on older WSN modules [9, 87], which hinders further routing and networking research.

- The firmware/software platform does not allow for remote configuration of the nodes and does not offer simple data collection and configuration for rapid deployment management (all).

- The node placement has not been properly studied from the wireless characterisation perspective. Although some deployments have been done for the specific purpose of testing the wireless propagation, they are incomplete and have their own particular issues, which are discussed in detail in Section 2.5.3.2.

- They have not been characterised for use in a high metal-content environment (all).

2.3.4 Conclusions

A large part of the work done for sensing and WSN in the marine environment has been related to monitoring the external environment by developing smart buoys and similar devices, instead of monitoring the offshore structures and platforms. When focusing on marine structures, the current hardware modules and WSN deployments suffer from similar issues as the ones described in the previous Section 2.2, further highlighting the need for integrated wireless sensor modules with an architecture and packaging that is reliable for the marine environment.

2.4 Wireless sensor modules

2.4.1 Introduction

Most of the sensing modules and systems used in the deployments described in the previous sections have at their core one of the well-known WSN nodes, also known as “motes”, usually selected for software compatibility and easy development. A

mote is composed of a low-power microcontroller, a radio transceiver, an external flash memory, a power source, and one or several sensors.

This section describes the most common WSN sensor modules used in research and their drawbacks, as well as other non-traditional WSN technologies.

2.4.2 2.4 GHz IEEE 802.15.4-compatible modules

IEEE 802.15.4-based radios transmitting at 2.4 GHz comprise the majority of research and applications for what is known as WSN, due to the good balance between power consumption, spectrum availability, and bandwidth.

The Telosb [64], also known as Tmote Sky in its earlier version, is by far the most widely-used platform and also offers the best software and OS support. They use a TI MSP430 microcontroller running at 8 MHz with 48 KB of flash and 10 KB of RAM, as well as a 1 MB EEPROM, which is enough for simple networking and sensing tasks but can be challenging to use with high data-rate sensors. The transceiver used is the TI CC2420. The power consumption depends on the application, with an average of around 20-25 mA when using the transceiver. It is powered by two AA batteries with no regulators or battery chargers, which can produce bad sensor readings when the battery voltage falls below the internal reference. It also includes on-board temperature/humidity and ambient light sensors, and the possibility to add more sensors through an external connector. It lacks any encapsulation and the bare PCB is mounted directly on the 2xAA battery holder. Although it has been the flagship sensor module for low-power network research for more than a decade, it is now hard to develop some of the newer protocols and applications due to memory restrictions.

The MicaZ [91] is similar to the Telosb in shape, battery configuration, and power consumption. It is based on an Atmega128L microcontroller, which has more flash than the Telosb (128 KB), but only 4 KB of RAM. It offers a wider range of sensors and data acquisition systems but they are all in external expansion boards that need to be attached.

SHIMMER [92] is a platform developed as a wireless wearable for biomedical research. It has the same radio chip and microcontroller as the Telosb, but adds an accelerometer, bluetooth and microSD card all in a smaller form factor. It is

Table 2.2: Comparison of different WSN platforms

Platform	CPU Model	CPU Speed	RAM	Flash memory	ADC sampling rate
TelosB	MSP430	8 MHz	10 kB	48 kB	10 Khz
MicaZ	Atmega128L	16 MHz	4 kB	128 kB	15 Khz
SHIMMER	MSP430	8 MHz	10 kB	48 kB	10 Khz
Waspmote	Atmega1281	8 MHz	8 kB	128 kB	15 Khz
This Work	CC2538	32 MHz	32 kB	512 kB	7.5 Khz

a step forward to integration, but even though it was developed later the choice of microcontroller and radio made the platform obsolete quickly.

The Waspmote [93] was originally developed for 802.15.4 technologies, using an XBee [94] radio module which is easily addressable with AT-style commands. The Waspmote has many different radio technologies and sensors available, all of them in different modules that are attached to the main platform, and it also includes an IDE for easy programming. This makes it an ideal platform for prototyping and testing but less reliable for deployment.

Although newer microcontrollers with integrated 802.15.4 radios and better performance have been available for some time, such as the CC2538 [95], there were not commercial modules available when this research was being carried out. A sensor node with a more powerful CPU and memory was necessary, i.e. higher processing speed and increased RAM, that could overcome the problems of the obsolete platforms being used in research, especially when sampling more than one high-data rate sensor at the same time, such as accelerometer data and audio.

Table 2.2 shows a comparative of these platforms.

2.4.3 Networked embedded OS

A major contribution to the expansion of WSN lies within the firmware and applications, particularly in the development of open-source embedded OS designed specifically for wireless networking in platforms with constrained resources. These, unlike traditional full-blown OS such as MS Windows or Linux, are

lightweight systems that are compiled with the application in a single binary to be loaded in the microcontroller. The most used networked embedded OS are TinyOS and Contiki-OS.

TinyOS [96] is based on a monolithic architecture and component model, in which the different modules regarding network protocols, file system, sensor drivers, etc. can be bundled depending on the application requirements. It uses nesC as a programming language, a pseudo-language similar to C. It supports simple multi-threading, in which the application has to explicitly manage concurrency by yielding the processor, adding an extra difficulty to the programmer. Although it still has a large userbase and support for most of the older platforms, its development has stagnated and there has not been any support added for newer protocols and hardware platforms.

Contiki-OS [65] has a modular architecture and event-driven model, but has threading-like support called protothreads. It is programmed in C and has a steeper learning curve than TinyOS but, at the same time, is more powerful and easier to extend. It also supports a large repository of protocols including TCP/IP, as well as sensor drivers and utility applications. The main advantage over TinyOS is that it is being actively developed and has a much larger community of users and contributing, supporting the newest networking protocols, applications, and hardware platforms and chips such as the mentioned CC2538.

Recently, similar platforms have emerged such as RIOT [97] OS and OpenWSN [98], but they are not a viable alternative due to their limited hardware and libraries support.

These operating systems can be used as a base to design sensing applications for WSN deployments; however, they make up only the skeleton of the system and a proper architecture built upon them needs to be developed depending on the application requirements.

2.4.4 Other technologies

Wifi and cellular technologies have been used in stand-alone buoys and wireless sensing nodes; however, their networking capabilities are very limited and their high-power make them less suitable for use in low-power nodes. Bluetooth can

be a viable alternative to 802.15.4-based networks but until very recently mesh networking was not possible and new standards still need to be developed and tested.

Newer technologies are now entering the market, such as Ultra-Wide Band (UWB) for short range, and LoRA and Sigfox for long range. UWB has a limited availability of devices and higher power consumption, and due to its characteristics it is being used mainly for indoor localisation. LoRA [99] and Sigfox [100] transmit in the sub-GHz band. They are a good alternative for urban networks and open environments, as they can offer more than 10 Km communication range. However, their bandwidth is very limited to accommodate high data rate sensors and their slow transmission time make them very hard to use in mesh networks.

2.4.5 Packaging of wireless sensor modules

Most of the commercial motes consist of only the bare PCBs and battery holder. While some of them are hosted in plastic boxes, these boxes are not waterproof and have large openings where dust and other contaminants can enter. Moreover, they are not mechanically strong to survive high vibrations or have not been tested for it. Therefore, it is usually left to the user to select or build a custom enclosure that is suited for the application which depends on the environment in which it will be deployed as well as the type of sensors.

Mainwaring *et al.* [8] describe a WSN for habitat monitoring, in which Mica motes are used. As they are deployed in the open for weather monitoring, an enclosure is designed to protect the node and sensors from humidity and other environmental stresses. The entire node except the sensors is covered in a thin layer of parylene sealant, and then it is placed in a transparent acrylic enclosure for mechanical protection (Fig. 2.7). Although this packaging is sufficient protection for this type of environment, it might not be enough for harsher marine environments, as the enclosure is not fully sealed.

Most of the WSNs described in the previous Section 2.3.3 that have been deployed in ships and other offshore environments are packaged in off-the-shelf waterproof boxes, as it can bee seen in Fig. 2.8. However, although a plastic enclosure has been proven to be robust enough while being lightweight and resistant

Figure 2.7: WSN node for habitat monitoring in an acrylic enclosure [8].

to corrosion, the lack of full encapsulation in these modules could provoke deterioration of the electronics in the long term, due to the humidity and salt in the environment. Fig. 2.8c shows also how the main processing and communication module are often in the box separated from the sensor itself, which is connected by cables.

Modular platforms composed of stacked boards, like the ones shown in [92, 101, 102], are common in custom wireless sensor nodes, as the boards are easy to replace and only the necessary ones for the application can be added. However, they tend to have higher power consumption, and the addition of extra boards and connectors decreases reliability due to thermomechanical stress, as well as increasing weight and cost. A single-board module that includes all sensors and electronics, whenever possible, reduces manufacturing costs and points of failure.

For structural monitoring, sensing in multiple axes can be necessary, as described in Section 2.2.2. Cuboid modules have been shown to provide a compact, robust, and easy to package configuration for multi-axial sensing. In [103], a 10 mm strain gauge based cuboid is described, using a novel board-folding method to electrically connect the PCBs to eliminate the connectors. The drawbacks of this module come from the requirements of external wiring to power it and extract

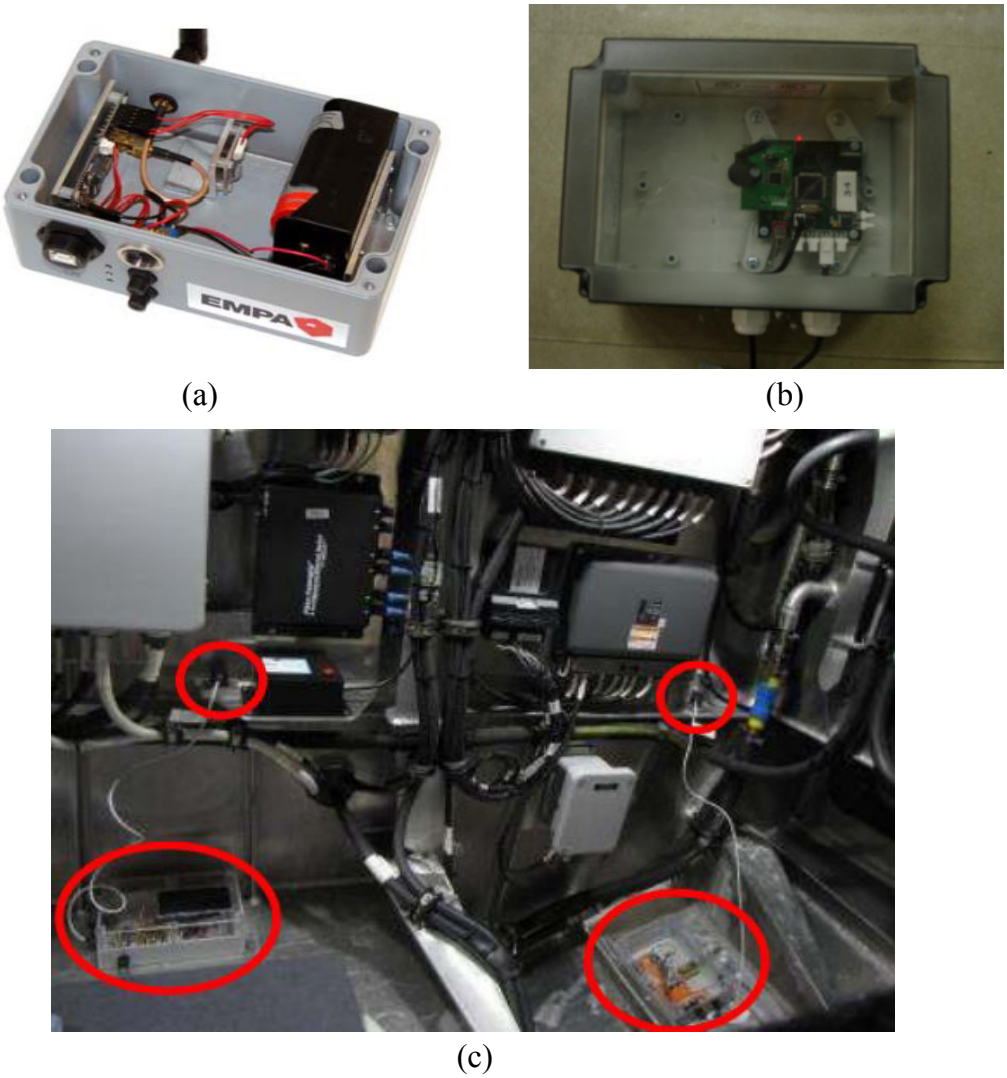

Figure 2.8: WSN nodes in plastic packaging for structural monitoring of bridges (a) [9] and ship hull (b) [10] - (c) [11].

the data, which limits its use as a standalone system, in addition to the need to be fully embedded in the material. A similar cuboid module for environmental monitoring is shown in [104], with integrated coin cell batteries, flex connectors and wireless communications. Although the small size of the battery and lack of charger limits the life of the module, it proves the feasibility of using PCBs as the structure of a cuboid module with plastic encapsulated batteries. The 3D-

integration presented in both modules can be adapted to develop an autonomous module for multi-axial sensing with integrated rechargeable battery and wireless communications.

2.4.6 Conclusions

IEEE 802.15.4-based networks in the 2.4 GHz band is the most widely researched technology in WSN. Moreover, the trade-off between power, range, and bandwidth makes them optimal for structural and machine monitoring, as vibration-based sensors need a high data rate, and a number of sensors can be networked together in a small space without the need of covering large distances. However, the WSN devices used in research are obsolete platforms limited in memory and performance, with no proper packaging beyond off-the-shelf plastic boxes, adapted to the sensing and environmental needs of marine scenarios. A plastic-encapsulated module with a more powerful architecture that integrates the necessary sensors could offer not only a robust platform for SMHM but also a better device for WSN researchers.

2.5 WSN Wireless performance characterisation

2.5.1 Introduction

Wireless characterisation is an important issue in WSN, as they are low-power lossy networks with limited range and resources. It becomes even more important when using high-data rate sensors such as vibration and audio, as loss of packets in these situations can yield excessive retransmissions that can flood the network making it unusable, as well as losing data fidelity. Moreover, the performance can be affected by characteristics of the environment, e.g. metal, temperature, humidity, electrical noise, etc.

This section presents the most common WSN performance characterisation techniques found in the literature, which includes data-driven modelling as well as experimental testbeds and real-world testing.

2.5.2 Wireless performance modelling and characterisation

2.5.2.1 Link quality estimators for WSN

Link quality estimation between transmitters and receivers is necessary for selecting the correct network topology and transmission parameters, which include routing path, data rate, transmission power, etc. [105, 106]. There are only three metrics that can be directly observed and therefore are commonly used for link quality estimation: Received Signal Strength Indicator (RSSI), Link Quality Indicator (LQI), and Packet Delivery Ratio (PDR) also referred to sometimes as Packet Received Ratio (PRR) [107–109]. RSSI and LQI are provided by the radio chip, extracted from the incoming packet, while PDR requires a more extended experimental evaluation.

The RSSI parameter provides the signal strength or intensity in the receiver, measured in dBm. In 2.4 GHz low-power WSN it generally ranges from -25 dBm to -100 dBm, depending on the sensitivity of the receiver and the maximum power of the transmitter. It is inversely proportional to the square of the distance from the receiver to the transmitter. RSSI can be used to estimate distance between transmitter and receiver, by deriving an environment-specific model from the path-loss generic formula [110]. The opposite is also calculated with this formula by estimating signal strength depending on the distance, which can be used when planning a deployment. This is explained in more detail in the next Section 2.5.2.2. A drawback of relying on RSSI is that, in presence of interferers, the measured value is the sum of RSSI and the noise floor. Noise floor can be considered as a special case of RSSI, in which the RSSI is measured when none of the known transmitters in the network are sending packets, providing an estimation of the current noise in the environment. An ideal noise floor in the absence of interferers from other transmitters or noisy machinery has to be close to the sensitivity of the radio receiver (e.g., -96 dBm in the most commonly used CC2420 [111] chip).

LQI was introduced in the IEEE 802.15.4-2003 standard [112], although the standard does not specify how it is calculated and which parameters to use.

Nonetheless, all chip vendors have a similar way of estimating it. The CC2420 and in general all of the TI CC* family transceivers provide a dimensionless correlation (CORR) to estimate the signal strength quality by calculating the average correlation of the first eight symbols of the received packet, which can be seen as an approximation of the chip error rate. The LQI is then calculated from this correlation following eq. (2.1), where α and β must be calculated empirically from the packet error rate.

$$LQI = (CORR - \alpha) \times \beta \tag{2.1}$$

Although LQI values can range from 0-255, the correlation value obtained directly from the chip (CORR) as the LQI estimation, with values ranging from 50 (worst) to 110 (best), is widely used in the literature. LQI can complement RSSI by providing a better estimation of the SNR than just using RSSI and noise floor [113].

PDR is the most relevant metric for WSN planning and characterisation, as it is what is ultimately useful for application designers and network managers [114, 115]. PDR for a specific transmitter-receiver link can be estimated by sending a defined number of probe packets to the receiver, then calculating the percentage of the received packets and sending it back to the transmitter. However, PDR, as well as RSSI and LQI, can have dramatic temporal variations depending on the environment: people walking [116], lack of Line-Of-Sight (LOS) [117], presence of vegetation [118], multi-path fading from metallic surfaces [119], and temperature [120], among others. Constantly calculating PDR is not feasible as it would consume too much power and it would drain the batteries quickly. To overcome this, many researchers have tried to find a correlation between PDR and RSSI/LQI, as they can be extracted from the incoming data packet [121, 122]. Zhao *et al.* [123] found out that having a high RSSI does not always correlate with a high PDR, and it is affected by link asymmetry, as it was also shown by [64, 124]. The presence of interfering signals can also contribute to the lack of correlation, by boosting the RSSI levels while yielding a lower PDR.

These issues are even more pronounced in the transition area, that is the area between full connectivity and no connectivity. Links located in this area have been shown to have erratic behaviour, and its width depends on the characteristics of the environment [108]. However, the combined metrics of RSSI, LQI, and PDR can provide a more accurate picture of the performance of a WSN [107, 125].

Another issue when calculating PDR is that, if higher-layer protocols and multi-hop are used while calculating the PDR, it becomes harder to calculate the real PDR, as retransmissions in the higher layers are frequently transparent and the real number of received packets is unknown. Until recently, no tools were available to calculate this real PDR where nodes send packets in an all-to-all fashion in a synchronised manner with no upper-layer protocols. This has resulted in many real-world performance experiments being lacking in proper methodology and reliability of the data, as described in the Section 2.5.3.2.

2.5.2.2 WSN performance modelling

Despite the limitations highlighted in the previous section that signal strength indicators have in predicting network performance, it is still the mostly widely used parameter for analytical modelling, as traditional wireless path loss models can be applied. The path loss indicates the attenuation of the signal between the transmitter and receiver, which is influenced mainly by the distance between the nodes but also by others environmental factors. The most common model to calculate the path loss is the log-normal shadow model, which can be used for general wireless systems in indoors and outdoors environments, and is calculated using eq. (2.2) [126]. The parameter d_0 is the near-earth reference distance, $\overline{PL}(d_0)$ is the path loss or attenuation at the reference distance d_0, , η is the exponential path loss index, and X_σ is a zero-mean Gaussian random variable. All these parameters can be adjusted for the specific environment from experimental data, with obstacles affecting greatly the path loss index. This has been done in multitude of studies for different scenarios [110, 127–130].

$$PL(d) = \overline{PL}(d_0) + 10\eta \log \frac{d}{d_0} + X_\sigma \tag{2.2}$$

Most of the simulation tools designed for WSN use this radio model at their core and, then build on it the different networking protocols to test [131, 132]. However, this model is limited to one dimension and it does not take into account multi-path reflections from obstacles. For this, different tools have also been developed that use different ray-tracing techniques for calculating the effect of multi-path in the received signal in a specific environment [133, 134], most of them in two dimensions and specifically targeted to indoor scenarios such as buildings [135]. Some of them have attempted to developed 3D ray-tracing tools for predicting signal strength [136–138], but it becomes computationally very expensive and is not feasible to use when the scenario is too complex and contains reflective metallic surfaces.

The main purpose of these tools, however, is not usually signal propagation but testing and simulation of networking protocols, and the radio model acts only as a support to try to approximate how the applications and protocols would behave in real scenarios. This is the case of Cooja [139], the most commonly used simulator in WSN, which supports ray-tracing and log-normal radio models although only in 2D simple scenarios.

There is no modelling or prediction tool that can accurately model WSN performance in the complex, 3D metallic environments that are characteristic of marine WSN deployments and a critical issue in all these tools still remains in the correlation between signal strength indicators and PDR. Therefore, experimental data from testbeds and real scenarios is still essential to obtain an accurate view of the performance of a WSN before full deployment. However, there is no standard methodology for systematically and efficiently collecting this experimental data. Developing and verifying such a methodology in representative marine environments is an objective of the research presented in this thesis.

2.5.3 Experimental deployments

2.5.3.1 Testbeds

To reduce the gap between simulations/mathematical models and real-world environments, many testbeds of wireless sensor nodes have been developed, some of them as a one-off experiment and others as permanent deployments that can

even be used remotely by the community of researchers. One of the most used of these permanent open testbeds is Motelab [140], which provides a network of wireless nodes deployed in a building at Harvard University, with USB connections that provide a backchannel to reprogram the nodes. This allows data logging and job scheduling via web interface, facilitating remote application deployment and rapid network protocol testing. However, this network is limited to the current nodes installed in the building and the environment conditions cannot be changed. Although the source code is available for researchers to deploy their own testbed, the need of cables and servers for the backchannel communication limits its usefulness in open or difficult environments. Indriya [141] is also a similar permanent testbed installed in a building in the University of Singapore, which also includes sensors in some of the nodes such as Passive Infrarred (PIR), magnetometer, and accelerometer, but still needs USB cables to connect each node to a gateway. Boano *et al.* tried to better approximate testing to real conditions by developing two particularly interesting testbeds: Jamlab [142] and Templab [143]. The first one allows for measuring and creating controlled interference patterns in the frequency of interest with off-the-shelf nodes. The second one allows the control of the on-board temperature of the sensor nodes, to understand how temperature affects network protocols, as temperature variations are common in outdoor deployments. Nonentheless, these two testbeds are still installed in buildings, which makes it difficult to emulate propagation in more complex outdoor or metallic scenarios. WINTeR [144] is a testbed setup for a complex industrial environment, deployed in a small mock-up of an oil rig, which includes a programmable EMI generator and remote control. Although it is a definitive step forward for emulating harsh industrial environments, the lack of physical access to the scenario hinders its usefulness due to the nodes not being able to be relocated, and other variables in the scenario such as multi-chamber communications and door openings cannot be studied, as the testbed size is only 3.5 x 7 m. Moreover, WINTeR testbed is only described on a high-level, with no measurement data shown and no apparent access to the use of the testbed.

These testbed deployments have shown that although an effort is being made to provide facilities for researchers to work on, they are still limited and focused more on networking protocols and not the study of specific environments. They

provide access to better data than simulations, but still real-deployments with physical access to the site are needed to understand the performance of the networks and study the different variables that can affect them.

2.5.3.2 Real-world deployments

A large number of application-oriented WSN have been deployed in indoor and outdoor environments [145–147], even in marine scenarios as described in Section 2.3.3, as well as measuring campaigns focused in characterising the communications in those environments [148, 149].

Regarding metal environments, Yuan *et al.* [150] tested a wireless sensor network inside food cargo containers, recording the RSSI and LQI as well as the sensor data. However, their focus was primarily on signal strength over distance, and the experiment was done with multi-hop and duty-cycling protocols. Similar analyses have been carried out for WSNs on board ships [151, 152]. These studies, using both simulations and practical measurements, show that communications between adjacent rooms and decks are possible due to signal leakage through bulkhead seals between compartments. In [153, 154], tests included more realistic shipboard variables, such us door opening and closing, operating machinery, and people movements. However, all of these were built on top of the XMesh and Zigbee protocols, focusing on the network topology and not on the analysis of physical links. PDR and RSSI were measured but, due to the use of upper-layer protocols that involve retransmissions and mesh network configuration, they do not provide a comprehensive understanding of the propagation environment.

A key variable that can affect WSN communications quality in marine metal environments, such as ships' engine rooms and off-shore platforms, is electromagnetic interference (EMI) from electro-mechanical machinery. Despite the literature showing some assessments of broadband and out-of-channel interference in IEEE 802.15.4 networks [155, 156], no experiments have been reported in a ship's engine room scenario with on/off switching of the machinery.

The common characteristic in most of these experiments, regardless of the type of environment and whether they are done in a testbed or real-deployment, is the lack of a consistent experimental methodology, which leads to a series of issues:

- No synchronisation between nodes. This can cause two nodes to send probes at the same time, which can have the effect of measuring a high noise floor in the receiver or losing the packet, due to collisions.
- Use of upper-layer and MAC protocols. These have error-corrections and retransmissions that are transparent to the user, therefore the real PDR cannot be accurately computed from this.
- No investigation of all or most relevant variables that can affect signal propagation in the specific environment.
- No study of the relevant metrics, many times focusing only on RSSI and distance-based models.

All these issues can yield unreliable results in the measurements that do not correspond with the real performance of the network. A new open-source tool, Trident [157], can alleviate some of these problems, providing a foundation for designing systematic experiments for WSN characterisation. It allows for remote wireless experiment configuration, which facilitates node relocation to run multiple experiments without having to carry cables and gateways for each node, as well as computing the real PDR by sending synchronised probes with no upper-layer protocols. The data from the experiments can also be collected wirelessly through a gateway node connected to a laptop. A Python interface running on the laptop provides experiment setup and control, as well as visualisation and exporting of the collected results. The only drawback is that, due to being based on TinyOS, an older networked embedded OS, it only supports older TelosB nodes. This tool has already been used succesfully in real-world scenarios. In [118] a WSN is deployed using Trident to study how the environmental factors in outdoor environments affect the communications. However, it has not been previously used for characterising metal marine environments.

2.5.4 Conclusions

One of the main lines of research in WSN focuses on wireless performance characterisation and modelling, as it is important due to the lossy nature of these

low-power networks. However, wireless communications are difficult to predict in 3D complex scenarios, even more when there are large amounts of metal and possible sources of EM noise. Therefore, experimental evaluation is necessary in these scenarios to assess the performance of a WSN. Limited experiments in testbeds and real scenarios have been done in these type of environments, but a multi-variable methodology has yet to be developed and validated with the correct metrics and experiment design.

2.6 Conclusions

The literature review presented in this chapter has shown that although WSN have been widely used for general structural and machinery health monitoring, there has only been limited used in off-shore marine applications such as oil and gas, wind energy, and ships. This is primarily due to:

- Lack of a wireless sensor module and software architecture that is designed and validated for the marine environment.
- The challenges that complex metal environments pose to wireless performance, which makes it impossible to predict.

These issues make hard to manage and deploy WSN to monitor structures and machinery in the marine environment.

The wireless sensing modules found in the literature are shown to be lacking in CPU power, memory, and the necessary sensors, as well as an integrated packaging that can withstand the marine environment conditions. These conditions include high humidity, vibration/shock from waves and wind, and high salt concentration from seawater. A plastic-encapsulated sensor with full WSN standards support, which includes vibration, acoustic, and environmental sensors can provide this hardware architecture to support WSN research and deployment in marine environments. To overcome the challenge of the high data rate that vibration-based sensors need, an optimised hardware-software architecture is necessary.

Moreover, monitoring of metal structures usually employs large optical or strain-based sensors that have high power consumption and cost. This makes the case for a multi-axial wireless autonomous module using eddy-current methods to measure relative displacement between adjacent beams in a metal structure, to be used as a prognostic tool. Eddy-current sensors can take advantage of the metal composition in these structures, as they can be used as a simple, contactless sensing method that only uses PCBs, which can be integrated into cube-shaped modules similar to the ones shown in the literature for different sensing mechanisms such as strain gauges.

Regarding wireless performance in marine environments, the literature has shown the difficulties of modelling and prediction when dealing with a complex multi-chamber metal scenario, therefore leaving real-world experiments as the only viable solution to assess wireless communication reliability. The limited experiments described suggest that a better methodology is necessary, which studies the multiple variables that can affect communications in these environments such as opening between compartments, operating machinery, and placement of the nodes, in addition to performing the experiments in a synchronised manner with no higher-layer protocols to improve the fidelity of the collected data.

In summary, to address these challenges, a whole systems integration approach that integrates hardware, packaging, wireless, reliability, firmware and software is necessary to develop this full marine WSN solution.

Chapter 3

Inductive Sensor Module for Displacement Measurement in Metal Structures

3.1 Introduction

Detection of atypical displacement is the focus of many structural health monitoring systems, which use a network of sensors deployed on the structure to recognise and prevent a possible structural failure. However, as shown in the literature review, these sensors have one or more of the disadvantages of large size, high power consumption, high cost, ability to measure only externally visible structural components, complexity in measuring movement in more than one dimension/axis, or requirement to embed during construction. As the skeleton that supports large structures such as buildings, cranes, ships, and marine platforms is mainly made of metal, eddy-current sensors can be used to detect displacement between adjacent components in these structures. Although they have been used for crack detection and position sensing in rotating machinery, their use for measuring displacement in multiple axes in structures has not been reported.

As well as being an appropriate way to measure metal displacement, eddy-current sensing's low sensitivity to the presence of moisture, dirt, and dust make it especially suitable for marine and similar open environments. For structural

monitoring, multi-axis sensing is desirable due to the complex nature of displacement and warping, especially in marine structures which are typically based on a steel framework that may, as in ships and some marine energy platforms, also be covered with steel plates that will themselves also displace relative to each other. Marine applications bring the further constraints of a salt-water environment reliability and the desirability of using battery-powered, wireless sensing to avoid having to run a network of wiring in what are often very challenging offshore deployment environments with difficult personnel access.

The primary research objectives of the research presented in this chapter were, therefore, to first design, develop and characterise an eddy-current displacement sensor suitable for marine and similar harsh environment applications and then, based on this sensor, to devise, fabricate and evaluate a systems integration approach for a self-contained, multi-axis, wireless eddy-current metal structural displacement sensor module that can operate reliably in the marine environment. To extend the functionality of the module and to allow reliability stressors to be also measured, the inclusion of mechanical shock/vibration and temperature/humidity sensors was also an objective.

3.2 Sensor research challenges

The challenges for the sensor design stem from the requirements found in the literature for structural monitoring.

The sensor needs to provide:

- Optimum eddy-current inductive sensing coil and driver/interface electronics design.
- Calibration of the sensing coil to measure over the required sensing range of 20 mm and resolution of 0.5 mm.
- For multi-axis applications, investigation of possible mutual interference effects on one eddy-current sensor due to the presence of eddy-current sensors on other, adjacent axes.

- Investigation of the effects of factors such as the presence of water on the sensor performance.

3.3 Inductive displacement sensor design

3.3.1 Sensor interface electronics

Nabavi and Nihtianov [50] present detailed design strategies for custom eddy-current sensor interface electronics. To reduce size, power consumption, and to optimise performance, in this work a COTS IC dedicated to inductive sensing is used. This is the LDC1614 [53] from TI, a 4-channel 28-Bit Inductance to Digital Converter (LDC), optimised for PCB planar inductors. This was selected as the LDC1xxx family from TI is the only commercial IC with proximity eddy-current sensing capabilities, and the specific LDC1614 handles up to 4 channels, allowing measurements in up to 4 different directions with a single IC. Although the LDC1614 could potentially be used with other type of coils, PCB planar inductors offer the best solution in terms of size, performance, and manufacturing cost.

The principle of operation is based on the circulating currents, known as eddy-currents, induced in a conductive material when it is brought near an AC magnetic field generated by an inductor. The eddy-currents generate their own magnetic field that oppose that of the inductor. This can be viewed as two coupled inductors whose global inductance changes as a function of the size, distance and/or composition of the target material. The LDC1614 generates the AC magnetic field using a resonant circuit driver connected to an LC tank formed by the PCB coil and a parallel capacitor. The inductance changes are measured by comparing the resonant oscillation frequency of the LC tank, given by eq. (3.1), with an external reference frequency. The digitised sensor data counts that are read from the sensor, DATAx, represent this ratio f_{SENSOR}/f_{REF}. The f_{SENSOR} can be calculated from the data counts using eq. (3.2), and thus the total inductance L from eq. (3.1). As the size and composition of the target material in SHM remains constant, the measured data counts will represent changes in

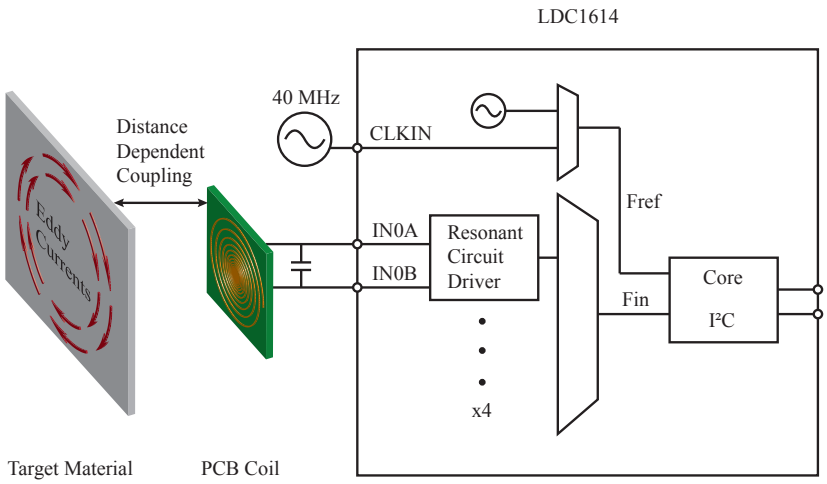

Figure 3.1: LDC1614 diagram and eddy-current sensing principle of operation.

the distance from the sensing PCB coil to the target. A diagram of the sensor operation and internals of the LDC1614 is in Fig. 3.1.

$$f_{SENSOR} = \frac{1}{2\pi\sqrt{LC}} \tag{3.1}$$

$$f_{SENSOR} = \frac{DATAx * f_{REF}}{2^{28}} \tag{3.2}$$

3.3.2 LC resonator and inductor design

The main design parameters for the sensing coil are the sensing range and resolution required by the application, i.e. 20 mm and 0.5 mm respectively. As miniaturisation is also important, the coil needs to be as small as possible while achieving the desired range and resolution. A high Q-factor, as defined by eq. (3.3), minimises resistive loses and maximises inductance, which gives a better sensing range and resolution.

$$Q = \frac{\omega L}{R} \tag{3.3}$$

The LDC1614 datasheet [53] and application report [158] set out design parameters for a high Q-factor sensing coil optimised for use with the IC. These guidelines are derived from theory and experiments found in the literature, as well as experimental data collected using the IC and different coil sensors.

The process for designing the PCB Coil is as follows:

- Although different shapes can be used, the experiments in [159] show that a circular coil has the highest sensitivity when used for linear displacement eddy-current sensing. This also maximises the size of the coil in a square PCB while leaving space for the four mounting holes in the corners. The purpose of these holes in the final assembly will be described in Section 3.5.5.

- From experimental data it is shown that the sensor resolution is best out to a range of approximately the external radius of the sensing coil. Sensing is possible beyond that range but the resolution is less. As the target application requires at most a 0-20 mm sensing range, a PCB coil of 35-40 mm diameter is therefore necessary. An inductor with a D_{out} of 38 mm can fit in a standard PCB size of 50x50 mm, including the above-mentioned mounting holes and connectors.

- As shown in the TI application report [158] and also demonstrated by Huang and Ngo in [160], an inductor inner-to-outer diameter ratio of $D_{in}/D_{out} > 0.3$ is ideal to have a high Q-factor. Therefore, an internal coil diameter of 12 mm is selected, which gives a D_{in}/D_{out} value of 0.32. If the ratio is increased, the number of windings would be too low and the inductance value would fall.

- The inductance value not only in planar but in any type of coil is increased with the number of turns. To maximise the number of turns for the selected coil size, it is necessary to select the minimum track size and track gap allowed by standard low-cost manufacturing, in this case 6-mil track and 6-mil gap.

- A standard 1.6 mm PCB thickness is selected, as a thinner PCB would not be strong enough when used in the final assembly.

- The number of layers selected for the inductor needs to be as high as possible to provide a high inductance while keeping a low resistance, due to mutual inductance between the layers. However, to maintain the desired frequency of operation of the sensor, the capacitor used in the resonator has to be decreased, as per eq. (3.1). As shown in the calculations below, to keep the optimal sensor frequency the capacitor value would fall below the minimum recommended specifications (100 pF) if the layer count increases beyond 2 layers.

In summary, the design parameters of the PCB sensing coils are: D_{out} = 38 mm, D_{in} = 12 mm, 6-mil track, 6-mil gap, 2 layers, 1.6 mm substrate thickness, and 50x50 mm total PCB size. Fig. 3.2a shows the planar PCB coil, with a two-pin connector at the bottom and a mounting hole in each corner that will be used when assembling the full module.

To select the correct capacitor to form the LC resonator tank, which determines the working frequency, and to evaluate the quality of the coil, the inductance and quality factor need to be calculated. These can be obtained with either of the two tools supplied by TI, an offline Excel sheet [161] or the online web WEBENCH tool [162], based on F.E. modelling and simulations. These tools also provide the value of the external capacitor for setting the sensor operating frequency and the self-resonant frequency and resistive component of the coil. Although the sensor can work from 1 kHz to 10 MHz, to achieve the best resolution TI recommends a ratio of $f_{SENSOR}/f_{REF} = 0.025$ and $f_{SENSOR} < 0.8 * f_{SR}$. Since f_{REF} comes from an external 40 MHz crystal oscillator, f_{SENSOR} is about 1 MHz. The inductance for the 38 mm coil, using WEBENCH, is L = 139.7 μH, with Q = 36.61 and self-resonant frequency f_{SR} = 6.731 MHz, with f_{SR} being the self-resonant frequency of the coil. With an external capacitor C = 120 pF, the working frequency of the LC resonator is f_{SENSOR} = 1.209 MHz, well below f_{SR}.

Although the TI design tools allow a quick design of the sensing coil, the calculated coil parameters are based on an ideal planar inductor. The tools do not

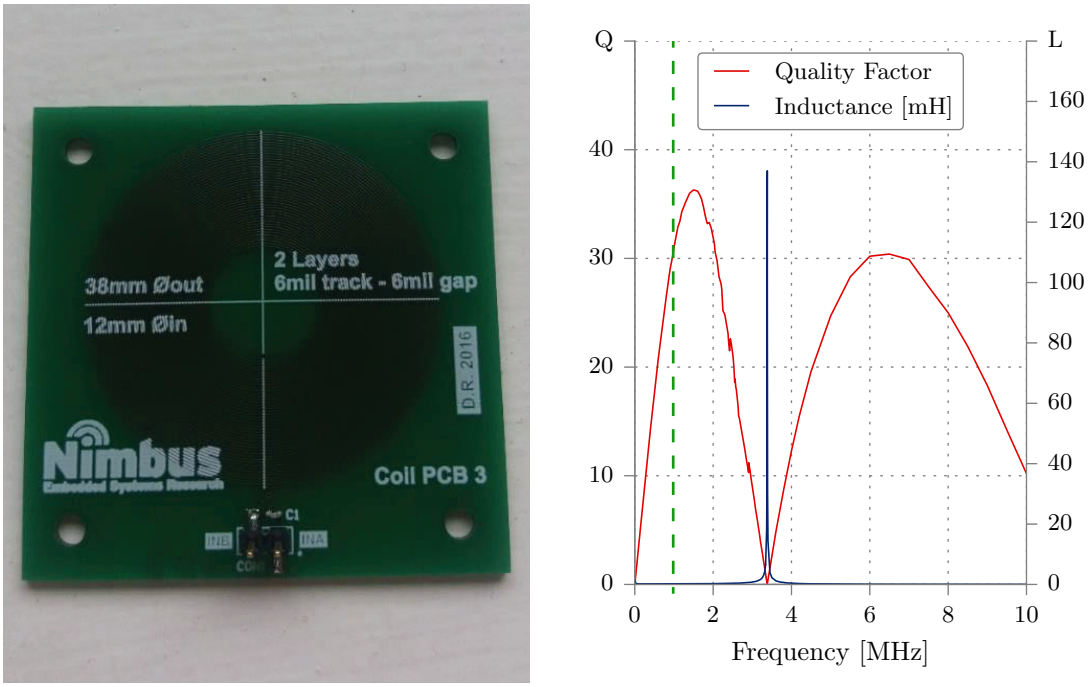

(a) (b)

Figure 3.2: (a) PCB Coil (b) Measurements of inductance and quality factor of the PCB coil using an impedance analyser (selected working frequency in dashed green line).

take into account the influence of connectors, connecting tracks, through holes and variations in line/space dimensions or dielectric thickness due to manufacturing. Therefore, the inductors were measured using a HP-4192A impedance analyser with a 10 kHz - 10 MHz sweep. Fig. 3.2b shows that higher quality factor was found between 1-2 MHz, while the inductance peak at 3.1 MHz indicates the self-resonant frequency, half of the design tool predicted value although in the same order of magnitude. With C = 120 pF, the measured inductance at 1 MHz is L = 185 μH with Q = 31 and f_{SENSOR} = 1.068 MHz, close to the recommended 1 MHz and still well below the measured self-resonance.

The LC tank circuit is not ideal and has a resistive component R_p, which is also a function of the target distance. The output current of the sensor I_{DRIVE} needs to be set to a value that allows to maintain a constant oscillation amplitude for the minimum R_p value. As the minimum measured value is $R_p = 36.9K\Omega$, the optimal sensor current calculated is $I_{DRIVE} = 40\mu A$ for each coil.

Although the sensing coil design methodology described in this section has produced an optimal coil, which can sense the desired 0-20 mm range and with a high Q-factor that could potentially yield a precision in the order of *um*, it still needs to be characterised with different metal targets under different conditions.

The maximum sensing range allowed by the TI LDC1614 is 70 mm, provided an optimal sensing coil is designed for this range, which would have an external diameter of 14 cm. This maximum range was obtained from TI WEBENCH tool.

3.4 Inductive sensor characterisation and calibration

3.4.1 Introduction

The sensor described in the previous section presented a novel concept for structural monitoring of metallic structures by measuring relative displacement between components in the structure. The state-of-the-art eddy-current IC used in the module needs to be fully characterised for the application, as little research has been yet conducted using this type of highly integrated sensor in this applications. However, the bending or displacement of real structures is hard to replicate in a laboratory, and the test systems can become complicated to design and operate. Therefore, new testing methods have to be designed that emulate these conditions, which are simple but accurate enough to validate and characterise the module. Moreover, these test systems have to allow for multi-axial displacement to evaluate interference between coils, as well as different variables such as target metal type and thickness, angle relative to the coil, presence of the battery near the sensor, potting resin, and water. To characterise the sensor for these varying parameters, two different custom test systems were designed to accurately emulate different displacements of metal parts.

3.4.2 Characterisation of the planar inductor sensor

3.4.2.1 Test system design

As thick steel is challenging to bend in a controlled way, a different approach was taken to allow for more precise measurements that kept the metal target static while the sensor could be displaced, emulating the effect changing the distance between the sensor and the plate. An L-shaped metal corner-plate was made and fixed in place, then the sensing coils were moved relative to the plate using a reconfigured pick-and-place machine. This allowed characterisation of the sensors in two orthogonal axes and investigation of possibly cross-coupling or interference between two adjacent coils and metal plates.

Fig. 3.3 shows the test system designed for characterising the sensor in one or two out of the four possible axes, with the retrofitted manual pick-and-place machine and several 3D-printed plastic components to fix the metal plate to the machine, as well as a base support to hold the sensing coils. This base is attached to the X-Y moving part of the pick-and-place, allowing location and locking of the sensor at any desired distance D from each plate side. To illustrate better this mechanism, a CAD diagram of the setup is shown in Fig. 3.4. To measure the actual displacement, two optoNCDT-142 [163] laser displacement sensors were used, mounted on the same base plate and pointing in the same direction as the sensing coils, which are set 25 mm back from the front face of the coil. This is due to the laser sensors needing a minimum distance of 25 mm to the target. The full range of the sensors is 25 mm, with a linearity of 20-25 μm and a repeatability of 1 μm, more than sufficient to characterise the sensors. For data collection, the sensors were connected to a laptop using the module interface electronics described in Section 3.5.3.

3.4.2.2 Experiment setup

To characterise the inductive sensor, a single planar PCB coil was used to measure distances from 0-20 mm at 1 mm, 0.5 mm, and 0.1 mm steps to 20x20 cm mild steel plates of four thicknesses of 4, 6, 8, and 10 mm. There were three different step sizes, first to observe the general behaviour of the sensor (1 mm), then to

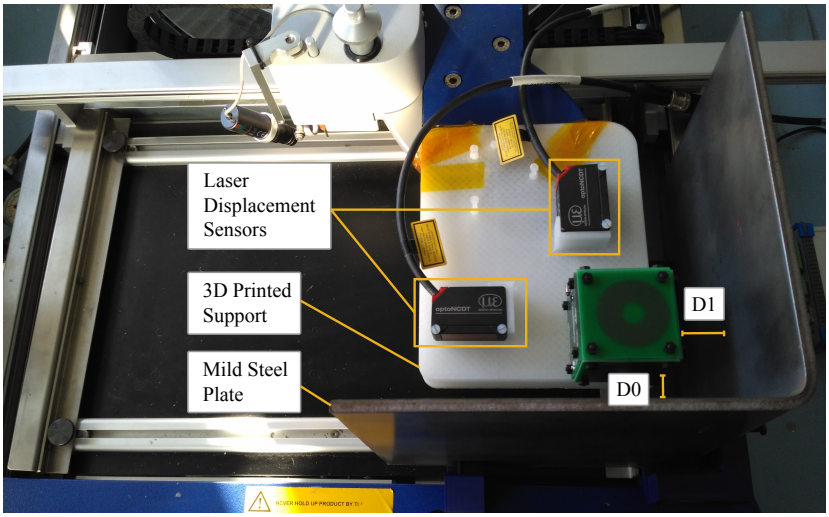

Figure 3.3: Test system setup, composed of a retrofitted pick-and-place machine with 3D-printed support parts and laser displacement sensors.

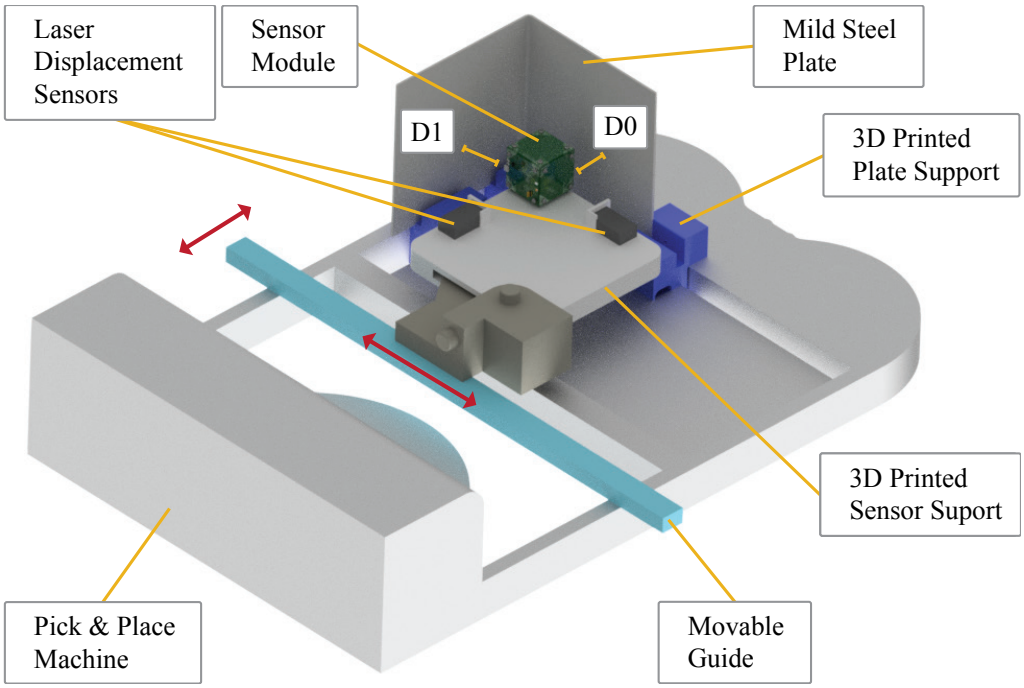

Figure 3.4: CAD diagram of the test system setup.

confirm that it can resolve the necessary 0.5 mm observed in the literature and, finally, to test if it could achieve a higher resolution (0.1 mm). The four metal

thicknesses allowed investigation of the effect of the material thickness in the measurements as described in Section 3.4.3.2 below.

The LDC1614 IC was configured with the parameters calculated with the WEBENCH tool for the designed coils. The reference count register limits the resolution of the sensor, and is inversely proportional to its maximum sample rate. As the samples were collected manually one by one, a high sample rate was not necessary and the maximum resolution possible was selected by setting the reference count register RCOUNT = 0xFFFF, limiting the maximum sample rate to 9.5 sps. This can be changed for different applications up to a maximum of 4.08 Ksps, allowing a theoretical vibration detection bandwidth of 2 kHz. In SHMS the sampling rate can be slow and at long intervals as the rate of displacement is typically slow and this will increase battery life. The addition of the IMU gives the option of increasing inductive sensing rates if a sudden large displacement, caused, for example, by structural failure, impact or seismic shock, is detected by the IMU.

3.4.2.3 Distance vs inductance results

Fig. 3.5 shows the sensor data counts (as defined in Section 3.3.1) for the inductor L1 for the four metal thicknesses over the 0-20 mm range, at 1 mm steps. The distance D0 is fixed at its farthest (20 mm), to minimise the interaction of this side of the plate with its orthogonal inductor L1 and therefore avoid interference with the D1 measurement (parallel plate). There are small differences between the curves for the different plates; however, as this behaviour occurred in all of the measurements, it is assumed they rather correspond to small errors introduced whenever a plate is inserted and the zero from the laser sensors is set again rather than due to an intrinsic effect of plate thickness. In fact, it is known that, due to the skin effect [164], most of the induced currents in the target plates will be confined to the surface of the conductor. If the skin depth is calculated for a mild steel plate using eq. (3.4), with ρ and μ being the resistivity and permeability of the material respectively, at $f = 1$ MHz sensor frequency it is approximately 4.3 μm, which is 1000 times smaller than the thinnest plate used

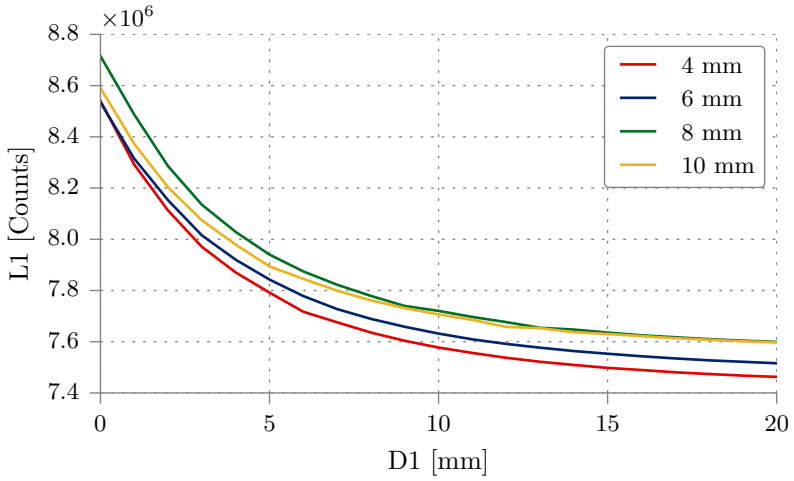

Figure 3.5: L1 counts vs D1 distance for the different plates, at D0=20 mm, with measurements done at 1 mm step.

(4 mm). Therefore, for thicker plates the generated eddy-currents and hence the measured inductance would be similar.

$$C\sigma = \sqrt{\frac{\rho}{\pi f \mu}} \tag{3.4}$$

3.4.2.4 Sensor resolution

The precision of the sensor is mainly determined by the reference count configuration and the ratio of the target distance vs the diameter of the coil. Although the theoretical resolution of the sensor can be less than 10 μm for up to 100% distance/coil diameter, the impact of external variables like the test system setup, the manual adjustments, and the laser sensors will lead to a lower resolution.

In Fig. 3.6, it can be seen that the measurements taken at 0.5 mm step have the same shape as the ones in Fig. 3.5, with monotonic decaying exponential curves, showing that a resolution of at least 0.5 mm is achieved. However, in Fig. 3.7 non-monotonic fluctuations are present when measuring at 0.1 mm step, due to the system setup not being able to accurately resolve 0.1 mm increment displace-

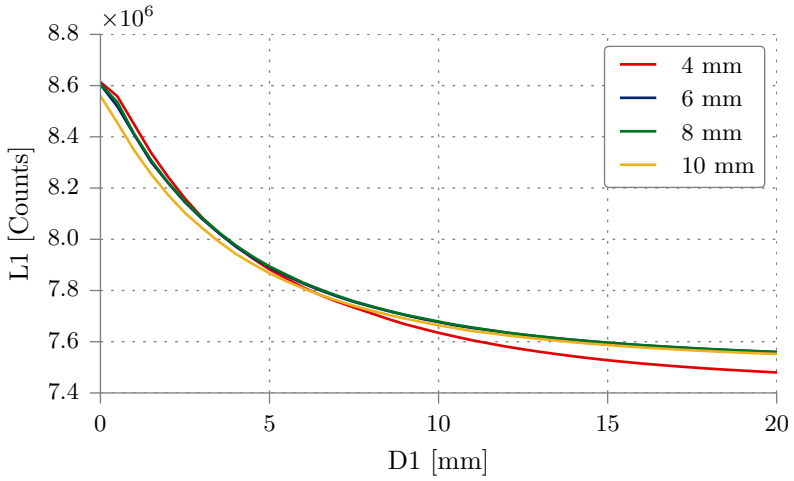

Figure 3.6: L1 counts vs D1 distance for the different plates, at D0=20 mm, with measurements done at 0.5 mm step.

ments. Comparing the 4 mm thickness plate at the 5 mm distance measurement, for the three figures, it can be seen a variation from 7.8×10^6 to 7.9×10^6 counts, which corresponds to a measurement uncertainty of approximately 2 mm. This is not an inherent uncertainty of the measurement method but happens because of the manual setup of each individual set of measurements. When a metal plate is inserted in the system, it must be moved until it touches the module screw tops. Then the laser sensors are set to zero at that position. This base position always varies slightly because of the multiple plastic parts in the setup, which bend slightly when tightening up the screws.

The overall conclusion from all of the above measurements is that the sensor module in the current test setup can detect displacement over a 0-20 mm range with at least 0.5 mm resolution. The apparent measurement uncertainty due to the limitations of the existing measurement setup will not affect a real-world measurement as the sensor module will be solidly fixed in place on its base structural member and will be measuring relative movement of an adjacent structural member.

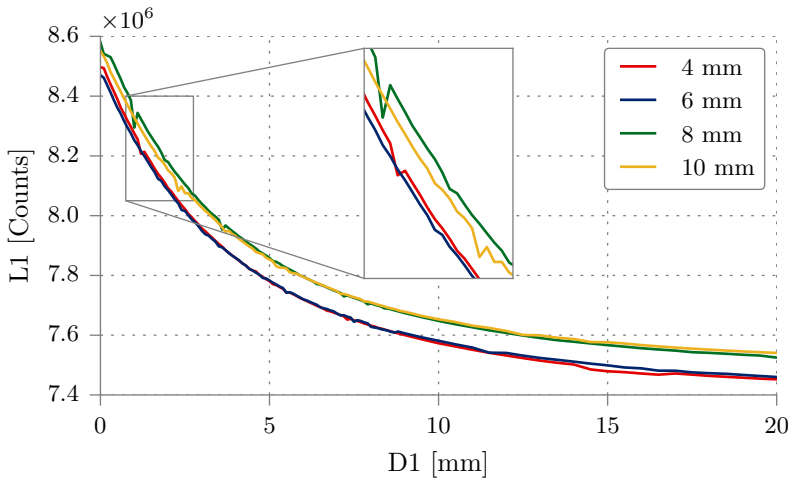

Figure 3.7: L1 counts vs D1 distance for the different plates, at D0=20 mm, with measurements done at 0.1 mm step.

3.4.3 Characterisation of the planar inductor sensor in two axes

3.4.3.1 Experiment setup

As described in the previous section, the planar PCB coils have to be adjacent to each other to measure displacement in two different directions to two orthogonal metal components and, therefore, cross-coupling and interference are possible. The test system allows this to be investigated by measuring distance from two coils to both sides of an L-plate, as previously shown in the test system setup in Fig. 3.3 and 3.4. A full set of measurements was performed for both of the coil-plate distances D0 and D1, coils L0 and L1 respectively, for the 0-20 mm range, at 0.5 mm steps.

The procedure to perform each set of measurements is as follows:

1. Place the sensor coils in the 3D-printed support attached to the X-Y table, as well as the laser sensors.

2. Move the X-Y table movable guide until the plastic screws of both sensor coils are touching the metal sheets.

3. Reset the zero of the laser sensors and start them on continuous measurement.

4. Move the X-axis of the guide until its corresponding sensor reads 0.5 mm and read the inductance value of both inductor sensors.

5. Keep moving the X-axis in 0.5 mm steps while keeping the Y-axis fixed, and read the sensors until it reaches 20 mm distance.

6. Move the inductors back to the origin against the metal plates.

7. Move the Y-axis 0.5 mm and keep it fixed, while repeating again the full X-axis measurements at 0.5 mm step until 20 mm distance.

8. Repeat again the same measurements, but separating another 0.5 mm the Y-axis.

9. Keep repeating full range sets of X-axis measurements while separating the Y-axis 0.5 mm after every set until it reaches 20 mm.

3.4.3.2 Effect of D0 distance on L1 inductor.

The effects of the proximity of a plate on its adjacent orthogonal coil are shown in Fig. 3.8, a 3D representation of all the curves for L1 data counts vs D1 for the whole range of D0 distances, for the 4 mm thick plate. It can be observed that the effect is minimal and only when the sensor is closer to the D0 plate, due to the higher sensitivity of the LDC1614 IC when the coil is closer to the target. The largest standard deviation for this plate is 55308 (0.65% of the maximum value) and occurs when D1=0, which is also the maximum found among all the different plates. In Fig. 3.9, the average of these L1 vs D1 curves for the D0 range is shown, for every plate thickness.

Overall, it can be concluded that the presence of even thick metal plates adjacent and orthogonal to a given sensing coil do not have a significant effect on the measurements made using that coil. Both sensors can therefore operate independently with identical performance.

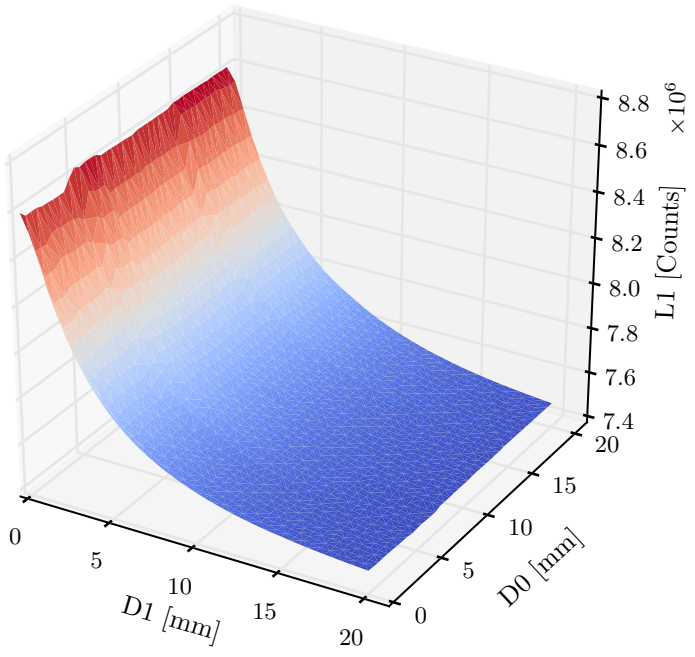

Figure 3.8: L1 counts vs D1 and D0 distance for the 4 mm plate, at 0.5 mm step.

3.5 Inductive displacement module design

3.5.1 Module research challenges

From the deficiencies of current sensors for structural health monitoring found in the literature as well as the issues of integrating the developed inductive sensor, the following design and application constraints arise:

- The module needs to have a package design/shape that is easy to encapsulate and can protect the module from the harsh environment conditions found in marine environments, i.e. high humidity and salt concentration as well as vibration and shock. It has to be rigid and sturdy enough to withstand these shocks without being damaged. This packaging has to allow for direct exposure of the coils close to the target surface.
- It needs to have wireless capabilities that support IEEE 802.15.4, the most

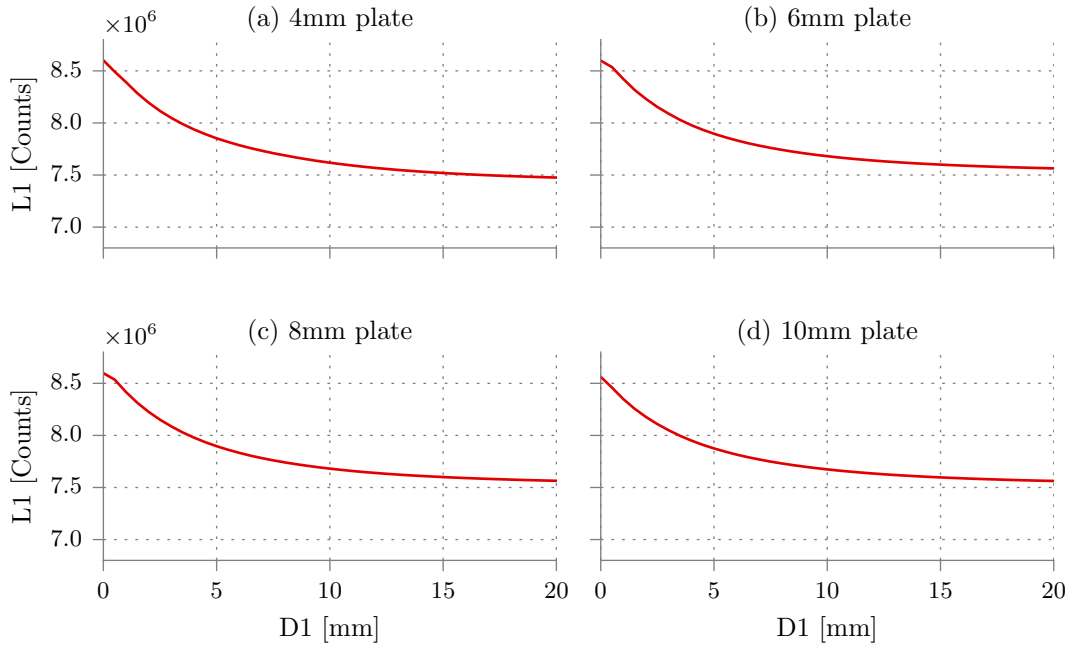

Figure 3.9: Average L1 counts vs D1 distance curves over the D0 range for the different plates.

widely used WSN technology, with a current embedded networked OS that allows remote control and data collection of the sensor module.

- Extra COTS sensors that allow for environmental monitoring and can complement the displacement measurements need to be integrated into the module.
- It has to be self-contained, battery-powered, and rechargeable.
- The module needs to be 3D so that it is able to present multiple, orthogonal sensing coils to adjacent metal structural members.
- The module must ensure that the coils are positionally stable relative to each other, ensuring that they measure only relative metal movement and not their own relative movement.
- The module needs to contain all required analog, digital, communications, RF and power electronics, and battery assembled in such a way that they

do not interfere with the multiple sensing coils.

- It, ideally, should be lower-cost than current systems, in terms not only of hardware but also deployment cost.

The research challenges arise primarily from the above application constraints:

- Identification of a 3D configuration and assembly method that meets all of these constraints.
- Characterisation of the measurement performance of the module.
- Encapsulation of the module for reliability in a marine environment.

3.5.2 Overall system design

To make the sensor a self-contained, wireless, autonomous module, the sensing coils and IC needs to be integrated with a processing unit, communications, power management, battery, and other sensors that complement its functionality. This presents a series of challenges: the coils need to be exposed, as the range is limited and the resolution is better when it is closer to the metal surface, therefore the module cannot be simply packaged inside a box; to measure relative displacement between two or more adjacent components in a structural framework, different coils need to be placed orthogonally. A cubic structure made out of PCBs is then an ideal solution. Fig. 3.10 shows a conceptual deployment of the module on a structure.

The size of the cube is defined by the 50 mm square PCB of the optimal coil described in Section 3.3.2. As the sensing IC supports up to 4 channels, 4 coils can be used, allowing relative displacement measurement between up to four structural components. This leaves two faces of the cube to use for the electronics and interconnects. Although the literature has, for example, shown a board-folding method to interconnect and assemble a cuboid module made out of PCBs [103], in this case it would not provide a sturdy enough structure due to the size of the module. Conventional metal-pin male-female connectors can, however, offer a simple and reliable choice, complemented with a 3D-printed internal scaffold

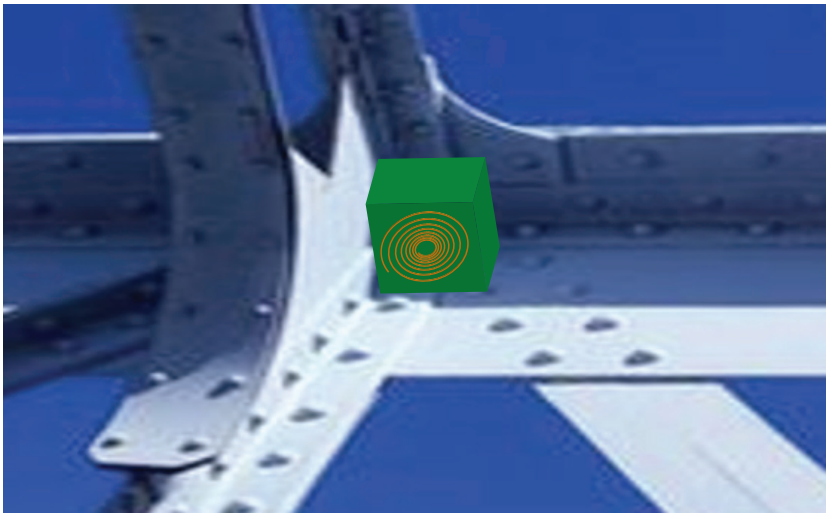

Figure 3.10: Conceptual deployment of the inductive module on a structure.

to hold the cube together as well as the battery, as previously shown in other battery-powered PCB cuboids [104]. Fig. 3.11a shows a CAD render of the cubic design and Fig. 3.11b an unfolded "crucifix" view of the individual PCBs. Four of the faces are planar sensing 'COIL' PCBs, three on the 'lateral' sides (L0 to L2) and one on 'top' (L3). The 'CONNECTOR' PCB at the crucifix center acts as a base for inter-PCB connectors and routes the lines from inductors L0, L1 and L2 to the 'ELECTRONICS' PCB with processing, communications, sensors, and power. The L3 PCB is connected directly to the 'ELECTRONICS' PCB. This arrangement provides sensing in three different directions on the horizontal plane and one on the vertical, minimising track length between the coils and the sensing IC. The full assembly is described in detail in Section 3.5.5.

3.5.3 Main electronics board

The ELECTRONICS PCB contains most of its components in the top layer, Fig. 3.12a, facing the inside of the cube, to protect them from the environment and to give some electrical shielding.

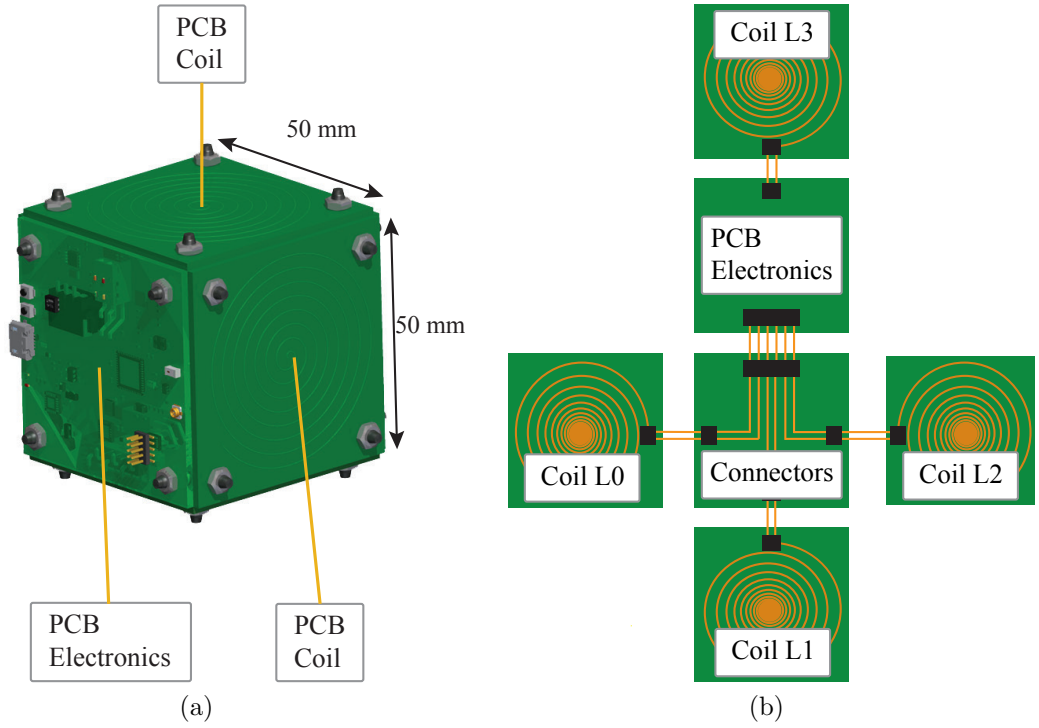

Figure 3.11: (a) Cube module concept (b) Unfolded cube concept.

3.5.3.1 CPU, communications, and sensors

The core of the platform is the CC2538 [95], a low-power ARM Cortex-M3 MCU with 32 KB RAM and 512 KB Flash, which includes a 2.4 GHz IEEE 802.15.4 radio and a wide range of peripherals, including an I^2C and SPI bus to interface with digital sensors. This microcontroller was chosen mainly for its increased processing power over old MSP430-based platforms, its integrated radio that reduces cost and power consumption, and its good Contiki-OS support (the networked embedded OS predominantly used in WSN research). There are three different types of sensors connected to the MCU I^2C bus: the inductive displacement sensor (described in Section 3.3.1), an LSM9DS1 [165] IMU (3-axis accelerometer, gyroscope and magnetometer), and an SHT21 [166] humidity/temperature sensor. The full IMU can provide extra features to the module, e.g. measuring of tilting of the whole structure, or activation of the inductive sensing IC only when a structural shock is detected, saving power. The humidity/temperature sensor allows the module to be used also as an environmental monitoring sensor and

the temperature sensor could be used to compensate for thermal expansion and contraction which can cause substantial movement in large structures.

On the opposite, outer face of the PCB (Fig. 3.12b) are the components that need external exposure, such as the humidity/temperature sensor. For battery charging and firmware updating, a microUSB connector is also on this side of the PCB, serving both functions with the same connector. Finally, opposite this connector is a surface mount chip antenna, as well as a small UF.L connector, to allow use of a higher gain external antenna to extend, if necessary, the wireless range or to locate the antenna at a distance if, for example, the module was inside an enclosed metal space.

3.5.3.2 Power management

Two 600 mAh rechargeable lithium-polymer batteries were chosen as a power source and integrated inside the cube, as lithium-polymer is the most common battery chemistry used in rechargeable embedded modules due to its safety and high capacity-size ratio. The power consumption is approximately 25 mA when measuring and 40 mA when transmitting data, with a quiescent current of less than 1 mA when in power down mode. This allows for 50 days of continuous operation if configured to measure and send 1 burst of samples/hour. A bigger battery cannot be fitted inside the module, but if longer autonomy is needed an external USB powerbank can be connected to the microUSB. As low power operation is important for the application, a DS2745 [167] battery monitor is also on the I^2C bus that samples the battery voltage, as well as the instant and accumulated current consumed by the node, which is useful to predict its battery life. For power management, a battery charger IC [168] is used, with two SMD LEDs to indicate the battery charging state (charging/charged), and an LDO regulator [169] which provides a stable 3.3 V from the nominal 4.2 V of the battery.

3.5.4 Firmware and software

The firmware developed for the module is built on top of Contiki-OS [65], an open source operating system for the Internet of Things, designed to wirelessly inter-

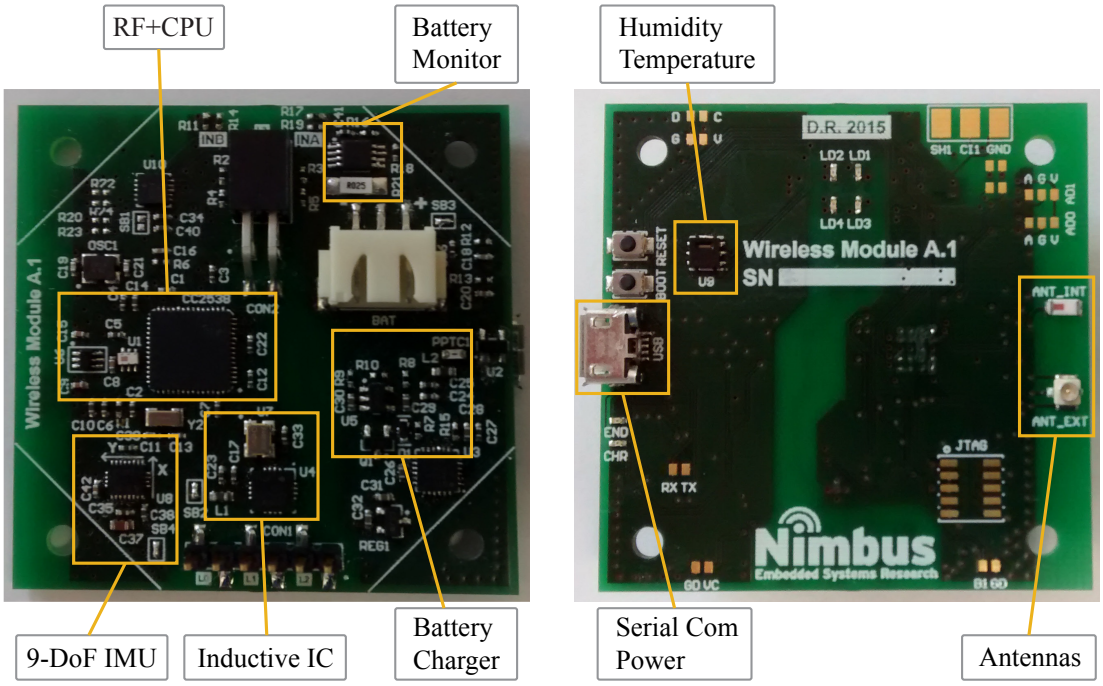

Figure 3.12: (a) Top layer PCB (internal side) (b) Bottom later PCB (external side)

connect battery-powered, low-cost, microcontroller based devices. Some of its features include support of recent low-power wireless communication standards, such as 6LoWPAN, RPL and CoAP, which provide full networking capabilities with a low overhead. To allow for remote command execution and sensor configuration, the main application is based on Contiki-shell, an interactive text-based console that allows for definition of different command functions in the node, to be triggered locally over a serial USB or remotely from the gateway to one or multiple nodes. This makes it easy to extend the platform by adding commands with different functionality. One of the limitations of Contiki-Shell is that when launching remote commands in a node, the node will not send back a response to the gateway. Thus, the Contiki-Shell core was modified and extended to receive responses from the nodes when necessary. These extensions done to Contiki-Shell are further explained in the following Chapter 4, section 4.5. All wireless communications use the RIME stack, which provides a layered set of lightweight communication primitives. Although the system architecture is designed to be

used in single-hop networks, it could be modified to work in multi-hop by using different RIME primitives. ContikiMAC is used for radio duty cycle, which keeps the radio off 99% of the time, saving power but increasing the communication delay. The remote control and data collection is done through a gateway node connected to a laptop, using a custom Python script. The firmware can be updated directly through the microUSB connector without the need for an external JTAG programmer, due to the embedded bootloader present on the microcontroller.

3.5.5 Module integration

3.5.5.1 Module electrical and mechanical assembly

To produce a reliable and robust module, its assembly has to be strong enough to withstand handling and deployment. As shown in the literature, the cuboid structure described in the previous section is ideal to overcome these challenges. To minimise interference with the inductive measurements, the materials surrounding the coils and the electronics should be non-conductive, the assembly therefore uses 3D-printed plastic assembly parts with nylon screws and standard 2.54 mm connectors.

Fig. 3.13a shows the internal module assembly. The CONNECTOR PCB at the base of the cube has a horizontal female 2x6 pin connector that mates at 90 degrees with the vertical male in the ELECTRONICS PCB, connecting with the differential inputs of the three inductive sensors. Only the top row of the female connector is used as the bottom row provides the necessary gap for the edges of the two boards to be at the same level. These six lines are then distributed to each of the three PCB coils on the sides through another set of connectors. The top coil is connected directly to a connector on the top of the ELECTRONICS PCB.

To hold the whole module together, a small 3D printed corner-piece is used in each of the eight cuboid corners, screwed with a 3 mm nylon bolt to each PCB corner, with the nuts facing outside. The corner pieces and the distance between the bolt holes are designed for an interference fit so that, when the bolts are inserted, the assembly holds itself together. This way the last side of the cube

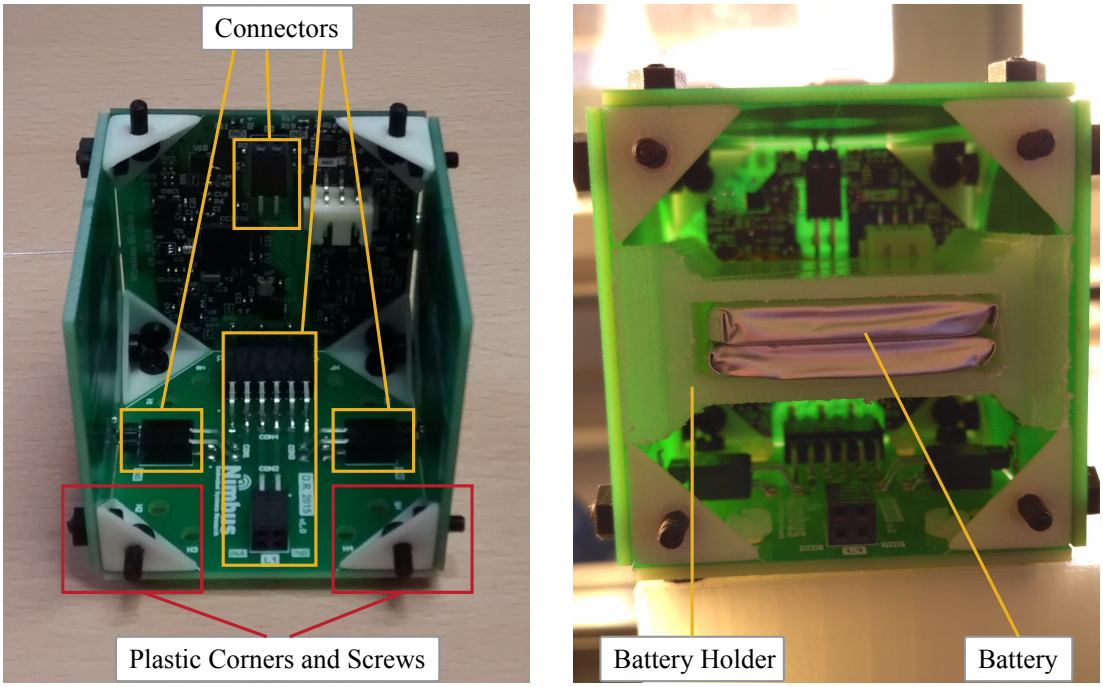

(a) (b)

Figure 3.13: (a) Module assembly with connectors, plastic corners and screws (b) Battery assembly inside the cube.

can be closed and the nuts screwed on from the outside, which will also facilitate the encapsulation process, as described in Section 3.5.5.3.

3.5.5.2 Battery integration

A 3D printed enclosure keeps the battery pack in the center of the cube, as far as possible from the coils and electronics to minimise interference. This enclosure slides in and is held between the 3D printed corners, Fig. 3.13b.

Fig. 3.14 shows the assembled cubic module with all integrated sensors and electronics.

3.5.5.3 Module encapsulation

As the final application of the module is to be installed in marine off-shore structures, it needs to be fully sealed and protected from the high humidity and salt

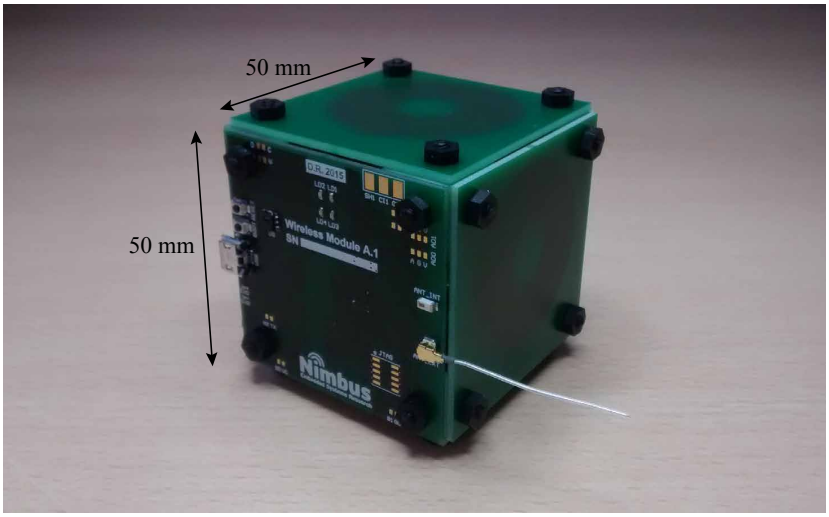

Figure 3.14: Fully assembled module in cuboid form, with four PCB faces for planar coils, one for the electronics and another for internal connectors.

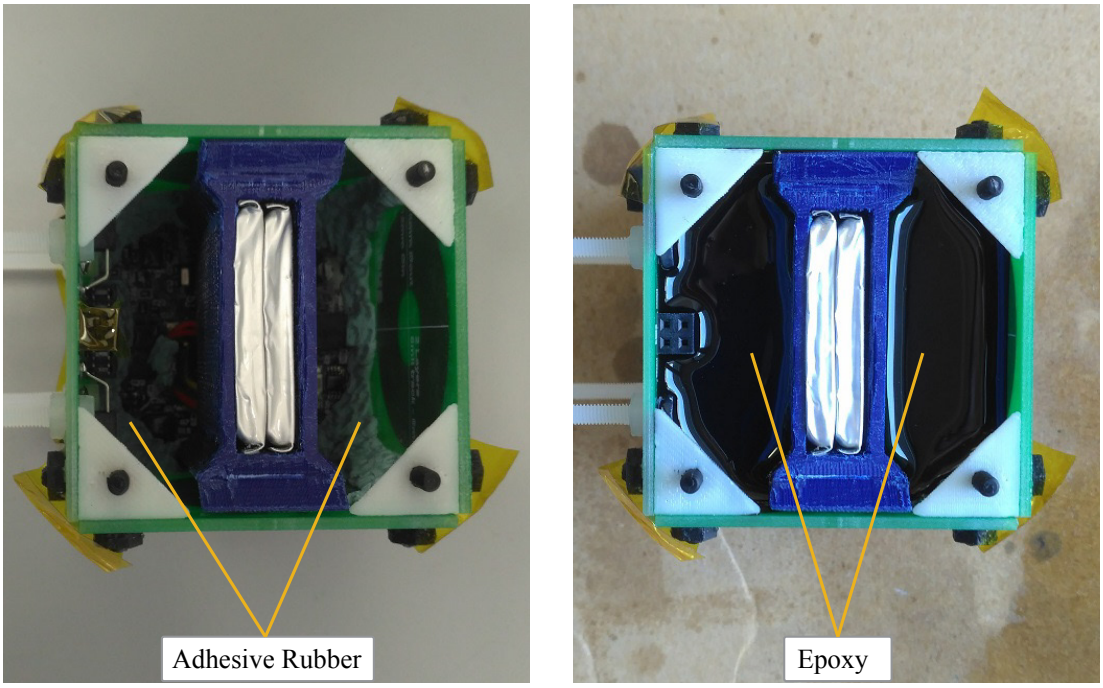

(a) (b)

Figure 3.15: (a) Cube module pre-potting sealing (b) Cube module encapsulated.

found in the environment. For this, a resin compound is necessary to encapsulate the internal electronics and battery. The encapsulation resin used is the

Electrolube UR5041 [170], a two-part ultra high performance resin system which features excellent resistance to sea water and low water absorption, as well as good temperature range performance (-60 to 125 ^oC) and high toughness, tear, and oxidation resistance. This was selected as it is the only commercial encapsulation resin found that is designed specifically for electronics in marine environments, and offers a high performance in a range of challenging environments.

A first attempt at using the resin showed a much lower viscosity before curing than expected by the value given in the datasheet (2500 mPa·s at 23^oC), causing leaking even through the vias of the PCB. As a consequence, special care had to be taken to cover all holes and slits in the pcb edges and vias, as well as sensitive components to avoid leaking. To seal the internals of the cube before potting, adhesive rubber was used between the edge of the PCBs, while the rest of the inner sides were covered by spraying conformal coating (Fig. 3.15a). The coating used is the Electrolube PUC polyurethane coating [171], to avoid material interactions with the encapsulation resin which is also polyurethane-based. The external sides of the cube were also covered by the polyurethane coating after potting, to further protect the PCB coils.

The procedure to encapsulate the module is as follows:

1. Assemble the bottom connector PCB, two side coils, top side coil, and electronics following the procedure described in Section 3.5.5.1, leaving out the side coil opposing the electronics PCB, as shown in Fig. 3.15a. The long bolts that will be used to attach the module to the structure or test system will have to be installed in the connector PCB also, as they are inserted from the inside.

2. Seal with Blu Tack adhesive rubber the internal gaps between the PCBs, as well as the plastic corners and bolts.

3. Place the battery into the battery holder and connect it to the electronics. After covering the last coil connector with 3M polyimide film tape 5419, spray the interior of the cube with a thin layer of polyurethane coating, covering all the sides of the PCBs facing the inside of the cube, and slide the battery inside the cube.

4. Pour the resin compound into the module, filling it up to the border without covering the connector (Fig. 3.15b).

5. Remove the tape from the connector, attach the last remaining PCB coil and let the resin cure for 24 h at ambient temperature.

6. After curing, spray the exterior of the cube with a thin layer of polyurethane coating for extra protection of the coils and electronics, covering all exterior PCB sides including the assembly nuts and bolts. Before applying the coating, the microUSB connector, buttons, and humidity/temperature filter cap have to be covered with tape which will be removed after the coating dries.

3.6 Inductive sensor module testing

3.6.1 Test setup

As the module is designed to be used as a fully autonomous wireless sensor, most of the test measurements performed were with the battery inserted in the plastic holder inside the module. However, for very noisy environments, or when wired power is available, a USB connection can be used for communication and power. This would also allow the connection of a larger battery pack to extend battery life or to keep the batteries remote from the module in case of possible interference with the displacement measurements. To test for this possible interference, the module performance was compared with both USB and battery power. As some SHMS applications could involve exposure to high humidity or rain, another test was also performed with water sprayed over one of the inductors, to assess its effects on the measurements, results below.

The sensor module has been characterised for parallel movement of the target material, but structural deformation may also involve bending or torsion. To simulate bending, a second test setup was designed (Fig. 3.16), where the inclination of a metal plate can be changed in one axis by a specified angle relative to the sensing coil. While most civil structures are made of steel, this test rig was also

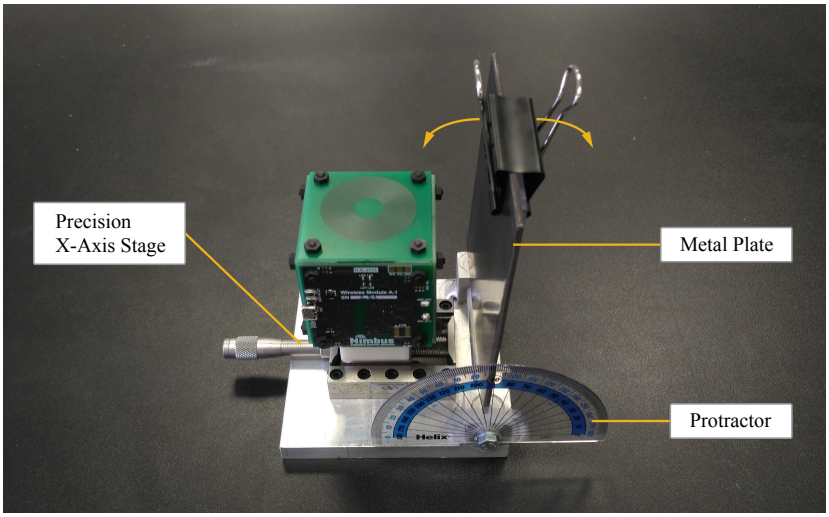

Figure 3.16: Test system setup for measuring angle of the plate, composed of a precision x-axis stage and a protractor to measure distance and angle of inclination.

used for single axis parallel displacement of other metals. The results from these measurements are later in this section.

3.6.2 Module performance

The fully assembled module performed as expected, with no packet data loss while sampling and transmitting. The temperature sensor recorded a minimum temperature of 24 ^oC and a maximum of 32.2 ^oC during the tests. The data from the humidity sensor and IMU were also successfully collected. Fig. 3.17 represents the curves for L0 and L1 vs the distance to their corresponding plates, when the distance to its opposing plate is at D=20 mm. On average L1 exhibits a higher L count (lower inductance). This is most likely due to the battery not being square, and then being closer to the L1 inductor than to L0. The battery covering is partly metallic and a small eddy-current is induced in the surface of the battery, lowering the total measured inductance. Although this will not have any effect on the accuracy, the offset will have to be taken into account when developing a model for a specific application.

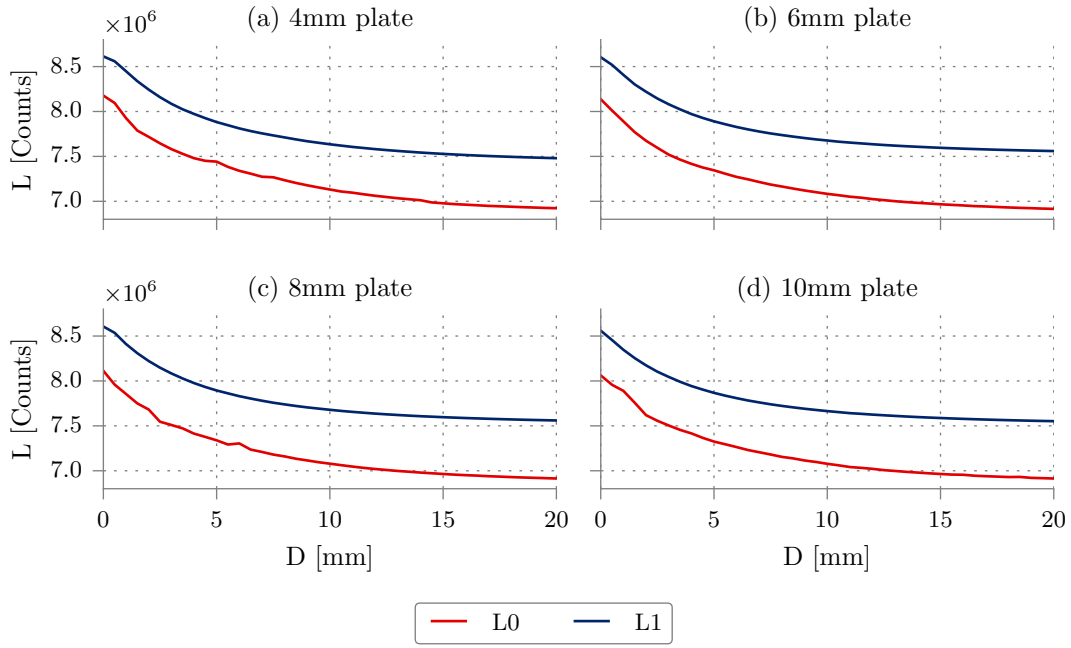

Figure 3.17: L counts vs D distance for the different plates for each inductor, when the distance from its adjacent orthogonal plate to its inductor is D=20 mm.

3.6.3 Effects of the battery and water

Fig. 3.18 confirms that having the battery inserted instead of the module being powered through USB causes an increase in the L1 counts, which corresponds to a decrease in the measured inductance due to the proximity of the metallic covering as explained in the previous section.

The experiments done when fresh water was splashed over the metal did not produce any variation in the results compared to the experiments with the plates dry, with only an RMS error of 1972 counts (0.024% of the maximum value). This test was done first with the dry plates and immediately after was repeated with water splashed, without removing the plates or the sensor nor recalibrating the laser sensors, therefore the curves of both experiments overlap. Although salt-water has higher conductivity, the fact that fresh water produced no change suggests that the effect of salt-water should not be major. This was confirmed by another test with a solution of sea salt and water splashed (3.5% salt concentra-

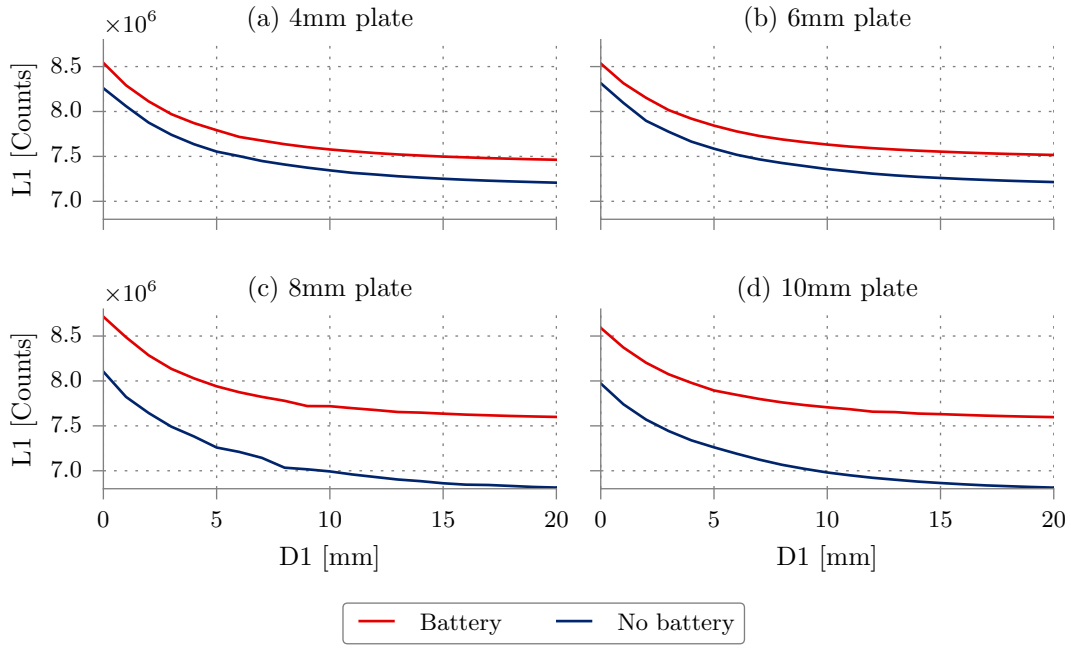

Figure 3.18: Effects of the battery integration on the L1 counts.

tion, corresponding to the average salinity of seawater), which still experienced an RMS error of 8028 counts (0.099% of the maximum value) with respect to the plates dry. This also demonstrates that changes in ambient humidity have a negligible effect on the sensor measurements. Temperature changes will have a bigger effect but temperature compensation is possible following the guidelines in the sensor IC application report [172]. Due to the size and operation of the test setup, which makes it impractical to use it in the climatic chamber, this effect was not investigated.

3.6.4 L sensor measurements vs plate inclination.

To show the sensor's ability to measure plate bending or inclination, a 2 mm mild steel plate was placed 10 mm from the measuring coil in the test setup of Fig. 3.16. The plate inclination was changed from 87 to 110 degrees relative to the measuring coil, in 1 degree steps, with the results shown in Fig. 3.19. This shows that the sensor can measure these changes, demonstrating a similar exponential

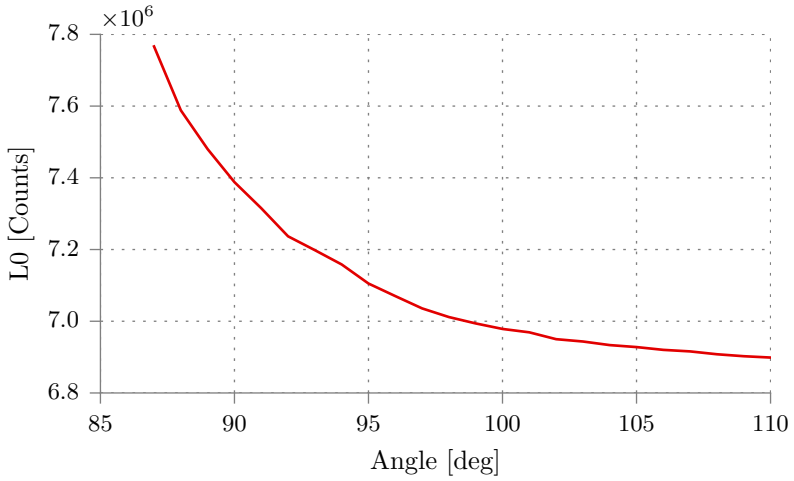

Figure 3.19: L0 counts vs angle of inclination, at D0=10 mm.

curve as observed with parallel plate movement. If detection of torsion of a plate in three dimensions is necessary, a PCB sensing coil could conceivably be designed to use multiple smaller coils on a single PCB; in this way a finer movement detection would be achieved. However, the module is primarily intended to detect anomalous structural movements from a baseline, however these movements are caused, and the measurements in this section show that it can do this.

3.6.5 L sensor measurements vs different metal materials.

As described in [173], different target materials can affect the measurements due to the differences in their conductivity. Fig. 3.20 shows the measurements for three different metals: aluminium, stainless steel and mild steel. Aluminium and this particular alloy of stainless steel have a very similar conductivity, therefore they present almost identical curves, while mild steel differs. However it is easy to compensate for these different conductivities by doing initial baseline measurements after sensor module installation on a structure.

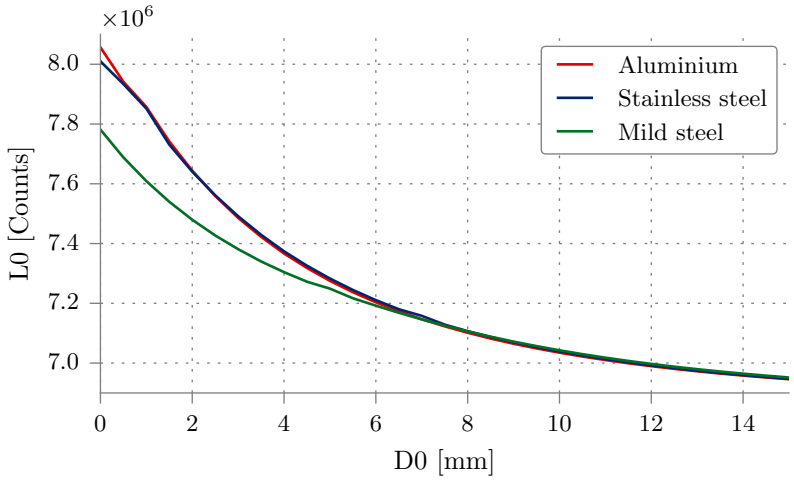

Figure 3.20: L0 counts vs different metal materials.

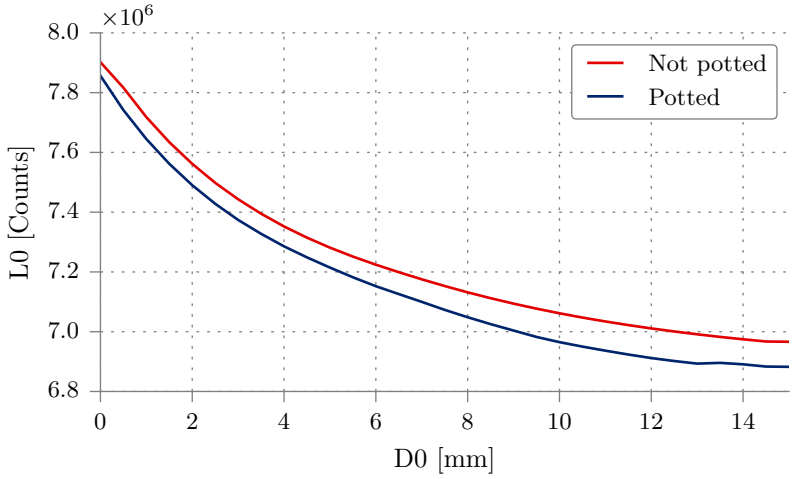

Figure 3.21: L0 counts for potted vs not potted modules.

3.6.6 L sensor measurements for potted vs not potted module, for the 4 mm plate.

Section 3.5.5.3 showed the process to encapsulate the module internally with a resin compound, as well as coating it externally, to protect it from high humidity environments. Although these compounds have low conductivity, it could still have an offset effect in the measured data from the sensing coils. Fig 3.21 shows

the results of measuring the distance of L0 against the 4 mm mild steel plate with two different modules, with and without potting, where only small differences of less than 2 mm can be observed, attributed to the errors in the test system.

3.7 Discussion

3.7.1 Advances to the state of the art

The literature review has shown that different technologies exist that can monitor large structural frames. However, most of these techniques need to have the sensor embedded inside or in the surface of the structure, and the contactless alternatives all present a series of drawbacks such as large size, high cost and power consumption. No contactless system has been shown to be integrated, low-cost, and autonomous, which can monitor a structural frame in different directions.

These challenges have been addressed here by presenting a novel concept for monitoring metal structures by using eddy-current sensing technologies to measure relative displacement between adjacent components in a steel framework, and integrating this concept into a full wireless module. This was possible with the use of a new eddy-current sensing coil interface IC, which avoids the need for complex interface circuit design and optimisation, allowing more straightforward development of eddy-current sensor applications such as the structural steel framework displacement measurement presented here. The module presented in this chapter has a simple cubic form for proof-of-concept but the module could conceivably also be trapezoidal in 3D, allowing displacement measurement between structural components that are not orthogonal or parallel. Assembly and encapsulation would be more complex but still feasible.

The sensor module has been tested and characterised in one and two axes for different conditions. The experiments performed have verified that, even with relatively simple two-layer planar inductors, the inductive sensing technique can measure relative displacement of up 20 mm with a resolution better than 0.5 mm, as well as angle of inclination with at least 1 degree of resolution. Changing the dimensions of the coils would allow different sensing ranges and resolutions, if

needed. The module could also be scaled-up in size without changing the inductor dimensions, i.e. a small inductor in the centre of a large-area PCB. This would retain the original range and resolution but would allow deployment of the module on larger-scale metal structures. The work has also demonstrated that sensors orientated to different axes can work without mutual interference even with other metal components in near proximity. The immunity of the inductive sensors to moisture/water makes them suitable for exposed and marine applications.

Although the module works well as a novel proof-of-concept, it can be improved with the characteristics added to the health monitoring module described in Chapter 4: an external flash, an on/off switch, and a waterproof microUSB connector (which was not commercially available at the time when the inductive module was developed). This would take the module to the next level required for harsh environment and industrial applications. As the module is autonomous and has wireless networking capabilities, multiple modules could form a WSN network across a complex structure.

3.7.2 Engineering advances

The module presented here represents an engineering advance in low-cost fully networked wireless sensor modules for structural monitoring. The use of 3D systems integration and miniaturisation techniques have allowed development of a multiaxial metal displacement sensing module and the integration of other sensors along with processing, wireless communications, and power to make a complete standalone wireless SHM module. This presents advantages over current systems: it is wireless and networked, contactless, small, and easy to install. It involves no specialised, large or expensive sensors such as strain gauges, mechanical displacement gauges, cameras or lasers, as well as being wireless, which removes the cost of cabling making the deployment of a network of sensors more practical. Because of all this, the module is of lower cost than existing techniques as well as easier to deploy and maintain. The module could also be used on non-steel structures by simply fixing a small metal plate to an adjacent concrete, wooden, or composite beam. As the sensor module is small and the eddy currents flow only in the surface layer, the plate will be small and thin and have a negligible

effect on the displacement of the structure. The use of minimal 3D-printed parts for support while using PCBs and standard connectors allows for a robust self-contained cube module, easy to encapsulate and protect. The method showed for encapsulating the module is simple and low-cost.

To solve the challenge of testing and characterising the module in laboratory conditions, two different test setup systems have been developed, one of which emulates plate movement by fixing the plates and displacing the sensor module itself, and the second plate angular displacement by changing the plate inclination.

Future work could include more comprehensive characterisation of the effect of coil design variables on measurement performance, as well as more comprehensive testing of the effect of environmental variables on measurement performance: temperature and humidity in particular. Moreover, a more precise and automated test setup system could be developed, to allow assessing further the resolution of the sensing coils as well as help in the development of a model for a real application. To develop a model, first the exponential fitting curve has to be found by selecting one of the measured curves and extracting a best-fit mathematical model (using MATLAB or a similar tool). After this, the experimental data is used to determine the different parameters of the model, which in the end will be reduced to a simple equation with data counts as an input and displacement in mm as an output.

Chapter 4

Wireless Sensor Module for Machine and Structural Health Monitoring

4.1 Introduction

Chapter 2 has shown the recent trend to replace wired sensors used in structural and machinery health monitoring with low-cost WSN using MEMS and other COTS sensors, not only to reduce hardware cost but also to facilitate installation and replacement. However, WSN technologies have yet to be fully adopted in marine and off-shore deployments. This is partially due to the challenging conditions of these environments, which complicates sensor packaging and reliability, as well as the existing gap between research devices and commercial sensors available for these environments. The objective of the research presented in this chapter is therefore to design and develop a sensor module for machine and structural monitoring that bridges the gap between research and real-world deployment, satisfying the technical and application requirements for both domains, allowing them to be used for research experimentation as well as real-world deployments.

The literature review showed that vibration and acoustic sensors have been widely used for prognostics and fault diagnosis of bearings, motors, and different types of machinery. This becomes important specially in remote locations and off-shore deployments such as marine platforms and ships, where their difficult

access and harsh environment conditions, which includes salt-water exposure, further complicate their maintenance and monitoring. However, the limitations of current hardware platforms and systems architecture makes them less suited for this type of applications. To solve this, a hardware-software co-design needs to be applied to design a WSN module that can survive these harsh marine conditions, with a firmware infrastructure oriented to sensing and software tools that serve both research and industry.

This chapter presents a hardware and software WSN architecture for monitoring machinery in marine and harsh environments using COTS vibration, acoustic, and temperature/humidity sensors, which overcomes the limitations of computational power, networking compatibility, integration and reliability of current WSN platforms described in the literature. The hardware module shares the CPU, radio, and power management architecture with the inductive module presented in Chapter 3 but incorporates different MEMS sensors as well as external flash memory, encased in a custom 3D-printed box for encapsulation against the marine environment. The firmware and software also builds upon the foundation of those developed for the inductive module, extending and improving their features and offering a full-featured UI which allows for data collection and visualisation, experiment control, and 3D-view support of the environment and node location. This system could also be used to monitor structures in other harsh environments.

4.2 Module research challenges

The challenges for the design of a WSN module for machine and structural monitoring that can be used in harsh environments arise from the combined necessities of both research and real-world deployment. The requirement challenges to be addressed are:

- Integrated electronics in a single PCB, including the range of sensors necessary for structural and machine monitoring, to reduce cost and improve

power consumption, as opposed to having different modules assembled together (e.g. CPU, battery charging, radio, sensors, etc.). This can improve mechanical reliability, as well as reduce manufacturing cost.

- A package design that can protect the module from the harsh environment conditions found in marine environments, i.e. high humidity and salt concentration as well as vibration and shock.

- A more powerful CPU architecture that can overcome the limitations of popular WSN devices used in research such as the TelosB, e.g. more processing power, increased RAM and flash memory, and support for higher data rate sensors (i.e. vibration and acoustic sensors).

- A common firmware and software framework, based on a current embedded networked OS, which allows remote control of, and data collection from, the sensor module. The firmware stack has to be focused on facilitating sensing experiments instead of the most common wireless networking experiments, while allowing flexibility for carrying out research also in the networking layers. This will allow researchers to incorporate and improve network and routing protocols in this platform that can improve the overall data reliability in real applications.

- The overarching research task is finding a systems integration solution that simultaneously addresses all of the above requirements.

4.3 Overall system design

The overall system concept is a sensing node, with a firmware/software architecture that allows interval sensing of vibration and audio from the machinery or structure, storing of the data, and sending the data wirelessly to the gateway on demand, to be analysed later to detect and predict failures. The performance of the sensing module developed in the previous chapter was demonstrated and met the necessary requirements for an autonomous wireless WSN node for harsh

environments. Therefore, the electronics for this module builds upon the previous one, sharing many of the components and form factor, but incorporating the necessary sensors and improvements.

The following sections set out the systematic research and development process that led to the final system integration solution, from the sensors 'front-end' to the 'back-end' management software for deploying and controlling a network of sensing nodes.

4.3.1 Sensors

The sensors selected will need to cover the necessary ranges found in the literature for measuring the vibration and audio associated with monitoring structures and machinery.

Although microphones typically have a 0-20 kHz bandwidth, this will require a very high sampling rate that will generate an excessive amount of data, which can be a problem for both storage and transmission. Sound produced by machinery is, however, usually low in frequency, and it has been demonstrated that a sampling rate of 3 kHz is sufficient to capture the most important features of noise in rotating machinery [67].

Regarding vibration, as shown in the literature [6, 56, 57], a bandwidth of 100-200 Hz is sufficient to detect faults using vibration data in motors, bearings, and similar machinery, while the requirement for structural health monitoring is even lower [7, 63]. For the sensing range however, it is the structural health case that gives the upper bound, as structures are exposed to forces higher than the vibration of machinery. Nonetheless, a review of MEMS-based accelerometers for structural vibration by Sabato *et. al* [63] defines an optimal sensing range of $\pm 14.71 m.s^{-2}$ ($\pm 1.5g$), which is comfortably within the capabilities of current MEMS accelerometers. The necessary resolution however will depend on the full scale of the measured signal and the signal-to-noise ratio, therefore the accelerometer would need to be configured in each case to have the minimum necessary full scale to maximise the resolution.

The addition of humidity and temperature not only provides environmental data but can also warn of machinery overheating. A typical range from 0-50^oC is

sufficient to measure air temperature surrounding typical heavy marine machinery (see measurements presented in the experiments of Chapter 5, where it rarely goes above 45^oC). By using a typical integrated temperature sensor, with a range from -40-125^oC, a higher temperature can be detected that would indicate overheating.

4.3.1.1 Microphone

Small size, low-cost, and low-power are characteristics that make MEMS microphones ideal for capturing audio when used in an embedded battery-powered module. MEMS microphones are commonly designed for smartphones, headsets, and similar applications, therefore they are optimised for human voice and environments with a medium level volume. Because the application of the module targets heavy machinery, a digital MEMS microphone can saturate its output when sensing in very noisy environments or placed on loud machines. Thus, an analog MEMS microphone is necessary that allows designing of a conditioning circuit with the necessary gain. This gain will, however, depend on the specific environment and conditions and, to maximise signal excursion and resolution without saturating the signal, the recommended amplifying circuit will need to be modified to allow for a variable gain.

The microphone selected was the analog output INMP504 [174] from Invensense, as it is a reputable brand and also has a low-cost evaluation board available for rapid prototyping. Importantly, this device has a bottom port so that it sits flat on the top layer of the PCB and the audio enters only through a hole in the PCB, allowing the microphone to be protected from the environment more easily. It is connected to the 12 bits ADC of the microcontroller through the signal conditioning circuit shown in Fig. 4.1, formed by an opamp-based inverter amplifier with a high-pass filter at the input and a low-pass filter at the output. The gain of the amplifier is adjusted by an AD5110 I^2C digital potentiometer controlled by the microcontroller, connected in series to the resistor R20. This yields a maximum gain of 58.8 and a minimum of 12. The minimum gain value was designed to avoid saturation if the captured sound is near the maximum value supported by the microphone, while the maximum gain corresponds to the one

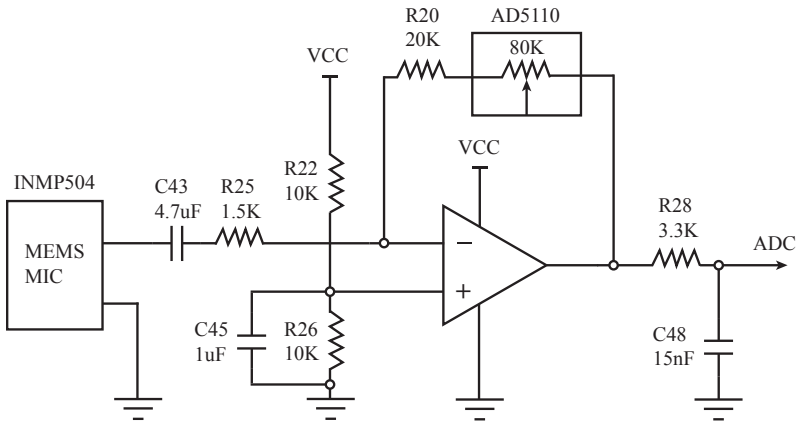

Figure 4.1: Microphone conditioning circuit with configurable gain.

fixed in the evaluation board of the microphone for standard use. The C43-R25 high-pass filter removes the DC before the resistor divider R22-R26 sets it to VCC/2 for maximum signal excursion. As the ADC of the CC2538 has a maximum sampling rate of 7.5 kHz, an anti-aliasing filter is needed before the signal is digitised. This is done by the R28-C48 filter, resulting in a 3.1 kHz microphone bandwidth, which is sufficient to cover the necessary range.

To adjust the gain, an auto-calibration mechanism was developed in the firmware. Before the first experiment in a new environment or conditions, the microphone will sample 5 s of audio with the gain set to the minimum value, measure the maximum signal received and calculate with this the corresponding gain for this signal to have the maximum excursion. After this, the value of the potentiometer will be saved in its own EEPROM and will keep its current value until the calibration command is launched again.

4.3.1.2 IMU

For vibration measurement, the LSM9DS1 [165] IC from ST that is used in the inductive module was selected, a full MEMS IMU that also contains a gyroscope and magnetometer instead of a simple accelerometer, to be able to also use the module for monitoring the wind- and wave-induced oscillations of offshore plat-

forms and floating devices. It was selected as ST accelerometers and IMUs are widely used in commercial devices, and also offer good support and documentation. Although this IC allows for an accelerometer sampling rate up to 952 Hz, due to the speed limitations of the microcontroller the sensor is configured to be used at 476 Hz, which is the maximum rate that can be used without losing frames, yielding a sensing bandwidth of around 235 Hz. The selected microcontroller, with a CPU of 32 MHz allows this higher sampling rate, compared to the 100 Hz sampling rate found in older platforms. The maximum sampling rate of the accelerometer and microphone at the same time cannot be calculated due to the many variables involved, therefore the firmware has to be optimised to allow maximum performance and it has to be experimentally tested. The accelerometer can be used up to ±16 g, but it is configured by default at a full scale of ±8 g, which is enough for machine and structural vibration monitoring. It is connected to the microcontroller through the I^2C bus.

4.3.1.3 Temperature and humidity

The sensor selected for humidity and temperature monitoring is the same as that used in the inductive module, the SHT21 [166], the next generation of the SHT11 found in older WSN platforms such as the TelosB. This sensor has a 0.01^oC resolution for temperature and a 0.04% for relative humidity, with a temperature range of -40-125^oC. To protect it against water, dust, and other contaminants, the sensor has a companion protective cap that can be easily attached to the PCB, consisting of a single piece of PBT thermoplastic and a filter membrane.

4.3.2 CPU, communications, and memory

The requirements for a CPU and communications module are similar to the ones for the inductive module presented in Chapter 3: a microcontroller capable of running Contiki-OS, so that networking functionalities can be added and extended, with integrated 2.4 GHz radio communications for lower size and cost. In addition, an integrated ADC is necessary with sufficient sampling rate to capture the analog output from the microphone.

The processing unit selected is the CC2538 [95], the same as that used for the inductive module, as the performance and software support was already verified in that module and having a common platform for both modules facilitates firmware development. The integrated 7.5 kHz ADC is also sufficient to sample the microphone audio without the need of an external ADC, which would increase cost and power consumption. This unit includes the most commonly used communication buses in microcontrollers: I^2C and SPI, which can be used to connect different sensors; serial UART, which is used for communicating with a host computer for debugging as well as firmware reprogramming.

As the module needs to be able to work autonomously, an external flash memory connected to the microcontroller is necessary to store the data of the experiments as well as configuration parameters. Moreover, even for temporarily storing the current burst of sampled data the memory would be necessary, as the data rate from the microphone and accelerometer combined is too high to be sent wirelessly in real-time due to the microcontroller CPU not being able to sample and then sending the data without losing frames, which was tested experimentally.

The low-power AT45DB641E [175] flash memory from Adestos was added, connected to the SPI bus, a common type of memory used for resource constrained wireless nodes. This memory has a size of 64 Mbit, the largest available, which allows storing of up to 90 samples of 5 s bursts of combined accelerometer and audio data. In addition to the main memory, it also contains two SRAM buffers of 256 bytes each, which can increase the system ability to write a continuous data stream. An SD-card memory was considered as alternative but was discarded due to the large size and high power consumption.

Fig. 4.2 shows a diagram of the communication buses used for the sensors and memory to communicate with the CPU of the microcontroller.

4.3.3 Power management

To power the module, a standard 4.2V rechargeable lithium-polymer battery of 4500 mAh capacity is used, with its voltage regulated by the same MCP1700 [169] LDO regulator used in the inductive module. The battery model was chosen as a

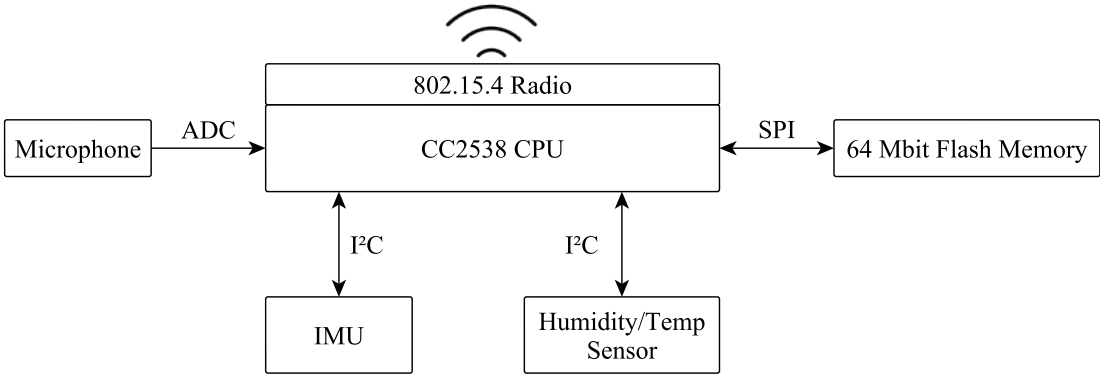

Figure 4.2: Diagram of the sensors and CPU communication architecture.

trade-off between physical size and capacity, as a smaller battery would have less autonomy and a larger one would be too costly. Battery charging and monitoring is also handled by the common MCP73831 [168] charger and DS2745 [167] monitor ICs, as their performance was proved already in the inductive module, with two SMD LEDs to indicate the battery charging state.

The module power consumption is approximately 25 mA when sampling data, 2 mA in command listening mode, and 35 mA when transmitting data. This allows around 90 days of operation if configured to capture and save samples of 5 s of audio and accelerometer at a rate of 1 sample/day, which corresponds also with the maximum number of samples the memory can store. The module can therefore be deployed to collect experimental data and be retrieved later, although a final commercial application would most likely involve an on-site gateway that collects the data from all sensors periodically.

4.4 Module integration

4.4.1 Electronics assembly

As the electronics will be fully-encapsulated, conventional PCB design assembly was used to maximise design flexibility and reduce cost. The components were assembled on a 50x50 mm PCB, with most of them on its top layer, as can

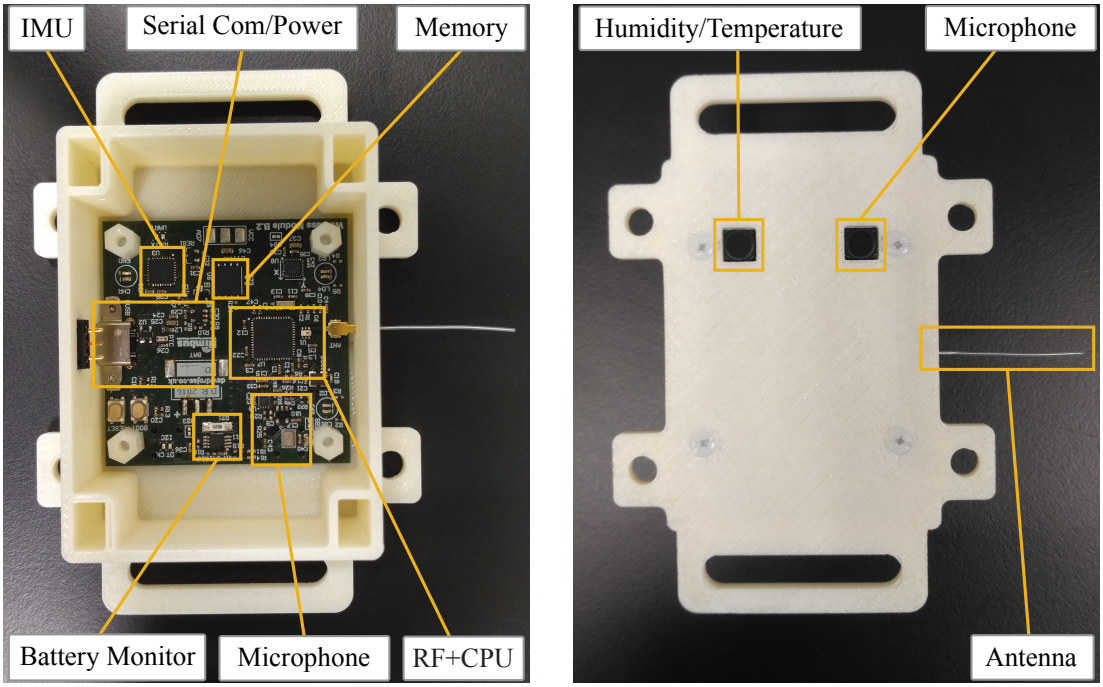

(a) (b)

Figure 4.3: (a) Top PCB inside the box (b) Bottom with covered sensors

be seen in Fig. 4.3a. The bottom layer holds only the humidity/temperature sensor. Although the microphone itself is placed on the top layer, to capture the sound there is a through-hole to the bottom layer, as discussed in Section 4.3.1.1, next to the humidity/temperature sensor. Both sensor openings are protected from dust and water by the same PBT thermoplastic protective cap, as can be seen in Fig. 4.3b. Fig. 4.4 shows a CAD drawing of the protective caps, which are attached by inserting the corners into four holes in the PCB. The external antenna is connected to an UF.L connector, and in this way it can be located at a distance or replaced by a higher gain one if necessary. The firmware uploading and battery charging is done through a waterproof microUSB connector, to allow module sealing, improving upon the regular microUSB used in the inductive module. The details of the assembly are explained in the next Section 4.4.2.

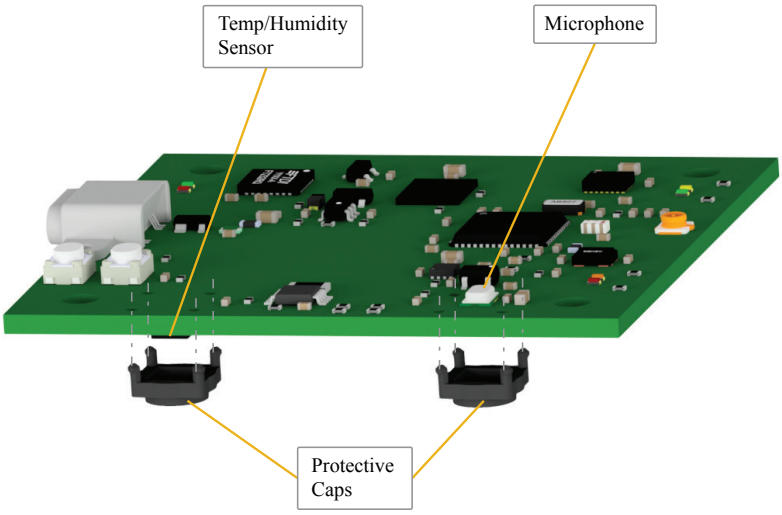

Figure 4.4: Attachment of the protective caps for the exposed sensors.

4.4.2 Module assembly

To ensure the operation and survival of the health monitoring module in harsh environments, a custom ABS 3D-printed box was designed to enclose the electronics and battery, with only the microUSB connector, on/off switch, antenna, humidity/temperature, and microphone opening exposed. The humidity/temperature and microphone holes are, however, covered by the two PBT thermoplastic protective caps, as it was shown in Fig. 4.3b. As there is no standard way to protect MEMS microphones, a simple audio test covering it with the same cap used for the humidity/temperature sensor proved that it did not have a noticeable effect in the recorded sound level or frequency response compared with the opening without cover, as it can be seen in Fig. 4.5. This was chosen after testing with other materials covering the microphone hole, such as polyimide tape and plastic, showing that these materials, which are not membrane-based, have a strong attenuating effect on the measured audio signal, capturing only a flat signal rendering the microphone useless (Fig. 4.6).

Fig. 4.7 shows an exploded view of the whole assembly. The PCB sits flat at the bottom of the enclosure, attached with four plastic screws and spacers. The battery is placed on top, held together between the spacers, the top enclosure, and another four screws that close the box going from the lid to the PCB spacers.

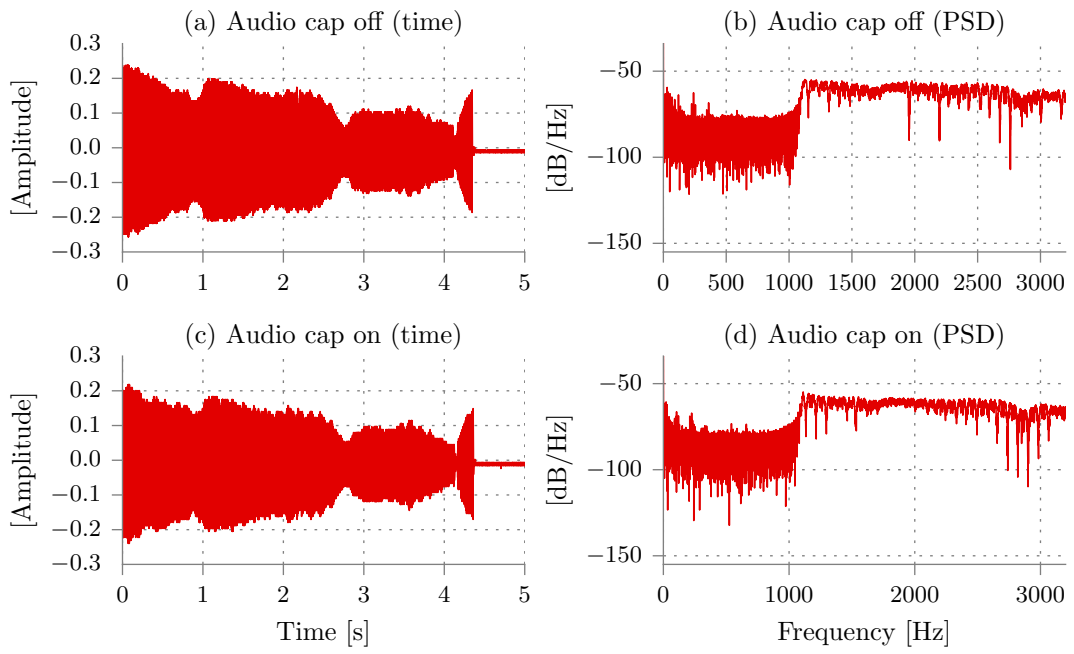

Figure 4.5: Microphone test with the protective cap on/off.

To be able to see the LED indicators when the box is closed, three light guides, inserted into holes in the lid, interface with the SMD LEDs in the PCB. Four flaps with holes extend from two sides of the box, as well as two larger handles on the other sides, which can be used to attach the node to the machine or structure with cable ties or screws. Finally, to facilitate the encapsulation of the module for extra protection against humidity and salt, two slits cut out on the top enclosure enable pouring of resin inside the box after the module is fully-assembled.

4.4.3 Module encapsulation

To encapsulate the health monitoring module, the same marine resin compound [170] and polyurethane coating [171] used for the inductive sensing module were used, using a similar process as that described in Section 3.5.5.3:

1. Seal with 3M polyimide film tape 5419 the edges of the filter caps used for the humidity/temperature sensor and microphone, and attach the electronics PCB to the plastic box. The filter caps have to be glued with Loctite

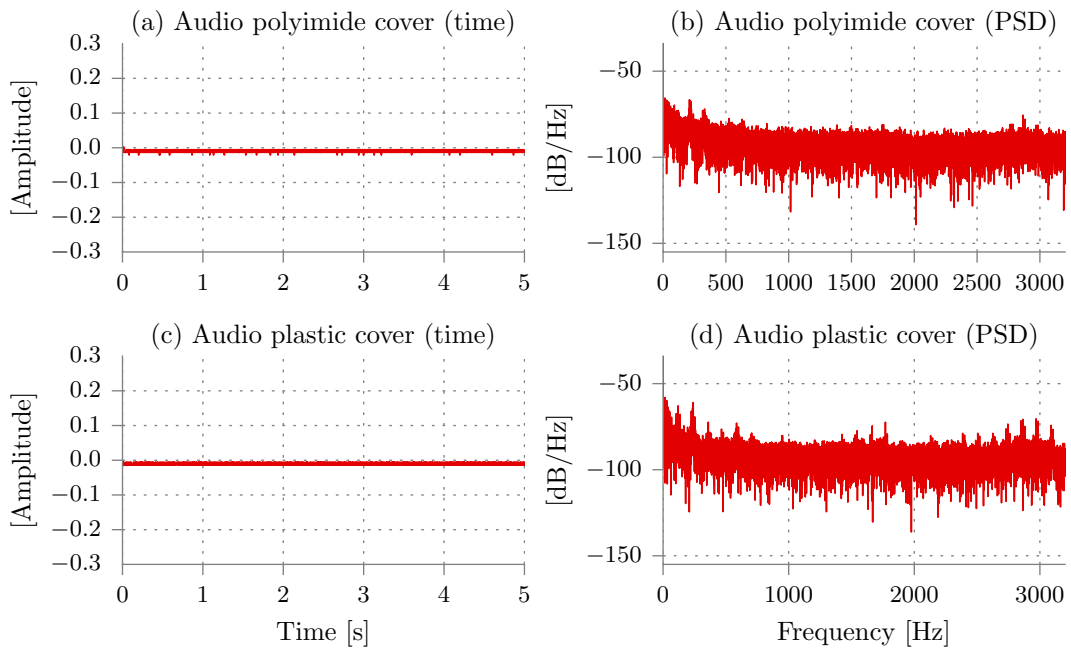

Figure 4.6: Microphone test with polyimide tape and ABS plastic covers.

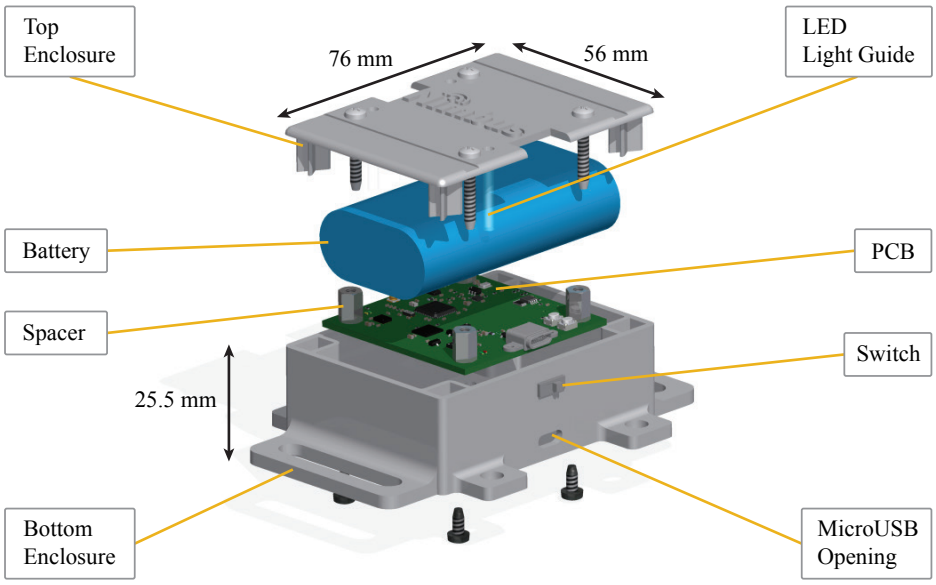

Figure 4.7: Health monitoring module assembly.

Ultra Gel Super Glue against the holes before placing the PCB flat at the bottom of the case, to avoid leaking. A small, hollow cylindrical plastic

socket has to be glued also on top of every LED, to later fit the light guides and avoid the black resin covering the LEDs (Fig. 4.8).

2. Seal with Blu Tack adhesive rubber the inside of the switch, microUSB connector, and antenna against the inner walls of the plastic box (Fig. 4.9a).

3. Spray polyurethane coating on the interior walls of the box, including the PCB. This is necessary to minimise resin leaking through, due to the 3D-printing creating a porous wall instead of a solid block.

4. Place the battery inside the box and close the lid.

5. Seal the edges of every screw on the top and bottom of the plastic case with the same Loctite Gel glue, to avoid leaking.

6. Pour the resin compound into the box through the slits, filling it up to the brim, and let the resin cure for 24 h at ambient temperature (Fig. 4.9b).

7. After curing, for extra protection spray the exterior of the box with the polyurethane coating and let it dry.

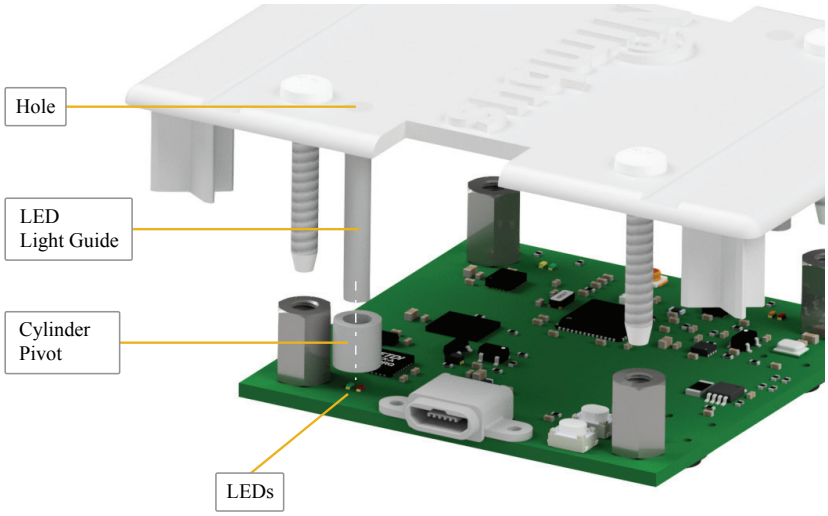

Figure 4.8: Light guide assembly before encapsulation.

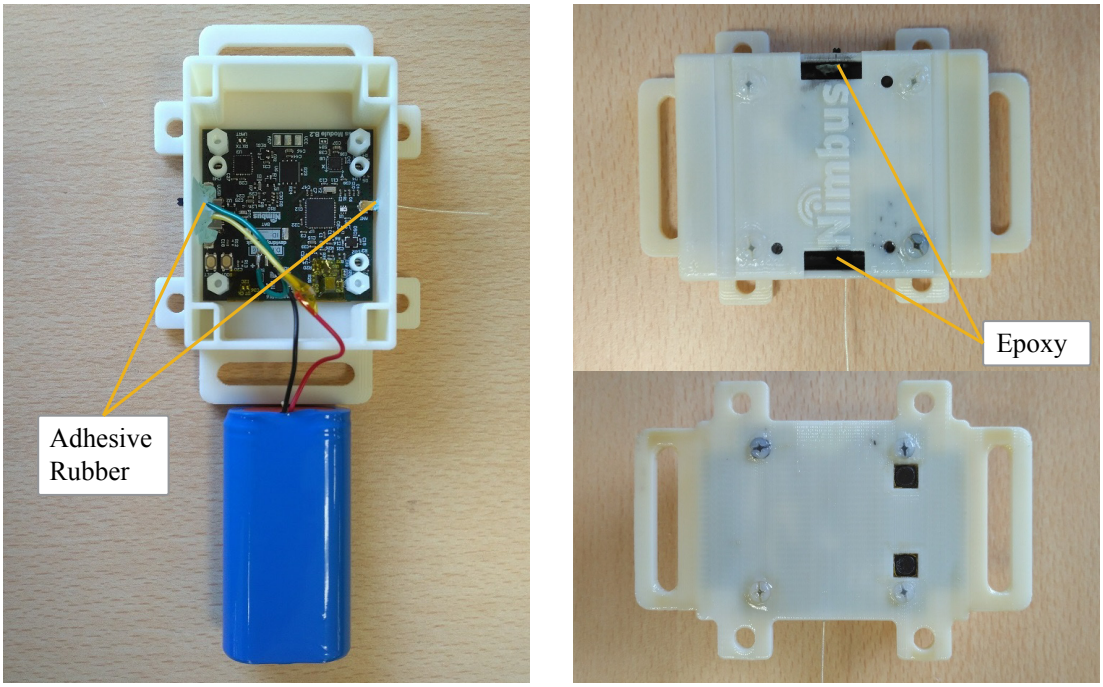

(a) (b)

Figure 4.9: (a) Health monitoring module pre-potting sealing (b) Health monitoring module encapsulated.

4.5 Firmware and software platform

4.5.1 Overall firmware and software architecture

As shown in the literature, there are some existing tools for WSN deployments, such as Trident [157], that allow for remote configuration and experiment control of the nodes through a gateway node. However, they are focused only on network testing experiments and not on sensor data collection. Therefore, a firmware/software architecture is necessary that supports on-demand remote control and configuration of sensing experiments, with a proper interface to allow researchers as well as engineers to easily manage these experiments without the need of node reprogramming. Also, nodes have to be able to work autonomously and store data periodically, with parameters set up with the same tool, to facilitate deployment by personnel not familiar with the technology who would only need to attach the node and switch it on.

These two modes of operation, shown in Fig. 4.10, can be summarised as:

- **On-demand experiments**: The PC connected to a gateway node will send commands to a specific node to start a sensing experiment. After the experiment is finished, the gateway sends another command to download the data.
- **Periodic unattended experiments**: The node will receive from the PC gateway the experiment parameters, and after that the node will repeatedly execute the command with the specified period. The list of commands will be stored in the node memory, thus the experiments can start autonomously if the node is reset or turned off/on.

All the communications from the gateway to the nodes need to be done wirelessly and support different commands to facilitate the control and configuration of the nodes, such as recording audio and vibration data, sensor calibration, logging battery level, setting transmission power, etc.

4.5.2 Firmware

Section 3.5.4 described the firmware developed for the inductive module, composed of a basic networking infrastructure and sensor drivers that allow interactive data collection from the module. This firmware, running on the CC2538 [95] microcontroller, uses Contiki-OS and an application based on Contiki-Shell. Contiki-OS provides process-like structures called protothreads that run on a loop, making it easy to create new processes as functions that interact with the network layers and microcontroller peripherals. Applications can then be created selecting the correct network parameters and sensors to collect and send the data. Thus, most of the Contiki-OS based applications are configured in the code, compiled, and flashed to the node which, after reboot, starts sending data periodically with the specified data rate. Although this functionality works for simple deployments, it lacks flexibility and reprogramming the node every time when different parameters are needed is cumbersome. Contiki-Shell is a module that improves this functionality by providing a command-like structure on top. These commands are

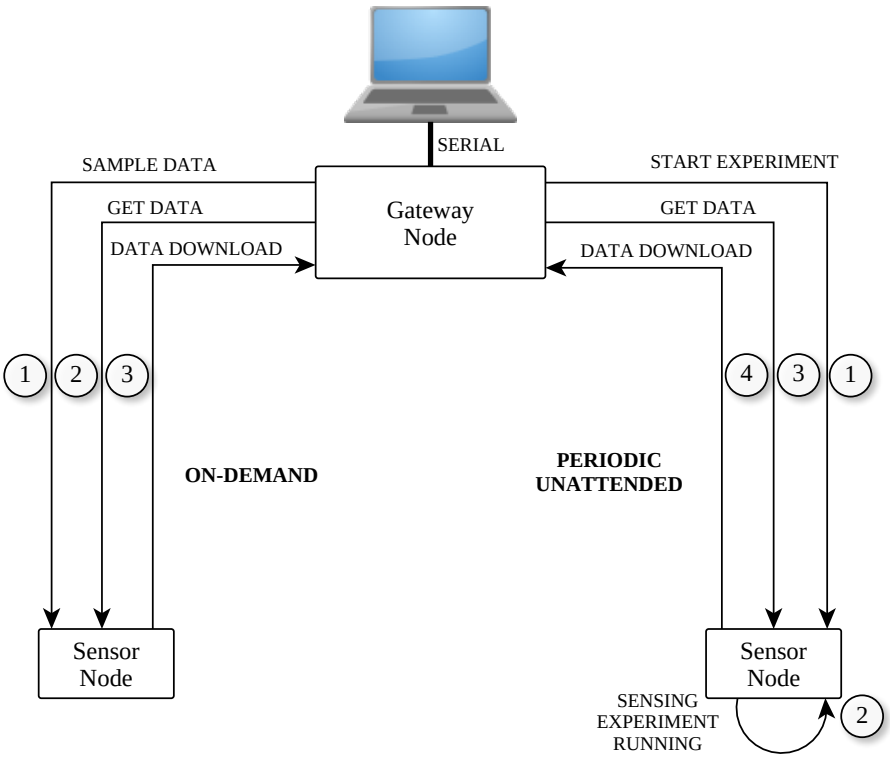

Figure 4.10: Firmware/Software main operation modes.

easily defined in code as new functions or protothreads, and they can be triggered locally through the serial port or sent remotely from the gateway node. However, Contiki-Shell does not allow getting messages or acknowledgements from the remote nodes, only from the local gateway node through the serial port. This hinders the functionality of Contiki-Shell as it cannot be used to define commands that ask remote nodes to sample data and send it back to the gateway.

Therefore, the firmware developed for the health monitoring module needed substantial expansion beyond this existing infrastructure by extending the Contiki-Shell functionality to support message replies from the nodes, allowing data collection on-demand and in this way supporting the modes of operation described in the previous section through remote shell commands. By default then, every command call that is preceded by *sendcmd ip* for individual nodes or *netcmd* for broadcast will receive a wireless reply from the nodes.

The periodic experiments can be any command available in the node that can also be used on-demand, which will be called from the gateway with the period and other parameters such as file name. These parameters will be saved in a file in the memory, then read and executed when the node is powered on or after reset. The memory also stores the calibration file for the IMU as well as the data files collected from every experiment, using the Contiki file system. The main primitives of this file system are also implemented as shell commands, to be able to remotely read and write files, format the memory, etc. As the memory did not have Contiki support, the driver for this particular memory and microcontroller had to be developed and integrated into the Contiki file system.

The libraries for the IMU, temperature/humidity, microphone, and battery monitor also had to be developed and integrated into the Contiki structure, as they are state-of-the-art sensors and the drivers were not available. Due to the performance constraints of the system, sampling high data rate sensors such as the audio and accelerometer at the same time, while saving the data to the memory, presents a challenge for these constrained devices and a new solution had to be found. This was done by using the different resources already available in the microcontroller and IMU IC. To unburden the CPU from the microphone sampling, the ADC was used with DMA and the blocks of data were stored in two ring buffer arrays in the microcontroller RAM. For the accelerometer sampling, a combination of the IMU IC internal buffer and another buffer in the microcontroller firmware was used. The file writing was also buffered in the external memory SRAM buffer before committing to the file. This architecture, shown in Fig. 4.11, ensured that both sensors can be sampled and saved at the required data rate without loss of frames. This represents an advance over the applications typically found in WSN with embedded networked OSs, as they do not usually handle high data rate sensors and therefore do not need a complex firmware architecture to avoid losing data.

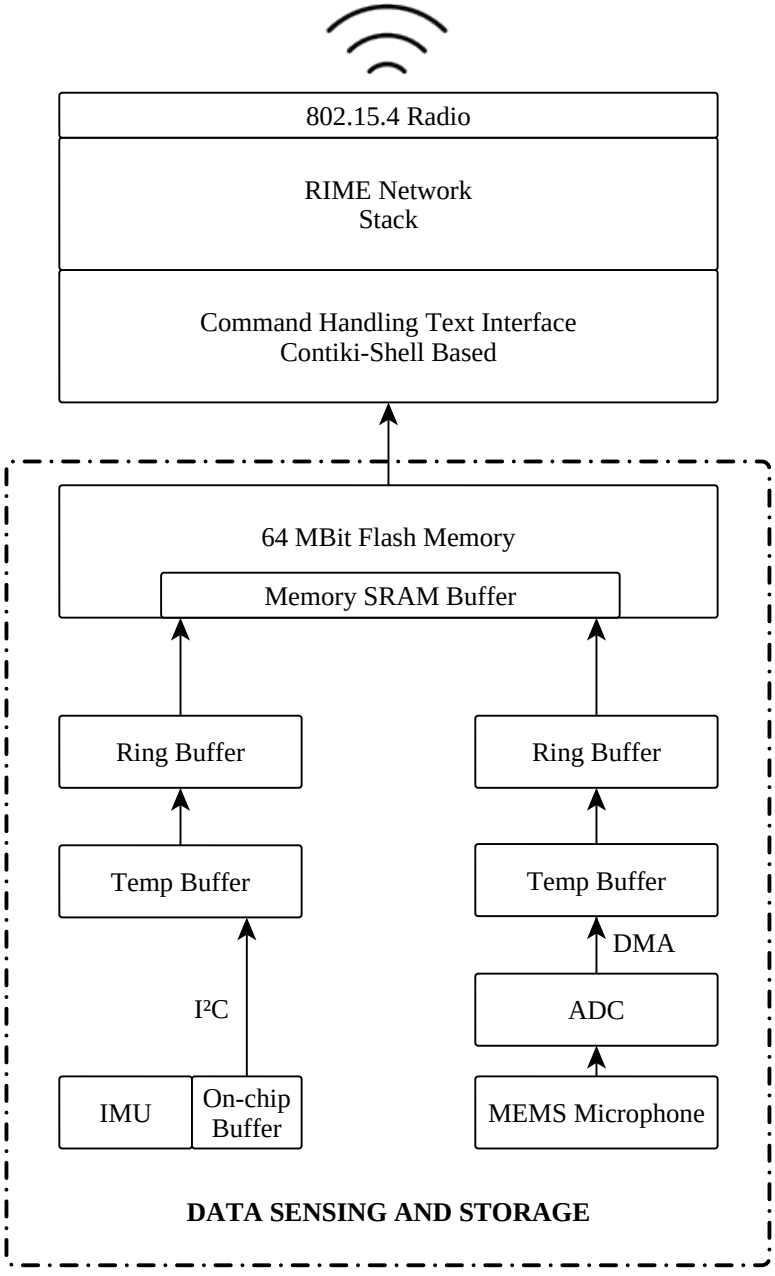

Figure 4.11: Firmware sensing architecture.

4.5.3 Software and user interface

The firmware developed allows full control of the nodes through a serial terminal connected to the gateway but downloading data through the terminal is not feasible as the bitstream needs to be saved in a file and converted to the proper format. Moreover, interacting via the terminal is tedious and becomes harder to manage when the network of nodes grows, besides not providing any visual information on the data and environment. It becomes important then to have a graphical interface that can ease the management of the nodes for on-demand experiments but also to configure the periodic experiment parameters in the nodes. Although some WSN tools exist that provide a graphical interface to interact with the nodes, most of them are not focused on sensing experiments, do not provide a 3D-view of the environment, and do not support the firmware architecture that was developed in this research. Therefore the software and user interface were developed from scratch.

For this, a custom Python application was developed to be run on a laptop, which connects through the serial port to a gateway node. Python was selected as it is an interpreted language that does not need compiling, allowing faster iterations of the software as well as being multi-platform. Also, it has available a large repository of modules including graphical libraries, statistical tools, etc., which makes development easier. The graphical interface was built using the PyQt module, as it is one of the most robust graphical libraries. The interface was divided in different tabs, which group the different functionalities.

The gateway console tab, Fig. 4.12, handles the serial connection to the gateway, displays the full activity log, and allows for manually sending commands. This way, new functionalities could be added to the firmware as new commands and could be executed from this graphical command line without the need to integrate them immediately to the user interface. All commands that are called from the other tabs that interact with the gateway are recorded in this window. A control was included to set the node gateway address in case the gateway node is replaced, and a broadcast command is sent to all nodes to inform them of this change as nodes always send back unicast messages to the gateway.

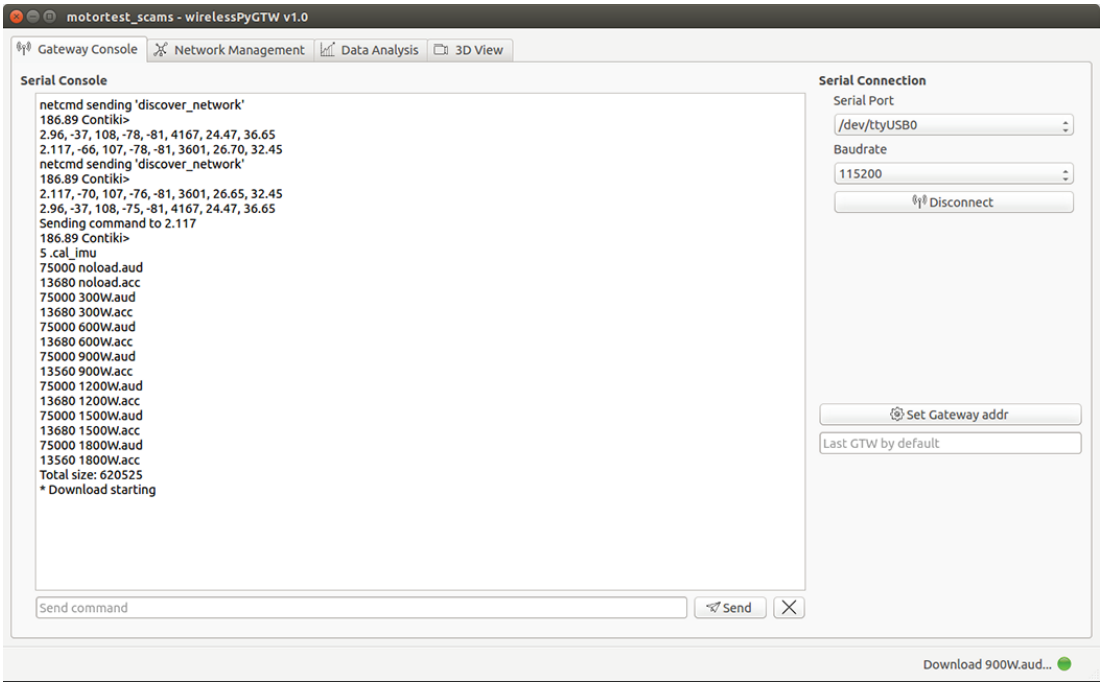

Figure 4.12: UI Gateway console view.

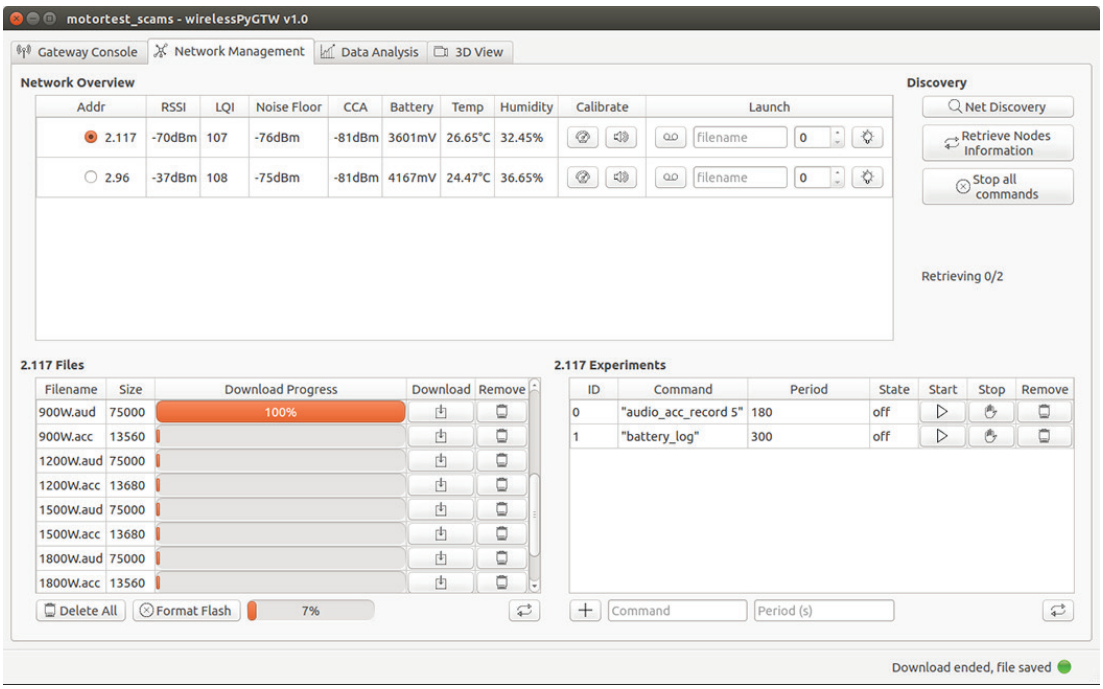

Figure 4.13: UI Network view.

Fig. 4.13 shows the network management tab, divided in three different areas. The right top side contains controls for network discovery. This sends a discovery broadcast command to all nodes in the range and retrieves information from them, displaying them on the left side in a list. This list contains the RSSI, LQI, noise floor, CCA, battery, temperature, and humidity for each individual node. Moreover, a calibration command can be called to adjust the audio gain or the accelerometer bias, as well as launching specific commands to a node with the selected recording time. The bottom left shows the files in the memory of the node that is selected on the list of nodes, and allows downloading of individual files as well as deleting and formatting the memory. A progress bar is shown for each file with the percentage of the current file being downloaded from the node. The bottom right of the panel lists the current periodic experiments set up on the node and permits adding, deleting, and stopping experiments. Different experiments can be active at the same time on the same node with different periods, e.g. recording audio and accelerometer every 180 s and the battery level every 300 s, as shown in the figure.

Fig. 4.14 shows the data analysis tab, where different plots can be displayed of the selected downloaded audio or accelerometer data in time (left side), as well as its power spectral density (right side), to quickly identify the peaks and frequencies of interest. The plot canvasses are interactive and can be zoomed in and hide/show the different axes when displaying the accelerometer data, as well as saving the images. This was developed using matplotlib, a Python library commonly used to produce publication-quality figures for academic papers, which can be integrated also in any PyQt-based Python application. On the righthand side, a file tree allows navigation through the downloaded data folders and selection of the audio and accelerometer files to display. This avoids having to process manually all files when looking for specific data by having a quick look over the time and frequency domain of the files to select the interesting data.

A 3D view tool was also implemented, as shown in Fig. 4.15, where an STL CAD file can be loaded to display the target environment where the network is deployed. On the right side is the configuration control panel and on the left side the environment view. A CAD file can be selected and imported into the view, as well as a CAD model for the nodes. The nodes that have been discovered by the

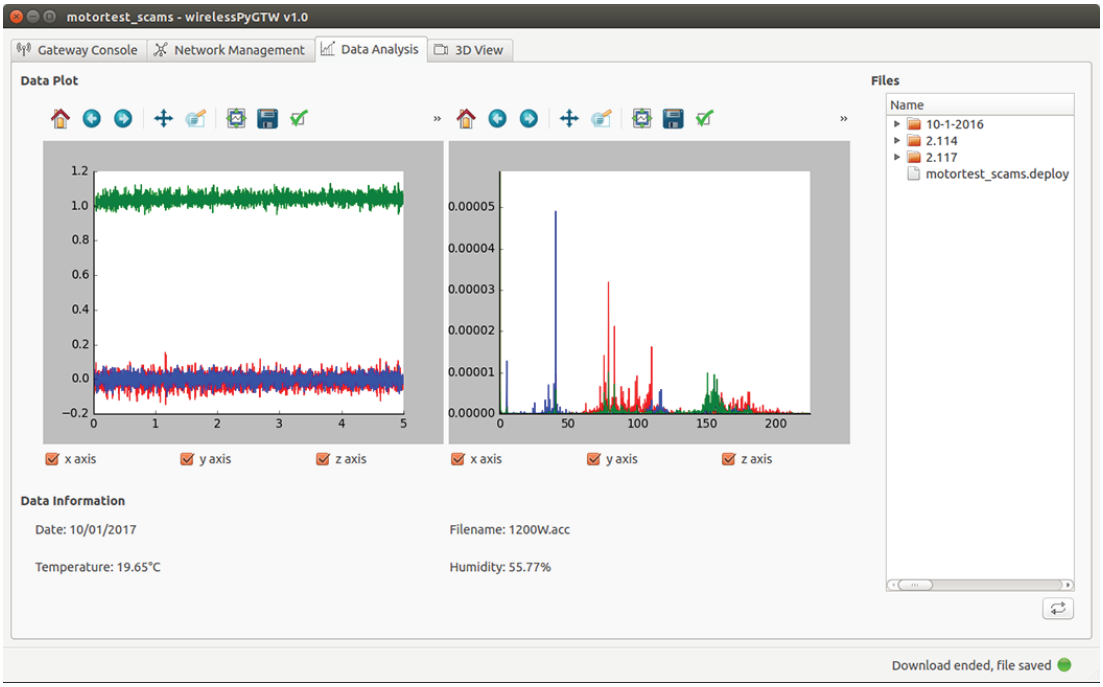

Figure 4.14: UI Data view.

discovery command appear here in the control panel in a dropdown menu, where each of them can be selected and then manually placed with the mouse by clicking in the environment scene on their location in the real scenario. This tool can be useful for studying the environment, making deployment decisions, and aiding the development of propagation models by the automatic calculation of distances between nodes in 3D space, in contrast with other tools that only allow nodes to be arranged in a 2D space. A button in the configuration panel allows saving of a list of the real distance in meters from each node to the others, provided that the nodes have been placed in the correct location and the environment CAD has been drawn with the correct dimensions. The environment view allows zoom in, pan, and rotation of the scene, which makes it easy to see which nodes have direct line of sight and which ones are blocked by an object.

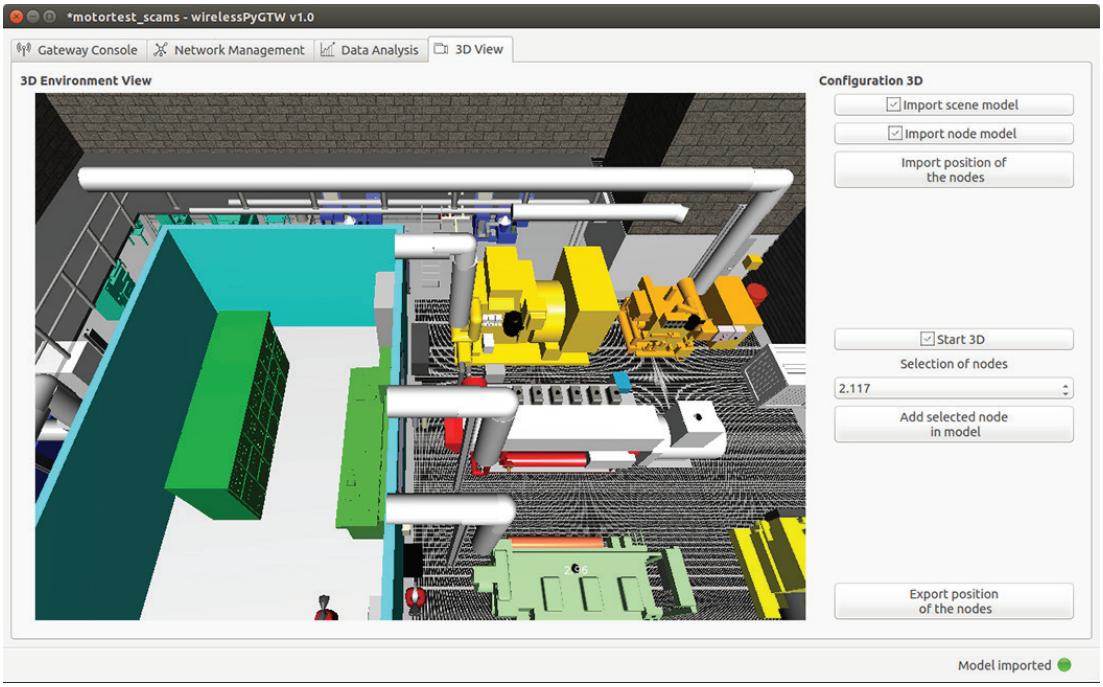

Figure 4.15: UI 3D Environment view.

4.6 Laboratory bench testing

4.6.1 Three-phase motor connected to a wind turbine

To validate the performance of the health monitoring module platform, and its associated firmware/software, several tests were done in laboratory conditions. The first test consisted of attaching one of the modules to a custom rig in the laboratory, composed of a SWEA 2 KW wind turbine connected to a three-phase TEC 1500 rpm motor and driven by an Optidrive Variable Speed Drive (VSD). This setup can be seen in Fig. 4.16, with the node placed on top of the wind turbine with the z-axis of the accelerometer pointing up. The experiments were performed with the motor configured at 320 rpm and a variable load, set up from 300 W to 1800 W in 300 W increments. For each load configuration, the sensor recorded 5 s of audio and accelerometer data.

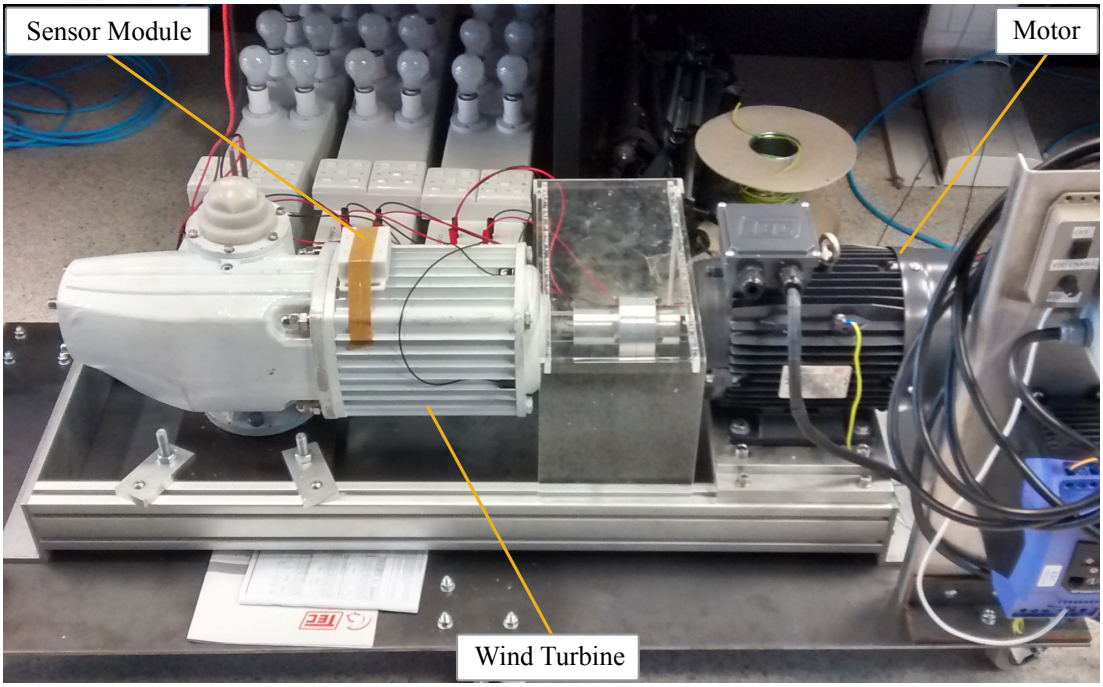

Figure 4.16: Experiment setup for the health monitoring module in a motor connected to a wind turbine.

As the motor and turbine were brand new and presented no flaws, there were no noticeable variations among the data collected for each experiment. Fig. 4.17a

displays the accelerometer data for the 1200 W load test. Its power spectral density (Fig. 4.17b) shows a noticeable peak at 45 Hz for the y-axis, several peaks around 75-110 Hz for the x-axis, and a smaller magnitude spread around the 150-160 Hz for the z-axis. The audio data for the same experiment can be seen in Fig. 4.17c, with the energy distributed across the spectrum with no visible peaks (Fig. 4.17d).

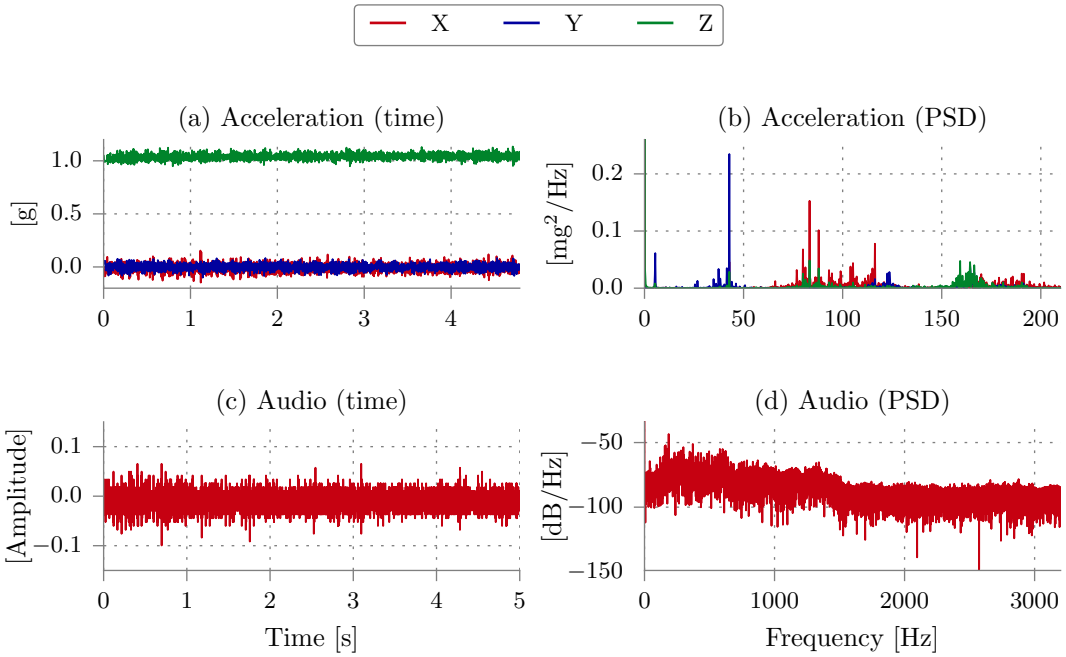

Figure 4.17: Accelerometer and audio data collected at 1200 W load collected from the motor and wind turbine setup.

4.6.2 Single-phase motor connected to a gearbox

For the second experiment setup, a single-phase WEG 1450 rpm motor was connected to a reduction gearbox through a flexible coupling (Fig. 4.18), to be able to misalign the rotating axis by slightly displacing the motor attachment to the table. Due to the safety cage built on the setup, there was no space available on the top of the motor, therefore the sensor module was placed on the side, with the accelerometer y-axis aligned with the motor rotor. As the gearbox contained

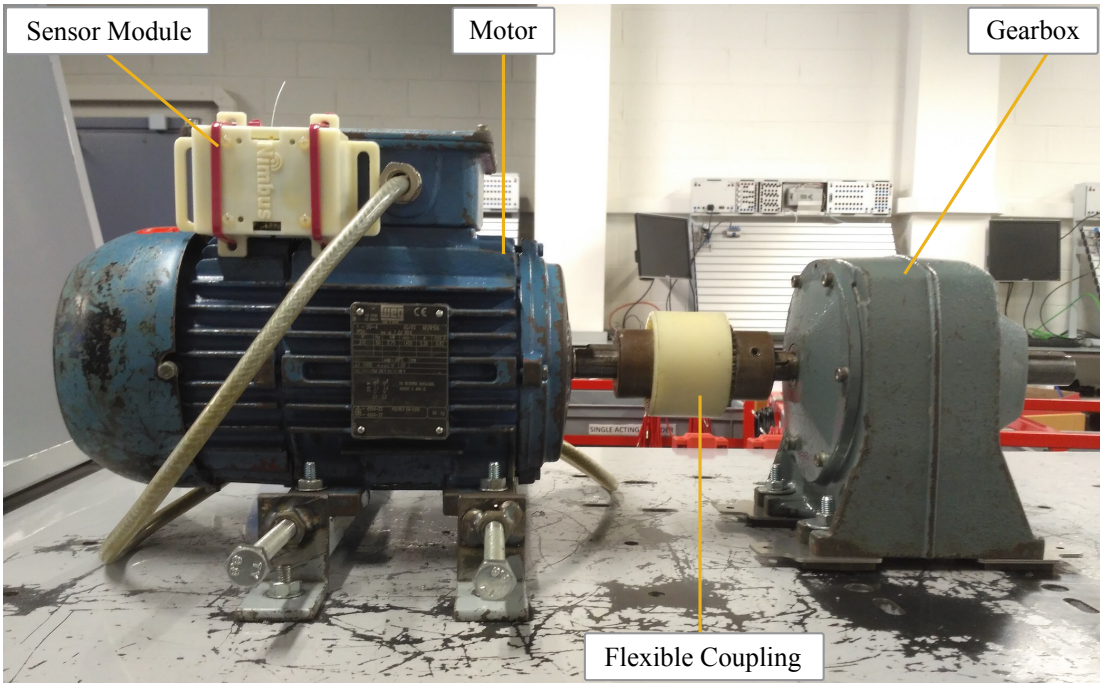

Figure 4.18: Experiment setup for the health monitoring module in a motor connected to a gearbox.

no load, the motor was run at full speed (1450 rpm). Three different tests were run, first with the motor properly aligned with the gearbox, then misaligning it by 2 mm and 4 mm, sampling 5 s of audio and accelerometer data for each test.

From the collected accelerometer data, a peak is observed around 100 Hz in all the tests for the three axes, as it is the typical working frequency for a 2-pole single-phase motor powered by a 50 Hz AC power supply. Fig. 4.19 shows the power spectral density for the y-axis for the three experiments, where we can see how its magnitude approximately doubles for every misalignment step. The audio data showed a spectrum similar to the one obtained in the previous setup, as the misalignment produced by the flexible coupling is not expected to produce a measurable noise. Faults produced in the motor itself such as bearing breakage would be more likely to produce an audible noise that could be picked up by the microphone.

For both experiment setups, the average time to download the audio was 3 min per file, while the accelerometer files took about 5 min due to the on-the-

fly conversion from the binary data to the corrected values. Although the use of ContikiMAC as a radio duty cycle increases the download time, the much lower power consumption makes it a necessary trade-off to maximise battery life if the current command-listening architecture described in Section 4.5 is to be used.

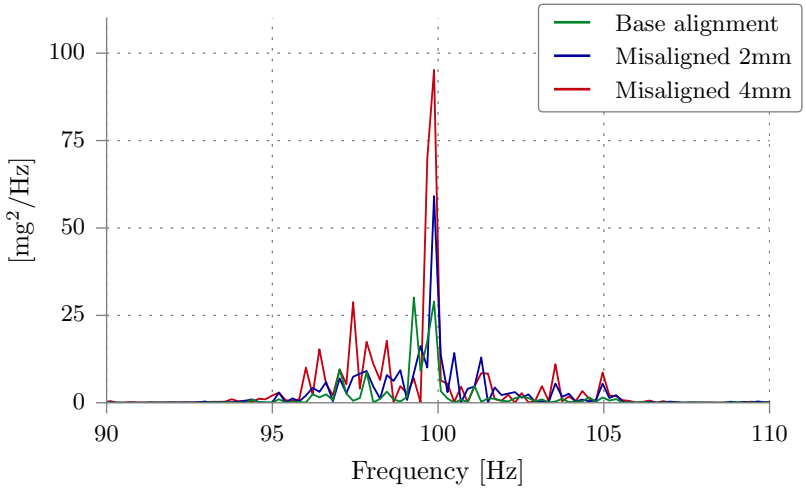

Figure 4.19: Power spectral density of the y-axis accelerometer data collected from the motor and gearbox setup.

Both of these experiments showed that the node worked as designed and could identify deliberately-induced mechanical faults.

4.7 Discussion

4.7.1 Advances to the state of the art

The literature review has highlighted the necessity for robust wireless sensing platforms (integrating sensing, processing, wireless communication, firmware, software and UI) that can be used reliably in marine harsh environments while also addressing research needs and compatibility with current standards, protocols, and embedded operating systems. The WSN platforms for machine and structural monitoring found in the literature are based on old platforms developed for networking research with limited processing capabilities and memory (e.g. TelosB and MICAz), which limits also the sampling rate of the sensors, or on more powerful platforms with higher power consumption and that do not support current standard WSN operating systems such as Contiki-OS. Moreover, they use different modules for communications, acquisition, and sensors attached with cables or connectors instead of a single integrated board, and do not provide a proper firmware/software architecture focused on sensing.

These problems have been addressed in this research by developing an integrated hardware-software WSN platform ready to be deployed in marine harsh environments. The hardware module consists of a single board based on the same state-of-the-art IEEE 802.15.4-compatible microcontroller, humidity/temperature sensors, and battery management used in the inductive module described in Chapter 3, but with MEMS vibration and microphone sensors instead of the inductive one, encased in a custom 3D-printed box designed for easy resin encapsulation. The firmware/software developed for this platform allow wireless data collection and visualisation, experiment control, and 3D view support of the environment and node location. This was developed based on the lessons learned from the previous module design. It was discovered that an external memory flash could be used to take full advantage of the high sampling rate of the accelerometer as well as the microphone. The addition of this memory also permitted the enhancement of the firmware, which now allows for periodic sensing experiments without the need of a gateway, as well as storing calibration parameters. A switch was also added to facilitate remote deployments, as it can be handed to the user to

install it and the sensing experiment will start when the node is switched on. However, this switch can be a potential point of failure and it should be replaced with a magnetic reed switch hosted inside the box, which can then be used to turn on/off the sensor with a magnet.

Due to the number of integrated sensors and analog components, as well as the firmware architecture that requires to be always listening for commands, the quiescent current of the module is higher than desirable for long term deployments. To extend the battery life, different strategies could be applied: the addition of a load switch controlled by the CPU that can turn off the power for all the sensors, memory, and other components when not in use; the adjustment of the firmware architecture to the specific application to optimise power consumption.

This platform was tested in laboratory conditions and has been further tested for reliability and in real deployments, work described in Chapter 6.

4.7.2 Engineering advances

The module presented here is a step forward in developing low-cost, fully-networked wireless sensor modules for machine and structural health monitoring. It consists of a single-board, microcontroller-based module with Contiki-OS support in a hardware-software co-design fashion focused on sensing and operability, which can work autonomously or as part of a network. The method shown for encapsulating the module is simple and low-cost.

The module overcomes several limitations of similar boards that use vibration or audio for machine monitoring: the firmware architecture allows for on-demand and periodic experiments, which has the advantage of being able to setup experiments wirelessly that will run when the nodes are turned on, without the need of a gateway, as well as interact with them through a gateway; the audio conditioning circuit solves the problem of the fixed gain that digital MEMS microphones have, which makes them less suitable for loud environments, by adding a programmable potentiometer to the signal chain; the developed sensing architecture allows for sampling and storing audio and accelerometer at high data rate at the same time using only the low-power microcontroller and embedded bus peripherals.

Chapter 5

Wireless Sensor Network Performance Characterisation

5.1 Introduction

To ensure reliable data collection from wireless sensor nodes, it is necessary to characterise the link quality in the actual target environment as modelling, for a large metal environment with 3D spatial complexity and with the presence of machinery, is highly challenging and is impractical for real-world environments. The literature review has shown that although there are methods to characterise WSN communications, they have only been applied to the most common scenarios, i.e., open fields and buildings, and have not been adapted and tested in complex metal marine environments. Moreover, the experiments and deployments shown in the literature for these marine environments have been focused on application-level or network-level topologies instead of the physical layer, due to this being the classic approach followed in 2D simple scenarios, where the physical behaviour is more easily predicted with distance-based models. However, a study of the higher layers would not reveal underlying problems that can occur in complex 3D environments. The objectives of the research presented in this chapter are therefore to:

1. Develop a systematic methodology to fully characterise the communications in a WSN for metal marine environments.

2. Validate the methodology in different complex metal environments by characterising the effects of the different variables that can affect wireless communications in these environments, such us node location, density of machinery and other metal objects, openings between compartments, and presence of electromagnetic noise.

5.2 Wireless characterisation challenges

Marine environments and structures such as ships, oil and gas rigs, and marine energy platforms are composed of large amounts of metal and complex layouts that make it very challenging to model the wireless propagation, and the use of watertight doors between compartments further complicates wireless planning. Moreover, the presence and density of heavy machinery in these environments can also have an effect on the communications.

To specify wireless network architectures and protocols, and to design applications for these metallic offshore environments, it is essential to measure the link quality in *situ*, as it cannot be accurately modelled and predicted. Although the literature has demonstrated several WSN deployments in different metal and ship environments, none used a methodology that can accurately characterise the link quality between each sensor node.

To address these challenges, the methodology described in this chapter had to have the following capabilities not collectively available in existing methodologies:

- Characterise wireless communications on the IEEE 802.15.4 physical layer, avoiding the bias introduced by higher-layer protocols such as Zigbee which includes transparent retransmissions in case of packet loss.
- Execute experiments in a synchronised manner, to avoid collisions that can introduce reading errors in RSSI and PDR.
- Detect asymmetries between links, to identify nodes or locations with unreliable communications.
- Display overall network performance, as well as the performance of individual nodes.

- Complete link characterisation and classification in an all-to-all fashion.
- Provide candidate nodes that can act as a sink.

5.3 Experimental methodology

5.3.1 Hardware and software tools

The hardware used for all three deployments consisted of 18 TelosB [64] nodes, plus an extra gateway node connected to a laptop to configure the experiment and download the data. They are composed of a low-power microcontroller, a 2.4 GHz IEEE 802.15.4 radio chip, an on-board PCB antenna, and several integrated environmental sensors. These nodes were chosen for their wide use in research and good software support.

To conduct the tests, the software used was an open-source tool TRIDENT [157] which, unlike similar tools available, allows to configure and run the experiments without the need for a separate wired infrastructure. This expedites the work of changing the location of the nodes between different experiments, as well as retrieving the data via multi-hop wireless communication. The tool permits the configuration of every node as a sender and receiver, synchronising the senders in a round-robin fashion to avoid collisions and ensuring that there will not be more than one node transmitting at the same time. This feature, along with the ability to send probes without any MAC or upper-layer protocols, are key to acurate characterisation of the physical medium. The nodes acting as receivers log the number of received packets, RSSI and LQI, besides the noise floor sensed by the sender before transmission and environmental variables. This tool has been previously successfully used in different open field deployments, e.g. [118, 176].

5.3.2 Testbed environments

The experiments used to develop and characterise the methodology were carried out in three different scenarios with increasing complexity and scale:

- The first deployment, in three outdoor freight containers, assessed the effect of door openings, node location and orientation on the communications.

- The second was in a shore-based full-sized ship's engine room training facility. This contained a large amount of piping and metal fixtures, as well as several electrical generators and a ship's engine that could be individually and collectively switched on and off to test the effect of electrical noise.
- The third deployment was on a seagoing Irish Naval Service (INS) ship's engine room and its adjacent compartments, where the opening of the sealed bulkhead door was varied as well as the switching of the main engine and generators.

To characterise link behaviour and to validate the methodology, a full factorial experiment was designed, in which one variable at a time is varied. Each experiment was designed to be completed in a single day with a randomized run order to minimise the confounding effects of the environmental variables of humidity and temperature. These scenarios and experiment designs are described in more detail below in their respective sections.

5.4 Experimental evaluation in a multi-chamber metal environment

5.4.1 Environment description & experiment design

The nodes were installed inside and outside three freight containers located in an outdoor yard and separated by 3 to 4 m, with various metal and concrete obstacles between them (Fig. 5.1). Containers 1 and 2 are 6 m x 3 m, while container 3 is slightly smaller at 6 m x 2.5 m. This constitutes an indoor/outdoor metal environment that more realistically replicates real-world environments. The distribution of the containers and the nodes can be seen in Fig. 5.2. The containers contain several pieces of furniture such as tables and metal shelves, including a small metal box where node 9 is placed. It should be noted also that container 2 has a double door, a metal exterior door and a wooden interior door, but these were opened and closed as one door and not considered as separate variables.

The set of variables and levels for this environment can be seen in Table 5.1. An important issue in these multi-chamber environments can be the size of the

Figure 5.1: Outside view of the freight container testbed

openings between adjacent rooms. Therefore, to emulate this, three different door openings for the containers were selected: fully closed, a minimum opening of 5 cm (approximately a half-wave for the frequency used), and a maximum opening of 40 cm, which corresponds to the size of an opening, such as a bulkhead door, that would allow a person to pass through. As sensor nodes will typically be used to monitor different parts of the structure and machinery, their height, position, and orientation will vary. Therefore two heights were selected: middle height (1.7 m), and ground level (0 m); and, because the antenna is not isotropic, the best and worst case for this were selected: node attached horizontally and vertically. Finally, as the software tool allows to interleave every round of packets with different transmission power levels, two levels of 0 dBm (maximum power) and -5 dBm were set, which would suppose around 20% reduction in power consumption. All combinations of these variables form a total of 24 experiments, organized in 12 different runs with two interleaved powers.

The nodes were placed inside containers 1 to 3, as shown in Fig. 5.2, to cover key points such as corners, doors, and problematic areas behind metal shelves

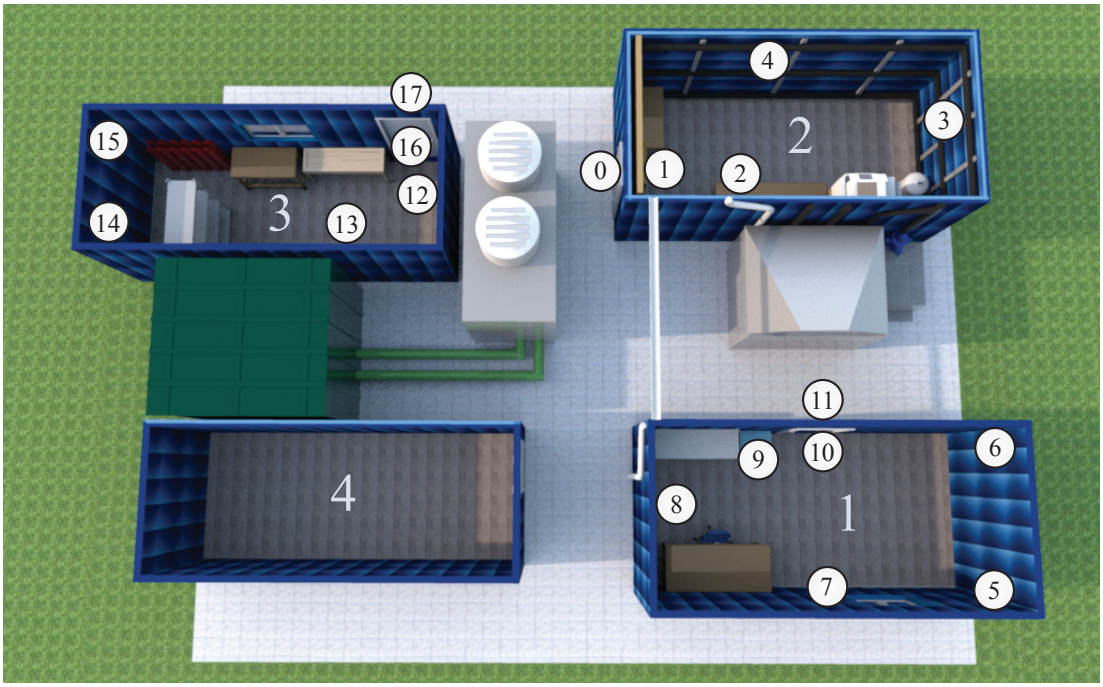

Figure 5.2: Node distribution in the containers

or furniture. Container 4 could not be used due to restricted access. Three nodes (0, 11, and 17) were also attached to the outside of the doors, to allow connectivity through the doors' leakage. Since node 0 acts as the master node for synchronising and distributing the experiment to all the nodes, its location was chosen to be at midpoint distance from the rest, and therefore the best candidate for the sink. This is not essential, as there are multi-hop capabilities for distributing the configuration but, nevertheless, a good location of the master node can facilitate it.

All experiment runs were performed on November 24th 2015, on a clear winter day. For each run configuration, four rounds of probes per node were sent, 2 at high and 2 at low power, with every round composed of 10 probes with a 750 ms gap between them, and each probe with a burst of 10 messages with 50 ms separation. This forms a total of 200 messages per round and power level per node. The decision to perform burst experiments was made based on the target application, considering that machine and structural monitoring often require data bursts from accelerometers and other high sample rate sensors. The probes

Table 5.1: Experiment variables

Variable	Levels
Transmission power	0 dBm, -5 dBm
Node distance from ground	0 m, 1.7 m
Node antenna orientation	Horizontal, Vertical
Container door openings	Closed, Open 5 cm, Open 40 cm

used channel 26, to avoid interference with Wi-Fi networks, and were configured not to use any MAC protocol. Each run configuration lasted for 10-15 min, accounting for the probe sending and the data writing to the memory which, along with changing the position of the nodes and data downloading, used the full day of experiments for the total set of 12 runs.

5.4.2 Results & analysis

5.4.2.1 Overall network analysis

As shown in the literature [108], a simple way to get a general understanding of the link quality of a wireless network is by looking at the RSSI, and its relationship with the PDR and LQI. Although the presence of interfering signals can boost the RSSI levels while yielding a lower PDR [123], the setup of the experiments guarantees a lower chance of that occurring, due to channel selection and environment isolation.

In Fig. 5.3, the PDR of each probe burst for the different combinations of rounds is represented, for high (0 dBm) and low (-5 dBm) power, with respect to the mean RSSI. A total of $n(n-1) = 306$ links, with $n = 18$ nodes, were analyzed for each round. The typical overturned "L" shape found in the literature [125,149] can be observed, with disconnected, transitional, and connected areas. This can also be seen in Fig. 5.4, which shows how LQI relates to RSSI. However, some outliers (circled) appear in both plots occurring in node 11, which is attached to the outside of the door in container 1, for the configurations with the doors open. Since external interference is unlikely, this could be due to the multipath caused by the amount of metal in the environment. Moreover, the overall noise floor

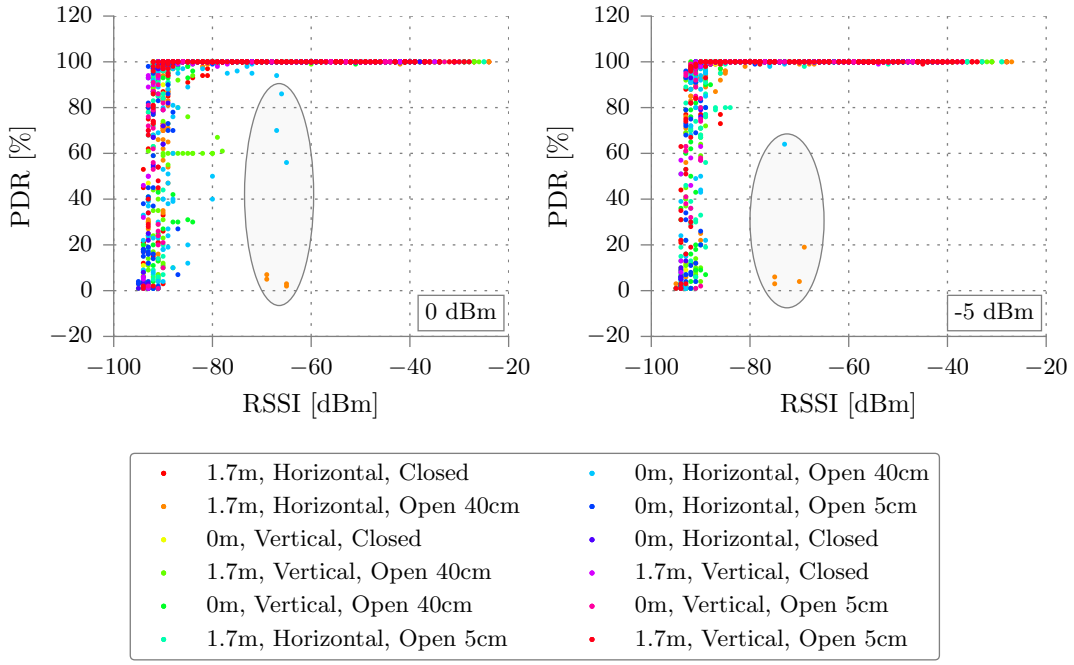

Figure 5.3: PDR vs RSSI.

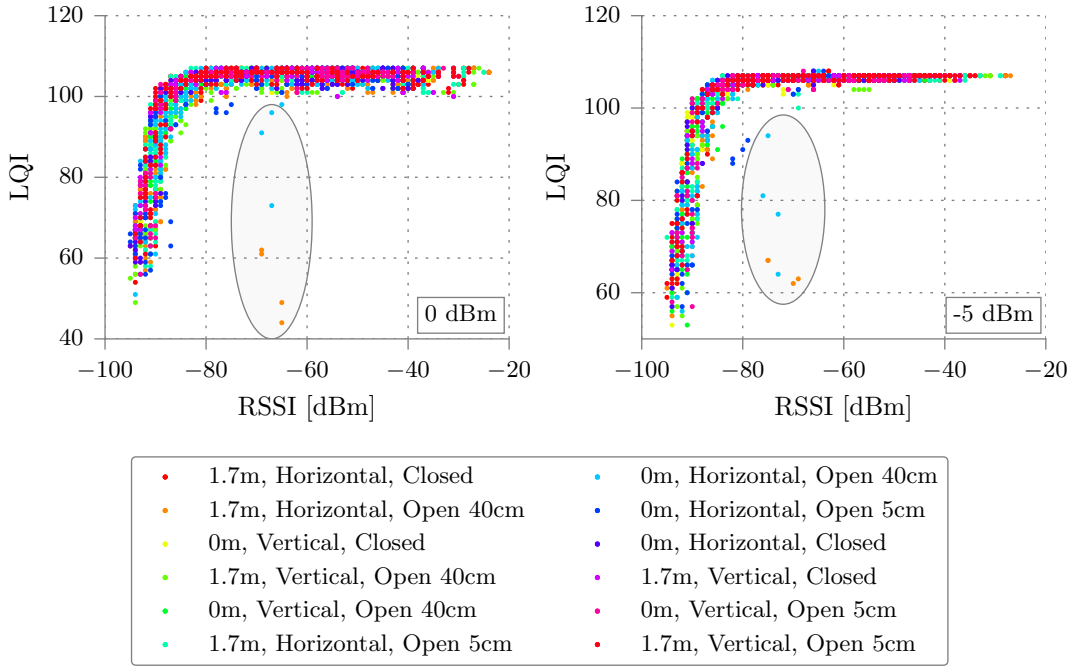

Figure 5.4: LQI vs RSSI.

measured is fairly constant and close to the sensitivity of the radio chip, with an average of -96 dBm and $\sigma = 1.28$, which excludes the presence of other external elements that could affect the signal integrity.

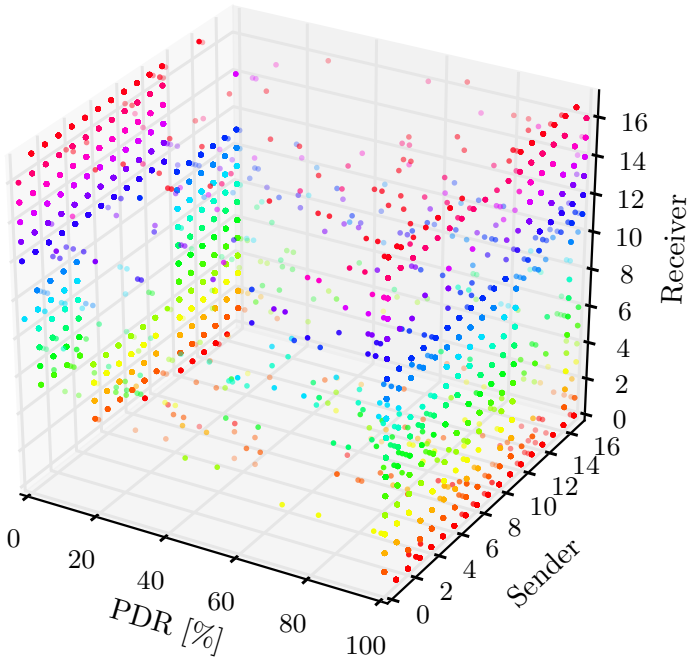

(a) Transmission power at 0 dBm

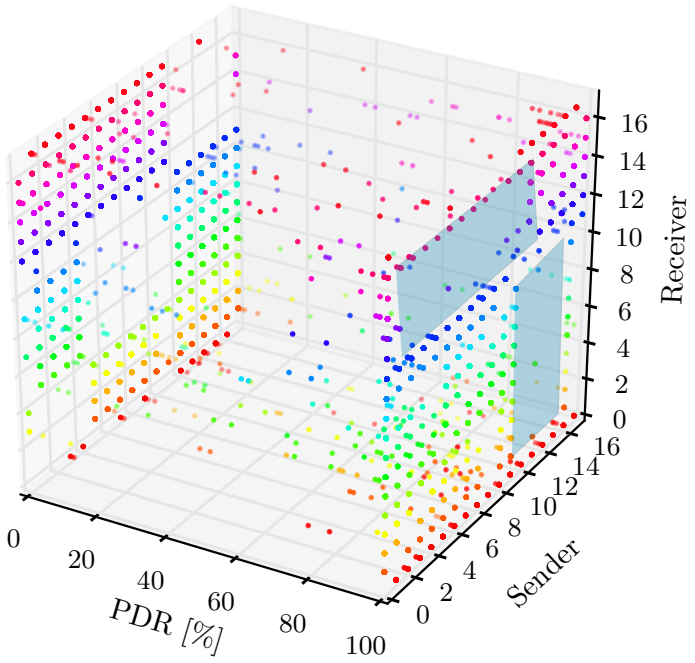

(b) Transmission power at -5 dBm

Figure 5.5: PDR [%] between each node for all rounds at different transmission powers.

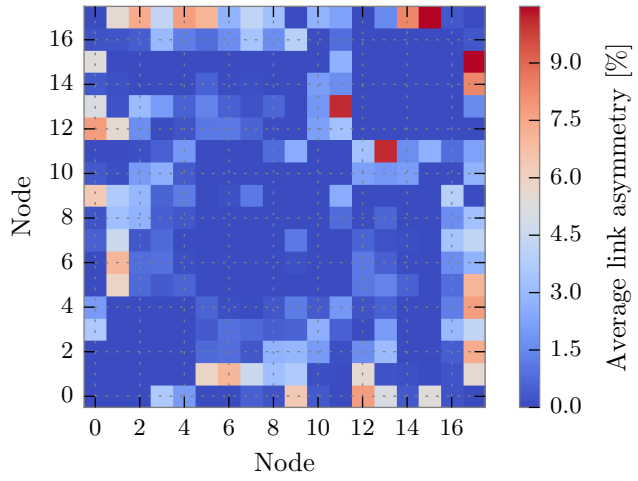

Figure 5.6: Link asymmetry calculated as $|PDR_{n\to m} - PDR_{m\to n}|$.

To have a global view of the performance of each node, Fig. 5.5 shows a 3D representation of the PDR per probe, accounting for each node being a sender or receiver, with each run of probes represented by a different colour, although the colours are not meaningful and their purpose is to help visually align the points. This type of 3D representation allows the rapid identification of problematic links in a deployment, as links between nodes with low PDR will be visible near the 0% plane and potentially problematic ones that need further study will have the probe messages between them distributed through the PDR axis. The first thing to notice is the high concentration of points near the 100% PDR plane, except for an empty rectangle between nodes 12-15 and 17, corresponding to the ones located in container 3, and with a concentration of points in a mirrored space on the 0% PDR plane. This could be due to two reasons: the door of this container faced away from the other two containers and the presence of the large metal block between container 2 and 3. This is more visible in the low power configuration. Also, the same empty block can be seen repeated, but rotated to the opposite side, suggesting a high degree of symmetry in the network. As asymmetry predicts the unreliability of a link, and has an impact on upper-layer protocols [177], a closer look at the average link asymmetry of individual nodes is necessary. In Fig. 5.6, the asymmetry as defined in [149] is represented, where a link is considered asymmetric if $|PDR_{n\to m} - PDR_{m\to n}| > 40\%$. This shows that

only links 11-13 and 15-17 exhibit a noticeable, although small, asymmetry (< 10%), while most of the links are almost fully symmetrical.

5.4.2.2 Effects of the variables on network performance

An interesting effect of the environment can be observed by looking at the average PDR and RSSI for each of the different door combinations, Table 5.2. Although a positive correlation between PDR and RSSI is seen when representing all bursts of probes in Fig. 5.3, the average values per combination shown in the table seem to indicate the opposite. This is due to the fact that, when any of the variables are set to have a negative effect on the signal range (e.g., closed doors), the average PDR computed over the whole network decreases; however, as the number of connected links also decreases, the average RSSI, which is calculated only over the remaining links, increases. This indicates that the network becomes more polarized, dropping links that were previously in the transitional region to the disconnected region. In Tables 5.3 and 5.4 we can see that this is less noticeable for the node height and orientation variables, as they have less impact on the PDR.

An increase of over 50% is observed in the total PDR from closed doors to fully open at full power, while for the node height and orientation it is much less. Therefore, the number and size of the openings will be the key variables to take into account when deploying wireless networks in these environments.

As expected, the best performance occurs when the nodes are transmitting at high power, located at 1.7 m in horizontal, and with the container doors fully open, yielding an overall PDR = 74.69% and mean RSSI = -69 dBm. On the other hand, the worst case is found at low power, nodes vertically oriented at ground level, and doors closed, with a resulting PDR = 37.25% and mean RSSI = -66 dBm.

Due to the season and geographical area, the environmental variables recorded during the tests did not undergo dramatic changes, with an average temperature of 13.44 ^oC, $\sigma = 1.63$, and relative humidity of 68.03%, $\sigma = 12.76$, outside the ranges that can affect significantly the performance of the node wireless communications.

Table 5.2: Average PDR and RSSI for different door openings.

Transmission power	Door state	PDR [%]	RSSI [dBm]
0 dBm	Closed	41.13	-64
	Open 5 cm	47.83	-67
	Open 40 cm	64.21	-70
-5 dBm	Closed	38.03	-66
	Open 5 cm	42.35	-68
	Open 40 cm	55.66	-71

Table 5.3: Average PDR and RSSI for different node heights.

Transmission power	Node height	PDR [%]	RSSI [dBm]
0 dBm	1.7 m	53.49	-67
	0 m	48.61	-68
-5 dBm	1.7 m	47.06	-68
	0 m	43.63	-69

Table 5.4: Average PDR and RSSI for different antenna orientations.

Transmission power	Orientation	PDR [%]	RSSI [dBm]
0 dBm	Horizontal	54.33	-67
	Vertical	47.78	-67
-5 dBm	Horizontal	48.17	-68
	Vertical	42.52	-69

5.4.2.3 Link classification and sink selection

Although the 3D plots above allow quick identification of problematic areas, a way is still needed to quantify the link reliability to each specific node. For this the link classification described in [118,149] is used, which aggregates the links in five groups: *dead* ($PDR = 0\%$), *poor* ($PDR < 10\%$), *intermediate* ($10\% \leq PDR \leq 90\%$), *good* ($90\% < PDR < 100\%$), and *perfect* ($PDR = 100\%$). Fig. 5.7 shows the

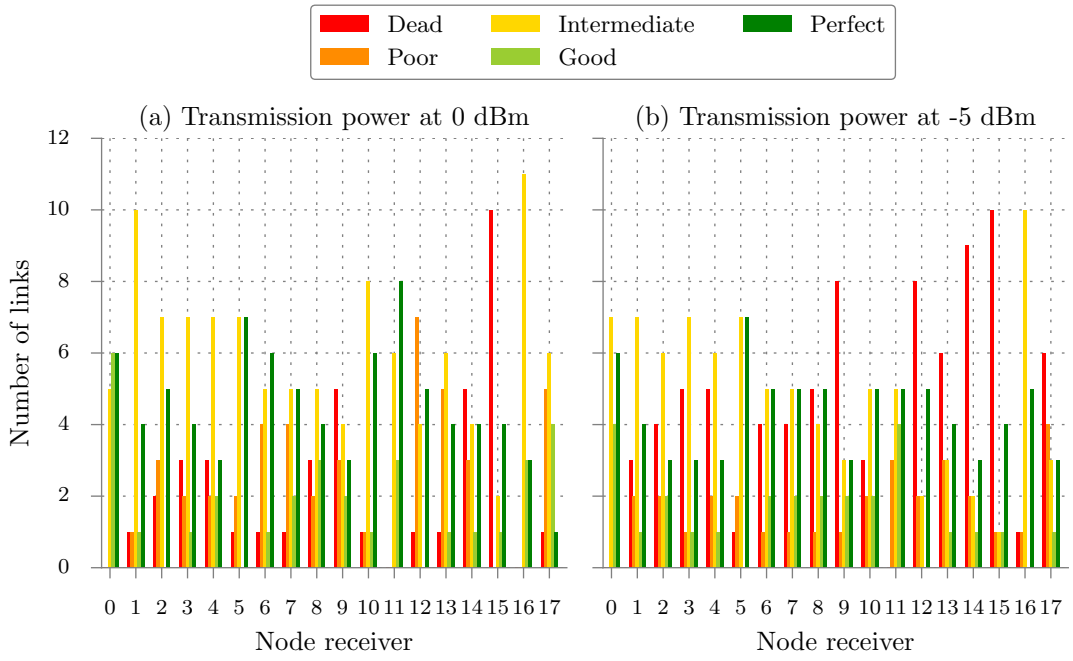

Figure 5.7: Number of *dead (PDR = 0%)*, *poor (PDR < 10%)*, *intermediate (10% ≤ PDR ≤ 90%)*, *good (90% < PDR < 100%)*, and *perfect (PDR = 100%)* links for each node.

number of links to each node distributed in each category, from a total of 17 possible links per node, for high and low power configurations. This representation, along with the average total PDR per node shown in Fig. 5.8, allows identification of the node with the best quality links that would be a good candidate for a sink in a one-hop network.

It can be noticed that even though the average PDR drop from high to low power per node is not large, the number of dead links increases considerably. This renders most of the nodes incapable of acting as a sink, with the exception of nodes 0 and 11, located outside containers 1 and 2, which keep all their links in the connected and transitional region, due to their strategic location. Looking at Fig. 5.8 confirms that the initial placement of the master node (node 0) as a sink candidate was correct, as it yields a better performance than the rest of the nodes, with an average PDR = 91.97% for all round combinations of high power.

Since it was previously established that the door openings are the most influential variable in this experiment, the average PDR and RSSI values is shown

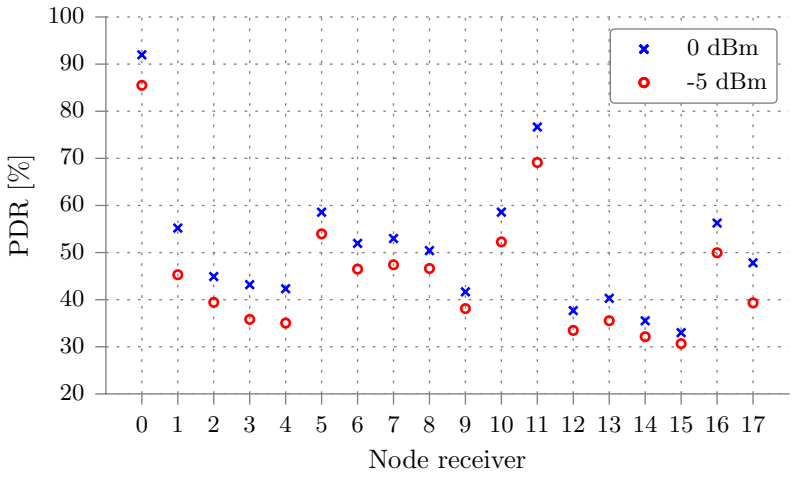

Figure 5.8: Average total PDR [%] per individual node.

Table 5.5: Average PDR and RSSI for different door openings (node 0).

Transmission power	**Door state**	**PDR [%]**	**RSSI [dBm]**
0 dBm	Closed	80.65	-74
	Open 5 cm	96.92	-73
	Open 40 cm	98.33	-68
-5 dBm	Closed	70.04	-78
	Open 5 cm	88.69	-76
	Open 40 cm	97.77	-73

in Table 5.5 for all the links to the sink candidate (node 0), for the different door configurations for both powers. In this case, unlike the previous case when the network links are shown as a whole, the expected increase in RSSI with the PDR can be observed, as a result of the links being stable under all different conditions. For the high power transmission, a PDR = 80.65% for the closed door and a PDR = 98.33% for the open door case is obtained, with a 6 dB difference between both states, and a PDR = 96.92% is achieved with only a 5 cm door opening. Even at the worst case, with the doors closed and low power, the average to the sink candidate is PDR = 70.04%.

5.5 Experimental evaluation in a ship's engine room emulator

5.5.1 Environment description & experiment design

The previous scenario showed the behaviour of the network in a simple metal multi-chamber environment. To increase complexity, the next deployment was done in a full-scale operational engine room emulator, with control room, located in the National Maritime College of Ireland (NMCI), which is normally used for marine engineering training. As shown in Fig. 5.9, this is a 16 m x 20 m, high ceilinged room with a high volume occupancy of various machinery, metal ducting and piping, gantries, etc., which are representative of the environment found not only in ships but in other off-shore structures. Moreover, from the control room in the centre, a real ship's engine connected to a variable load can be switched on/off, as well as an auxiliary generator. The ship engine is a MaK 60M20 running at 1000 RPM and the auxiliary generator a Caterpillar running at 1500 RPM. The 18 nodes were distributed to cover the whole room, as shown in Fig. 5.10. Nodes 2 and 4 were placed on top of the main engine, while node 3 was attached under the cover, and node 6 on top of the working auxiliary generator. Node 0 (master) was placed at the most central position, on the window sill outside the control room, at around 1.5 m from the ground.

In this scenario, the operation of the main engine and auxiliary generator were modified to test the effect it could have in the network performance, as well as the transmission power (Table 5.6). Also, because the environment is an open space and can potentially yield a higher connectivity, an extra lower power level (-10 dBm) was added to the test rounds, to assess if the transmission power could be reduced further to save energy.

The experiments were also completed in a single day, on July 19th 2016, with the same configuration as in the previous one in terms of channel selected and messages per probe. However, because of the of the addition of the extra power level the number of rounds of probes per node was 6 (2 rounds per power).

Figure 5.9: Engine room emulator.

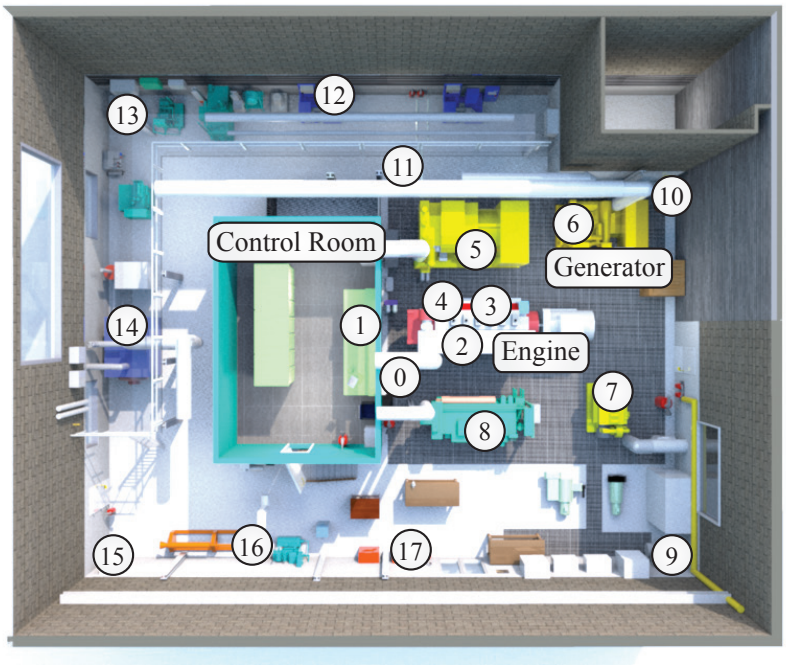

Figure 5.10: Node distribution in the NMCI engine room.

Table 5.6: Experiment variables

Variable	Levels
Transmission power	0 dBm, -5 dBm, -10 dBm
Machinery status	All off, Aux generator on, Aux generator + main engine on, All on + 200 KW load

5.5.2 Results & analysis

5.5.2.1 Overall network analysis

Fig. 5.11 and 5.12 show the PDR for each probe and average LQI with respect to the RSSI, respectively, for the three powers tested. Although the L-shaped pattern and the different connectivity areas can still be discerned, more outliers appear compared to the previous environment, despite having a shorter number of experiment runs. As the outliers are distributed among the different rounds, including the ones with machinery off, the conclusion is that having the engine

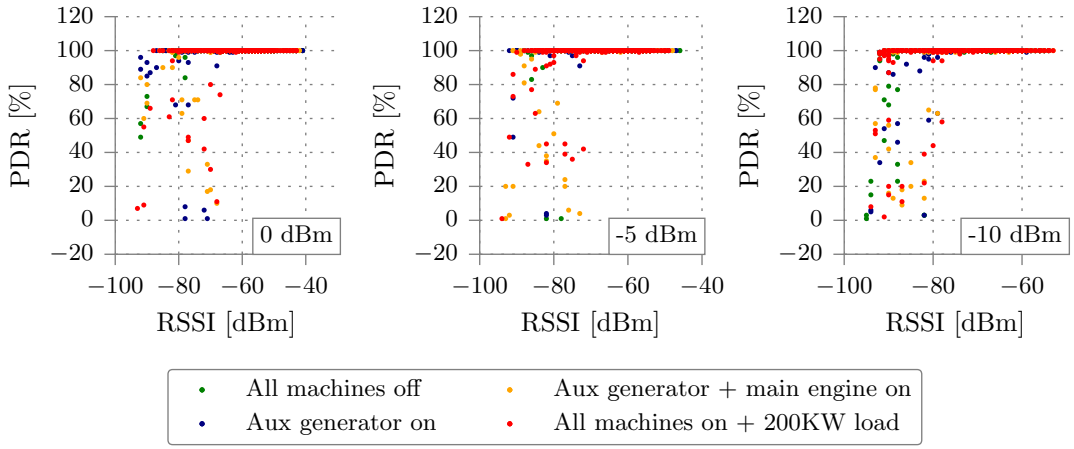

Figure 5.11: PDR vs RSSI for the engine room emulator environment.

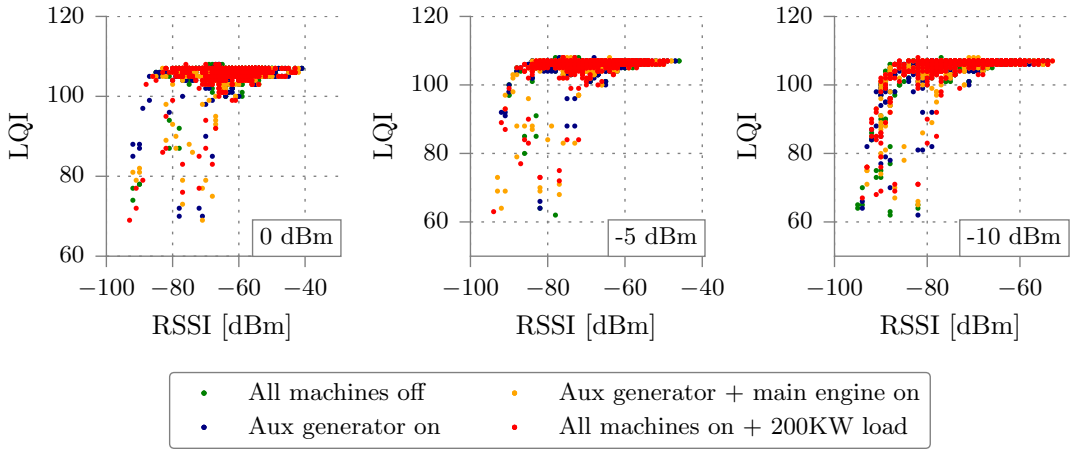

Figure 5.12: LQI vs RSSI for the engine room emulator environment.

or generators on is not causing them. This increase could be produced, however, from the increase in the complexity of the environment i.e. the large amount of piping, machinery and metal surfaces present in the room, all of which can contribute to multipath. The noise floor stayed constant at -96 dBm, as in the previous scenario.

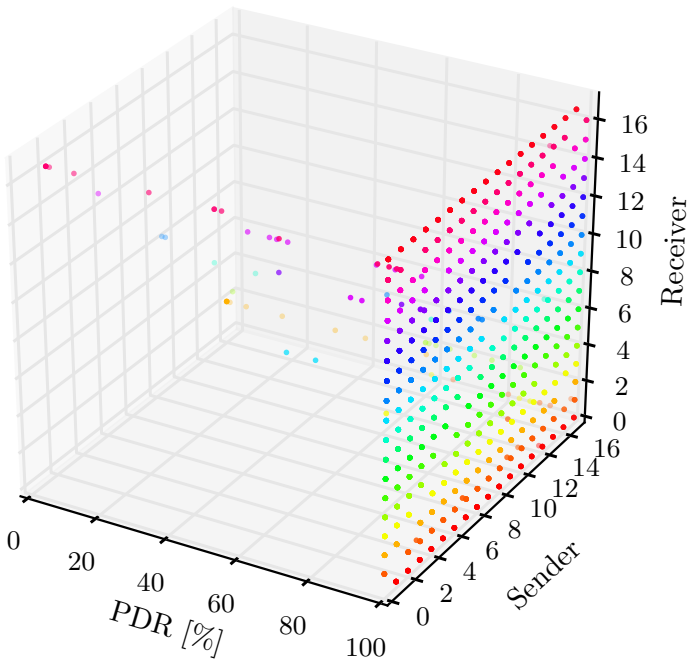

(a) Transmission power at 0 dBm

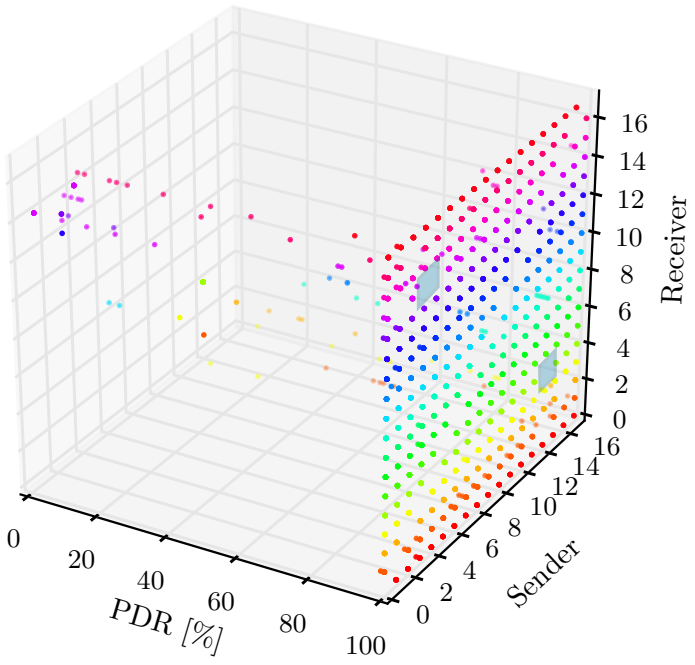

(b) Transmission power at -10 dBm

Figure 5.13: PDR [%] between each node for all rounds at different transmission powers, for the engine room emulator environment.

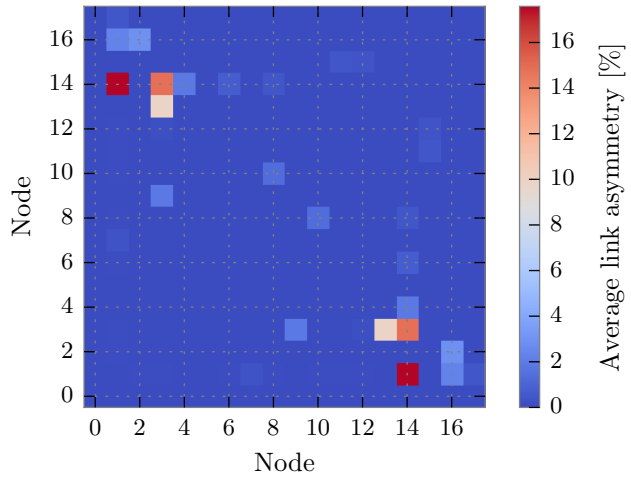

Figure 5.14: Link asymmetry calculated as $|PDR_{n\to m} - PDR_{m\to n}|$, for the NMCI engine room.

Due the environment being composed of a single relatively small open room, most of the probes were received with an average PDR close to 100% even for the low power configuration (-10 dBm), as it can be seen in the 3D representation in Fig. 5.13, with the exception of nodes 14 and 4. The lowest PDR occurs in the link between them, consistent among all rounds. Although this may be due to the lack of line of sight between both nodes, node 3 should be exhibiting similar or worse behaviour, since it is located in the same place as node 4 but under the cover of the engine. However, node 3 performed better than node 4 overall, again suggesting that multipath can have unpredictable effects on the communications. Looking at the asymmetry representation of the links in Fig. 5.14, node 14 shows more than a 10% asymmetry in two of its links, which confirms this location as particularly unreliable.

5.5.2.2 Effects of the variables on network performance

Table 5.7 shows the average PDR and RSSI obtained for the three powers tested for each machinery setting. The network on average showed a high connectivity for all the conditions, with over 97% PDR even for the worst case at -10 dBm; we can see the expected average 5 dB drop in RSSI with for every 5 dB reduction

Table 5.7: Average PDR and RSSI for different machinery states.

Transmission power	Machinery state	PDR [%]	RSSI [dBm]
0 dBm	All off	99.05	-62
	Aux generator on	99.12	-62
	Aux gen + engine on	98.85	-62
	All on + 200 KW	98.78	-62
-5 dBm	All off	98.65	-66
	Aux generator on	98.55	-67
	Aux gen + engine on	98.30	-67
	All on + 200 KW	98.31	-67
-10 dBm	All off	97.91	-72
	Aux generator on	97.94	-72
	Aux gen + engine on	97.07	-72
	All on + 200 KW	97.27	-73

in transmitted power, indicating that the network maintained stable links with only a small decrease in PDR.

A slight reduction in average PDR can also be observed when different machines are turned on, although this could be due to the increase in temperature in the nodes located on top of the turned on devices instead of the electrical noise, which in some cases reached 40 ^oC for the nodes on top of the main engine. The average temperature for all rounds was 25.16 ^oC, stable for most of the nodes but with a $\sigma = 2.6$ due to the contribution to the average of those nodes.

5.5.2.3 Link classification and sink selection

Looking at the number of links per node in each category, as previously defined for estimating link reliability, it can be seen in Fig. 5.15 that all the nodes have most of their links with perfect connectivity for high power (0 dBm) and even for low power (-10 dBm). The exception is nodes 4 and 14, already identified as problematic, with the link between them dead for the low power configuration. Node 3 also presents a lower number of perfect links, due to the node being inside

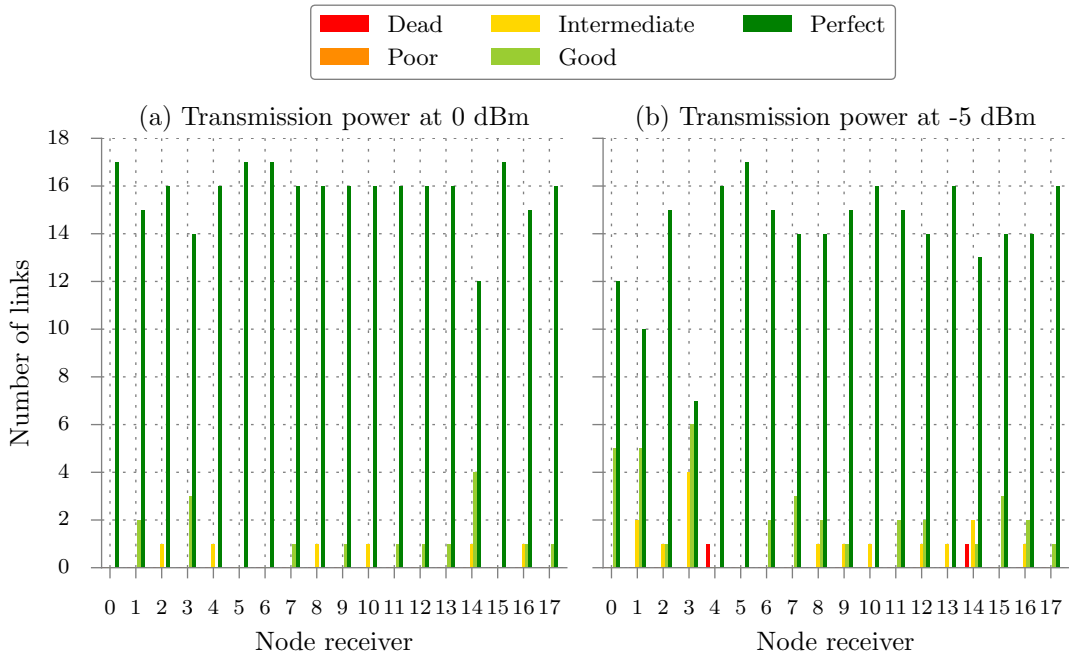

Figure 5.15: Number of *dead (PDR = 0%)*, *poor (PDR < 10%)*, *intermediate (10% ≤ PDR ≤ 90%)*, *good (90% < PDR < 100%)*, and *perfect (PDR = 100%)* links for each node, for the engine room emulator environment.

the enclosure of the main engine, although none of them dead or poor.

Fig. 5.16 shows that, when using a high power (0 dBm) configuration, all of the nodes present more than 95% PDR, therefore every node could act as a data sink if necessary. Avoiding node 14 would allow network reliability to be preserved, even at -10 dBm, saving power.

5.6 Experimental evaluation in a Naval vessel engine room

5.6.1 Environment description & experiment design

To perform a final set of experiments in a more realistic scenario, the same 18 nodes were deployed in the *LE Joyce* offshore patrol vessel of the Irish Naval Service (INS), Fig. 5.17. The nodes were installed in the 10 m x 12 m engine

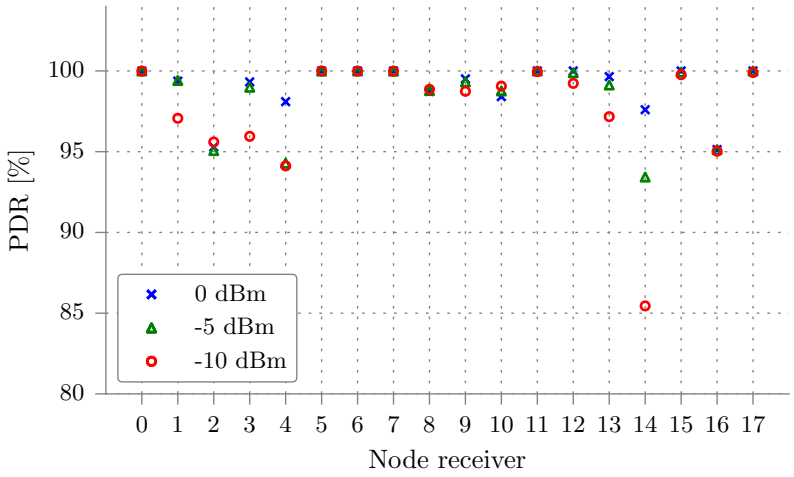

Figure 5.16: Average total PDR [%] per individual node, for the engine room emulator environment.

Figure 5.17: LE Joyce INS offshore patrol vessel.

room and its adjacent 9 m x 4 m compartment, connected by a waterproof sliding bulkhead door. Fig. 5.18 shows different views of the rooms, showing similar piping as in the NMCI emulator room but with overall higher volume occupancy of metal, with many more metal components and machinery. The main engine is a Wartsila 16V26D2 and the auxiliary generator sets are MTU Motor 16V2000 M60. The distribution of the nodes is shown in Fig. 5.19: Node 0 (master) in

Table 5.8: Experiment variables.

Variable	Levels
Transmission power	0 dBm, -5 dBm, -10 dBm
Machinery status (main engine + generator)	on, off
Door opening	Closed, Open 5 cm, Open 40 cm

the most centered place of the deployment, in the adjacent compartment on top of a cardboard box close to the door at 1.5 m; nodes 1 and 2 on the floor at the opposite side of the adjacent room, while nodes 3 and 4 at 1.5 m elevation on top of metal boxes; nodes 5 and 6 on the floor one on each side of the door; one node on top of each generator set (7 and 8, although only the generator below node 8 was turned on); node 9 on the floor at the top corner of the engine room; node 10 on top of a metal box at 1.5 m; nodes 13 and 14 on top of the main engine, and nodes 11 and 15 at the bottom; Node 12 on top of the companion ladder to the upper deck; node 16 and 17 on each side of the gearbox attached to the engine.

Although the previous experiments in the engine room emulator did not show a notable effect of the machinery in the communications, since this engine is more powerful and the scenario more complex, the communications were tested with the machinery on/off (main engine, one generator set, and pumping system). This was combined with the same three powers as in the previous scenario, adding also the door opening as a variable with the three opening levels used in the freight containers, Table 5.8, to form a full factorial experiment of 6 runs per power. The experiments were completed on April 20th 2017, with the same configuration parameters as in the other environments.

5.6.2 Results & analysis

5.6.2.1 Overall network analysis

Since this environment is even more complex than the engine room emulator, a larger number of outliers is observed in the PDR and LQI vs RSSI measurements

Figure 5.18: Naval ship's engine room.

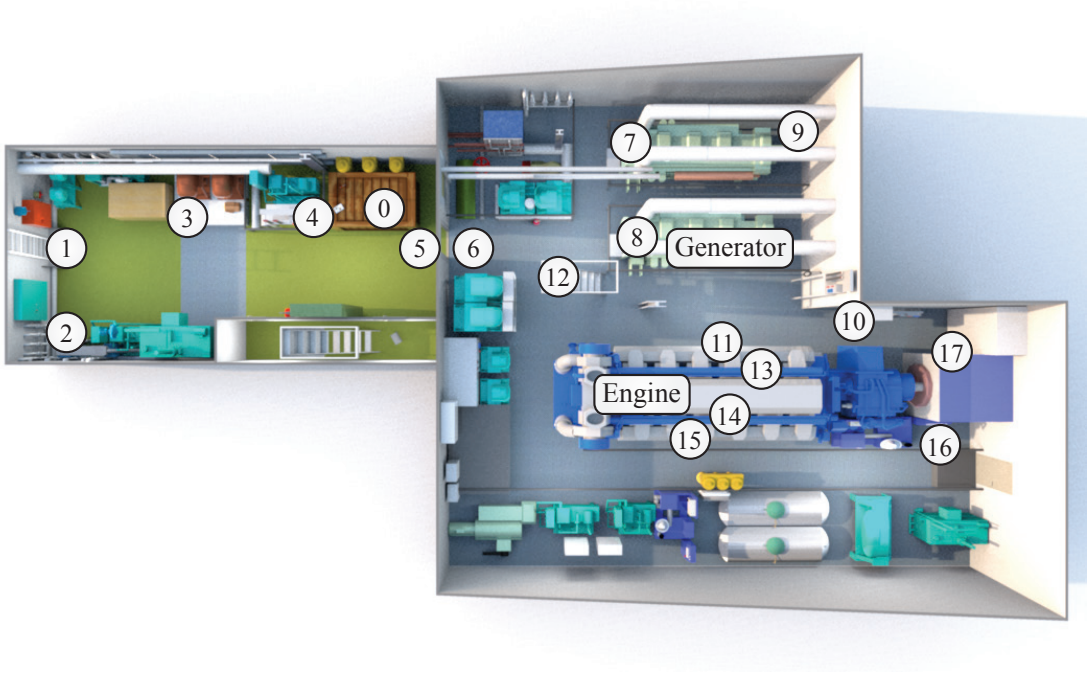

Figure 5.19: Node distribution in the naval ship's engine room

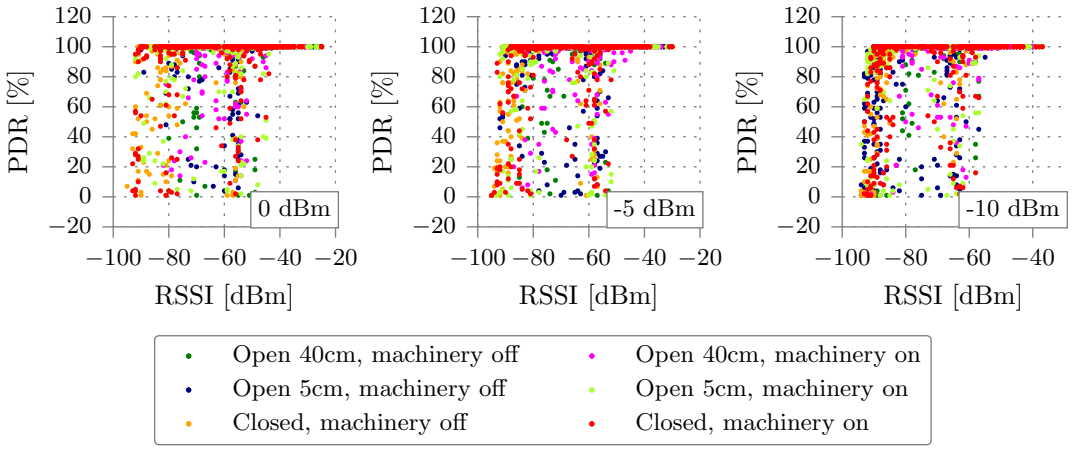

Figure 5.20: PDR vs RSSI for the naval ship's engine room environment.

(Fig. 5.20 and Fig. 5.21), such that the L-shape is no longer visible. An extra transition band is also formed around -60 dBm for all powers tested, showing that even with a very high average signal strength and packet delivery (RSSI = -62 dBm, PDR = 91.87%) the communications are very unpredictable. This is confirmed

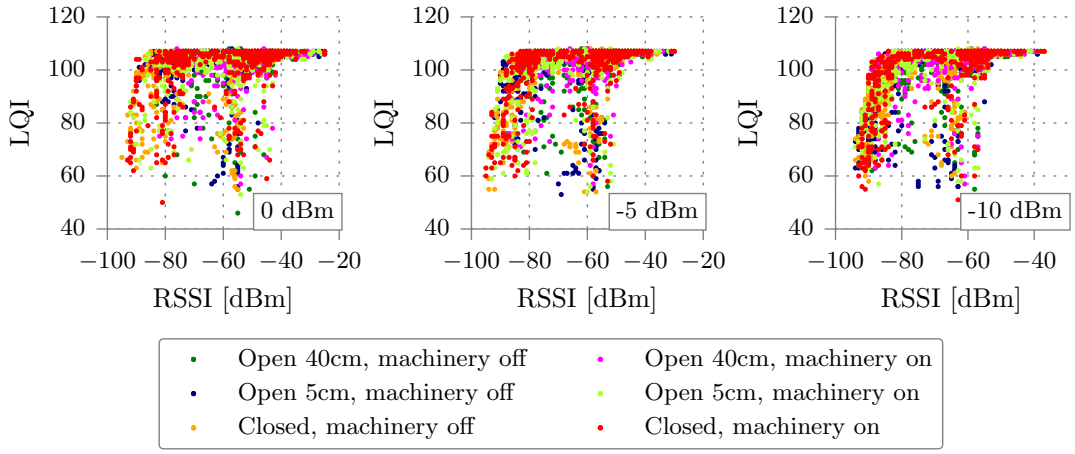

Figure 5.21: LQI vs RSSI for the naval ship's engine room environment.

in the 3D plots in Fig. 5.22, where, despite having a large number of the probes in the 100% plane, a cloud of probes appears randomly distributed across the rest of the space. Particularly, node 2 displays an accumulation of probes in the 0% plane, as it is the farthest on the floor of the adjacent room. As expected, the noise floor remained at -96 dBm average.

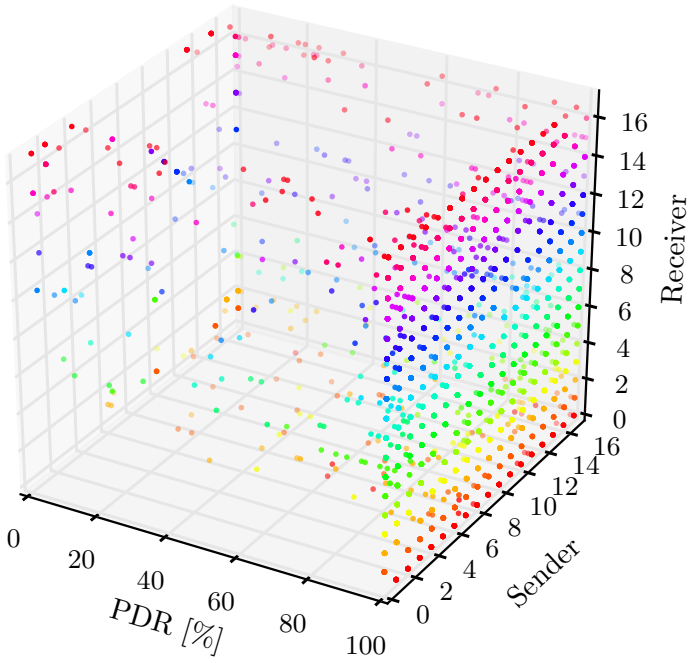

(a) Transmission power at 0 dBm

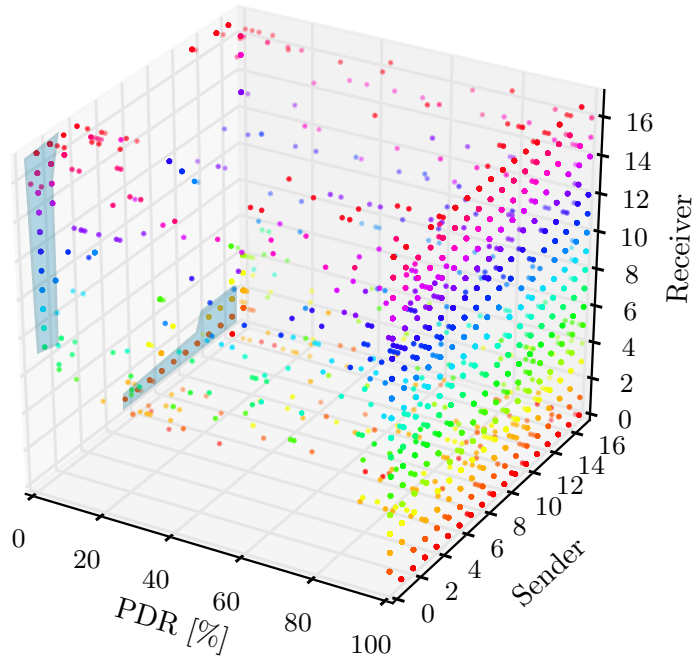

(b) Transmission power at -10 dBm

Figure 5.22: PDR [%] between each node for all rounds at different transmission powers, for the naval ship's engine room environment.

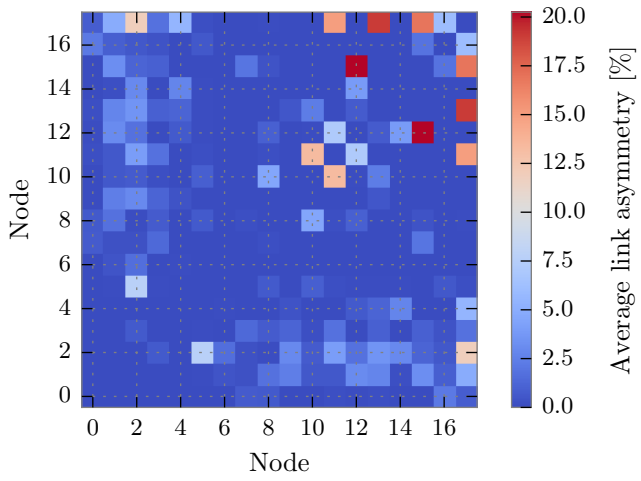

Figure 5.23: Link asymmetry calculated as $|PDR_{n\to m} - PDR_{m\to n}|$, for the naval ship's engine room environment.

It can be observed further how the unreliability is increasing in this environment by looking at the asymmetry between links in Fig. 5.23, where it reaches up to 20% for nodes 12-15, but still below the 40% defined as asymmetric.

5.6.2.2 Effects of the variables on network performance

To explore the effect the machinery has on the communications, Table 5.9 shows the average PDR and RSSI per power with the machines on/off. As it was observed in the engine room scenario, although a small drop in PDR can also be seen here, it does not have an important effect. Even for the low power configuration (-10 dBm) there is a decrease only from 89.09% to 88.93%. A greater impact is produced by the door opening (Table 5.10), as reported in the freight containers environment. Despite the door being waterproof sealed when closed, there is only a reduction from 88.76% at 5 cm opening to 81.29% when closed, at -10 dBm transmission power. This is most likely due to propagation through the rubber door seal, possibly in combination with propagation through other bulkhead seals where piping and ducting pass through.

The average temperature was kept constant by the AC system at 24.85 ^oC, with a $\sigma = 4.63$, again due to the increase in the surface temperature of the

Table 5.9: Average PDR and RSSI for different machinery states.

Transmission power	Machinery state	PDR [%]	RSSI [dBm]
0 dBm	Off	94.02	-58
	On	94.17	-57
-5 dBm	Off	92.75	-62
	On	92.25	-62
-10 dBm	Off	89.09	-67
	On	88.93	-67

Table 5.10: Average PDR and RSSI for different door openings.

Transmission power	Door state	PDR [%]	RSSI [dBm]
0 dBm	Closed	91.28	-61
	Open 5 cm	94.38	-58
	Open 40 cm	96.64	-54
-5 dBm	Closed	87.43	-65
	Open 5 cm	93.20	-63
	Open 40 cm	96.87	-59
-10 dBm	Closed	81.29	-69
	Open 5 cm	88.76	-68
	Open 40 cm	96.98	-64

machines measured by the nodes placed on them.

5.6.2.3 Link classification and sink selection

While the PDR vs RSSI and 3D plots suggested an unstable network, the average links per node all show above 10% PDR connectivity for high and low power, as shown in Fig. 5.24. However, for the worst case rounds where the machines are on and the door closed (Fig. 5.25), all the nodes that are farther from the sliding door show dead links. Nodes 0, 4, 5, 6, 7 and 8 present no dead links, which makes them good sink candidates. Although node 12 is also close to the

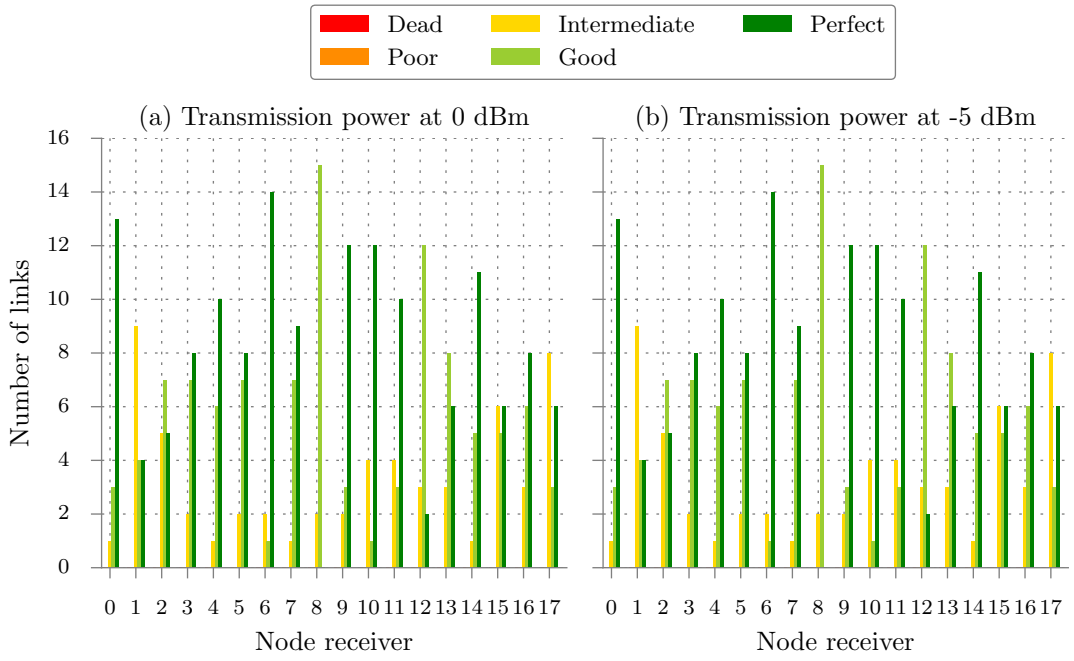

Figure 5.24: Number of *dead (PDR = 0%)*, *poor (PDR < 10%)*, *intermediate (10% ≤ PDR ≤ 90%)*, *good (90% < PDR < 100%)*, and *perfect (PDR = 100%)* links for each node, for the naval ship's engine room environment.

door, it performs worse due to being placed on top of the companion ladder with no line of sight. Fig. 5.26 shows that node 6, located next to the door in the engine room, presents the highest overall PDR, with around 97% for the three power configurations, while nodes 1, 2 and 17 (located at the end of each room) have the lowest with around 75% for the low power configuration. This suggests that whenever there are sealed doors that could be closed, a sink or node with forwarding capabilities needs to be placed near the door.

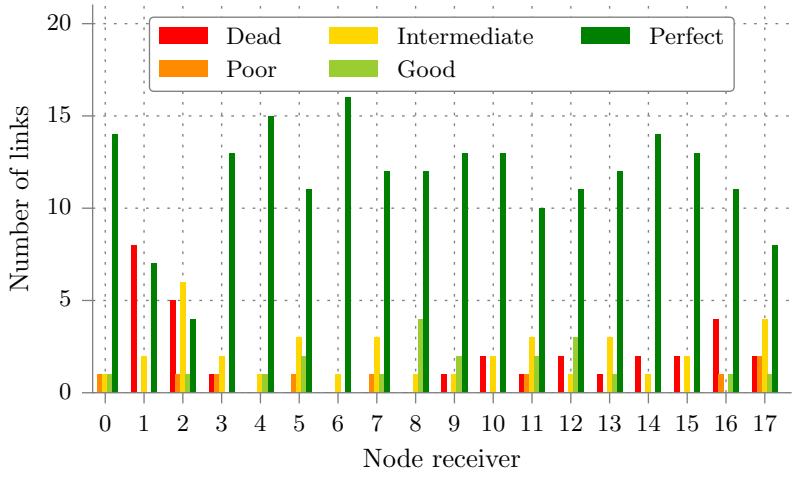

Figure 5.25: Link classification for the closed door and machinery on round, at -10 dBm.

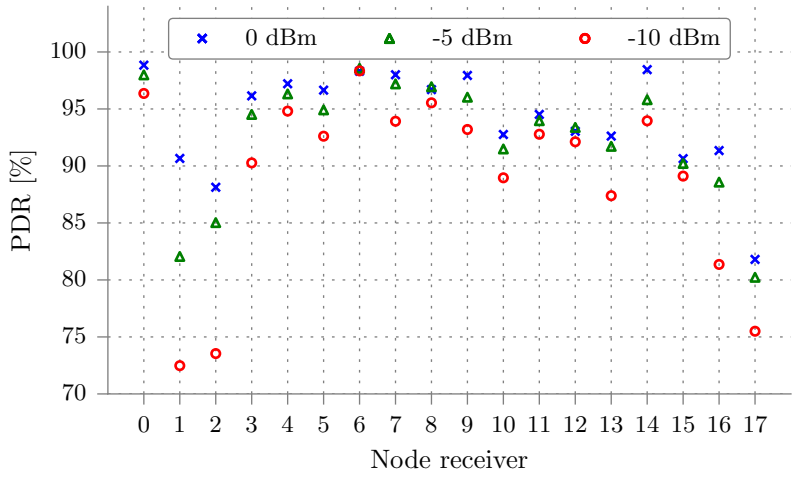

Figure 5.26: Average total PDR [%] per individual node, for the naval ship's engine room environment.

5.7 Application of methodology in a similar non-marine scenario: A WSN deployment in a data centre

5.7.1 Introduction

An important aspect of the management and control of modern data centres is cooling and energy optimisation. Airflow and temperature measurements are key components for modelling and predicting environmental changes and cooling demands. For this, a WSN can facilitate the sensor deployment and data collection in a changing environment. However, these scenarios present challenging characteristics that make it difficult to predict network behaviour and therefore make network planning and deployment difficult. Some of these characteristics are common to the other scenarios studied in this work, i.e. large amounts of metal surfaces, wiring, and machinery that can produce electrical noise such as the servers and AC units.

In this section, a final validation of the WSN connectivity analysis methodology, described in the preceding sections, to resolve connectivity problems in a completely different application environment is reported. The application was a 17-month duration deployment of a WSN in a data centre, as part of the GENiC EU project [178]. The original deployment was done by the GENIC researchers (without any involvement of the author of this thesis) and with no prior connectivity assessment in the environment or planning, unforeseen network connectivity problems emerged. The research reported in this section therefore deals with the study of the data collected from these sensors, as well as the execution of wireless connectivity experiments with Trident, with the objective of finding and correcting the node communication problems. As well as being an interesting research problem in itself, this will demonstrate the broader applicability and adaptability of the WSN characterisation methodology described in the previous sections as well as its use for WSN problem-solving.

5.7.2 Deployment description

5.7.2.1 Deployment scenario

The deployment was done in a typical medium-size university data centre room that houses large communications equipment for the campus. The layout of the windowless room, with a floor area of 34 m^2 (7.3 m x 4.7 m), is depicted in Fig. 5.27. There are 8 server racks in the room, arranged in two rows, forming one cold aisle in the center of the room and two hot aisles between the rear of the racks and the walls. Cooling is provided by a Computer Room Air Conditioning (CRAC) unit from the adjacent room via underfloor vents through four perforated floor tiles in front of the racks of the cold aisle. A backup air conditioning (AC) unit is placed in the server room itself. The power is fed to the cabinets from four bus bars, which run above the two rows of cabinets, as shown in Fig. 5.28a.

5.7.2.2 Hardware and software

The deployment consists of 30 TelosB nodes, including a sink node with a serial connection to a PC gateway, that measure humidity and temperature. To measure the air velocity, each node incorporates a compact airflow probe sensor, either the EE575-V2B1 [179] or the newer EE671-V2XDKD [180]. To interconnect the airflow sensors with the nodes, a custom PCB was designed by the GENiC researchers, allowing nodes to switch on and off the sensors to minimize power consumption, and adapting the airflow voltage readings to the ADC voltage reference of the TelosB nodes. Moreover, due to the voltage requirements of the airflow sensor, an external pack of 12 AA batteries was added to supply enough power to the sensor and the mentioned PCB, while the TelosB was powered by the standard 2AA battery pack. The nodes also report the battery voltage of the node and the airflow battery pack, RSSI, and LQI for offline link analysis.

The TelosB nodes run a custom Contiki application that measures and reports the parameters mentioned. The data rate of the application is configurable and set to 1 message every 5 minutes by default. Due to the room size, multihop communication was discarded, and the nodes simply formed a one-hop network, using the reliable unicast (runicast) primitive of Contiki's Rime stack [181] to

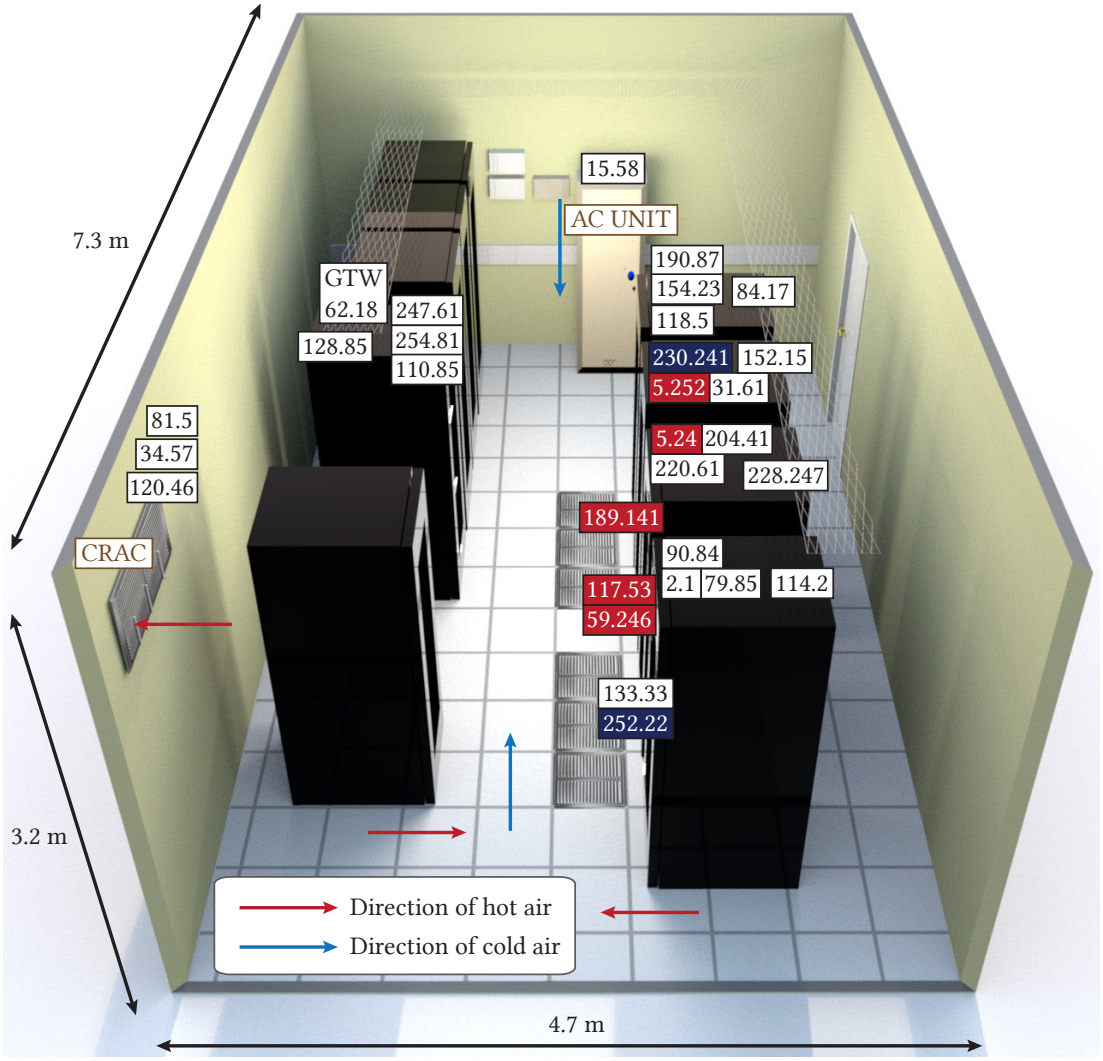

Figure 5.27: Sensor nodes and gateway distribution in the room. Problematic nodes marked with red and blue.

report the measured information to a sink node. To reduce power consumption, the nodes only switch on the radio to transmit the packet every reporting period and retransmit it up to four times when necessary. The sink keeps the radio always on, as it is USB-powered. To avoid collisions, nodes employ a CSMA MAC layer and also randomize the exact transmission time within the last four seconds of the reporting period. Furthermore, nodes transmit at the maximum power (0 dBm) and use channel 26 to avoid cross-technology interference.

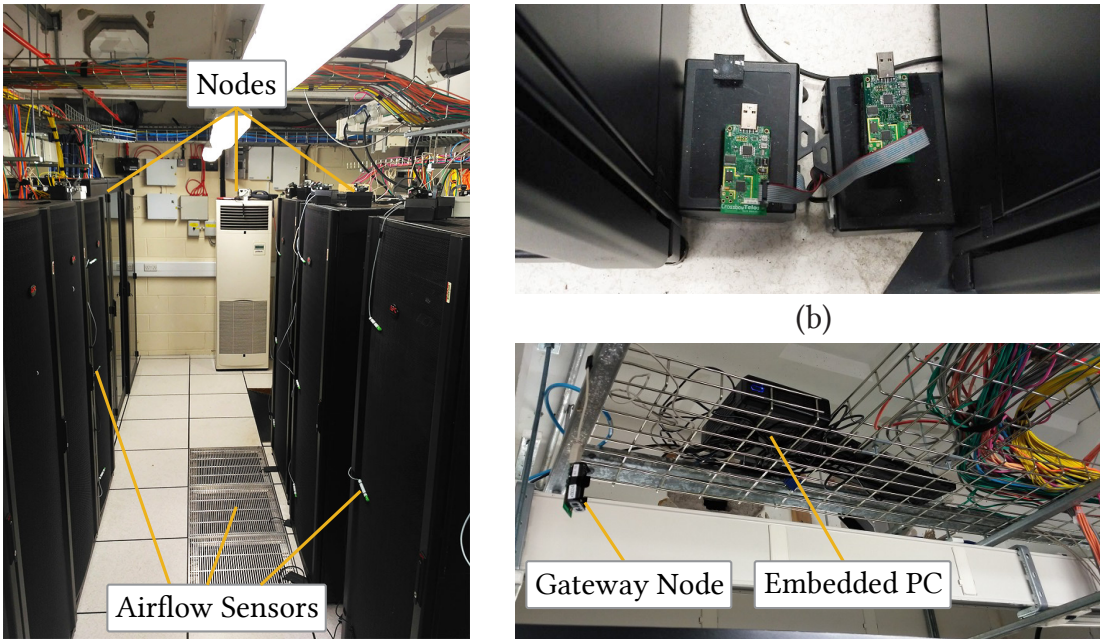

Figure 5.28: Node and airflow sensor placement.

5.7.2.3 Node deployment

The distribution of the nodes can be seen in Fig. 5.27. The MAC addresses in the figure indicate the position of the TelosB nodes, which were placed either on top of the racks or in between them (Fig. 5.28b), except the nodes monitoring the CRAC unit and the sink (Fig. 5.28c), which were placed on top of the metal bars. The airflow sensors, which are connected to the TelosB by cables, are fixed with cable ties at rack inlet and outlet, below the tiles in front of the racks and at the CRAC unit, as shown in Fig. 5.28a.

5.7.3 Analysis of the deployment

5.7.3.1 Overview

Fig. 5.29 shows the PDR for all the nodes during the 17 months of the duration of the deployment, from October 23rd 2014 to March 23rd 2016, split in three main periods:

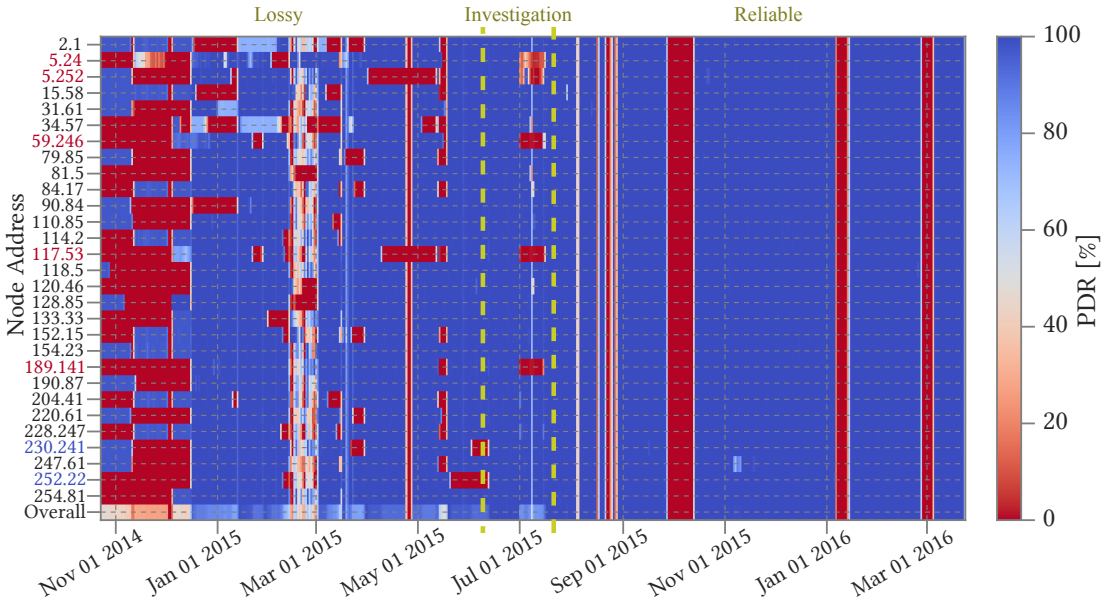

Figure 5.29: Overall PDR per node per day during the complete life of the deployment.

1. From October 23rd 2014 to June 12th 2015 – Lossy: The network was installed in different phases, including firmware and application gateway updates. This, along with battery replacements and hardware updates, produced an expected highly unreliable period.

2. From June 12th to July 16th 2015 – Investigation: Several nodes were systematically failing to communicate with the sink, without any apparent hardware or software issue. This investigation is described in detail below.

3. From July 17th to March 23rd 2016 – Reliable: After the investigation period, the network problems were fixed, yielding an overall PDR of 99.92%.

5.7.3.2 Communication issues: investigation and correction

The period where the nodes were having unknown problems is divided in two investigations. The packets received from the affected nodes during the whole period can be seen in Fig. 5.30, with the blue line marking the first investigation and the red line the second. The nodes involved are also marked in red and blue

respectively in the deployment distribution (Fig. 5.27) and the overall deployment PDR (Fig. 5.29) respectively.

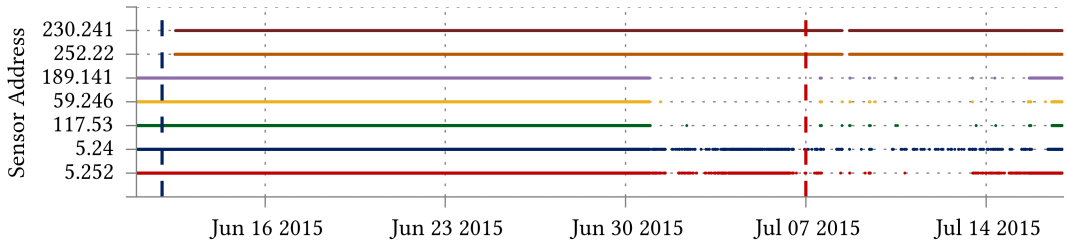

Figure 5.30: Packets received from problematic nodes during the period with problems reported.

The first investigation was done due to nodes 230.241 and 252.22 not reporting data since the beginning of June 2015, as can be seen in Fig. 5.30. A *short* 20 min. experiment was run using Trident in all the nodes to assess the connectivity, during which each node sent 40 packets, at a rate of 1 packet/s. Looking at the data from this experiment, all 29 nodes had perfect connectivity. Both problematic nodes had a strong RSSI/LQI: 230.241 was -44 dBm/107 and 252.22 was -56 dBm/106. The noise floor for both was low, at -93 dBm. After reprogramming the nodes with the application and slightly repositioning them closer to the rack and facing the sink, the whole network was reporting correctly with a 99.96%. This suggested that just the small repositioning produced when the nodes were programmed with Trident and then reprogrammed later changed the multipath conditions that most likely were causing the issue. Even nodes that were close to the failing nodes were reporting correctly before. This is consistent with the experiments described in the ship's engine room emulator in Section 5.5, where two nodes close together with high RSSI yielded a very different PDR performance.

On July 7th 2015, a second investigation was necessary due to intermittent or total failure in the nodes marked red in the Figures 5.27 and 5.29, from July 1st 2015. Looking at the previous results from the *short* experiment, the nodes in red recorded the highest noise floor. A *long* test was run then on July 8th 2015 for six hours, equivalent to 12 consecutive rounds with the same configuration as the *short* one, to account for the variations in time induced by the environment on the

collected metrics. All but the group of nodes reported in Table 5.11 were exposed to low noise floor levels, below -90 dBm, for both experiments. When looking at the failing nodes' data collected from the gateway on the day of the failure, in Fig. 5.31 it can be seen that overheating affected the data center causing a temperature increase to 44^oC, probably due to some failure in the AC systems. This must have triggered the auxiliary AC unit, as the temperature went down quickly. However, the failing nodes stopped reporting fully or intermittently and they did not recover after the event, as the noise floor value kept high. The main issue with this was the CCA (Clear Channel Assessment) threshold, which was configured in the application at -90 dBm, lower than the noise floor of those nodes. As the channel is sensed by the node before sending a packet, due to the inherent noise being higher than the configured CCA, the node was never sending the packet, as it was confusing this noise with an interfering packet being sent from another node. The solution was to change this CCA threshold to a higher value, thereby allowing the node to ignore the noise and send the packet. After this, the network operated reliably with near 100% for the remaining life of the deployment, except for the moments when the application gateway was down.

5.7.4 Conclusion

Although the deployment studied in this section presented some similarities with the previous scenarios, such as high amount of metal and wiring, it also had some differences such as the type of machinery running (computer servers and AC units) which probably played a role in the noise floor problems encountered. This machinery could have switching circuitry around 2.4 GHz, causing this high noise floor, unlike the large engines found in the other scenarios which switch at typical low frequencies in the 0-120 Hz. However, it is emphasized here that assessing the characteristics of the links in the environment where the WSN must be deployed is key for supporting the deployment and informing the selection of communication parameters that make the protocols and the application apt for the target environment. This shows the wider applicability of the connectivity analysis methodology and also its impact as a problem-solving tool in real-world applications.

Table 5.11: Noise floor and RSSI of problematic nodes.

	Short		Long	
Node address	**Noise [dBm]**	**RSSI [dBm]**	**Noise [dBm]**	**RSSI [dBm]**
189.141	-84	-51	-84	-59
117.53	-85	-57	-85	-57
5.252	-87	-48	-85	-59
59.246	-84	-43	-81	-52
5.24	-88	-48	-84	-49
220.61	-88	-48	-89	-48
133.33	-88	-45	-89	-46
228.247	-90	-45	-90	-47
152.15	-90	-48	-91	-48

The research presented in this section led to a co-authored publication as a third author. The first three authors have agreed that their contributions to the work should be regarded as equal, while the last three were granted honorary authorship.

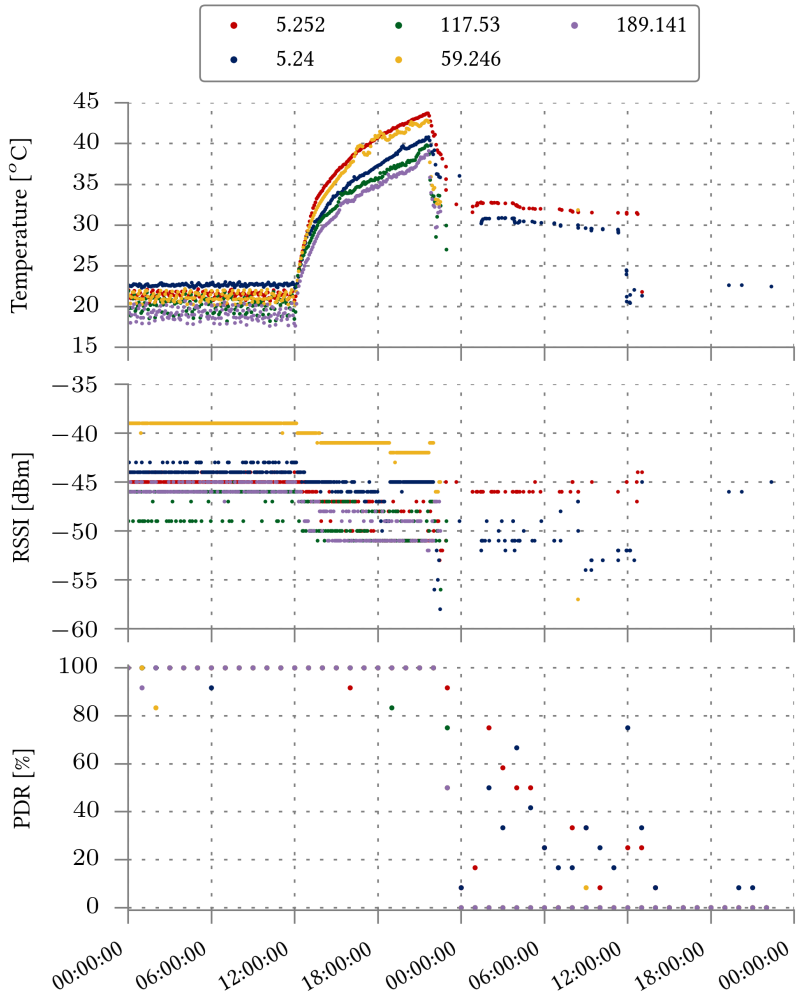

Figure 5.31: Temperature, RSSI, and PDR of the failing nodes during June 30 and July 1, 2015.

5.8 Discussion

5.8.1 Advances to the state of the art

The literature review has shown that wireless communications are possible in all-metal marine environments such as on board ships, even between adjacent rooms and decks separated by watertight doors due to signal leakage through bulkhead seals between compartments. However, the nature of the environment makes it sensitive to multipath propagation and electromagnetic noise, which can cause signal degradation even at short distances. This highlights the necessity to perform a practical study in different environments to characterise and better understand the wireless performance, with a focus on the physical layer which gives an accurate view of the performance by removing the bias of the upper layer protocols.

The methodology described in this chapter provides a framework for these studies by defining structured multi-variable experiments and a systematic analysis of the results, giving a global network view, as well as individual node performance and link quality. This new framework consists of current state-of-the-art physical layer WSN experimental methodologies combined with standard design of experiments and new added representations of the collected metrics, i.e. 3D node-to-node PDR plots and link asymmetry heatmaps, as well as selected ones from the literature such as link quality classification. This provides a tool for engineers and researchers to assist the design and deployment of WSN in harsh environments. The 3D node-to-node PDR representation is a novel and very useful way of representing the data, as it allows quick visualisation in a single plot of the problematic areas in all the links of a deployment. This representation could be further improved by assigning colours to each of the probes depending on their PDR percentage, which would highlight the problems more clearly.

The methodology presented has been validated in three different metal scenarios with increasing complexity. The first one composed of three freight containers, creating an indoors-outdoors multi-chamber metal environment, accounting for the effects of node position and orientation, door openings, and transmission power. The second one consisting of a large engine room emulator containing

a ship's engine, several generators and large amounts of metal piping, ducting, and gantries, where the effects of running machinery are tested. The third one was performed in a real naval ship's engine room and its adjacent compartment, accounting for the opening/closing of the waterproof door between the rooms as well as the switching of the machinery. The collected data and analysis contributes to the understanding of the performance on these complex scenarios, to help push forward the use of WSN as a low-cost alternative to wired networks.

After the first tests, the experiment design changed to focus on the variables that made the most impact on the PDR, i.e., the node placement, transmission power, and door openings, while discarding node height and antenna orientation. The most notable discovery was the large performance difference between close nodes in some specific placements, where a node inside a motor was performing much better than another one placed on top outside. Future research could look into these unexpected behaviours in more detail by experimenting with a large number of nodes together in that specific area. Moreover, another line of research can focus on comparing this established WSN technology with newer ones, such as LoRa or ultrawideband, which might have a better multipath immunity but are not yet fully integrated into the WSN paradigm.

Finally, a study performed in a data centre for a related research project highlighted the need for these methodologies to assess the link performance of difficult scenarios with metal and machinery before the deployment, as multipath fading and switching noise can cause unexpected communication problems that can by alleviated with node relocation or application/protocol reconfiguration.

5.8.2 Engineering & scientific merit

The studies performed have shown a high overall connectivity for all the scenarios, with more than 80% PDR even in the worst conditions with a network of nodes in different metallic chambers with the doors closed and low transmission power, and at least one node was found to be placed in an optimal position to be acting as a sink with no dead links to the rest of the nodes. Moreover, electromagnetic noise from ship engines and generators only showed a minor effect on the communications. With the increasing complexity of every scenario, i.e. larger amount

of piping and metal fixtures, an increase is also found in the number of outliers when correlating the RSSI with the PDR and LQI. This is different from what is found in the literature for different scenarios such as open fields or buildings, which have a well defined transition zone. In the naval ship scenario, as it is the most complex of the three, the transition zone is wide enough to cover most of the area, making the prediction of the PDR in a node very difficult. Therefore, a path-loss model based on distance and RSSI as it is usually done in the literature would not have any meaningful capabilities of predicting the PDR of each node in these environments. This makes it necessary instead to perform a practical study of each specific target scenario, including a connectivity assessment following the methodology demonstrated in this chapter, to identify areas of difficult connectivity and optimal sink location.

Despite the unpredictability and unreliability in the communications that has been shown in the more complex scenarios, as the PDR remains high the loss of packets can be mitigated with retransmissions and error correction codes in the upper layer protocols, making a WSN a viable solution for these environments for non-critical data.

Chapter 6

Validation

6.1 Introduction

The work presented in the preceding chapters developed systems integration and packaging methodologies for two structural and machinery health monitoring sensor modules, associated firmware and software, and an overarching framework for deployment design and for in-situ wireless network link quality analysis. All of this was focused on deployment and reliable operation of health monitoring wireless sensing networks in high metal-content marine environments. The final stages of the research were, first, validation using accelerated stress testing that the modules themselves would be reliable for long-term deployment in the marine environment and, second, verification that the modules could be successfully deployed in a variety of machinery and structural health monitoring applications.

6.2 Validation tasks

The two main tasks for validating the work presented in the previous chapters are:

- To select and carry out application-focused accelerated stress tests to verify that the systems integration, packaging, and encapsulation methodologies developed through the research are sufficient to ensure reliability in the marine environment.

- To verify that the methodologies for WSN deployment and data collection would allow operation in real-world marine environment health monitoring scenarios.

6.3 Accelerated stress testing

6.3.1 Introduction

This section presents the accelerated reliability stress testing performed in the laboratory on both the inductive and health monitoring sensor modules. This involved vibration, humidity/temperature, and salt atmosphere exposure testing to ensure their reliability in harsh marine conditions.

6.3.2 Vibration reliability test

6.3.2.1 Test description

The health monitoring and inductive modules were both tested for vibration reliability following Lloyd's Test Specification Number 1 [182], an industry standard for performance and environmental testing of electronic systems used in marine applications, based on several IEC standards. This specification defines two different vibration tests, one with lower acceleration (Vibration test 1) and another one with higher (Vibration test 2). The modules are to be mounted on the vibration table in their normal orientation with respect to the vertical, corresponding to how they would be installed in the real environment.

Vibration test 1 The first test is divided in two parts: the first one has to be carried out using a sine sweep with varying frequency, displacement, and acceleration in accordance with Table 6.1, to detect resonance frequencies in the module.

The second part of the test consists of an endurance test of 90 minutes at 30 Hz, with an acceleration of ± 0.7 g. This is a relevant test to assess the reliability of these modules, as they will be mounted on vibrating machinery or

Frequency range	Displacement	Acceleration
2^{+3}_{-0} – 13.2 Hz	±1.0 mm	
13.2 – 100 Hz		±0.7 g

Table 6.1: Test specification standard 1

swaying structures and therefore they will be subject to low frequency vibration for long periods of time.

Vibration test 2 The second vibration test is similar to the first one, with a varying sine sweep following the profile in Table 6.2, and an endurance test.

The endurance test is performed for 90 min at 30 Hz like in the test 1, but with an acceleration of ±4 g.

Frequency range	Displacement	Acceleration
2^{+3}_{-0} – 25 Hz	±1.6 mm	
25 – 100 Hz		±4.0 g

Table 6.2: Test specification standard 2

Figure 6.1: Vibration test setup for the health monitoring module (encapsulated).

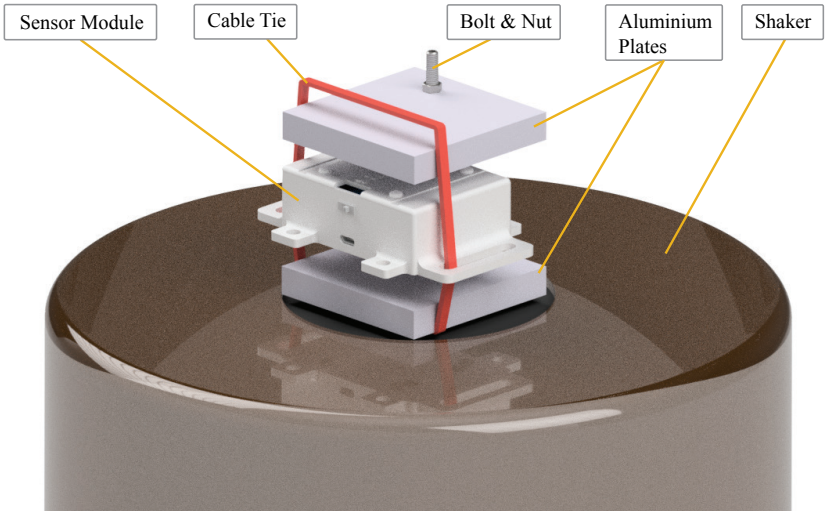

Figure 6.2: Diagram of the vibration test setup.

6.3.2.2 Health monitoring module testing

Fig. 6.1 shows the setup test for the health monitoring module on the vibration platform (an electrodynamic shaker, B&K Model V455 [183]). The sensor module was placed between two aluminium plates, the bottom one attached with screws to the vibration platform and the upper one on top of the module. Both aluminium plates were pressed against the box by a pass-through bolt and nut, and further fastened with a cable tie, as shown in Fig. 6.2. This mounting method was chosen due to it being previously used in vibration tests (unpublished) by other researchers in Nimbus and now used as common internal practice. General practice for clamping to a shaker is that it should be as rigid as possible to minimise stray secondary vibrations and resonances. This method performs that function well for odd-shaped test specimens that cannot be bolted down directly to the mounting plate. It is also similar to the mounting methods used in the field deployments described below. One sample of the module was tested, as only a small number of samples were available and the majority were being used for the deployments and could not be risked.

The sweep test was run over 1 min, with a sweep rate of 5 oct/min, at 0.7 g (Vibration test 1) and 4 g (Vibration test 2). Because the encapsulated module forms a single block, no resonance frequencies were expected to be found. How-

ever, as shown in Fig. 6.3, in both Vibration test 1 and 2 a resonance appeared during the sweep at around 50-60 Hz in the x-y axes. As it is unlikely to be coming from the sensor module, this could be either from the vibration table itself, i.e. a loose component, or from the anchoring of the vibration table to the floor. This was confirmed in further tests with the inductive module and an external accelerometer, presented in the next Section 6.3.2.3.

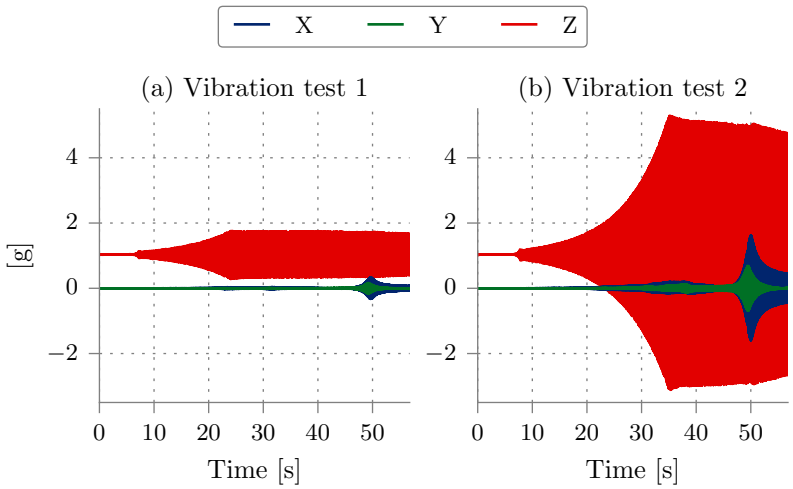

Figure 6.3: Vibration test frequency sweeps for the health monitoring module.

After performing the endurance tests for the vibration 1 and 2 specifications, the module was still fully functional, with data being collected periodically every 15 min. during the tests and afterwards. Fig. 6.4 shows the accelerometer data and its calculated PSD, collected during the higher vibration endurance test (Vibration test 2), where it can be seen that the accelerometer successfully tracked the shaker vibration profile.

6.3.2.3 Inductive module testing

Fig. 6.5 shows the setup of the inductive module in the vibration platform, with an external, battery-powered accelerometer placed on top of the module. The module was fixed in the same way as the health monitoring module in the previous section, with the external accelerometer fixed with polyimide tape. As in

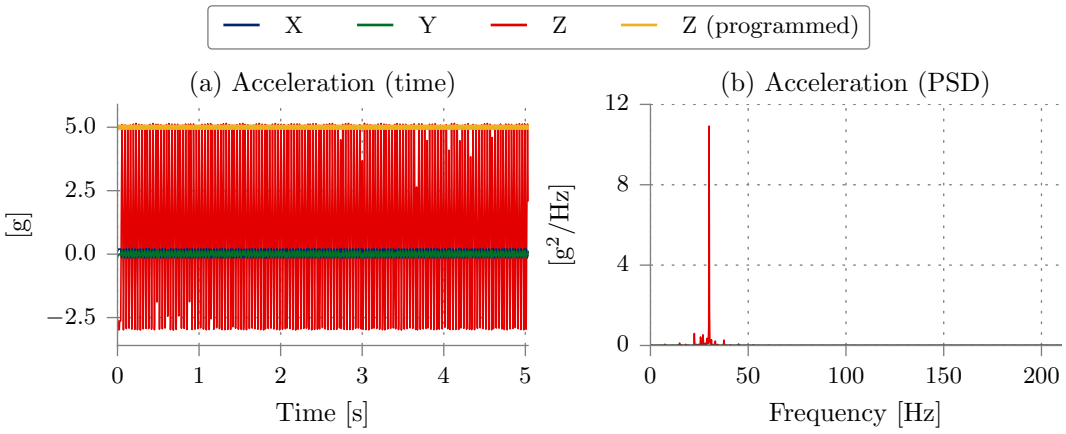

Figure 6.4: Vibration endurance test 2 at 30 Hz for the health monitoring module.

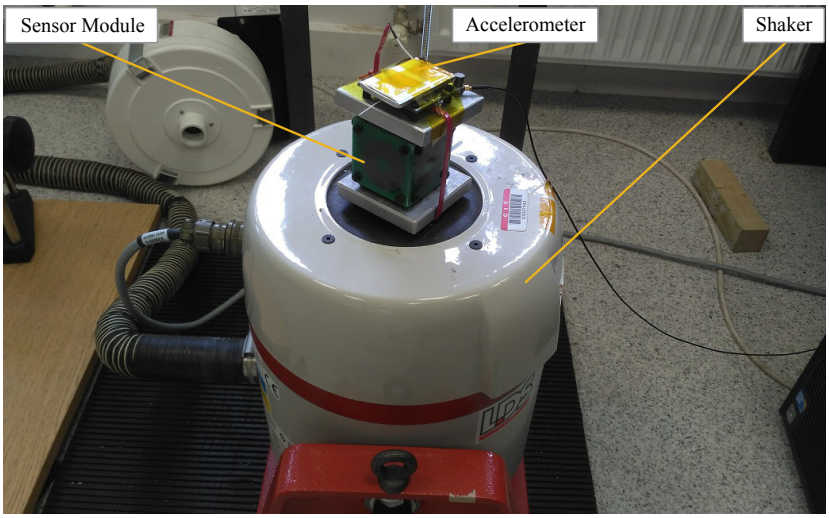

Figure 6.5: Vibration test setup for the inductive module (encapsulated).

the previous tests done in the health monitoring module, a similar resonance frequency was found at around 50-60 Hz in x-y axes (Fig. 6.6). A sweep test was repeated with only the accelerometer board mounted on top of the top aluminium plate, obtaining a similar result but with less amplitude (Fig 6.7), confirming that the resonance frequency is due to the vibration platform setup and not the sensor modules.

The Vibration test 1 and 2 endurance tests were also successfully performed with the same parameters used for the health monitoring module (90 min at

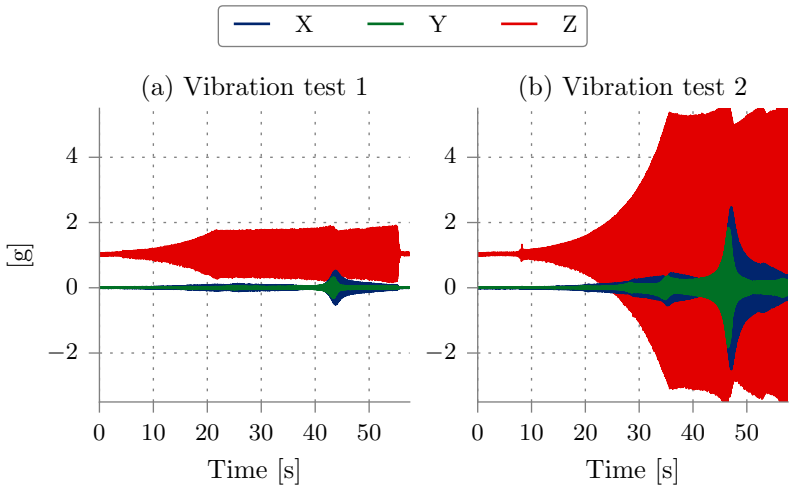

Figure 6.6: Vibration test frequency sweeps for the inductive module.

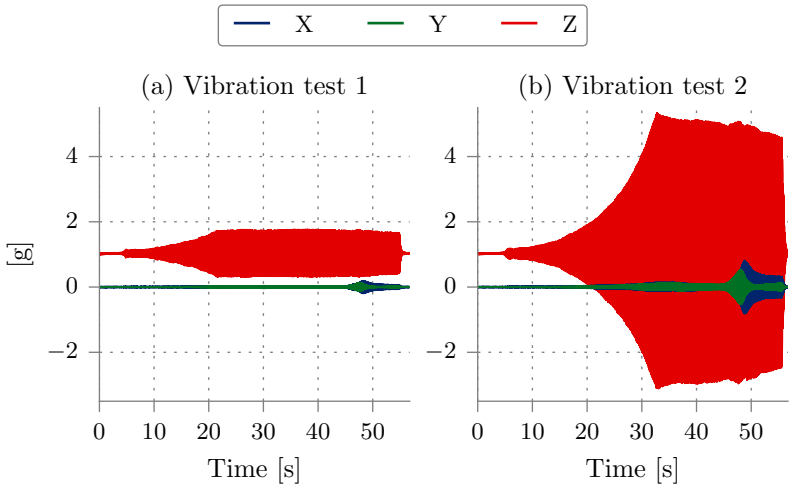

Figure 6.7: Vibration test frequency sweeps with external accelerometer only.

30 Hz), testing the operation of the module every 15 min by wirelessly reading the values of the sensing coils. Fig. 6.8 shows the external accelerometer data and its calculated PSD, collected during the higher vibration endurance test (Vibration test 2).

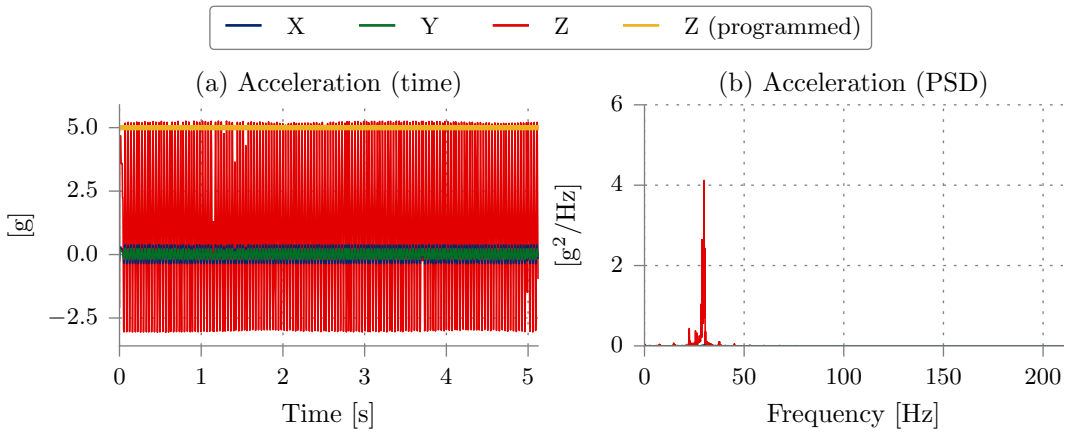

Figure 6.8: Vibration endurance test 2 at 30 Hz for the inductive module.

6.3.3 Humidity/temperature reliability test

The Lloyd's Test Specification Number 1 [182] for marine electronics followed in the previous section also defines standard tests for humidity/temperature endurance testing: cyclic and steady. Both modules were tested simultaneously following this specification using a WEISS WKL 100 climate test chamber [184]. The temperature and humidity were recorded every minute with the health monitoring module.

6.3.3.1 Humidity cyclic test

The test parameters for the cyclic test according to the reference specification are:

- Temperature: 55 ^oC.
- Humidity: 95%.
- Duration: 2 cycles (12+12) hours' duration.

The cyclic test in the reference defines a controlled temperature starting at 20^oC, ramping up to 55^oC, keeping it steady for 12 hours and then cooling back down to 20^oC for 8 hours. The humidity is kept between 90-100% during the high temperature period and 80-100% during the cooldown. After this, the cycle is repeated again starting from a low humidity (0-20%) and 20^oC temperature. Fig. 6.9 shows this T-H test profile programmed in the climatic chamber (green colour).

Although the standard defines interval functional testing of the specimen between the cycles and at the end, this was not necessary for the two modules, due to the memory in the health monitoring module and the wireless data transmission capabilities of both modules; this allowed continuous functionality monitoring of the modules during the tests. Fig. 6.9 shows the recorded humidity and temperature in memory by the health monitoring module during the cycles, where it can be seen that the module successfully tracked the T-H profile. During the cooldown period of the cycle it can be seen that the humidity falls below the set specification, due to the chamber not being able to keep such high humidity

with low temperature, as relative humidity is dependent on the temperature. The inductive module was wirelessly tested every 24 hours, reading the values of the four coils to verify that the microcontroller and radio were operating correctly. Both modules continued to function without any deterioration in parameters or reliability for the full duration of the tests.

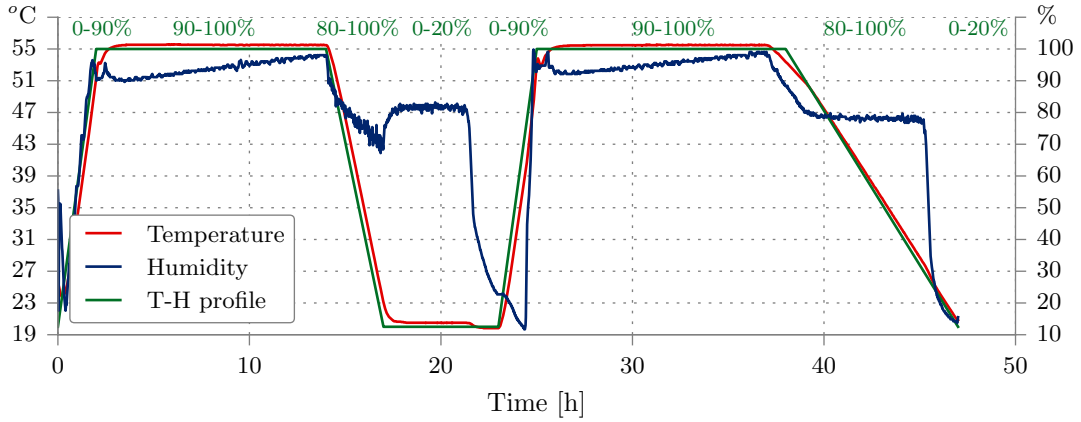

Figure 6.9: Temperature and relative humidity recorded by the health monitoring module inside the humidity chamber during the cycle testing.

6.3.3.2 Humidity steady test

As with vibration testing, long exposure is an important test to assess the reliability of the modules. The steady state test for humidity/temperature is defined with an initial 20^oc temperature, raised to the specified maximum operating temperature (in this case 55^oC, as in the previous test) and maximum relative humidity (100%). These conditions have to be maintained for a period of at least 96 hours, followed by a reduction in temperature back to 20^oC within a period of between one and two hours.

The humidity and temperature collected by the health monitoring module during the duration of the test is shown in Fig. 6.10, as well as the programmed T-H profile, demonstrating that it not only survived the test but also successfully tracked the T-H profile. The values of the sensing coils of the inductive module were also successfully read every 24 h. During and after the completion of the test, both modules were fully functional and there was no visible deterioration.

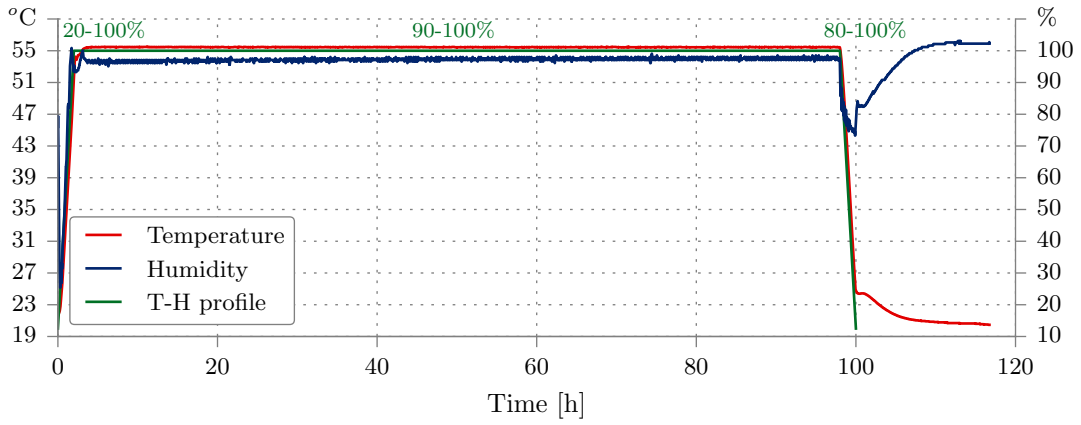

Figure 6.10: Temperature and relative humidity recorded by the health monitoring module inside the humidity chamber during the steady testing.

6.3.4 Salt mist test

The high concentration of salt in the ambient at sea can affect the reliability and durability of electronics due to the corrosion affecting the components and PCB traces during long exposure to salt. As the nodes are developed to be used in marine environments, a salt mist test was performed on both sensor modules (inductive and health monitoring) in a Heraeus HSN 400 salt spray test chamber.

The standard used for this was the MIL-STD-883 test method 1009.8 [185], designed as an accelerated laboratory corrosion test simulating the effects of seacoast atmosphere on devices and package elements. This standard defines the setup conditions of an exposure chamber that uses a salt fog to maintain the necessary conditions. The salt fog should be maintained at 35 ^{o}C, with a salt concentration between 0.5 to 3.0% by weight in deionized or distilled water, and a pH between 6.5 and 7.2. The test was programmed to run for 96 h continuously (Test condition C).

The modules were left in the testing facility and were not accessible, therefore the performance of the module could not be assessed periodically but the health monitoring module was programmed to record temperature and humidity every 15 min. The result is shown in Fig. 6.11. It can be seen on the figure that a sudden dip in temperature occurred on the second day of the test. This was due

to a failure in the deionised water system that feeds the salt chamber and which caused a shut down of the system. Although the test had to be stopped due to the system failure, it shows that the module successfully detected the failure, validating its functionality as a machine health-monitor. After this, the test was restarted from the beginning.

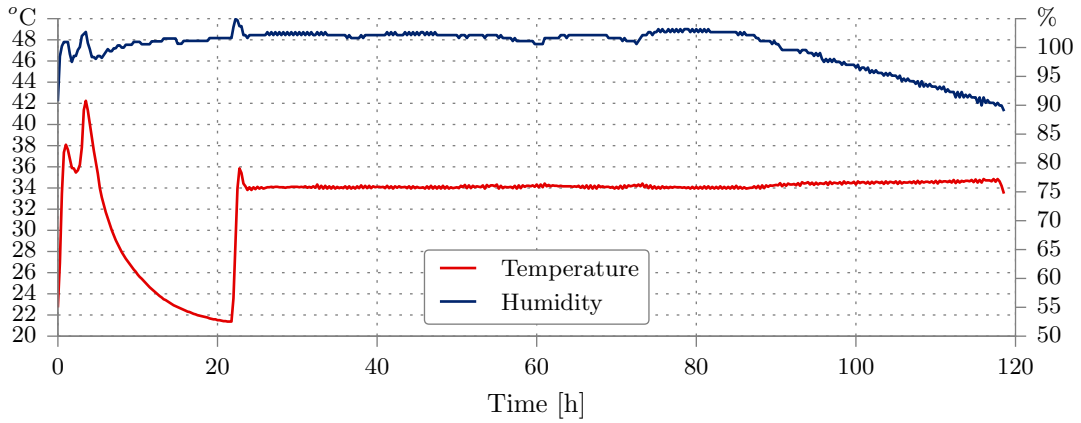

Figure 6.11: Temperature and relative humidity recorded by the health monitoring module during the salt mist test.

After the test, the health monitoring module was cleaned with water to remove the salt traces deposited on the outside of the box. It presented no visible deterioration and was still working correctly. The only exposed components, i.e. the microUSB connector, antenna, and filter caps, were not affected by the salt mist.

For the inductive module however, as the electronics PCB contains more exposed components that are not robust or waterproof and are not protected by a box, the salt mist had a heavy visible effect, causing corrosion. Fig. 6.12 shows the electronics PCB side after the exposure. The microUSB was severely damaged, as were the buttons. Nonetheless, a simple test collecting data wirelessly from the sensing coils showed that the module was still functional, and humidity/temperature could be measured as well as the sensor coils. Shortly after that, the module ran out of battery and it had to be recharged. Due to the damage of the connector, when attempting to recharge the module a short-circuit destroyed

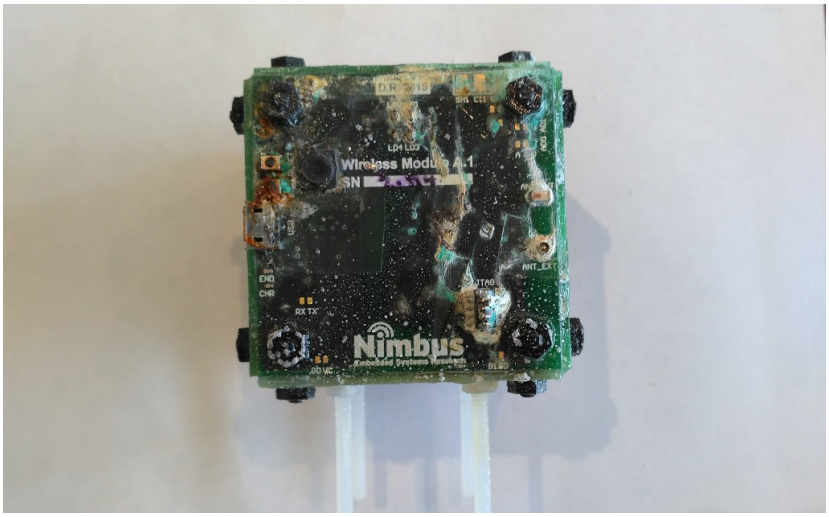

Figure 6.12: Inductive module after accelerated salt mist exposure.

the electronics with no possibility of recovery. When trying to remove the charging cable, the connector was also accidentally ripped off from the PCB, including the pads. This showed that although the module works as a proof-of-concept, a newer version would need to include the same waterproof microUSB as the one used in the health monitoring module.

6.4 Validation in real-world module deployments

6.4.1 Introduction

To demonstrate the health monitoring module's ability to collect data and survive in outdoors marine and harsh environments, several long and short deployments in real-world scenarios were performed.

6.4.2 Module testing in a RIB

The first real-world test to verify the functionality of the health monitoring module was performed at sea on a rigid-inflatable boat (RIB), Fig. 6.13. An encapsulated module was attached with cable ties to the steering system that connects both engines of the RIB, as shown in Fig. 6.14. The RIB was at sea for approximately 5 hours and 30 min. As the RIB was used by a group of marine biologists to collect samples, during the trip there were periods of travelling and periods were the boat was at sea completely still. Accelerometer, audio, temperature, and humidity were sampled and saved every 5 min., with a duration of 5 s for every accelerometer and audio sample.

Figure 6.13: RIB used for the testing.

Figure 6.14: Health monitoring module testing installed on the steering system connected to the RIB engines.

Fig. 6.15 shows accelerometer and audio data collected during one of the still periods. Although the RIB was not moving, the accelerometer shows some high peaks up to 4 g induced by wave slap. Those large peaks of the wave slaps are produced every 4.5 s approximately, which can also be noticed in the audio data plot and can even be heard if the audio is played. The PSD shows also a low vibration at around 23 Hz, most likely due to the engines being on despite the RIB remaining still.

The data collected for one of the periods when the RIB was travelling are shown in Fig. 6.16. A strong acceleration data can be seen around 60 Hz of up to 1 g, especially for the x-axis, corresponding to the vibration of the engines. Another peak is seen around 50 Hz in the z-axis, with strong components spread around the 40-60 Hz band, reaching up to 2.2 g. The audio also showed a much stronger amplitude than when the RIB was still, nearly to the point of saturating the microphone.

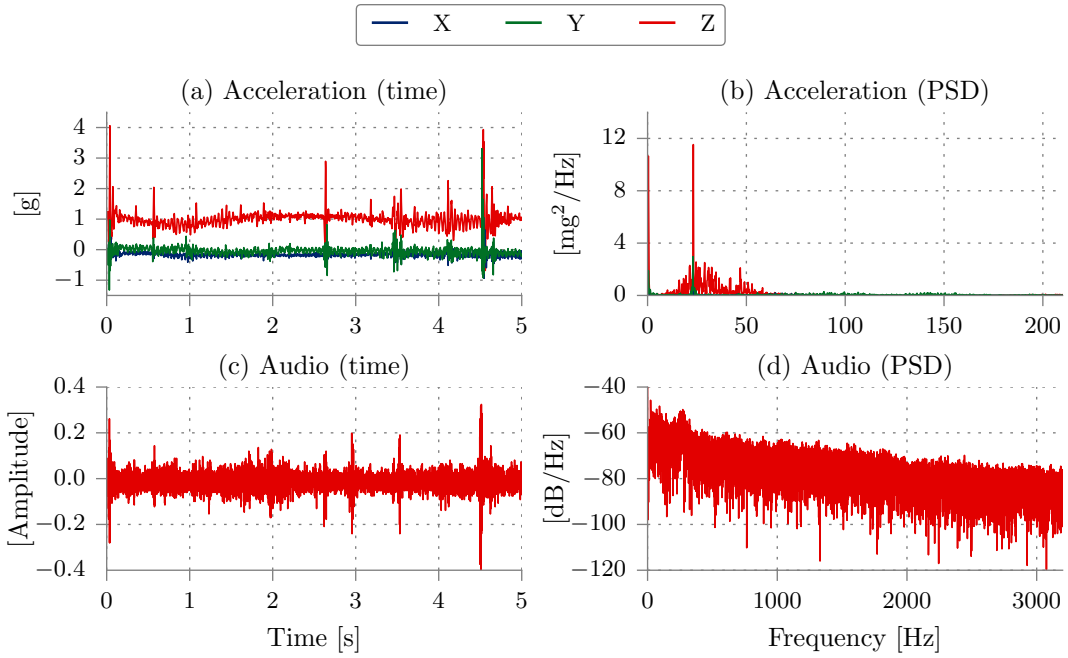

Figure 6.15: Acceleration and audio collected when the RIB was still in the water.

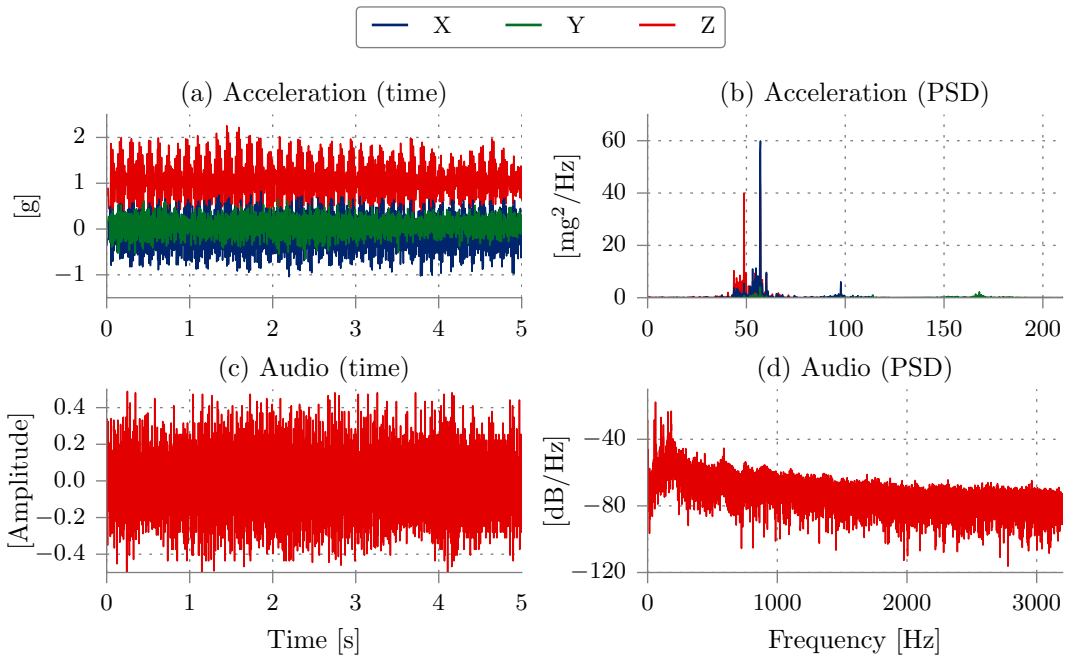

Figure 6.16: Acceleration and audio collected when the RIB was in movement.

Fig. 6.17 shows the temperature and relative humidity collected over the whole rib outing. Overall, the RIB test validated the module performance and reliability in an exposed and demanding application environment.

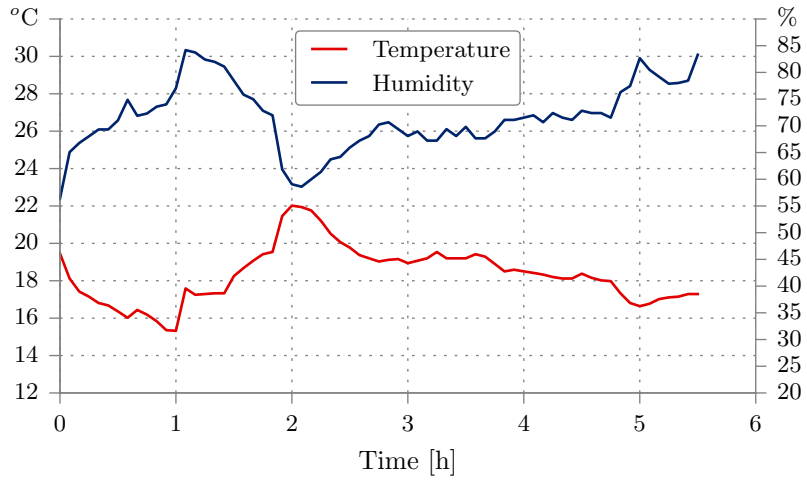

Figure 6.17: Temperature and relative humidity collected during the RIB deployment.

6.4.3 Module testing on a river bridge

River bridges are large outdoor structures, typically of metal and/or concrete, placed in high humidity environments, which makes them an ideal location for testing the health monitoring module. Daly's bridge in Cork City (Fig. 6.18), also known as The "Shakey Bridge", is a wrought iron suspension bridge opened in 1927 and now suffering serious corrosion to the point where its closure is threatened on safety grounds. It is a particularly interesting structure to monitor as it oscillates when even one person walks over it and also in strong winds. One of the health monitoring sensor modules was attached to the frame at the center of the bridge (Fig. 6.19) during the night of the Ophelia post-tropical hurricane that hit Ireland in October 2017. This was the most severe recorded storm of the past decades, with wind gusts reaching 84 knots (155.6 Km/h) in the Cork region. The state of the bridge is evident in the close-up picture of the sensor attached to one of the corroded metal braces of the bridge.

Figure 6.18: Daly's 'shakey' bridge in Cork.

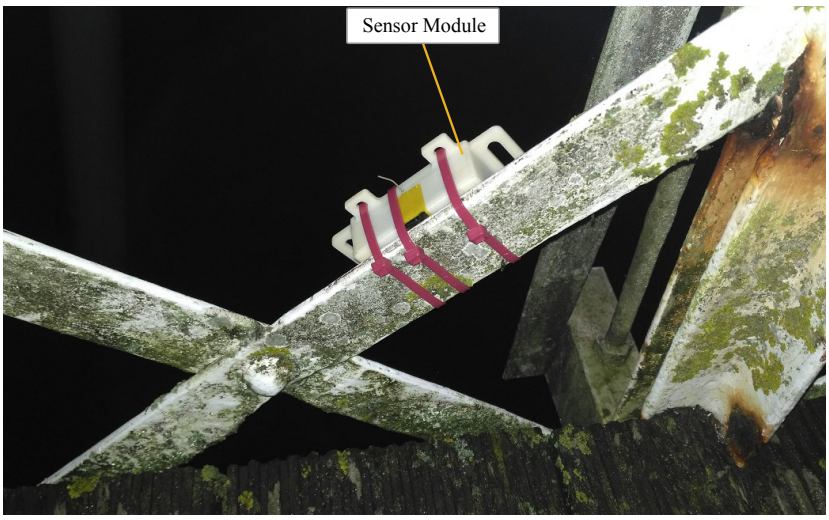

Figure 6.19: Health monitoring module testing installed on a bridge before the storm.

The module recorded temperature/humidity and 5 s of acceleration data every hour during 33 hours, starting at 20:00 on the day before the forecast arrival of the storm. Fig. 6.20 shows the spectrogram of the acceleration in the z-axis over time during the deployment. A high peak can be observed at Hour 15 (11:00), with the highest value around 80 Hz, coinciding with the period when the strength of the storm was also as its highest in Cork City.

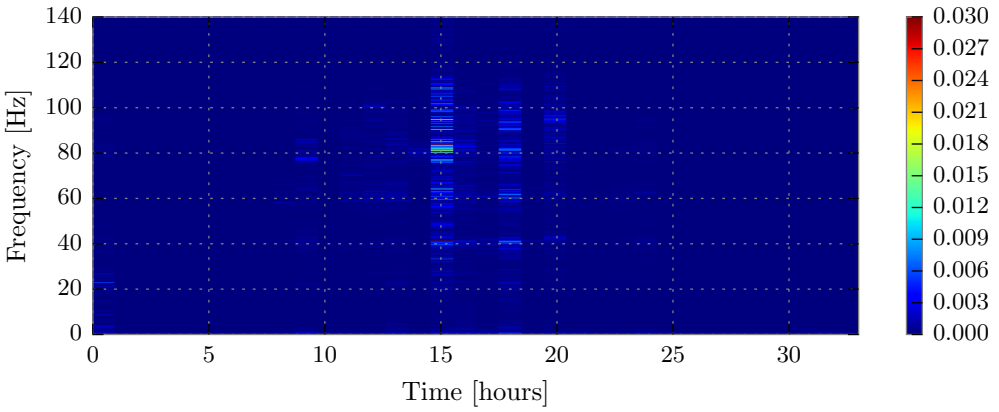

Figure 6.20: Frequency response on the z-axis of the bridge during the Storm Ophelia.

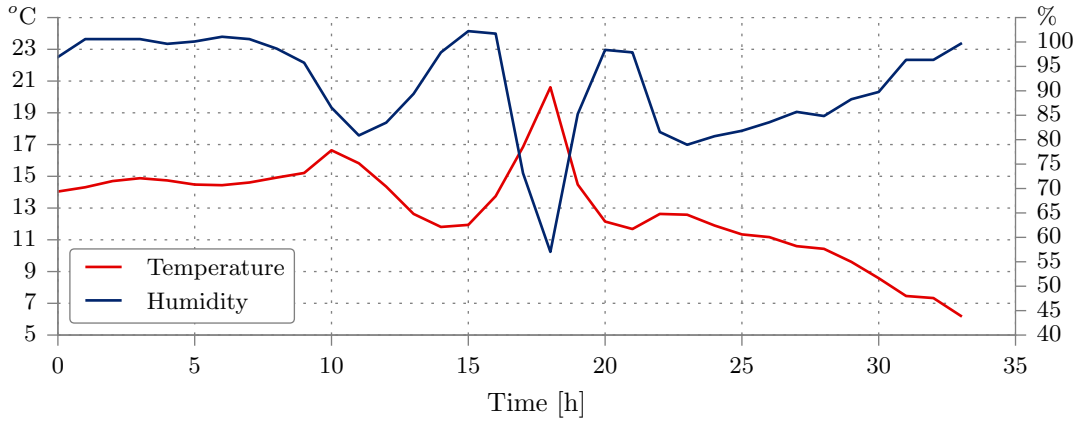

Figure 6.21: Temperature and relative humidity collected on the bridge during the Storm Ophelia.

Fig. 6.21 shows the recorded temperature and humidity. Temperature was stable except for a peak around 14:00 on the day of the storm, corresponding to a brief sunny period, which warmed and dried the sensor, then slowly started declining as night approached. It can be seen how humidity rose slightly above 100% at some points, due to heavy rain which covered the sensor cap. This can produce readings above 100% relative humidity, a phenomenon called supersaturation.

The module was recovered after the experiment, fully functional and with no visible deterioration, showing that it can collect data without interruptions

during very harsh conditions.

6.4.4 Module WSN deployment in a Navy ship

As a final validation, a long-term deployment was done with a network of 5 nodes in the same P60-class INS ship used in the wireless performance experiments described in Chapter 5.6. Four sensors were placed next to several pieces of machinery in the engine room: the water pumps, the main engine, the gearbox, and the boiler. Another sensor was placed in the Machinery Control Room (MCR) adjacent to the engine room. The sensors collected temperature/humidity every hour, and 5 s of audio and accelerometer data every 5 hours, during a typical 16-day patrol voyage. While 4 out of the 5 sensors recorded data during the full duration of the trip, the fifth, however, placed at the boiler, stopped recording at day 12. This could be due to a sensor hardware failure or human error. As the sensor was tested again after the deployment with no issues, it was either a transient hardware fault or an accidental switching off of the sensor module during engine room operations.

Fig. 6.22 to 6.26 shows the recorded temperature/humidity for all the sensor modules for the duration of the deployment, and 6.27 to 6.31 the spectrogram of the acceleration on the z-axis (normal to the surface of the sensors' placement).

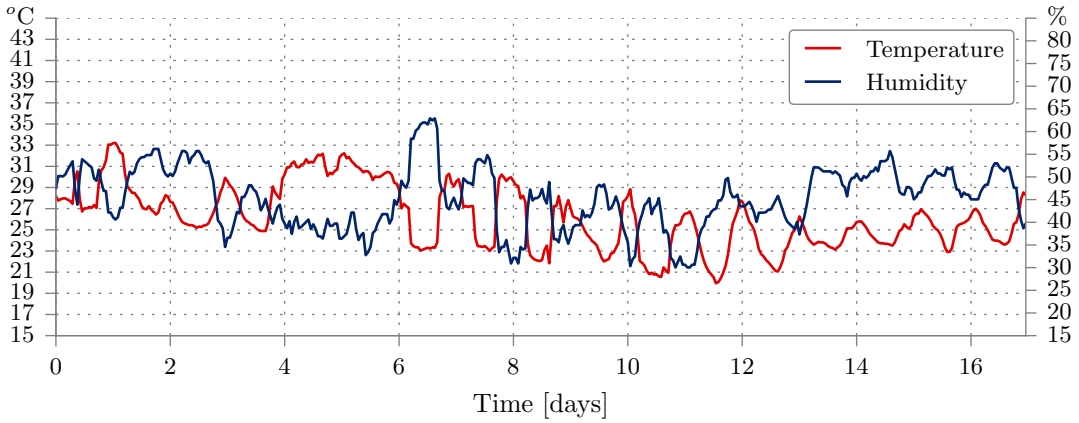

Figure 6.22: Temperature and relative humidity – Pumps.

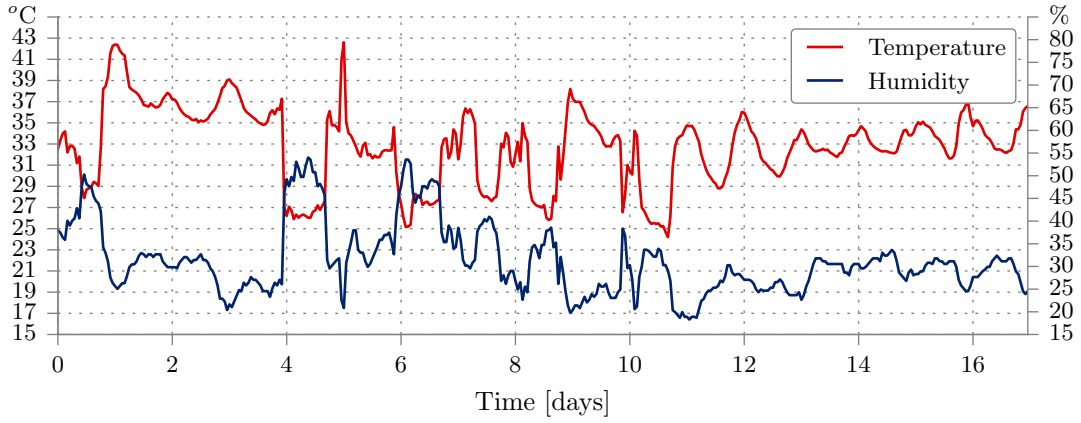

Figure 6.23: Temperature and relative humidity – Engine.

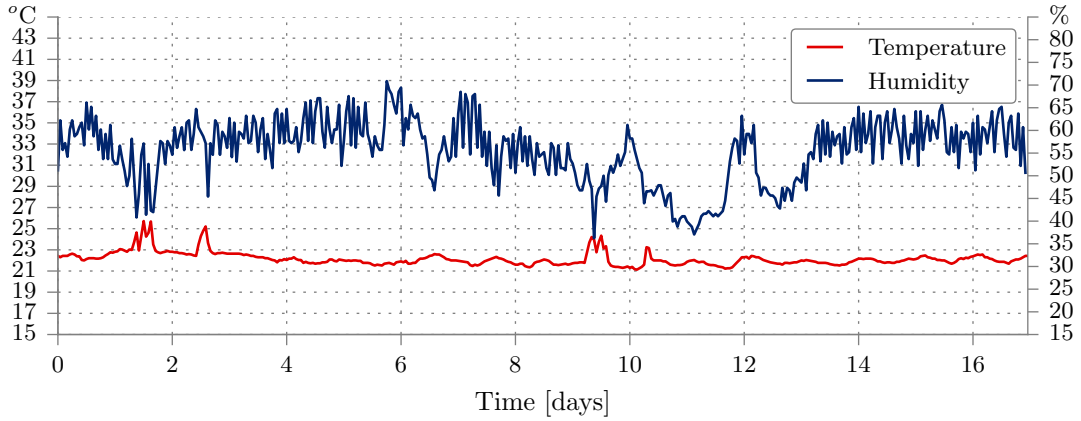

Figure 6.24: Temperature and relative humidity – Machinery Control Room (MCR).

On the day after the deployment, a peak in temperature is observed on the pumps (33^oC), engine (42^oC), gearbox (35^oC), and boiler (36^oC), while the MRC was stable due to it being in another deck, with no machinery near and an AC system on. On Day 5, another temperature peak is seen in the engine and boiler, with the pumps and gearbox experiencing also higher temperature on that day, the previous and the day after. This probably indicates that the machinery is being operated at higher power to bring the ship back to shore, as the 2-week patrol cycles are split in half where the ship is brought back to shore briefly

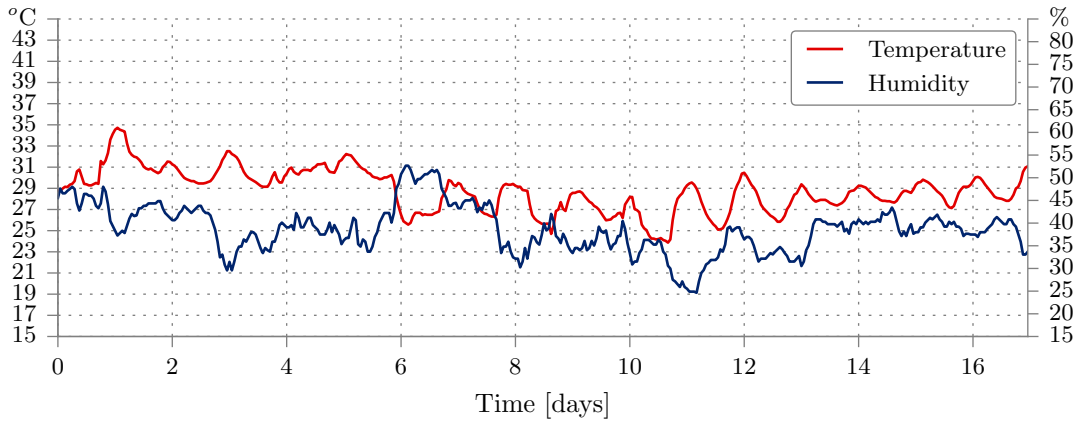

Figure 6.25: Temperature and relative humidity – Gearbox.

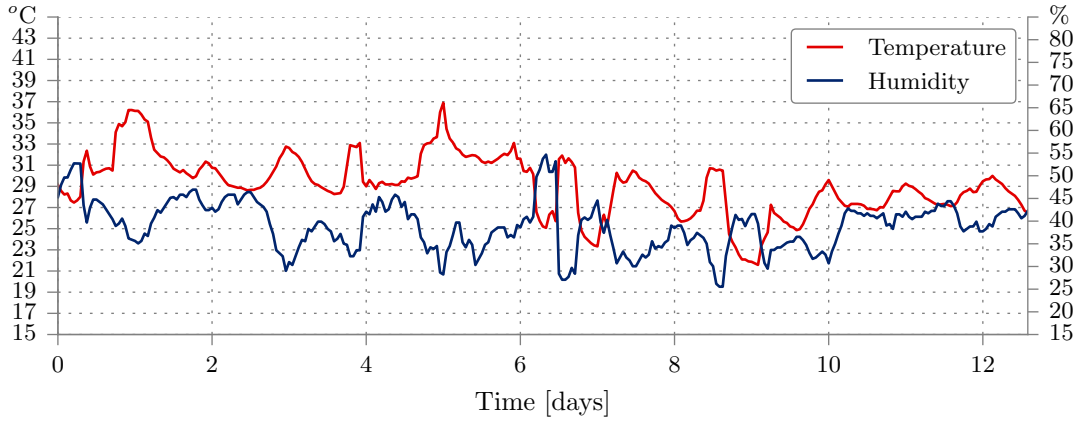

Figure 6.26: Temperature and relative humidity – Boiler.

before going back to sea. Except for the one in the MCR, all sensors recorded daily periodic up and down temperature cycles. The relative humidity was always below 70%, as the compartments are sealed from the outside and a ventilation system is in place.

Looking at the vibration spectrogram, the mid-trip cycle increase in machinery activity that was perceived in the temperature plots can be observed. On Days 5-7, a higher vibration was detected in the pumps (50 Hz) and boiler (50 Hz and 100-130 Hz wide band signal), which was also picked up by the MCR even though it is in a different deck. The gearbox showed smaller vibration on Day 5,

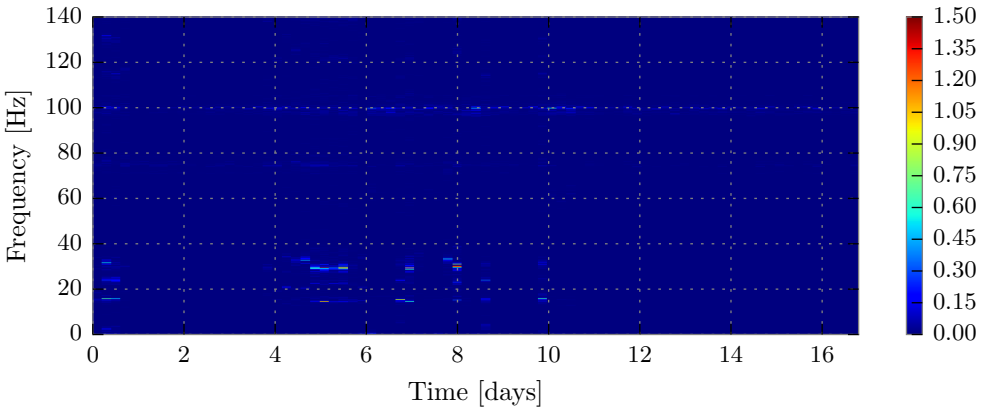

Figure 6.27: Frequency response on the z-axis – Pumps.

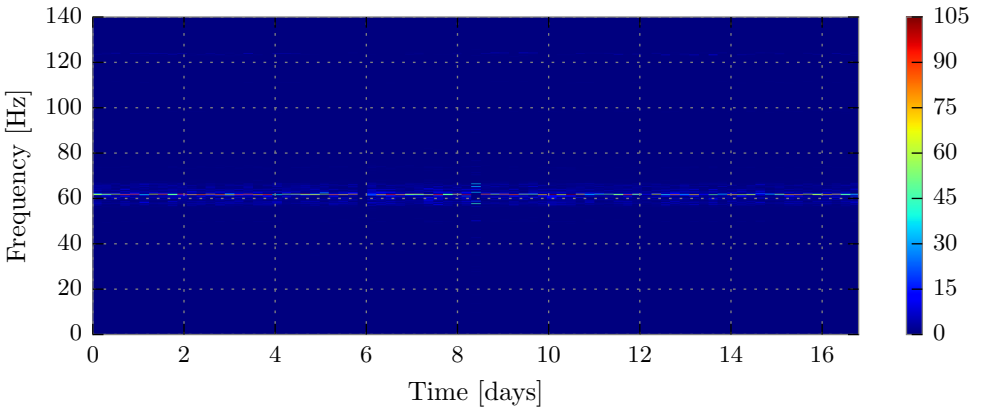

Figure 6.28: Frequency response on the z-axis – Engine.

but higher on Day 7 (50 Hz), while the highest was found on Day 8, coinciding with the higher vibration of the pumps (30 Hz). On Day 1, vibration was detected by all the sensors, due to the machines being set up for departure. The engine presented a constant narrow band vibration with the highest magnitude, around the typical frequency found in large engines (60 Hz), during the whole duration of the deployment.

Overall, this test validated both the module performance over an extended deployment in a highly-dense, completely metallic environment with a range of large, operating machinery and continuous personnel activity.

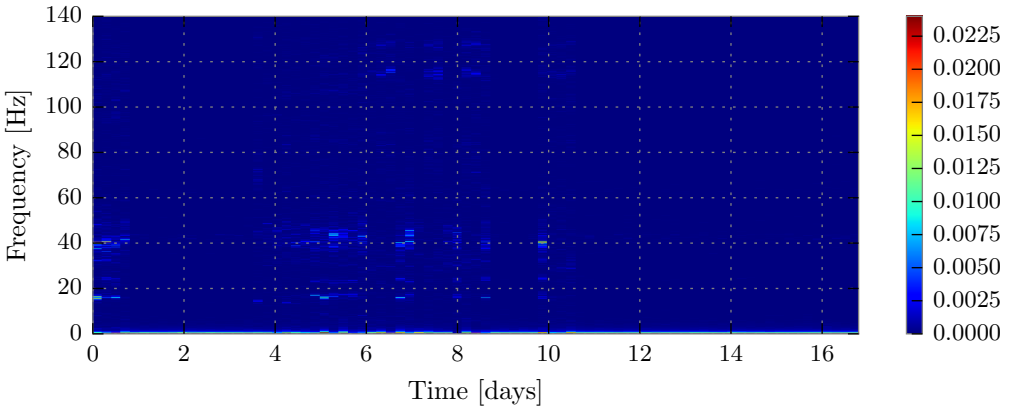

Figure 6.29: Frequency response on the z-axis – Machinery Control Room (MCR).

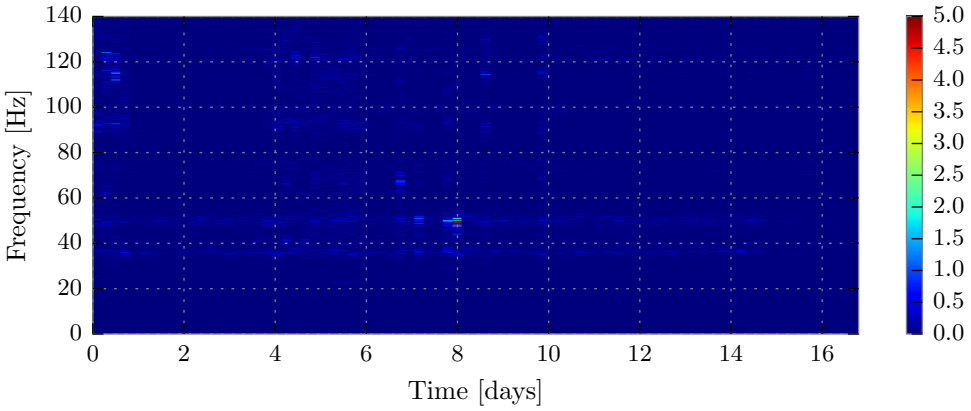

Figure 6.30: Frequency response on the z-axis – Gearbox.

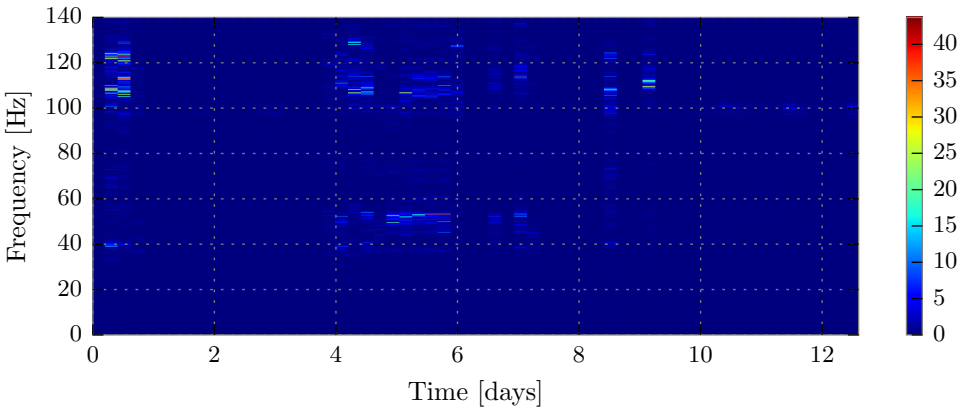

Figure 6.31: Frequency response on the z-axis – Boiler.

6.5 Discussion

6.5.1 Advances to the state of the art

The literature review has shown a variety of wireless sensing platforms developed to be used in different industrial and indoor environments. However, none of them have been tested for reliability following marine standards and also deployed in real-world harsh marine environments.

The research presented in this chapter has addressed these issues by testing the inductive and the health monitoring sensor module for vibration stresses and humidity/temperature following the Lloyd's Test Specification for marine electronics, using a vibration plate and a climatic chamber. The modules were also tested for salt mist following the MIL-STD-883 as an accelerated corrosion test that simulates the salt water conditions found in marine environments. Although both modules have been proved to survive all testing, the inductive module would still need further development and tests to be able to be used in real applications, as evidenced by the damage produced by the salt mist test in some of the sensor external components.

Several health monitoring modules have been deployed in different marine real-world scenarios, showing that it can collect data reliably during short and long periods in harsh conditions. This presents a complete validation of the preceding design and development work. The data collected showed that vibration from the accelerometer can provide immediate information more easily observed about the status of the machinery and structure, while audio data would need further processing and might only be useful for detecting specific flaws, provided the background noise is not excessively loud. Although the modules have shown to reliably save data in memory and it has been retrieved in the laboratory, to further validate the application a gateway PC would need to be installed and be controlled remotely, to be able to sense and retrieve data in real-time.

Chapter 7

Conclusions & Future Work

The thesis has presented research on the theme of systems integration that addresses several key gaps in existing knowledge and technology to allow deployment of WSNs to marine offshore structures and the machinery they contain. There have therefore been contributions to both research and applications in these several topics.

7.1 Advances and contribution to the state of the art

Through original research, the work presented in this thesis has achieved the objective of covering key gaps in SMHM for marine applications by developing and verifying a whole-systems integration methodology for design and development of WSN in offshore marine metal environments. In the literature review, it had been identified that:

- No plastic-encapsulated multi-sensor WSN modules were found that offered the necessary range of sensors, capabilities, hardware-software integration, and reliability for the use in the marine environment.
- A systematic methodology did not exist for characterising wireless link performance in metal marine environments with operating machinery.

This thesis have addressed these issues by original research in the following areas.

7.1.1 Contribution to wireless sensor modules for SMHM

Monitoring of steel structures is still an ongoing research problem, as it is not easy to embed sensors in them and the ones used currently such as FBG (Fiber Bragg Grating), strain gauge, and optical sensors tend to be large, costly, and with high power consumption. A novel concept has been developed to address this, by designing and characterising an eddy-current based sensor module that measures bending or displacement in two or more adjacent axes, as large structures tend to bend due to the forces from the environment; this way it could be detected if this displacement is too large and the structure is in danger of collapse. Different test setups were designed to characterise the module, proving it meets the required range and resolution in one and two axes, and the effects of different variables have been investigated such as metal characteristics, presence of water, proximity of the battery, and encapsulant.

Vibration and acoustic sensors are the most widely used method for machine and structural monitoring. A wireless sensor module has been developed that addressed the issues of current WSN modules for machinery health monitoring in terms of power, reliability, and compatibility. The module integrates a microcontroller, memory, 802.15.4-compatible radio and the necessary vibration, acoustic, and temperature/humidity sensors. It has been validated in laboratory conditions in different motor test setups and in the engine room of a naval vessel.

7.1.2 Contribution to systems integration and packaging for reliability

By using 3D systems integration, a cuboid module has been developed to assemble the inductive sensor, with PCB sensing coils in four of its sides, allowing for multi-axial displacement sensing. The use of inductive sensing ICs has allowed further miniaturisation and power reduction. The battery is hosted inside the cube using plastic holders, which makes the module a low-cost and fully autonomous solution. It is rechargeable and wireless, and it can be easily deployed autonomously or as part of a network of modules.

The vibration and acoustic health monitoring platform has been enclosed in a 3D-printed plastic custom box, with LED light guides, waterproof microusb connector, and PTFE-based membrane caps to cover the sensors while maintaining their sensing fidelity. This makes it easy to encapsulate it for protection in marine harsh environments.

Both modules were fully encapsulated in marine-graded resin compounds and further covered with resin coating. The packaging and encapsulation of both modules were validated for the marine environment by performing accelerated stress testing following marine standards for vibration, humidity/temperature, and salt-mist.

Moreover, the health monitoring module was tested in real-world applications: a RIB, a river bridge during a post-tropical hurricane, and a network of modules in a naval ship at sea. This testing validated the capabilities of the module as well as the packaging to withstand real marine harsh conditions.

7.1.3 Contribution to hardware/firmware/software co-design for WSN

The firmware-software developed for the hardware modules provides full remote wireless configuration and control of the nodes, with the ability to set up on-demand and periodic self-starting sensing experiments, data file management, and calibration. This is an advance over other platforms, as it makes it easier to deploy and manage WSN and to set up sensing experiments. By building the system on top of Contiki-shell and Contiki-OS, and enhancing them with application-focused additions, it is possible to extend the platform with new commands as well as networking protocols. The developed sampling strategy, using a combination of DMA, hardware and software buffers allowed for optimised high data rate sensing without the need for extra components. The configurable gain for the MEMS microphone makes it possible to adjust it depending on the sound level of the environment, avoiding saturation and maintaining the best signal-to-noise ratio. The user interface provides visual feedback of the environment in 3D and placed nodes, as well as basic visualisation of the recorded audio and vibration data in time and frequency. The control of the experiments, data and memory

management, and discovery of the network of nodes can also be done from this user interface.

7.1.4 Contribution to wireless link quality performance evaluation

The literature shows numerous studies of wireless performance in different environments, and in some cases even simple propagation models derived from data from low-complexity scenarios. It has been shown that communications are possible in complex metallic environments such as ships and shipping containers. However, the lack of a proper methodology is a known issue in most of these experiments: they are performed with upper-layer protocols that include retransmissions, nodes are not synchronised, and the necessary metrics are not provided, among others. Therefore, the conclusions derived from these studies are incomplete and an improved methodology is necessary.

Until recently, no tool was available for performing proper WSN wireless characterisation and being able to design an experimental framework with a scientific methodology. By using Trident as a testing tool, which includes the aforementioned capabilities of disabling upper-layer protocols and node synchronisation, a proper design of experiments can be developed, which has been proved in studies in forests and open fields but not marine environments. In the research presented in this thesis, this tool is used to perform similar experiments in metal marine environments, but with a different structured multi-variable experiment design with a systematic analysis of the results to assess the link quality of the network as well as individual nodes. Three environments were studied: multiple freight containers, a large engine room emulator containing a ship's engine, and a naval ship's operational engine room and its adjacent compartment. Different variables such as opening/closing of doors, node placement and position, and activation of machinery were studied. It was proven that a high connectivity was found in most of the cases, and a WSN can be a viable monitoring system to be used in these challenging scenarios. However, a minor change in the placement of a node can cause a dramatic impact in the link quality of the node, due to multi-path fading, as it was highlighted in the engine room scenario, where two nodes placed

under and over the engine cover produced very different results, with the node under the cover even having better connectivity than the one outside. This was proven in a fourth scenario, where a real application in a data centre was running with reliability issues in some nodes. By analysing the application data and running connectivity experiments the problem was found and fixed. Therefore, it is not possible to ensure the reliability of the network unless these studies are performed before deployment. The methodology developed through the research in this thesis now overcomes this.

7.2 Impact on the research and application fields

Until now, there has been a gap between the sensors used in commercial marine applications and the wireless sensor nodes used by researchers to test and develop reliable wireless networking protocols. The modules developed in this work can act as a stepping stone for future researchers working towards developing research modules and applications that are closer to industry needs, using commercial-off-the-shelf components and low-cost manufacturing processes. In some applications such as marine renewable energy, miniaturisation and low-cost of these sensors could help driving down deployment costs, which increase their chances of expansion in an industry greatly impacted by reliability and cost over-run issues. The use of plastic-encapsulated microcontrolled-based wireless sensing modules has been proven to be reliable to be used in harsh marine environments to replace commercial sensors.

The developed hardware-software architecture provides researchers and users alike a flexible platform that can be used for networking research as well as a rapid WSN deployment and management tool. The capability of wireless node experiment pre-configuration allows for operators not familiar with WSN deployments to easily deploy these networks by just attaching and turning on the modules. This has been proven in the navy ship's scenario, were nodes were shipped pre-configured and collected data for two weeks. This is particularly interesting in marine offshore scenarios, as they are often remote and a WSN expert cannot always obtain access to the site.

The developed inductive module has proven that the use of state-of-the-art eddy-current displacement ICs can be used to detect relative displacement between adjacent components in metal structures. This has shown the potential of developing low-cost commercial sensor modules not only for marine structures but also for buildings, bridges, and general large metal-based structures. It also opens up an area of research for developing prognostic mathematical models that can correlate different types of relative displacement with impending failures, where these modules can provide a low-cost solution for collecting displacement data.

The methodology designed for wireless performance characterisation can allow researchers and engineers to study *in-situ* the reliability of a WSN prior to and during deployment, as its prediction is not practical using currently available approaches. It identified the variables, metrics, and graphical representations that are important to understand the environment and make deployment decisions. The experiments performed in the different scenarios have proven not only this methodology but also that, despite the high amount of metal and machinery, the multipath effects can be mitigated by appropriate node and sink placement.

Marine researchers can now monitor structural and machine reliability in-situ, allowing research on the reliability of new marine structural concepts and machinery deployments or the impact of, for example, more extreme weather conditions, caused by climate change, on the reliability of existing marine structures. In the commercial application field, those responsible for marine structures now have both the hardware, software, and deployment methodology to use WSNs.

7.3 Peer-reviewed publications

The originality of the research presented in this thesis has been demonstrated by producing five peer-reviewed publications: two conference papers, two journal papers, and a co-authored conference paper.

- **David Rojas** and John Barrett. Link Quality Evaluation of a Wireless Sensor Network in Metal Marine Environments, *Wireless Networks, Springer.* April 2018. This journal paper continues on from the methodology and experiments presented in the conference paper *Experimental Analysis of a*

Wireless Sensor Network in a Multi-Chamber Metal Environment, evaluating two more complex scenarios: a shore-based, full-sized, operational ship's engine room training facility and a naval ship's engine room. These new scenarios include the study of the effect of operating marine machinery.

- **David Rojas** and John Barrett. A Novel 3D Embedded Module for Displacement Measurement in Metal Structures, *IEEE Transactions on Components, Packaging and Manufacturing Technology.* Volume: 7, Issue: 11, Nov. 2017. The inductive sensor is presented in this paper, including the characterisation in one and two axes and the study of the effects of different variables, as well as the description of the module integration and the design of the two testing rigs.

- **David Rojas** and John Barrett. A Hardware-Software WSN Platform for Machine and Structural Monitoring, *28th Irish Signals and Systems Conference.* Killarney, Ireland, pp. 1-6, June 2017. The design, development, and laboratory testing of the health monitoring module is presented, as well as the firmware-software platform and whole-systems integration approach.

- **David Rojas** and John Barrett. Experimental Analysis of a Wireless Sensor Network in a Multi-Chamber Metal Environment, *Proceedings of the 22nd European Wireless Conference (European Wireless 2016).* Oulu, Finland, pp. 1-6, May 2016. A first study of a WSN in a scenario composed of several freight containers is shown in this paper, with a multi-variable experiment design to assess the possible effects of these variables in the wireless communication performance.

- Ramona Marfievici, Pablo Corbalan, **David Rojas**, Alan McGibney, Susan Rea, and Dirk Pesch. Tales from the C130 Horror Room: A Wireless Sensor Network Story in a Data Center, *FAILSAFE'17, the* 1^{st} *ACM International Workshop on the Engineering of Reliable, Robust, and Secure Embedded Wireless Sensing Systems.* Delft, The Netherlands, pp. 24-31, November 2017. A study on a high-metal content data centre scenario is presented in this collaborative paper. Connectivity issues that were causing failures were

found and fixed by applying the methodologies developed for the marine scenarios in this research.

7.4 Future research

The systems integration research in this thesis has achieved the objectives of designing, developing, packaging, connecting and testing of wireless sensor modules for monitoring marine structures and devices. It has been shown that these modules in particular and WSN technologies in general can work reliably in these scenarios. However, future research has also been highlighted.

The ideal validation of the systems integration concept would be long-term deployment of a large WSN in an exposed marine environment. However, this was beyond the time and resources available and only more limited validations were possible. This means that problems or weaknesses not evident from these limited validations could be exposed by a long-term deployment, particularly in reliability. However, the first steps were taken in showing that such a large-scale deployment would be justified based on the success of the deployments reported in this thesis. For a long-term deployment, a real application would need to be developed, to be able to remotely monitor and control the status of the network. This application would have to be built on top of the developed software platform, and it would include one or more remotely controlled sinks acting as gateways connected to internet. This way, a network of nodes can be deployed in a structure, e.g. a bridge, ship, or off-shore platform to collect and analyse the data. This would help further the adoption of these technologies in industrial real-world applications.

Another area of interest could focus on developing data and signal processing algorithms to be run in the nodes, which would improve the features of both modules. This opens up a wide area of research, as different problems can be investigated, such as data compression or methods that could detect early failures in the node, saving power. However, it is very challenging to implement these type of algorithms in low-power microcontrollers, and it is a topic that goes beyond the scope of the research objectives of this thesis. It may become easier in the near future to do this as chip companies are launching low-power designs with

embedded algorithm/AI processing to meet demands for edge-processing in the IoT. It is a very promising area of research for reliability prognostics.

Although the inductive sensor has been tested in laboratory test rigs as a proof-of-concept, it would need further testing in structural applications, as well as characterisation of the effect of environmental variables, to be validated in real-world environments. The steps to validate this sensor module for real structural applications would be: first, to develop a high precision, possibly automated testing setup that can identify the actual resolution of the sensor module in different configurations. This testing setup will include not only plate/sensor displacement but actual beam/plate bending. Second, to deploy several nodes in a real structure that suffers frequent movement, e.g. the 'Shakey' bridge where the health monitoring module was deployed.

Finally, the wireless characterisation experiments have proven the feasibility of a WSN deployment in different metal marine scenarios. However, it has only been tested using TelosB devices, as the testing tool (Trident) is based on TinyOS and is therefore limited to be used with older radio ICs. If Trident is ported to ContikiOS, newer ICs will also be supported, such as those used for the sensor modules in this thesis. This opens up the possibility of evaluating how the improved sensitivity and resistance against multi-path fading of newer chips actually affects the performance in these networks. With this, the core of Trident could be incorporated in the Contiki-Shell based firmware application developed in this thesis and, in this way, periodic connectivity assessments can be run remotely from the deployed network to detect if there have been changes in the environment and reassess the network reliability.

References

[1] Stress Alert - Hull Stress Monitoring Ssystem. [Accessed Feb. 1, 2018]. [Online]. Available: http://www.jhmenge.com/strainstall/files/stressalert_short.pdf

[2] Bridge monitoring systems - Alliance Sensors Group. [Accessed Feb. 1, 2018]. [Online]. Available: http://alliancesensors.com/bridge-monitoring-systems

[3] J. García-Martín, J. Gómez-Gil, and E. Vázquez-Sánchez, "Non-destructive techniques based on eddy current testing," *Sensors*, vol. 11, no. 3, pp. 2525–2565, 2011.

[4] O. Kypris and A. Markham, "3-d displacement measurement for structural health monitoring using low-frequency magnetic fields," *IEEE Sensors Journal*, vol. 17, no. 4, pp. 1165–1174, 2017.

[5] Keyence - Eddy Current Displacement Sensor. [Accessed Feb. 5, 2018]. [Online]. Available: https://www.keyence.com/ss/products/measure/measurement_library/type/inductive/

[6] S. Schirrmacher, L. Overmeyer, and S. Lorisch, "Wireless condition monitoring of a marine gearbox," *Ship Technology Research*, vol. 63, no. 1, pp. 38–49, 2016.

[7] R. Severino, R. Gomes, M. Alves, P. Sousa, L. Ramos, R. Aguilar, E. Tovar, and P. B. Lourenço, "A wireless sensor network platform for structural health monitoring: enabling accurate and synchronized measurements

through cots+ custom-based design," *IFAC Proceedings Volumes*, vol. 43, no. 17, pp. 375–382, 2010.

[8] A. Mainwaring, D. Culler, J. Polastre, R. Szewczyk, and J. Anderson, "Wireless sensor networks for habitat monitoring," in *Proceedings of the 1st ACM international workshop on Wireless sensor networks and applications*. Acm, 2002, pp. 88–97.

[9] J. Meyer, R. Bischoff, G. Feltrin, and M. Motavalli, "Wireless sensor networks for long-term structural health monitoring," *Smart Structures and Systems*, vol. 6, no. 3, pp. 263–275, 2010.

[10] A. Lawal, P. Cooper, G. Awcock, S. Busbridge, J. Spenceley, D. Rodriguez Sanmartin, and E. Stipidis, "Enabling wireless sensors for shipboard measurement applications," in *Proc. of KTP Associates Conference, University of Brighton*, 2012, p. not available.

[11] N. R. JOHNSON, S. M. OCONNOR, A. K. MAGNUS, M. D. COLLETTE, and J. P. LYNCH, "Rapidly deployable wireless hull monitoring system for fatigue life assessment of naval vessels in high seas," in *8th European Workshop On Structural Health Monitoring (EWSHM 2016)*, 2016, p. not available.

[12] M. Schumacher, "Seawater corrosion handbook," 1979.

[13] R. E. Melchers, "Corrosion uncertainty modelling for steel structures," *Journal of Constructional Steel Research*, vol. 52, no. 1, pp. 3–19, 1999.

[14] ——, "The effect of corrosion on the structural reliability of steel offshore structures," *Corrosion science*, vol. 47, no. 10, pp. 2391–2410, 2005.

[15] R. Ambat, S. G. Jensen, and P. Moller, "Corrosion reliability of electronic systems," *ECS Transactions*, vol. 6, no. 24, pp. 17–28, 2008.

[16] N. Abdussamie, G. Thomas, W. Amin, and R. Ojeda, "Wave-in-deck forces on fixed horizontal decks of offshore platforms," in *ASME 2014 33rd International Conference on Ocean, Offshore and Arctic Engineering*. American Society of Mechanical Engineers, 2014, p. V01AT01A048.

[17] G. Chaudhury and W. Dover, "Fatigue analysis of offshore platforms subject to sea wave loadings," *International Journal of Fatigue*, vol. 7, no. 1, pp. 13–19, 1985.

[18] G. Ersdal, J. D. Sørensen, I. Langen *et al.*, "Updating of structural failure probability based on experienced wave loading," in *The Thirteenth International Offshore and Polar Engineering Conference*. International Society of Offshore and Polar Engineers, 2003, p. not available.

[19] J.-Y. Chen, R. B. Gilbert, F. J. Puskar, and S. Verret, "Case study of offshore pile system failure in hurricane ike," *Journal of Geotechnical and Geoenvironmental Engineering*, vol. 139, no. 10, pp. 1699–1708, 2013.

[20] M. Collins, F. J. Vecchio, R. G. Selby, and P. R. Gupta, "The failure of an offshore platform," *CONCRETE INTERNATIONAL-DETROIT-*, vol. 19, pp. 28–36, 1997.

[21] Dramatic failure of materials in drilling platforms at sea. [Accessed Feb. 15, 2017]. [Online]. Available: http://www.dierk-raabe.com/dramatic-material-failure/oil-drilling-platforms/

[22] P. Wirsching, "Fatigue reliability in welded joints of offshore structures," *International Journal of Fatigue*, vol. 2, no. 2, pp. 77–83, 1980.

[23] P. H. Wirsching and Y.-N. Chen, "Considerations of probability-based fatigue design for marine structures," *Marine Structures*, vol. 1, no. 1, pp. 23–45, 1988.

[24] M. Pate-Cornell, "Risk analysis and risk management for offshore platforms: lessons from the piper alpha accident," *Journal of Offshore Mechanics and Arctic Engineering. Transactions of the ASME*, vol. 115, no. 3, pp. 179–190, 1993.

[25] A. Toffoli, J. Lefevre, E. Bitner-Gregersen, and J. Monbaliu, "Towards the identification of warning criteria: analysis of a ship accident database," *Applied Ocean Research*, vol. 27, no. 6, pp. 281–291, 2005.

[26] W. Musial, D. Heimiller, P. Beiter, G. Scott, and C. Draxl, "2016 offshore wind energy resource assessment for the united states," National Renewable Energy Lab.(NREL), Golden, CO (United States), Tech. Rep., 2016.

[27] A. Badcock-Broe, R. Flynn, S. George, R. Gruet, and N. Medic, "Wave and tidal energy market deployment strategy for europe," *SI Ocean*, 2014.

[28] F. d. O. Antonio, "Wave energy utilization: A review of the technologies," *Renewable and sustainable energy reviews*, vol. 14, no. 3, pp. 899–918, 2010.

[29] T. Setoguchi, S. Santhakumar, H. Maeda, M. Takao, and K. Kaneko, "A review of impulse turbines for wave energy conversion," *Renewable energy*, vol. 23, no. 2, pp. 261–292, 2001.

[30] I. López, J. Andreu, S. Ceballos, I. M. de Alegría, and I. Kortabarria, "Review of wave energy technologies and the necessary power-equipment," *Renewable and Sustainable Energy Reviews*, vol. 27, pp. 413–434, 2013.

[31] Z. Chen, J. M. Guerrero, and F. Blaabjerg, "A review of the state of the art of power electronics for wind turbines," *IEEE Transactions on power electronics*, vol. 24, no. 8, pp. 1859–1875, 2009.

[32] Wartsila 16V26D ship engine. [Accessed Feb. 15, 2017]. [Online]. Available: https://www.wartsila.com/products/marine-oil-gas/engines-generating-sets/diesel-engines/wartsila-26

[33] W. Ostachowicz and A. Güemes, *New trends in structural health monitoring*. Springer Science & Business Media, 2013, vol. 542.

[34] H. Jo, J.-W. Park, B. Spencer, and H.-J. Jung, "Develoment of high-sensitivity wireless strain sensor for structural health monitoring," *Smart Struct. Syst*, vol. 11, no. 5, pp. 477–496, 2013.

[35] J. Zhang, W. Hong, Y. Tang, C. Yang, G. Wu, and Z. Wu, "Structural health monitoring of a steel stringer bridge with area sensing," *Structure and Infrastructure Engineering*, vol. 10, no. 8, pp. 1049–1058, 2014.

[36] D. W. Ha, H. S. Park, S. W. Choi, and Y. Kim, "A wireless mems-based inclinometer sensor node for structural health monitoring," *Sensors*, vol. 13, no. 12, pp. 16 090–16 104, 2013.

[37] T. Nguyen, T. H. Chan, D. P. Thambiratnam, and L. King, "Development of a cost-effective and flexible vibration daq system for long-term continuous structural health monitoring," *Mechanical Systems and Signal Processing*, vol. 64, pp. 313–324, 2015.

[38] X. Chen, M. Khaleghi, I. Dobrev, W. Tie, and C. Furlong, "Structural health monitoring by laser shearography: experimental and numerical investigations," in *Experimental and Applied Mechanics, Volume 6*. Springer, 2015, pp. 149–155.

[39] G. Luzi, M. Crosetto, and C. Gentile, "Radar interferometry as a tool for structural health monitoring: Current situation and perspectives of the technique for the next decade," in *Life-Cycle of Engineering Systems: Emphasis on Sustainable Civil Infrastructure*. CRC Press, 2016, p. 145.

[40] M. Mitra and S. Gopalakrishnan, "Guided wave based structural health monitoring: A review," *Smart Materials and Structures*, vol. 25, no. 5, p. 053001, 2016.

[41] N. Kaur, S. Bhalla, R. Shanker, and R. Panigrahi, "Experimental evaluation of miniature impedance chip for structural health monitoring of prototype steel/rc structures," *Experimental Techniques*, vol. 40, no. 3, pp. 981–992, 2016.

[42] Y. Yang and X. B. Yu, "Real time measurement of the dynamic displacement field of a large-scale arch-truss bridge by remote sensing technology," in *SENSORS, 2016 IEEE*, 2016, pp. 1–3.

[43] Stellar Tech LVDT Displacement Sensor. [Accessed Feb. 1, 2018]. [Online]. Available: https://www.stellartech.com/products/lvdts/

[44] D. Goyal and B. Pabla, "The vibration monitoring methods and signal processing techniques for structural health monitoring: A review," *Archives of Computational Methods in Engineering*, vol. 23, no. 4, pp. 585–594, 2016.

[45] D. Gagar, P. Foote, and P. Irving, "Effects of loading and sample geometry on acoustic emission generation during fatigue crack growth: Implications for structural health monitoring," *International Journal of Fatigue*, vol. 81, pp. 117–127, 2015.

[46] S. Jiao, L. Cheng, P. Li, and X. Li, "Study on fatigue crack monitoring of metallic aircraft structure based on attached eddy current sensor," in *Structural Health Monitoring and Integrity Management: Proceedings of the 2nd International Conference of Structural Health Monitoring and Integrity Management (ICSHMIM 2014), Nanjing, China, 24-26 September 2014*. CRC Press, 2015, p. 223.

[47] K. Chana, V. Sridhar, and D. Singh, "The use of eddy current sensors for the measurement of rotor blade tip timing: Development of a new method based on integration," in *ASME Turbo Expo 2016: Turbomachinery Technical Conference and Exposition*. American Society of Mechanical Engineers, 2016, p. V006T05A019.

[48] L. Wang, "Stretchable eddy current noncontact gap sensor based on spiral conductive polymer composite," *IEEE/ASME Transactions on Mechatronics*, vol. 21, no. 2, pp. 1072–1079, 2016.

[49] S. D. Roach, "Designing and building an eddy current position sensor," *Sensors-the Journal of Applied Sensing Technology*, vol. 15, no. 9, pp. 56–74, 1998.

[50] M. R. Nabavi and S. N. Nihtianov, "Design strategies for eddy-current displacement sensor systems: Review and recommendations," *IEEE Sensors Journal*, vol. 12, no. 12, pp. 3346–3355, 2012.

[51] G. Y. Tian, A. Sophian, D. Taylor, and J. Rudlin, "Multiple sensors on pulsed eddy-current detection for 3-d subsurface crack assessment," *IEEE Sensors Journal*, vol. 5, no. 1, pp. 90–96, 2005.

[52] LDC1000 Inductance to Digital Converter (LDC) for Inductive Sensing. [Accessed Feb. 15, 2017]. [Online]. Available: http://www.ti.com/lit/ds/symlink/ldc1000.pdf

[53] LDC1614 Multi-Channel 28-bit Inductance to Digital Converter (LDC) for Inductive Sensing. [Accessed Feb. 15, 2017]. [Online]. Available: http://www.ti.com/lit/ds/symlink/ldc1614.pdf

[54] J. Li, H. Hao, K. Fan, and J. Brownjohn, "Development and application of a relative displacement sensor for structural health monitoring of composite bridges," *Structural Control and Health Monitoring*, vol. 22, no. 4, pp. 726–742, 2015.

[55] B. Lu, Y. Li, X. Wu, and Z. Yang, "A review of recent advances in wind turbine condition monitoring and fault diagnosis," in *Power Electronics and Machines in Wind Applications, 2009. PEMWA 2009. IEEE.* IEEE, 2009, pp. 1–7.

[56] S. A. McInerny and Y. Dai, "Basic vibration signal processing for bearing fault detection," *IEEE Transactions on education*, vol. 46, no. 1, pp. 149–156, 2003.

[57] T. C. A. Kumar, G. Singh, and V. Naikan, "Effectiveness of vibration monitoring in the health assessment of induction motor," *International Journal of Prognostics and Health Management*, vol. 6, no. Special Issue Uncertainity in PHM) 007, pp. 1–9, 2015.

[58] S. Astapov, J. Preden, T. Aruvali, and B. Gordon, "Production machinery utilization monitoring based on acoustic and vibration signal analysis," in *Proc. 8th Int DAAAM Baltic Industrial Engineering Conf*, 2012, pp. 268–273.

[59] P. Henriquez, J. B. Alonso, M. A. Ferrer, and C. M. Travieso, "Review of automatic fault diagnosis systems using audio and vibration signals," *IEEE Transactions on Systems, Man, and Cybernetics: Systems*, vol. 44, no. 5, pp. 642–652, 2014.

[60] R. Coppolino, S. Rubin *et al.*, "Detectability of structural failures in offshore platforms by ambient vibration monitoring," in *Offshore Technology Conference*, 1980, p. not available.

[61] V. Giurgiutiu, *Structural health monitoring: with piezoelectric wafer active sensors*. Elsevier, 2007.

[62] S. Chandrasekaran and T. Chitambaram, "Health monitoring of offshore structures using wireless sensor network: experimental investigations," in *SPIE Smart Structures and Materials+ Nondestructive Evaluation and Health Monitoring*. International Society for Optics and Photonics, 2016, pp. 980 416–980 416.

[63] A. Sabato, C. Niezrecki, and G. Fortino, "Wireless mems-based accelerometer sensor boards for structural vibration monitoring: A review," *IEEE Sensors Journal*, vol. 17, no. 2, pp. 226–235, 2017.

[64] J. Polastre, R. Szewczyk, and D. Culler, "Telos: enabling ultra-low power wireless research," in *Information Processing in Sensor Networks, 2005. IPSN 2005. Fourth International Symposium on*. IEEE, 2005, pp. 364–369.

[65] A. Dunkels, O. Schmidt, N. Finne, J. Eriksson, F. Österlind, and N. T. M. Durvy. (2011) The contiki os: The operating system for the internet of things. [Accessed Feb. 15, 2017]. [Online]. Available: http://www.contikios.org

[66] O. Basir and X. Yuan, "Engine fault diagnosis based on multi-sensor information fusion using dempster–shafer evidence theory," *Information Fusion*, vol. 8, no. 4, pp. 379–386, 2007.

[67] N. Baydar and A. Ball, "A comparative study of acoustic and vibration signals in detection of gear failures using wigner–ville distribution," *Mechanical systems and signal processing*, vol. 15, no. 6, pp. 1091–1107, 2001.

[68] M. Mieloszyk and W. Ostachowicz, "An application of structural health monitoring system based on fbg sensors to offshore wind turbine support structure model," *Marine Structures*, vol. 51, pp. 65–86, 2017.

[69] P. Faulkner, P. Cutter, and A. Owens, "Structural health monitoring systems in difficult environmentsoffshore wind turbines," in *6th European workshop on structural health monitoring*, 2012, pp. 1–7.

[70] H. B. Glasgow, J. M. Burkholder, R. E. Reed, A. J. Lewitus, and J. E. Kleinman, "Real-time remote monitoring of water quality: a review of current applications, and advancements in sensor, telemetry, and computing technologies," *Journal of Experimental Marine Biology and Ecology*, vol. 300, no. 1-2, pp. 409–448, 2004.

[71] L. Adornato, A. Cardenas-Valencia, E. Kaltenbacher, R. H. Byrne, K. Daly, K. Larkin, S. Hartman, M. Mowlem, R. D. Prien, and V. Garçon, "In situ nutrient sensors for ocean observing systems," in *Proceedings of the Oceanobs 09: Sustained Ocean observations and Information for Society Conference*, vol. 2, 2009, p. not available.

[72] A. P. Klimley, B. J. Le Boeuf, K. M. Cantara, J. E. Richert, S. F. Davis, and S. Van Sommeran, "Radio-acoustic positioning as a tool for studying site-specific behavior of the white shark and other large marine species," *Marine Biology*, vol. 138, no. 2, pp. 429–446, 2001.

[73] V. Franzitta, V. Di Dio, A. Viola, C. Giaconia, P. Ferrara, and M. Trapanese, "Experimental results of a low cost weather buoy," in *Oceans-San Diego, 2013*. IEEE, 2013, pp. 1–5.

[74] R. Srinivasan, S. Zacharia, T. Thamarai, T. Sudhakar, and M. Atmanand, "Design and performance of a low power moored data buoy system," in *OCEANS, 2011 IEEE-Spain*. IEEE, 2011, pp. 1–6.

[75] C.-C. Teng, L. Bernard, B. Taft, and M. Burdette, "A compact wave and ocean data buoy system," in *OCEANS, 2005. Proceedings of MTS/IEEE*. IEEE, 2005, pp. 1249–1254.

[76] C. Liu and B. Fu, "Development of a compact marine environmental monitoring module based on smt32," in *Engineering and Technology (S-CET), 2012 Spring Congress on.* IEEE, 2012, pp. 1–4.

[77] D. Song, S. Gao, M. Xu, X. Wang, and Y. Wang, "Hardware design of a submerged buoy system based on electromagnetic inductive coupling," in *MATEC Web of Conferences*, vol. 75. EDP Sciences, 2016, p. 01001.

[78] J. Kelly, D. OSullivan, W. Wright, R. Alcorn, and A. Lewis, "Challenges and lessons learned in the deployment of an offshore oscillating water column," *COMPEL: The International Journal for Computation and Mathematics in Electrical and Electronic Engineering*, vol. 33, no. 5, pp. 1678–1704, 2014.

[79] C. Albaladejo, P. Sánchez, A. Iborra, F. Soto, J. A. López, and R. Torres, "Wireless sensor networks for oceanographic monitoring: A systematic review," *Sensors*, vol. 10, no. 7, pp. 6948–6968, 2010.

[80] J. Trevathan, I. Atkinson, W. Read, N. Bajema, Y. J. Lee, A. Scarr, and R. Johnstone, "Developing low-cost intelligent wireless sensor networks for aquatic environments," in *Intelligent Sensors, Sensor Networks and Information Processing (ISSNIP), 2010 Sixth International Conference on.* IEEE, 2010, pp. 13–18.

[81] G. Xu, W. Shen, and X. Wang, "Applications of wireless sensor networks in marine environment monitoring: A survey," *Sensors*, vol. 14, no. 9, pp. 16 932–16 954, 2014.

[82] P. Barbosa, N. White, and N. Harris, "Wireless sensor network for maritime deployment: Modeling and simulation," in *MELECON 2010-2010 15th IEEE Mediterranean Electrotechnical Conference.* IEEE, 2010, pp. 1009–1014.

[83] S. Nittel, N. Trigoni, K. Ferentinos, F. Neville, A. Nural, and N. Pettigrew, "A drift-tolerant model for data management in ocean sensor networks," in *Proceedings of the 6th ACM international workshop on Data engineering for wireless and mobile access.* ACM, 2007, pp. 49–58.

[84] M. reza Akhondi, A. Talevski, S. Carlsen, and S. Petersen, "Applications of wireless sensor networks in the oil, gas and resources industries," in *Advanced Information Networking and Applications (AINA), 2010 24th IEEE International Conference on*. IEEE, 2010, pp. 941–948.

[85] A. O. Adejo, A. J. Onumanyi, J. M. Anyanya, and S. O. Oyewobi, "Oil and gas process monitoring through wireless sensor networks: A survey," *Ozean Journal of Applied Science*, vol. 6, no. 2, p. not available, 2013.

[86] D. A. Gelineau, J. R. Davis, and J. A. Rice, "Investigating extreme event loading on coastal bridges using wireless sensor technology," in *Sensors and Smart Structures Technologies for Civil, Mechanical, and Aerospace Systems 2017*, vol. 10168. International Society for Optics and Photonics, 2017, p. 101681Z.

[87] M. Reyer, S. Hurlebaus, J. Mander, and O. Ozbulut, "Design of a wireless sensor network for structural health monitoring of bridges," in *Sensing Technology (ICST), 2011 Fifth International Conference on*. IEEE, 2011, pp. 515–520.

[88] R. A. Swartz, J. P. Lynch, S. Zerbst, B. Sweetman, and R. Rolfes, "Structural monitoring of wind turbines using wireless sensor networks," *Smart structures and systems*, vol. 6, no. 3, pp. 183–196, 2010.

[89] X.-y. Xiong, F. Wei, J.-w. Li, M. Han, and D.-h. Guan, "Vibration monitoring system of ships using wireless sensor networks," in *Mechatronics and Automation (ICMA), 2014 IEEE International Conference on*. IEEE, 2014, pp. 90–94.

[90] R. A. Swartz, A. T. Zimmerman, J. P. Lynch, J. Rosario, T. Brady, L. Salvino, and K. H. Law, "Hybrid wireless hull monitoring system for naval combat vessels," *Structure and Infrastructure Engineering*, vol. 8, no. 7, pp. 621–638, 2012.

[91] MICA Wireless measurement system. [Accessed March. 30, 2017]. [Online]. Available: http://www.openautomation.net/uploadsproductos/micaz_datasheet.pdf

[92] A. Burns, B. R. Greene, M. J. McGrath, T. J. O'Shea, B. Kuris, S. M. Ayer, F. Stroiescu, and V. Cionca, "Shimmer–a wireless sensor platform for noninvasive biomedical research," *IEEE Sensors Journal*, vol. 10, no. 9, pp. 1527–1534, 2010.

[93] Libelium Waspmote platform. [Accessed March. 30, 2017]. [Online]. Available: http://www.libelium.com/products/waspmote/

[94] Digi Xbee ieee 802.15.4 module. [Accessed March. 30, 2017]. [Online]. Available: https://www.digi.com/xbee

[95] TI CC2538 A Powerful System-On-Chip for 2.4-GHz IEEE 802.15.4-2006 and ZigBee Applications. [Accessed Feb. 15, 2017]. [Online]. Available: http://www.ti.com/lit/ds/symlink/cc2538.pdf

[96] P. Levis, S. Madden, J. Polastre, R. Szewczyk, K. Whitehouse, A. Woo, D. Gay, J. Hill, M. Welsh, E. Brewer *et al.*, "Tinyos: An operating system for sensor networks," in *Ambient intelligence*. Springer, 2005, pp. 115–148.

[97] E. Baccelli, O. Hahm, M. Gunes, M. Wahlisch, and T. C. Schmidt, "Riot os: Towards an os for the internet of things," in *Computer Communications Workshops (INFOCOM WKSHPS), 2013 IEEE Conference on*. IEEE, 2013, pp. 79–80.

[98] T. Watteyne, X. Vilajosana, B. Kerkez, F. Chraim, K. Weekly, Q. Wang, S. Glaser, and K. Pister, "Openwsn: a standards-based low-power wireless development environment," *Transactions on Emerging Telecommunications Technologies*, vol. 23, no. 5, pp. 480–493, 2012.

[99] LoRA - Long Range Transceivers. [Accessed March. 30, 2017]. [Online]. Available: https://www.semtech.com/products/wireless-rf/lora-transceivers

[100] Sigfox - IoT Connectivity service. [Accessed March. 30, 2017]. [Online]. Available: http://www.sigfox.com/

[101] B. O'Flynn, S. Bellis, K. Delaney, J. Barton, S. C. O'Mathuna, A. M. Barroso, J. Benson, U. Roedig, and C. Sreenan, "The development of a novel minaturized modular platform for wireless sensor networks," in *Proceedings of the 4th international symposium on Information processing in sensor networks*. IEEE Press, 2005, p. 49.

[102] J. Portilla, A. De Castro, E. De La Torre, and T. Riesgo, "A modular architecture for nodes in wireless sensor networks." *J. UCS*, vol. 12, no. 3, pp. 328–339, 2006.

[103] L. Moore and J. Barrett, "Embedded module for 3-d mechanical strain measurement," *IEEE Transactions on Components, Packaging and Manufacturing Technology*, vol. 2, no. 6, pp. 1002–1011, 2012.

[104] R. V. Martinez-Catala and J. Barrett, "A modular wireless sensor platform with fully integrated battery," *IEEE Transactions on Components and Packaging Technologies*, vol. 32, no. 3, pp. 617–626, 2009.

[105] P. Jacquet, P. Muhlethaler, T. Clausen, A. Laouiti, A. Qayyum, and L. Viennot, "Optimized link state routing protocol for ad hoc networks," in *Multi Topic Conference, 2001. IEEE INMIC 2001. Technology for the 21st Century. Proceedings. IEEE International*. IEEE, 2001, pp. 62–68.

[106] S. Lanzisera, A. M. Mehta, and K. S. Pister, "Reducing average power in wireless sensor networks through data rate adaptation," in *Communications, 2009. ICC'09. IEEE International Conference on*. IEEE, 2009, pp. 1–6.

[107] C. A. Boano, M. Zuniga, T. Voigt, A. Willig, and K. Römer, "The triangle metric: Fast link quality estimation for mobile wireless sensor networks," in *International Conference on Computer Communication Networks, 2010, Zurich, Switzerland*, 2010, p. not available.

[108] N. Baccour, A. Koubâa, L. Mottola, M. A. Zúñiga, H. Youssef, C. A. Boano, and M. Alves, "Radio link quality estimation in wireless sensor networks: a survey," *ACM Transactions on Sensor Networks (TOSN)*, vol. 8, no. 4, p. 34, 2012.

[109] F. Entezami, M. Tunicliffe, and C. Politis, "Find the weakest link: Statistical analysis on wireless sensor network link-quality metrics," *IEEE vehicular technology magazine*, vol. 9, no. 3, pp. 28–38, 2014.

[110] J. Xu, W. Liu, F. Lang, Y. Zhang, and C. Wang, "Distance measurement model based on rssi in wsn," *Wireless Sensor Network*, vol. 2, no. 08, p. 606, 2010.

[111] TI, "Cc2420: 2.4 ghz ieee 802.15. 4/zigbee-ready rf transceiver," 2006, [Accessed March. 30, 2017]. [Online]. Available: https://www.ti.com/lit/ds/symlink/cc2420.pdf

[112] IEEE. IEEE Standard 802.15.42003. [Accessed March. 30, 2017]. [Online]. Available: http://standards.ieee.org/getieee802/download/802.15.4-2003.pdf

[113] J. Zhao, L. Wang, W. Yue, Z. Qin, and M. Zhu, "Load migrating for the hot spots in wireless sensor networks using ctp," in *Mobile Ad-hoc and Sensor Networks (MSN), 2011 Seventh International Conference on*. IEEE, 2011, pp. 167–173.

[114] R. Draves, J. Padhye, and B. Zill, "Routing in multi-radio, multi-hop wireless mesh networks," in *Proceedings of the 10th annual international conference on Mobile computing and networking*. ACM, 2004, pp. 114–128.

[115] D. S. De Couto, D. Aguayo, J. Bicket, and R. Morris, "A high-throughput path metric for multi-hop wireless routing," *Wireless networks*, vol. 11, no. 4, pp. 419–434, 2005.

[116] S. Lin, G. Zhou, M. Al-Hami, K. Whitehouse, Y. Wu, J. A. Stankovic, T. He, X. Wu, and H. Liu, "Toward stable network performance in wireless sensor networks: A multilevel perspective," *ACM Transactions on Sensor Networks (TOSN)*, vol. 11, no. 3, p. 42, 2015.

[117] S. Srirangarajan and A. H. Tewfik, "Localization in wireless sensor networks under non line-of-sight propagation," in *Global Telecommunications Conference, 2005. GLOBECOM'05. IEEE*, vol. 6. IEEE, 2005, pp. 5–pp.

[118] R. Marfievici, A. Murphy, G. Picco, F. Ossi, and F. Cagnacci, "How environmental factors impact outdoor wireless sensor networks: A case study," in *Mobile Ad-Hoc and Sensor Systems (MASS), 2013 IEEE 10th International Conference on*, Oct 2013, pp. 565–573.

[119] D. Sexton, M. Mahony, M. Lapinski, and J. Werb, "Radio channel quality in industrial wireless sensor networks," in *Sensors for Industry Conference, 2005.* IEEE, 2005, pp. 88–94.

[120] C. A. Boano *et al.*, "Hot Packets: A Systematic Evaluation of the Effect of Temperature on Low Power Wireless Transceivers," in *Proc. of ExtremeCom*, 2013, p. not available.

[121] K. Srinivasan, P. Dutta, A. Tavakoli, and P. Levis, "Understanding the causes of packet delivery success and failure in dense wireless sensor networks," in *Proceedings of the 4th international conference on Embedded networked sensor systems.* ACM, 2006, pp. 419–420.

[122] A. Woo, T. Tong, and D. Culler, "Taming the underlying challenges of reliable multihop routing in sensor networks," in *Proceedings of the 1st international conference on Embedded networked sensor systems.* ACM, 2003, pp. 14–27.

[123] J. Zhao and R. Govindan, "Understanding packet delivery performance in dense wireless sensor networks," in *Proceedings of the 1st international conference on Embedded networked sensor systems.* ACM, 2003, pp. 1–13.

[124] A. Cerpa, N. Busek, and D. Estrin, "Scale: A tool for simple connectivity assessment in lossy environments," Center for Embedded Network Sensing, UCLA, Tech. Rep., 2003.

[125] M. Rondinone, J. Ansari, J. Riihijärvi, and P. Mähönen, "Designing a reliable and stable link quality metric for wireless sensor networks," in *Proceedings of the workshop on Real-world wireless sensor networks.* ACM, 2008, pp. 6–10.

[126] T. S. Rappaport *et al.*, *Wireless communications: principles and practice.* prentice hall PTR New Jersey, 1996, vol. 2.

[127] G. Mao, B. D. Anderson, and B. Fidan, "Path loss exponent estimation for wireless sensor network localization," *Computer Networks*, vol. 51, no. 10, pp. 2467–2483, 2007.

[128] J. Miranda, R. Abrishambaf, T. Gomes, P. Gonçalves, J. Cabral, A. Tavares, and J. Monteiro, "Path loss exponent analysis in wireless sensor networks: Experimental evaluation," in *Industrial Informatics (INDIN), 2013 11th IEEE International Conference on.* IEEE, 2013, pp. 54–58.

[129] G. Mao, B. D. Anderson, and B. Fidan, "Wsn06-4: Online calibration of path loss exponent in wireless sensor networks," in *Global Telecommunications Conference, 2006. GLOBECOM'06. IEEE.* IEEE, 2006, pp. 1–6.

[130] A. Martinez-Sala, J.-M. Molina-Garcia-Pardo, E. Egea-Ldpez, J. Vales-Alonso, L. Juan-Llacer, and J. Garcia-Haro, "An accurate radio channel model for wireless sensor networks simulation," *Journal of Communications and Networks*, vol. 7, no. 4, pp. 401–407, 2005.

[131] E. Weingartner, H. Vom Lehn, and K. Wehrle, "A performance comparison of recent network simulators," in *Communications, 2009. ICC'09. IEEE International Conference on.* IEEE, 2009, pp. 1–5.

[132] L. Bergamini, C. Crociani, A. Vitaletti, and M. Nati, "Validation of wsn simulators through a comparison with a real testbed," in *Proceedings of the 7th ACM workshop on Performance evaluation of wireless ad hoc, sensor, and ubiquitous networks.* ACM, 2010, pp. 103–104.

[133] K. Rizk, J.-F. Wagen, and F. Gardiol, "Two-dimensional ray-tracing modeling for propagation prediction in microcellular environments," *IEEE Transactions on Vehicular Technology*, vol. 46, no. 2, pp. 508–518, 1997.

[134] Z. Ji, B.-H. Li, H.-X. Wang, H.-Y. Chen, and T. K. Sarkar, "Efficient ray-tracing methods for propagation prediction for indoor wireless communications," *IEEE Antennas and Propagation Magazine*, vol. 43, no. 2, pp. 41–49, 2001.

[135] A. Guinard, A. McGibney, and D. Pesch, "A wireless sensor network design tool to support building energy management," in *Proceedings of the First ACM Workshop on Embedded Sensing Systems for Energy-Efficiency in Buildings*. ACM, 2009, pp. 25–30.

[136] G. E. Athanasiadou and A. R. Nix, "A novel 3-d indoor ray-tracing propagation model: The path generator and evaluation of narrow-band and wide-band predictions," *IEEE transactions on Vehicular Technology*, vol. 49, no. 4, pp. 1152–1168, 2000.

[137] H. Kim and H.-S. Lee, "Accelerated three dimensional ray tracing techniques using ray frustums for wireless propagation models," *Progress In Electromagnetics Research*, vol. 96, pp. 21–36, 2009.

[138] M. Korkalainen and M. Sallinen, "A survey of rf-propagation simulation tools for wireless sensor networks," in *Sensor Technologies and Applications (SENSORCOMM), 2010 Fourth International Conference on*. IEEE, 2010, pp. 342–347.

[139] F. Osterlind, A. Dunkels, J. Eriksson, N. Finne, and T. Voigt, "Cross-level sensor network simulation with cooja," in *Local computer networks, proceedings 2006 31st IEEE conference on*. IEEE, 2006, pp. 641–648.

[140] G. Werner-Allen, P. Swieskowski, and M. Welsh, "Motelab: A wireless sensor network testbed," in *Proceedings of the 4th international symposium on Information processing in sensor networks*. IEEE Press, 2005, p. 68.

[141] M. Doddavenkatappa, M. C. Chan, and A. L. Ananda, "Indriya: A low-cost, 3d wireless sensor network testbed," in *International Conference on Testbeds and Research Infrastructures*. Springer, 2011, pp. 302–316.

[142] C. A. Boano, T. Voigt, C. Noda, K. Römer, and M. Zúñiga, "Jamlab: Augmenting sensornet testbeds with realistic and controlled interference generation," in *Information Processing in Sensor Networks (IPSN), 2011 10th International Conference on*. IEEE, 2011, pp. 175–186.

[143] C. A. Boano, M. Zúñiga, J. Brown, U. Roedig, C. Keppitiyagama, and K. Römer, "Templab: A testbed infrastructure to study the impact of temperature on wireless sensor networks," in *Proceedings of the 13th international symposium on Information processing in sensor networks*. IEEE Press, 2014, pp. 95–106.

[144] J. Slipp, C. Ma, N. Polu, J. Nicholson, M. Murillo, and S. Hussain, "Winter: architecture and applications of a wireless industrial sensor network testbed for radio-harsh environments," in *Communication Networks and Services Research Conference, 2008. CNSR 2008. 6th Annual*. IEEE, 2008, pp. 422–431.

[145] T. Arampatzis, J. Lygeros, and S. Manesis, "A survey of applications of wireless sensors and wireless sensor networks," in *Intelligent Control, 2005. Proceedings of the 2005 IEEE International Symposium on, Mediterrean Conference on Control and Automation*. IEEE, 2005, pp. 719–724.

[146] X. Yu, P. Wu, W. Han, and Z. Zhang, "A survey on wireless sensor network infrastructure for agriculture," *Computer Standards & Interfaces*, vol. 35, no. 1, pp. 59–64, 2013.

[147] B. Rashid and M. H. Rehmani, "Applications of wireless sensor networks for urban areas: A survey," *Journal of Network and Computer Applications*, vol. 60, pp. 192–219, 2016.

[148] W.-S. Jang and W. M. Healy, "Wireless sensor network performance metrics for building applications," *Energy and Buildings*, vol. 42, no. 6, pp. 862–868, 2010.

[149] K. Srinivasan, P. Dutta, A. Tavakoli, and P. Levis, "An empirical study of low-power wireless," *ACM Transactions on Sensor Networks (TOSN)*, vol. 6, no. 2, p. 16, 2010.

[150] S. Yuan, M. Becker, R. Jedermann, C. Görg, and W. Lang, "An experimental study of signal propagation and network performance in monitoring of food transportation," in *Sensor, Mesh and Ad Hoc Communications and Networks Workshops, 2009. SECON Workshops' 09. 6th Annual IEEE Communications Society Conference on.* IEEE, 2009, pp. 1–3.

[151] H. Kdouh, H. Farhat, G. Zaharia, C. Brousseau, G. Grunfelder, and G. Zein, "Performance analysis of a hierarchical shipboard wireless sensor network," in *Personal Indoor and Mobile Radio Communications (PIMRC), 2012 IEEE 23rd International Symposium on.* IEEE, 2012, pp. 765–770.

[152] H. Kdouh, G. Zaharia, C. Brousseau, G. Grunfelder, H. Farhat, and G. El Zein, "Wireless sensor network on board vessels," in *Telecommunications (ICT), 2012 19th International Conference on.* IEEE, 2012, pp. 1–6.

[153] H. Kdouh, C. Brousseau, G. Zaharia, G. Grunfeleder, and G. Zein, "A realistic experiment of a wireless sensor network on board a vessel," in *Communications (COMM), 2012 9th International Conference on.* IEEE, 2012, pp. 189–192.

[154] H. Kdouh, G. Zaharia, C. Brousseau, G. El Zein, and G. Grunfelder, "Zigbee-based sensor network for shipboard environments," in *Signals, Circuits and Systems (ISSCS), 2011 10th International Symposium on.* IEEE, 2011, pp. 1–4.

[155] K. Ferens, L. Woo, and W. Kinsner, "Performance of zigbee networks in the presence of broadband electromagnetic noise," in *Electrical and Computer Engineering, 2009. CCECE'09. Canadian Conference on.* IEEE, 2009, pp. 407–410.

[156] M. Bertocco, G. Gamba, and A. Sona, "Assessment of out-of-channel interference effects on ieee 802.15. 4 wireless sensor networks," in *Instrumentation and Measurement Technology Conference Proceedings, 2008. IMTC 2008. IEEE.* IEEE, 2008, pp. 1712–1717.

[157] T. Istomin, R. Marfievici, A. L. Murphy, and G. P. Picco, "Trident: In-field connectivity assessment for wireless sensor networks," in *Proceedings of the 6th Extreme Conference on Communication and Computing (ExtremeCom)*, 2014, p. not available.

[158] TI Application Report - LDC Sensor Design. [Accessed Feb. 15, 2017]. [Online]. Available: http://www.ti.com/lit/ds/symlink/ldc1614.pdf

[159] N. Misron, L. Q. Ying, R. N. Firdaus, N. Abdullah, N. F. Mailah, and H. Wakiwaka, "Effect of inductive coil shape on sensing performance of linear displacement sensor using thin inductive coil and pattern guide," *Sensors*, vol. 11, no. 11, pp. 10 522–10 533, 2011.

[160] X. Huang and K. Ngo, "Design technique for a spiral planar winding with geometric radii," *IEEE transactions on aerospace and electronic systems*, vol. 32, no. 2, pp. 825–830, 1996.

[161] Inductive Sensing Design Calculator Tool for LDC1xxx. [Accessed Feb. 15, 2017]. [Online]. Available: http://www.ti.com/lit/zip/slyc137

[162] WEBENCH Designer for Inductive Sensing Applications. [Accessed Feb. 15, 2017]. [Online]. Available: https://webench.ti.com/webench5/ldc/

[163] Micro-epsilon optoNCDT 1420 - Smart Laser Triangulation Displacement Sensor. [Accessed Feb. 15, 2017]. [Online]. Available: http://www.micro-epsilon.co.uk/download/products/cat--optoNCDT--en.pdf

[164] W. Weeks, L. Wu, M. McAllister, and A. Singh, "Resistive and inductive skin effect in rectangular conductors," *IBM Journal of Research and Development*, vol. 23, no. 6, pp. 652–660, 1979.

[165] ST iNEMO inertial module: 3D accelerometer, 3D gyroscope, 3D magnetometer. [Online]. Available: http://www.st.com/resource/en/datasheet/lsm9ds1.pdf

[166] Sensirion SHT21 Digital Humidity and Temperature Sensor. [Accessed Feb. 15, 2017]. [Online]. Available: https://www.sensirion.com/products/humidity-sensors/humidity-temperature-sensor-sht2x-digital-i2c-accurate/

[167] Maxim DS2745 Low-Cost I2C Battery Monitor. [Accessed Feb. 15, 2017]. [Online]. Available: https://datasheets.maximintegrated.com/en/ds/DS2745.pdf

[168] Mcp73831 Microchip Li-Polymer Charge Management Controller. [Accessed Feb. 15, 2017]. [Online]. Available: http://ww1.microchip.com/downloads/en/DeviceDoc/20001984g.pdf

[169] Mcp1700 Microchip Low Quiescent Current LDO. [Accessed Feb. 15, 2017]. [Online]. Available: http://ww1.microchip.com/downloads/en/DeviceDoc/20001826C.pdf

[170] Electrolube UR5041 Polyurethane Resin. [Accessed May. 26, 2017]. [Online]. Available: https://www.electrolube.com/core/components/products/tds/044/UR5041.pdf

[171] Electrolube PUC Polyurethane Coating. [Accessed May. 26, 2017]. [Online]. Available: https://www.electrolube.com/core/components/products/tds/044/PUC.pdf

[172] TI Application Report - LDC1000 Temperture Compensation. [Accessed Feb. 15, 2017]. [Online]. Available: http://www.ti.com/lit/an/snaa212/snaa212.pdf

[173] TI Application Report - LDC Target Design. [Accessed Feb. 15, 2017]. [Online]. Available: http://www.ti.com/lit/an/snoa957a/snoa957a.pdf

[174] Invensense INMP504 Ultra-Low Noise Microphone with Bottom Port and Analog Output. [Accessed March. 20, 2017]. [Online]. Available: https://www.invensense.com/wp-content/uploads/2015/02/INMP504.pdf

[175] AT45DB641E 64-mbit spi serial flash memory. [Accessed March. 20, 2017]. [Online]. Available: https://www.adestotech.com/wp-content/uploads/DS-45DB641E-027.pdf

[176] M. Ceriotti, M. Chini, A. L. Murphy, G. P. Picco, F. Cagnacci, and B. Tolhurst, "Motes in the jungle: lessons learned from a short-term wsn deployment in the ecuador cloud forest," in *Real-World Wireless Sensor Networks*. Springer, 2010, pp. 25–36.

[177] D. Ganesan, B. Krishnamachari, A. Woo, D. Culler, D. Estrin, and S. Wicker, "Complex behavior at scale: An experimental study of low-power wireless sensor networks," Citeseer, Tech. Rep., 2002.

[178] GENiC - Globally Optimised Energy Efficient Data Centres. [Accessed Nov. 24, 2017]. [Online]. Available: http://projectgenic.eu/

[179] ELEKTRONIK. EE575 HVAC Miniature Air Velocity Transmitter. [Accessed Nov. 7, 2017]. [Online]. Available: http://downloads.epluse.com/fileadmin/data/product/ee575/datasheet_EE575.pdf

[180] ——. EE671 HVAC Miniature Air Velocity Transmitter. [Accessed Nov. 7, 2017]. [Online]. Available: http://downloads.epluse.com/fileadmin/data/product/ee671/datasheet_EE671.pdf

[181] A. Dunkels, "Rime - a lightweight layered communication stack for sensor networks," in *Proceedings of the European Conference on Wireless Sensor Networks (EWSN), Poster/Demo session, Delft, The Netherlands*. Citeseer, 2007, p. not available.

[182] Lloyd's Register Type Approval System Test Specification Number 1 - Marine Applications. [Accessed May. 26, 2017]. [Online]. Available: https://www.cdlive.lr.org/information/documents/Approvals/TASystem/TestSpec/Test%20Spec1.pdf

[183] B&K Model V455 Electrodynamic Shaker. [Accessed Oct. 10, 2017]. [Online]. Available: https://www.bksv.com/en/products/

shakers-and-exciters/LDS-shaker-systems/permanent-magnet-shakers/V455

[184] Weiss wkl 100 Climate test chamber. [Accessed Oct. 10, 2017]. [Online]. Available: http://www.labotec.co.za/wp-content/uploads/2016/07/WTL-WKL-Compact-Chambers-Brochure.pdf

[185] MIL-STD-883 Department of Defense Test Method Standard Microcircuits. [Accessed June. 26, 2017]. [Online]. Available: http://everyspec.com/MIL-STD/MIL-STD-0800-0899/download.php?spec=MIL-STD-883K.054326.pdf

Appendix A

Circuit schematics

A.1 Inductive module ELECTRONICS PCB

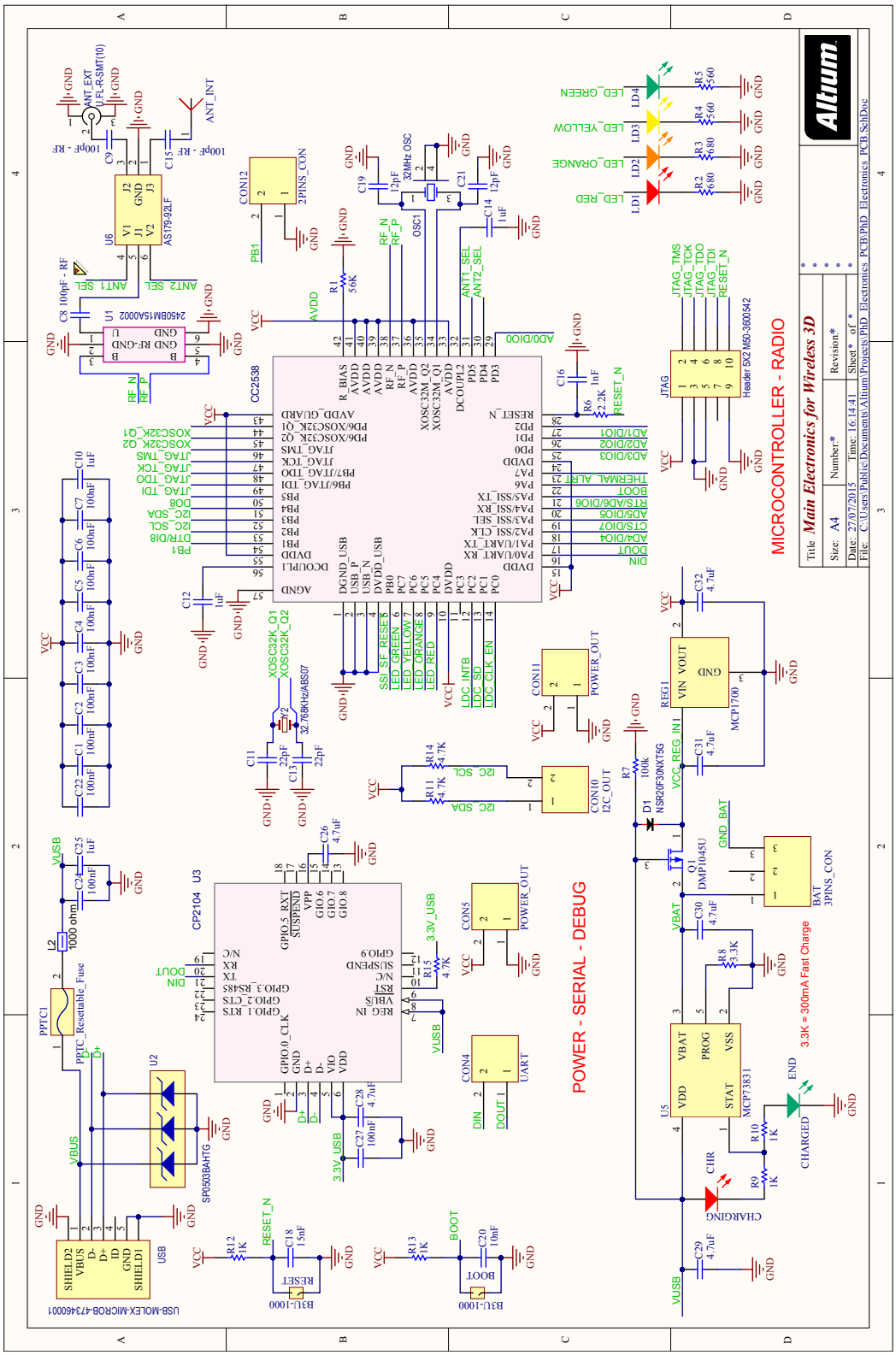

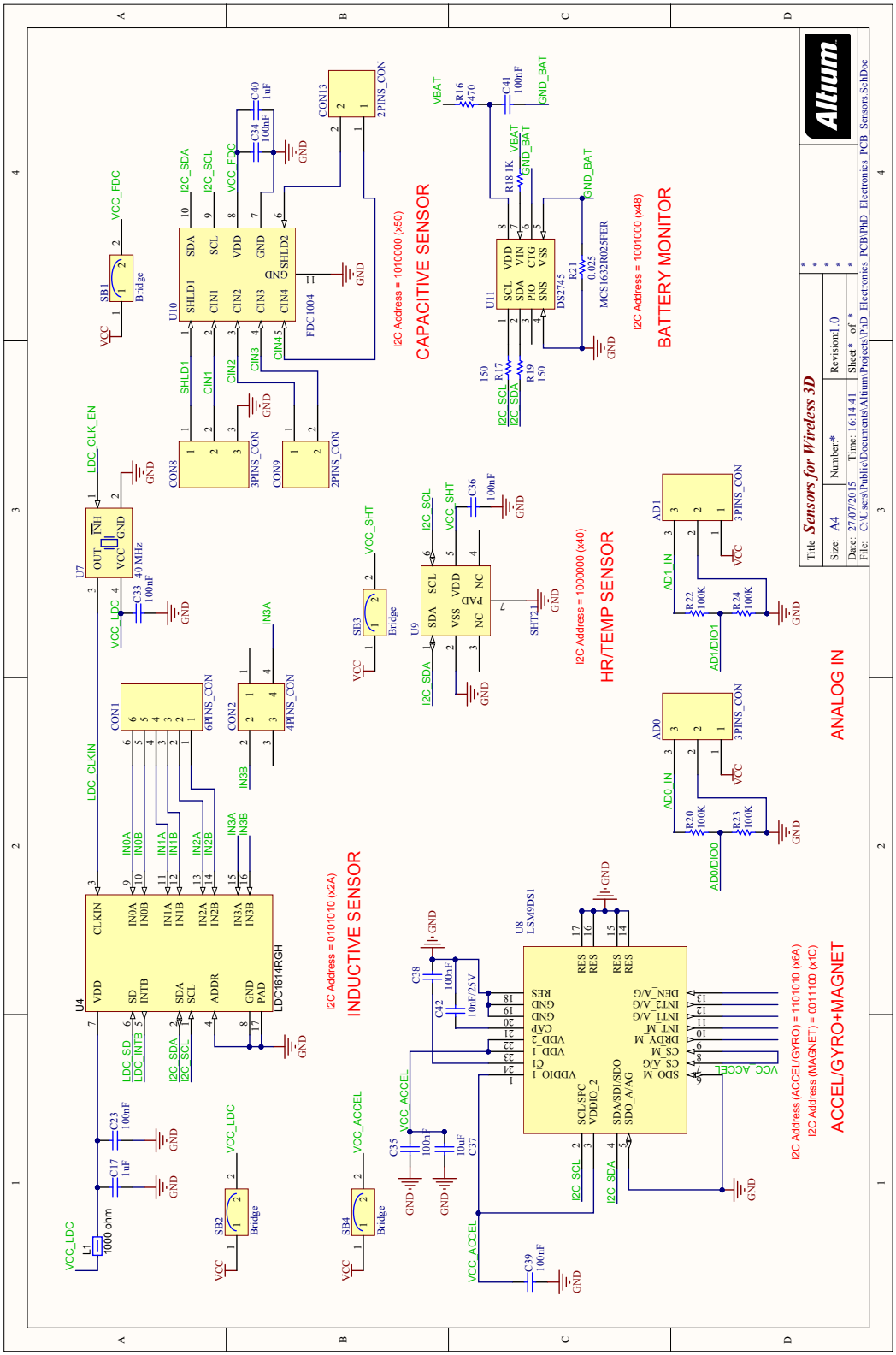
Sensors for Wireless 3D
Size: A4
Number:*
Revision:1.0
Date: 27/07/2015
Time: 16:14:41
Sheet* of *
File: C:\Users\Public\Documents\Altium\Projects\PhD Electronics PCB\PhD Electronics PCB Sensors.SchDoc
INDUCTIVE SENSOR
I2C Address = 0101010 (x2A)
CAPACITIVE SENSOR
I2C Address = 1010000 (x50)
HR/TEMP SENSOR
I2C Address = 1000000 (x40)
BATTERY MONITOR
I2C Address = 1001000 (x48)
ANALOG IN
ACCEL/GYRO+MAGNET
I2C Address (ACCEL/GYRO) = 1101010 (x6A)
I2C Address (MAGNET) = 0011100 (x1C)
LDC1614RGH
LSM9DS1
FDC1004
SHT21
DS2745
MCS1632R025FER

A.2 SMHM module ELECTRONICS PCB

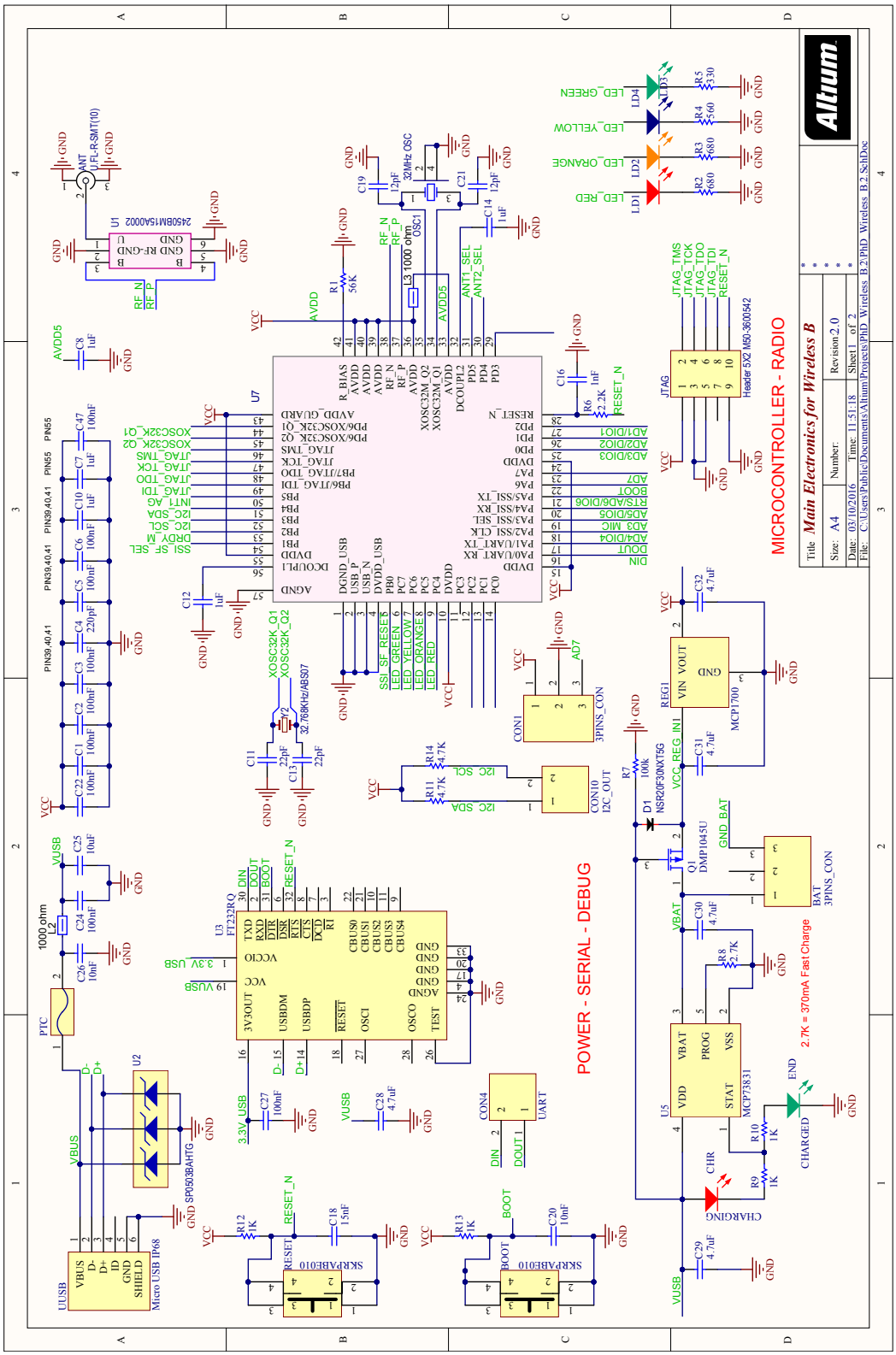

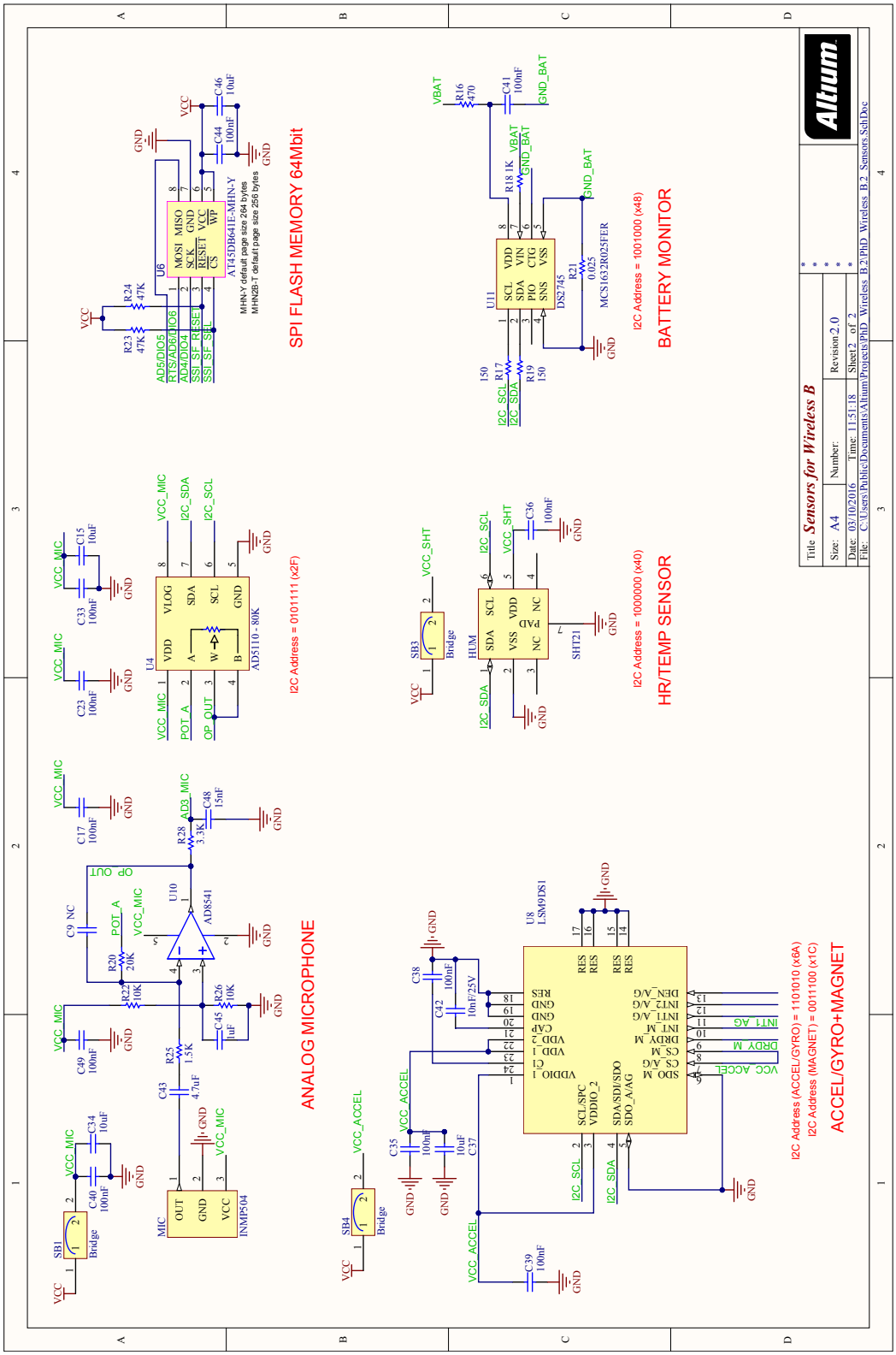
SPI FLASH MEMORY 64Mbit
I2C Address = 0101111 (x2F)
ANALOG MICROPHONE
I2C Address = 1001000 (x48)
BATTERY MONITOR
I2C Address = 1000000 (x40)
HR/TEMP SENSOR
I2C Address (ACCEL/GYRO) = 1101010 (x6A)
I2C Address (MAGNET) = 0011100 (x1C)
ACCEL/GYRO+MAGNET
Sensors for Wireless B
Revision 2.0
Sheet 2 of 2
Altium

Appendix B

CAD 3D-printed parts

B.1 Inductive module support parts

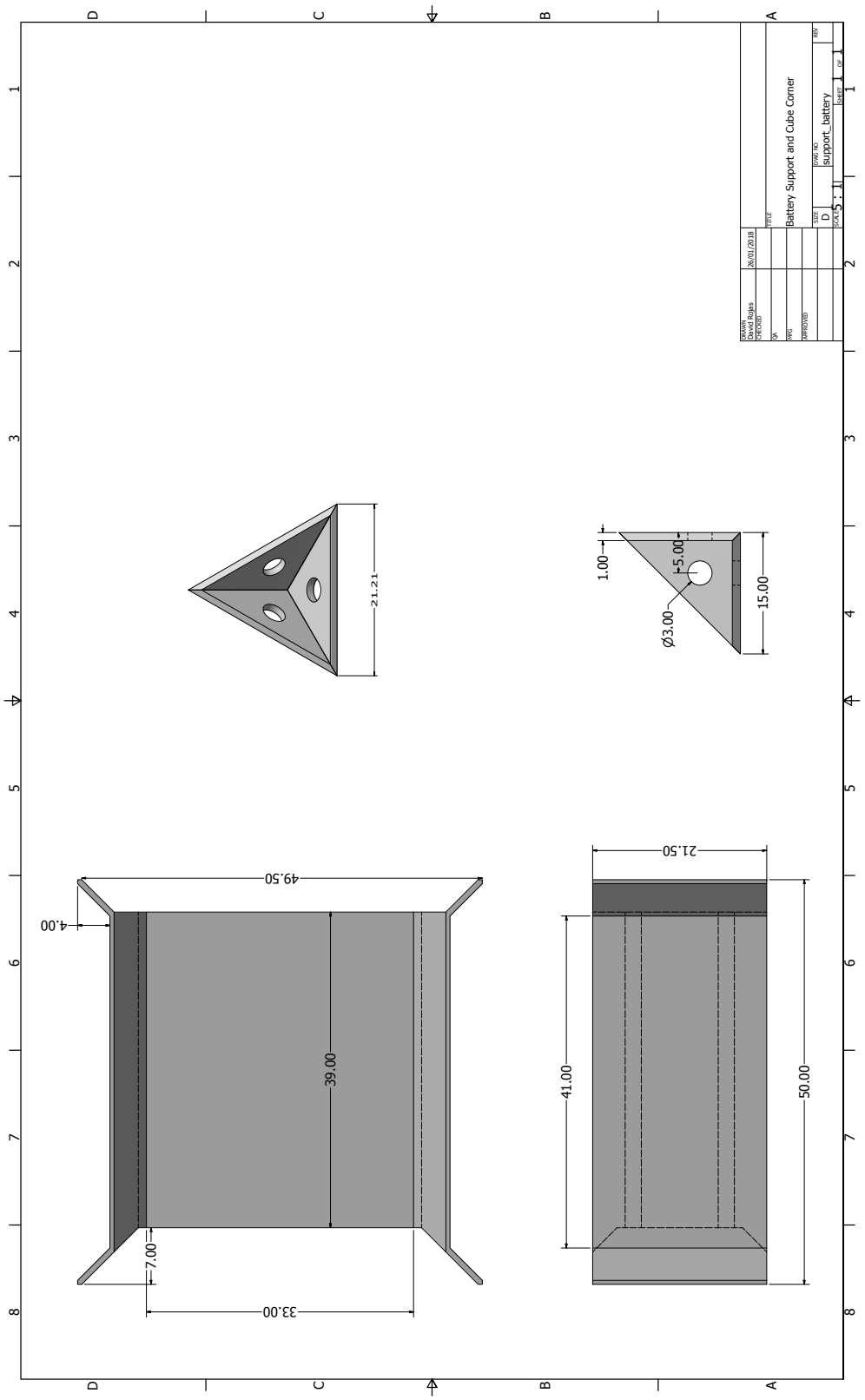

B.2 Inductive module test setup support parts

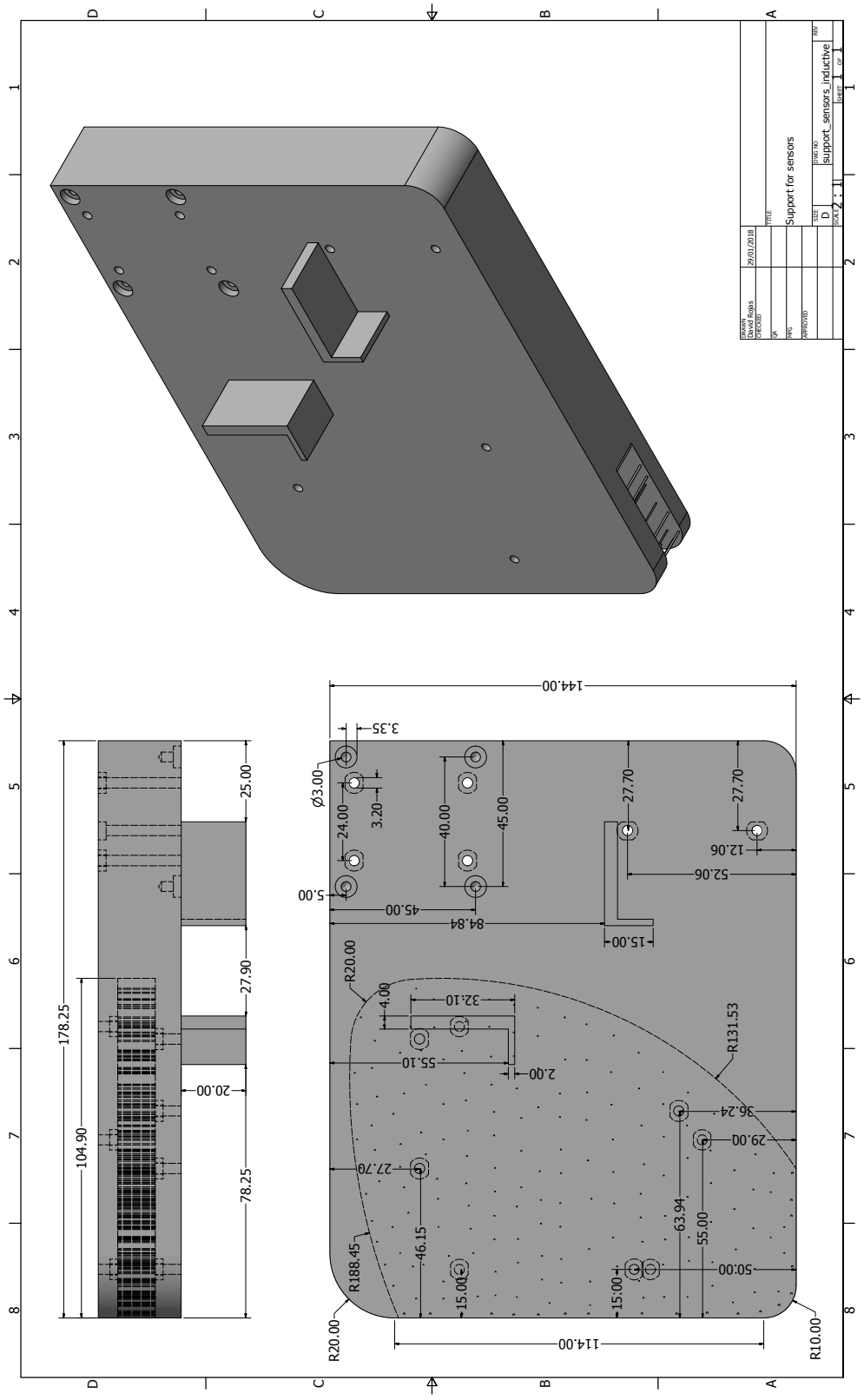

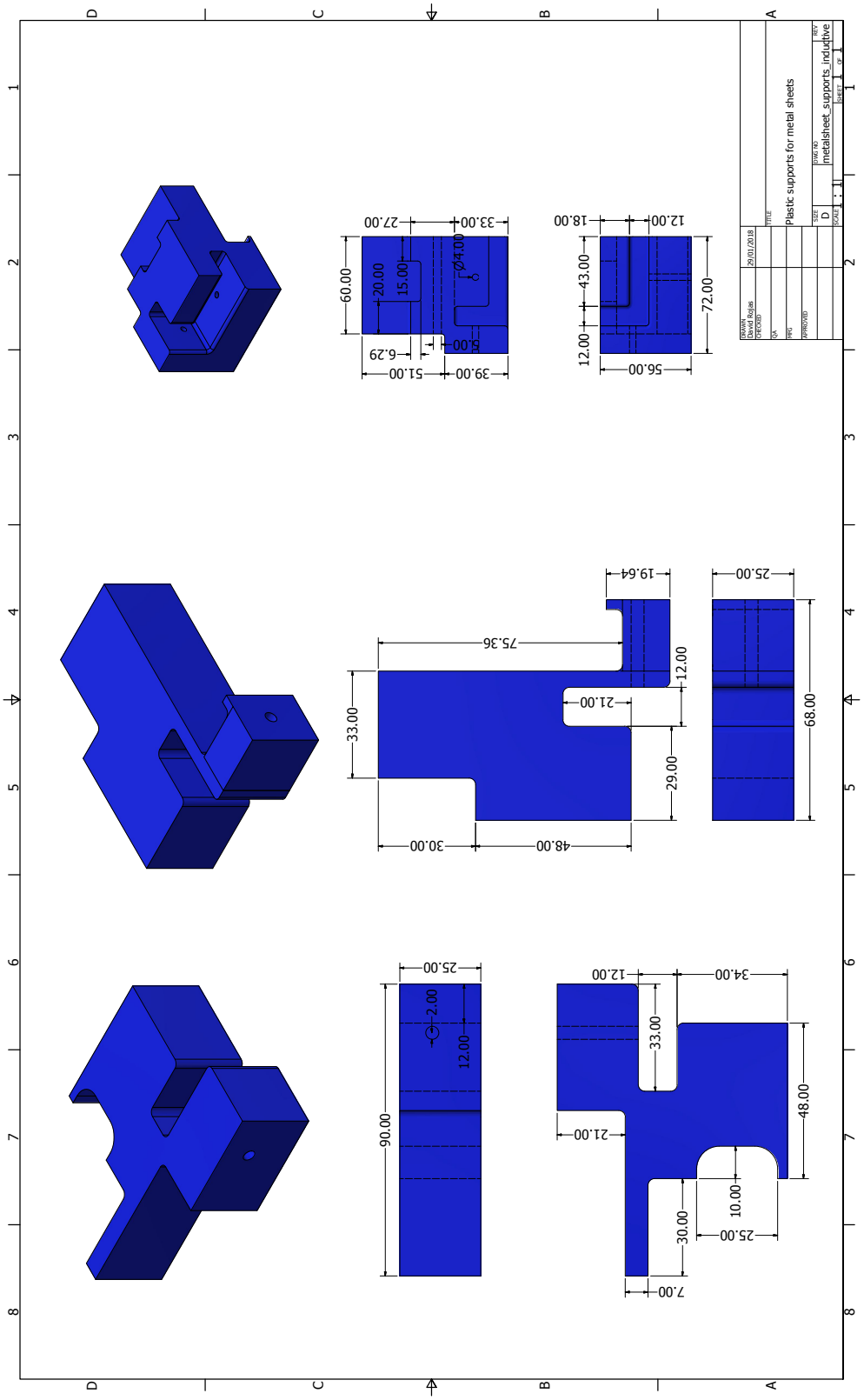
Plastic supports for metal sheets
metalsheet_supports_inductive
29/01/2018
Dawid Rojas
SIZE D
SCALE 2 : 1
SHEET 1 OF 1
REV
DRAWN
CHECKED
QA
MFG
APPROVED
DWG NO
TITLE
27.00
33.00
Ø4.00
60.00
20.00
15.00
6.29
5.00
51.00
39.00
18.00
12.00
43.00
72.00
12.00
56.00
19.64
25.00
75.36
12.00
21.00
33.00
68.00
29.00
30.00
48.00
25.00
2.00
12.00
90.00
12.00
34.00
33.00
48.00
21.00
10.00
30.00
25.00
7.00

B.3 SMHM module box and LED pivot

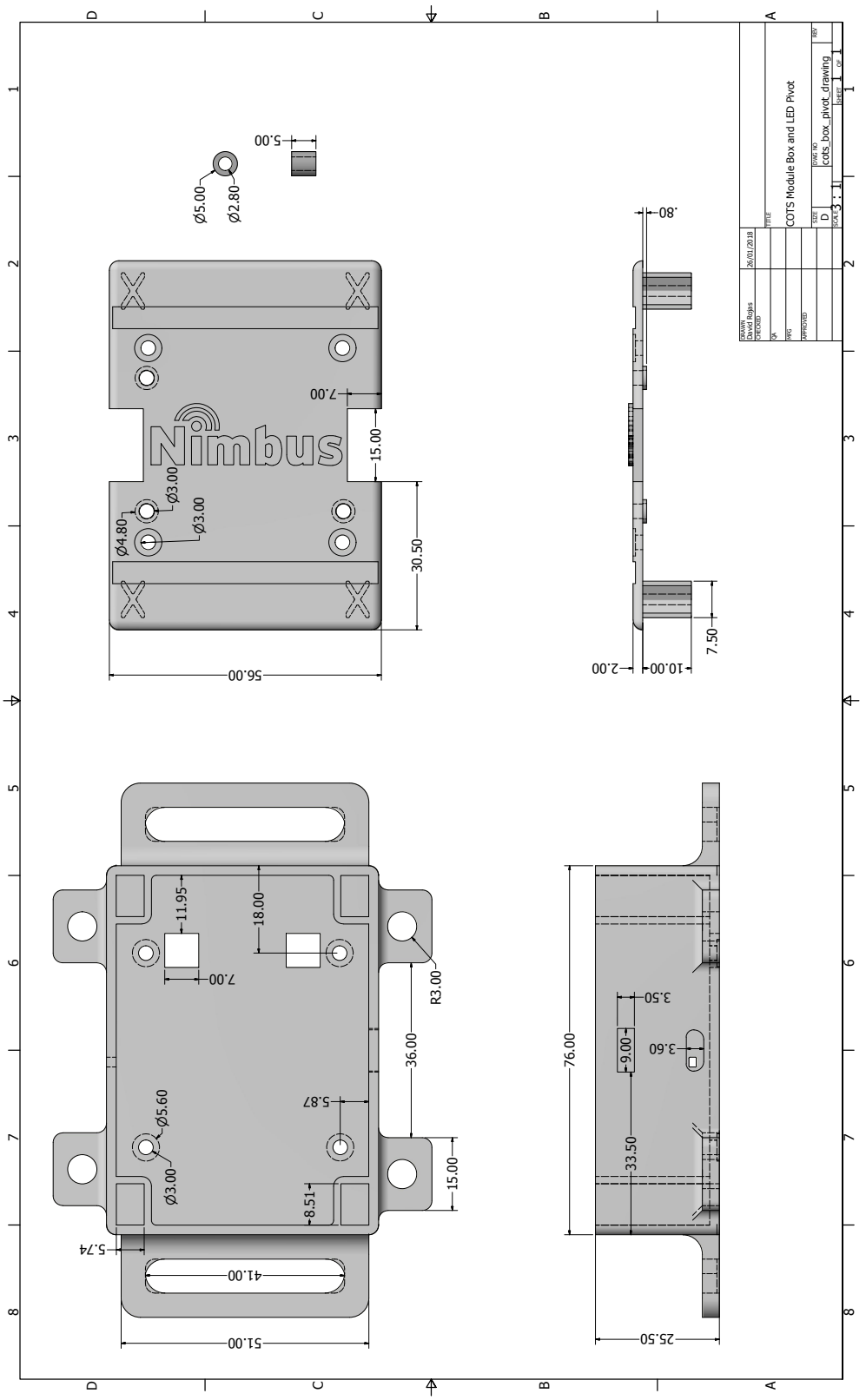

Appendix C

Firmware and Software

C.1 Firmware

- **contiki_code:** This contains the firmware developed for both wireless sensing modules. The *contiki* folder has the unmodified Contiki 2.6 core, while the rest of the folders include all the firmware specifically developed for this thesis.
  Download: http://www.davidrojas.co.uk/contiki_code.zip

C.2 Software

- **wirelessPyGTW:** This contains the software scripts and UI developed in Python and Qt to control and manage the network of sensing modules.
  Download: http://www.davidrojas.co.uk/wirelessPyGTW.zip
- **trident_scripts:** This contains the python scripts developed to analyse and plot the raw data from the Trident wireless characterisation experiments reported in this thesis.
  Download: http://www.davidrojas.co.uk/trident_scripts.zip